

CONTROL, SENSING, AND TELEMANIPULATION
OF SURGICAL CONTINUUM ROBOTS

By

Andrea Bajo

Dissertation

Submitted to the Faculty of the
Graduate School of Vanderbilt University
in partial fulfillment of the requirements
for the degree of

DOCTOR OF PHILOSOPHY

in

Mechanical Engineering

May 2013

Nashville, Tennessee

Approved

Dr Nabil Simaan
Dr Robert J. Webster III
Dr Michael Goldfarb

© 2013 by Andrea Bajo
All Rights Reserved

MECHANICAL ENGINEERING

CONTROL, SENSING, AND TELEMANIPULATION
OF SURGICAL CONTINUUM ROBOTS

ANDREA BAJO

Dissertation under the direction of Professor Nabil Simaan

New surgical paradigms such as natural orifice surgery and single port access surgery present technological challenges such as indirect routes of access, constrained workspace, sensory presence, higher degrees of freedom manipulators, force feedback and control. This research investigates design and control aspects of continuum robots as enabling technology that overcomes these new technological challenges while offering surgeons safe and intelligent surgical tools.

Although research in the area of continuum robots has grown exponentially in the last ten years, several knowledge gaps remain un-addressed in the area of control and sensing of these devices such as unified methods for enhanced tracking performance, real-time constrained motion planning, direct force control, collision detection, contact estimation, shape and stiffness characterization of unknown environments. This doctoral dissertation investigate algorithms and methods for addressing these technological gaps and evaluates them on state-of-the-art robotic systems for laparoscopy, transurethral bladder tumor resection, and transnasal access to the throat developed at the Advanced Robotics and Mechanisms Application Laboratory at Vanderbilt University.

ACKNOWLEDGEMENTS

First of all, I would like to thank my mentor Dr. Nabil Simaan for his attentive and continuous guidance since I first began working with him as a summer undergraduate intern in 2007. Dr. Simaan's ethics, passion, and dedication for research and innovation persuaded me to pursue an advanced degree in engineering. During all these years (2007-2013), he has forged the engineer I am by always telling me what I needed to hear and know in order to succeed on my own. He took a bet with bringing me to Columbia University and since then he has never failed to convey how important I was for the A.R.M.A. Laboratory and its research. His esteem gave me the confidence to conclude my doctoral studies.

I also wish to thank the brilliant scientists I had the honor and pleasure to work with: Dr. Roger Goldman, Dr. Austin Reiter, Dr. Stephen Tully, Dr. Latif Dharamsi, Dr. Rayan Pickens, Dr. Peter Allen, Dr. Howie Choset, Dr. Dennis Fowler, Dr. James Netterville, and Professor Alessandro De Luca. Furthermore, I would also like to thank current and former A.R.M.A. Lab members: Mr. Jason Pile, Mr. Long Wang, Mr. Haoran Yu, Miss Kyoko Yoshida, Dr. Kai Xu, Dr. Jian Zhang, Dr. Wei Wei, Dr. Jienan Ding, Dr. Alessio Salerno, and Mr. Saleem Hamid. Finally, I would like to thank my colleagues at Ximedica LLC: Mr. Corey Libby, Dr. Peter Cameron, and Mr. Rene Robert.

Special thanks go to all the people who made my (personal and academic) life easier: Professor Raimondo Betti, Dr. Nicola Chiara, Mr. Ettore Morelli, Dr. Matteo Caligaris, Ing. Mario Grassi, Mr. Giuseppe Del Giudice, Mr. Fahad Faruqui, Mr. Dennis Rief, Mr. Urs Luedi, Ms. Rebecca Chambers, Ms. Suzanne Weiss, Ms. Jean Miller, Ms. Myrtle Daniels, and Mr. John Fellenstein.

My master and doctoral research would have not been possible without the generous support of NSF grant No. IIS-1063750, NIH grant No. 7R21EB007779, the Honor Center of Italian Universities (H2CU), Dr. Samuel Rubinstein's family, and Columbia University and Vanderbilt University internal funds.

Finally, I would like to thank my parents, Alfredo and Daniela, for raising me to be the person I am and my love and best friend, Kaleena, for unconditionally believing in me and sharing her life with me.

TABLE OF CONTENTS

ACKNOWLEDGEMENTS	iii
LIST OF TABLES	viii
LIST OF FIGURES	ix
Chapter	
I. INTRODUCTION	1
Motivation and Scope of Work	1
Related Work	4
Motion Control of Continuum Robots	4
Constrained Motion Control	7
Collision Detection and Estimation of Contact Location	8
Force Sensing and Control	9
Outline	12
II. MODELING OF MULTI-BACKBONE CONTINUUM ROBOTS	15
Theoretical Kinematics	15
Direct Kinematics	15
Direct Instantaneous Kinematics	18
Constrained Kinematics	21
Direct Constrained Kinematics	23
Direct Constrained Instantaneous Kinematics	24
Statics	26
Actuation Compensation	26
III. MOTION CONTROL OF MULTI-BACKBONE CONTINUUM ROBOTS	29
Mixed Feedback for Improved Tracking Performance	29
Configuration Space Controller (CSC)	30
Experimental Setup	31
Experimental Evaluation	34
Effects of the Controller on Phase Lag	34
Tracking in Configuration Space and Coupling Effects Between Segments	34
Single-DoF Configuration Space Tracking	35
Multi-DoF Configuration Space tracking	36

External Wrench Disturbance	39
End-disk Orientation Error	40
Telemanipulation Architecture	43
Desired slave pose	44
Slave Tracking Error	46
Slave desired twist	48
Redundancy Resolution	50
Constrained Motion Control	52
Constrained Redundancy Resolution	52
Virtual Fixture Design and Implementation	54
Conclusions	57
IV. CONTACT DETECTION AND ESTIMATION OF CONTACT LOCATIONS	59
Force-Based Collision Detection	59
Joint Force Deviation	60
Contact Detectability	60
Experimental Results	61
Kinematics-Based Collision Detection	63
Screw Motion Deviation	63
Collision detection	69
Experimental Results	71
Single-Contact Collision Detection	71
Multi-Contact Collision Detection	74
Repeatability of Collision Detection	80
Kinematic-Based Estimation of Contact Location	80
Experimental Results	83
Conclusions	85
V. HYBRID MOTION/FORCE CONTROL OF MULTI-BACKBONE CONTINUUM ROBOTS	88
Control Architecture	90
A First-order Model of Contact	90
Projection Matrices	93
Control Architecture	93
Compensation of Uncertainties	96
Wrench Estimation	97
Experimental Results	98
The Continuum Manipulator	100
Estimation of Uncertainties	106
Methods	106
Results	106

Force regulation	110
Methods	110
Results	110
Force Regulated Shape Estimation	112
Methods	118
Results	119
Stiffness Imaging	120
Methods	126
Results	126
VI. CLINICAL APPLICATIONS	128
A Telesurgical System for Single Port Access Surgery	128
Clinical Motivations	128
Surgical Slave System	130
Direct Kinematics	131
Joint-Space Kinematics	133
Telemanipulation	135
Telemanipulation Architecture	135
Compensation	137
Backlash Compensation	138
Actuation Compensation	138
Augmenting the Workspace	139
Preliminary Evaluations	140
Pick and place and hand exchange	141
Passing surgical needles and knot tying	142
Conclusions	142
A Telesurgical System for Transurethral Resection of Bladder Tu- mors (TURBT)	145
Clinical Motivations	145
Surgical Slave System	147
Direct Kinematics	148
Differential Kinematics	149
Telemanipulation Architecture	151
Experimental Results	152
Ex-Vivo Bovine Bladder	152
Laser delivery	152
Biopsy	153
Constrained Motion Control	155
Conclusions	159
A Telesurgical System for Transnasal Microsurgery of the Throat	161
Introduction	161
Clinical Motivation	163
The Telerobotic System	165

The Surgical Slave	166
Control Architecture	169
Experimental Evaluation	175
Rapid Deployment	175
Targeting in Deep Surgical Sites	176
Cadaveric Evaluation	179
Discussion	180
Conclusions	183
VII. CONCLUSIONS	185
Summary of Findings	185
Future Research Directions	188
REFERENCES	189

LIST OF TABLES

Table	Page
III.1. Dimensional specifications for the continuum robot	33
IV.1. Contact estimation along the first segment. Units of mm	84
IV.2. Contact estimation along the second segment. Units of mm	85
IV.3. Contact estimation along the third segment. Units of mm	86
V.1. Kinematic and static parameters of the continuum robot used for the experiments	105
V.2. Experimental result of force regulation in the \hat{x} direction for three configurations $\theta = 80^\circ, 60^\circ, 40^\circ$, and three force magnitudes 5 gr, 10 gr, and 15 gr.	111
V.3. Experimental result of force regulation in the \hat{y} direction for three configurations $\theta = 80^\circ, 60^\circ, 40^\circ$, and an applied force of 10 gr.	111
VI.1. Slave telemanipulation parameters	136
VI.2. Slave linear velocity parameters	151

LIST OF FIGURES

	Page
Figure I.1. Commercially available robotic and manual systems for SPAS. (a) The Transenterix Spider hand instruments. (b) The Olimpus HiQ LS Curved 5 mm hand instruments. (c) The Storz Endocone hand instruments. (d) The Intuitive daVinci.	5
Figure I.2. (a) The Insertable Robotic Effectors Platform (IREP) for Single Port Access Surgery (SPAS). (b) The Rapidly Deployable Robotic Platform (RDRP) for transurethral resection and surveillance. (c) The RDRP for trans-nasal access to the throat.	5
Figure I.3. A multi-segment continuum robot detecting a single collision (a), multiple collisions (b), and total-arm constraint (c).	9
 II.1. Kinematic nomenclature of two consecutive segments	17
II.2. Simulation sequence of the interaction of a single segment continuum robot with an obstacle according to the proposed constrained kinematics model.	21
II.3. Overlay of a single continuum segment before and after collision with a static object. The constrained part (bottom) remains fixed while the unconstrained part bends like a shorter continuum segment.	22
II.4. Constrained kinematic nomenclature. Segment k is constrained at the third disk. Contact frame C_k describes position and orientation of the static portion of the segment. End disk frame G_k describes position and orientation of the end disk of the segment.	24
 III.1. Block diagram of the proposed tiered mixed feedback controller for multi-segment multi-backbone continuum robots.	32
III.2. The experimental setup consist of a nine-axis actuation unit, a 3-segment continuum robot, a magnetic field generator, and four magnetic sensors attached to the robots base (0), the end disk of the first segment (1), the end disk of the second segment (2), and robots end-effector (3).	33
III.3. Phase lag affecting the first segment with and without CSC	35

III.4.	Phase lag affecting the second segment with and without CSC	36
III.5.	Phase lag affecting the third segment with and without CSC	37
III.6.	Tracking performance for θ_{L_1}	38
III.7.	Coupling effect between δ_1 and θ_{L_1}	38
III.8.	Coupling effect between the second segment and θ_{L_1}	39
III.9.	Coupling effect between the third segment and θ_{L_1}	40
III.10.	Errors in the configuration of the first segment	41
III.11.	Errors in the configuration of the second segment	42
III.12.	Errors in the configuration of the third segment	43
III.13.	External wrench disturbance setup. (a) a calibration weight is attached to the end-effector using a rope and a frictionless pulley. (b) the continuum robot with no load applied. (c) the continuum robot with the external load applied.	44
III.14.	Response of the controller to an external wrench disturbance. (a) time history of θ_{L_1} , θ_{L_2} , θ_{L_3} . (b) time history of δ_1 , δ_2 , and δ_3	45
III.15.	Roll error affecting the orientation of the third segment as a function of bending angle θ_{L_3}	46
III.16.	Definition of end-effector coordinate system of the continuum arm (left) and the Phantom Omni (right)	47
III.17.	Control architecture of the surgical robotic system.	52
III.18.	The configurations of a three-segment continuum robot are estimated by a learning-based algorithm that interpolates a stereo feature descriptor manifold using Radial Basis Functions (Reiter, Bajo <i>et al.</i>).	56
IV.1.	Force-based collision detection experiments using a two-segment continuum robot equipped with load cells. Difference in ξ (a) with and without contact during a pre-determined motion (b).	62

IV.2.	The group of ISAs after the contact is appreciably shifted toward the ED of the segment because of the smaller radius of curvature of the unconstrained portion of the segment. The closer the disk in contact is to the end disk, the closer the post-contact ISAs will be to the end disk.	65
IV.3.	Comparison between the theoretical axode of motion (green) and the real one (magenta) obtained by extrinsic sensory information when no contact is applied to the continuum segment.	66
IV.4.	Comparison between the theoretical axode of motion (green) and the real one (magenta) obtained by extrinsic sensory information when a contact is applied to the continuum segment.	67
IV.5.	Comparison of the ISA's for a perfect sensor (a) and for a noisy sensor (b). The dashed ISA's indicates that the magnitude of the angular velocity is smaller than 0.1 rad/s	68
IV.6.	Constraint acting at the first segment. (a) time history of μ_1 , (b) time history of μ_2 , (c) time history of μ_3	75
IV.7.	Constraint acting at the second segment. (a) time history of μ_1 , (b) time history of μ_2 , (c) time history of μ_3	76
IV.8.	Constraint acting at the third segment. (a) time history of μ_1 , (b) time history of μ_2 , (c) time history of μ_3	77
IV.9.	Collision detection experiments using a three-segment continuum robot equipped with magnetic sensors. (a) Constraint acting at the first segment. (b) Constraint acting at the second segment. (c) Constraint acting at the third segment. (d) Collision with another flexible arm.	78
IV.10.	Detection of multiple collisions: (a) time history of μ_1 , (b) time history of μ_2 , (c) time history of μ_3	79
IV.11.	Multiple collision detection experiments using a three-segment continuum robot equipped with magnetic sensors. (a) Dual collision detection with detected at the first and second segment. (b) Total constraint acting at all segment simultaneously.	80
IV.12.	Repeatability analysis of contact detection. Time history of μ_2 . . .	81
IV.13.	Effects on shape deviation when assumption A2 is violated.	85

V.1.	Classic hybrid motion/force control of rigid-link industrial manipulators [56]. Ω and $\bar{\Omega}$ are projection matrices, \mathbf{J} is the Jacobian matrix of the manipulator, \mathbf{B} is the inertia matrix of the manipulator, $\boldsymbol{\Gamma}_{des}$ is the joint torques vector that accomplishes the desired motion and force tasks, and $\hat{\boldsymbol{\Gamma}}_{des}$ is the joint torque vector that includes the feedback linearization term.	90
V.2.	Proposed hybrid motion/force control of multi-backbone continuum robots with intrinsic force sensing. Ω and $\bar{\Omega}$ are projection matrices, \mathbf{J}_{xy} is the Jacobian matrix, \mathbf{K} is the configuration-space stiffness matrix, Ψ is the configuration space vector, \mathbf{K}_a is the joint-space stiffness matrix.	91
V.3.	Wrench and twist screw bases corresponding with a frictionless point contact (adapted from [67])	92
V.4.	Kinematics nomenclature used in this paper.	99
V.5.	Error between the expected and actual actuation force on backbone 1 versus bending angle θ for different values of δ	108
V.6.	Error between the expected and actual actuation force on backbone 2 versus bending angle θ for different values of δ	108
V.7.	Error between the expected and actual actuation force on backbone 3 versus bending angle θ for different values of δ	109
V.8.	Experimental setup for force regulation experiments. The setup consist of the continuum manipulator, the ATI Nano 17 force/torque sensor, and a hand-controlled linear actuator for the placement of the sensor at different heights.	109
V.9.	Force step response on a silicone block in the \hat{x} direction from starting configuration $\theta = 80^\circ$, $\delta = 0^\circ$	113
V.10.	Force step response on a silicone block in the \hat{x} direction from starting configuration $\theta = 60^\circ$, $\delta = 0^\circ$	114
V.11.	Force step response on a silicone block in the \hat{x} direction from starting configuration $\theta = 40^\circ$, $\delta = 0^\circ$	115
V.12.	Force step response on a silicone block in the \hat{y} direction from three starting configurations: 1) $\theta = 80^\circ$, $\delta = 0$, 2) $\theta = 60^\circ$, $\delta = 0$, and 3) 1) $\theta = 40^\circ$, $\delta = 0^\circ$	116

V.13.	Experimental setup for shape estimation of a silicon diamond-shaped extrusion (a). The base plane of the extrusion is placed at approximately 18 mm from the origin along the x direction (b). The user actively controlled motion of the probe in the y and z directions. The force controller regulates a force with a magnitude of 0.1 N in the x direction.	117
V.14.	Probe for the manual scan of the phantom tissue. A similar probe is attached to a non-magnetic rod. A \odot 0.9 mm is secured to the probe.	119
V.15.	Estimate shape under force-regulated scan.	121
V.16.	Ground truth shape.	122
V.17.	Shape estimation error.	123
V.18.	Setup measurements to localize the mockup blood vessel. The image shows the setup, a ruler, and pixel measurements taken with the Matlab Image Processing Toolbox. From the image is possible to define a scaling factor that relates pixels to mm, the distance of the centerline of the blood vessel from the base of the robot and its width.	124
V.19.	Colormap of the estimated surface during the first scan (5 gr).	124
V.20.	Colormap of the estimated surface the last scan (25 gr).	125
V.21.	Stiffness imaging	125
VI.1.	The Insertable Robotic Effectors Platform (IREP) with two continuum arms, wrists, grippers, stereo vision camera head, and illumination system	130
VI.2.	Kinematics nomenclature for one arm of the IREP	134
VI.3.	Telemanipulation integration architecture of the IREP. The notation q_{ij} is used as shorthand notation to vector $q_i \dots q_j$	135
VI.4.	Snapshots taken from the vision tracker during data collection	137
VI.5.	current versus commanded x position of the moving ring	138
VI.6.	Weight profile for the insertion stage and different values of n	140
VI.7.	Sequence of pick and place using the dexterity peg board	143
VI.8.	Sequence of pick soft object swap between hands	143

VI.9.	Sequence of knot tying under bimanual telemanipulation	144
VI.10.	Overview of the TURBT procedure. The resectoscope is inserted through the urethra to access the bladder.	145
VI.11.	Kinematics nomenclature of the surgical system. Five coordinate systems are defined: 1) base frame $\{\hat{x}_0, \hat{y}_0, \hat{z}_0\}$, 2) first segment base disk frame $\{\hat{x}_1, \hat{y}_1, \hat{z}_1\}$, 3) second segment base disk frame $\{\hat{x}_2, \hat{y}_2, \hat{z}_2\}$, 4) end-effector frame $\{\hat{x}_3, \hat{y}_3, \hat{z}_3\}$, and 5) tool frame $\{\hat{x}_4, \hat{y}_4, \hat{z}_4\}$	149
VI.12.	Telemanipulation architecture.	151
VI.13.	The experimental setup consists of an explanted bovine bladder, an external 30° scope, a 6 DoF Sensable Phantom Omni, the robot's actuation unit, and control computer that also provide the vision feedback from the on-board fiberscope.	152
VI.14.	Picture sequence of laser delivery. The laser fiber is deployed through the continuum manipulator and the end-effector commanded via the master manipulator.	153
VI.15.	Picture sequence of laser delivery result. The bovine bladder wall was cut and the target area inspected.	154
VI.16.	En-block resection demonstration.	154
VI.17.	En-block resection results. The tissues was successfully extracted from inside the bladder and examined.	155
VI.18.	Constrained motion experiment. The surgical slave is commanded to retract into the resectoscope ($q_{ins} < 0$). The virtual fixture law automatically straightens the continuum robot (θ_1 and θ_2 grow). . .	157
VI.19.	The experimental setup consists of a 7-axes actuation unit, a urologic resectoscope, a 2-segment continuum robot, a 250 ml beaker, and three tubes with various diameters. The beaker approximates the size of an average-sized bladder when inflated while the tubes were used for testing targeting accuracy.	158
VI.20.	Image sequence of constrained targeting in the interior quadrant. The first continuum segment is partially retracted inside the resectoscope. Its motion is autonomously limited by the configuration space virtual fixture while allowing for the completion of the task. .	160

VI.21.	Picture sequence of bladder coverage. The slave manipulator, under telemanipulation control, is guided to cover progressively the posterior and interior quadrants. The manipulator goes from a completely deployed configuration to a completely folded configuration into the urologic resectoscope.	160
VI.22.	Top: overview of the anatomy. Middle: The flexible robotic stem and a 4 mm bronchoscope are deployed to the larynx through the nasal cavity. Bottom: The robotic end-effector carries a needle for vocal fold repair and a 1.2mm fiberscope.	162
VI.23.	Procedure overview for the treatment of vocal fold nerve paralysis. Collagen is injected into the paralyzed side of the vocal fold in order to close the gap between the vocal fold lips and allows for proper speech and swallowing.	165
VI.24.	The actuation unit consists of a linear stage for stem insertion, six pistons for the continuum segments actuation, potentiometers for homing and redundant positioning information, and load cells for force sensing and compliant insertion.	166
VI.25.	Kinematics nomenclature used in this section.	167
VI.26.	Telemanipulation mapping between the robot's end-effector, the master manipulator and the fiberscope view.	171
VI.27.	Control architecture of the telesurgical system.	171
VI.28.	The experimental setup consists of a $\varnothing 5$ mm continuum robot with flexible actuation lines, a 34Fr nasopharyngeal tube, a Nasco AMBU intubation trainer, an Ascension Technology trakSTAR 2 with flat transmitter, one $\varnothing 0.9$ mm magnetic coil, and an ATI Gamma force/torque sensor.	175
VI.29.	Experiment #1's time history of the insertion and extraction forces exerted on the ATI Gamma sensor.	177
VI.30.	Experimental setup for the targeting evaluation. The surgeons guided the surgical slave using a Sensable Phantom Omni and the image provided by the onboard fiberscope.	177
VI.31.	Picture sequence of the surgeon targeting pre-determined points on the true vocal folds using 2D vision through the onboard fiberscope. Top row: view from the additional HD endoscope. Bottom row: view from the onboard fiberscope.	178

VI.32. Experimental setup of the cadaveric evaluation of insertion and targeting of the voice box: 1) robots actuation unit, 2) cadavers head, 3) traksSTAR 2 flat transmitter, 4) bronchoscope, 5) visualization station, 6) surgeon.	180
VI.33. Image sequence of the insertion from the auxiliary bronchoscope inserted through the second nostril. The tip of the robot emerges from the nasopharyngeal tube, bends down to avoid the epiglottis, and continues the navigation of the upper airway cavity to reach the voice box.	181
VI.34. Image of robots needle puncturing the left vocal fold.	182

List of Algorithms

1.	Compute Desired Pose	47
2.	Compute Desired Twist	49
3.	Virtual Fixture	56
4.	Collision detection	72
5.	Estimation of Contact Location	81

CHAPTER I

INTRODUCTION

Motivation and Scope of Work

Minimally invasive surgery (MIS) has gradually developed into a standard of care in many disciplines of surgery such as urologic, neurologic, cardiothoracic, head and neck, and gynecologic surgery. This paradigm trades surgeon's physiological limitations such as fatigue, dexterity, accuracy, and precision for patient's reduced trauma, faster post-operative recovery, and fewer complications. In the past fifteen years, Robotically-Assisted MIS (RAMIS) has greatly enhanced the outcome of MIS procedures and enabled less invasive or endoscopic procedures that are very difficult or impossible to perform conventionally such as single port access surgery (SPAS) or natural orifice transluminal endoscopic surgery (NOTES).

However, the outcomes promised by SPAS and NOTES are yet to be fully demonstrated because of the lack of surgical assistants and algorithms designed to meet the challenges of these new paradigms. Hand-held instruments for SPAS such as the Transenterix Spider®, the Olimpus HiQ LS®, and the Storz Endocone® have been developed along with modifications of current FDA approved robotics systems such as the SPAS daVinci® (Figure I.1). However, these systems lack dexterity, arm co-ordination, means of ablation, anastomosis, intracorporeal tissue management, and any kinesthetic feedback.

As surgeons explore ways of reaching deep surgical sites with less incisions, the limitations of current surgical instruments do not allow to exploit the full potentials of these new paradigms. Future surgical systems designed to meet the challenges of

SPAS and NOTES will require multiple high degrees-of-freedom (DoF) robotic manipulators to augment surgical skills and tele-presence; enhance dexterity in confined spaces; provide an adequate set of surgical tools, vision, force feedback; and be able to intelligently react to undesired contacts along their entire structures.

Continuum robots are continuously-bending manipulators that offer an opportunity to overcome the limitations of current rigid-link robotics and hand instruments because of their inherent compliance, multiform designs and actuation means [83, 105], reduced backlash due to the absence of serial links, down-scalability, MRI-compatibility [98], and force sensing capabilities [115, 117, 86]. However, there are some technical challenges that need to be addressed in order to make continuum robots perfect candidates for future MIS, SPAS, and NOTES robotic systems.

First, as researchers rely on passive compliance for safeguarding the anatomy, continuum and wire-actuated robots suffer performance degradation in terms of payload carrying capability, position accuracy, tracking fidelity, and responsiveness. Despite the fundamental theoretical work done in the field of actuation compensation and modeling of continuum robots, there is a lack of delineation of the role of extrinsic feedback and model-based actuation compensation for the telemanipulation of hybrid systems including continuum, rigid-link, and wire-actuated mechanisms. As the complexity of robotic systems increases, additional sensory information is required for improving the performances of these devices.

Second, as robots aim to reach deep surgical sites along increasingly tortuous paths, there is a need to free the surgeon from the onus of safeguarding against surgical trauma and guarantee safe coexistence of multiple surgical instruments sharing the same workspace. This added complexity requires intelligent surgical slaves that are able to detect collisions with the surrounding anatomy to prevent inadvertent trauma

to the patient. These robots will need to support automated or semiautomated insertion into the anatomy, estimate contact locations along their structure, regulate their contact forces, and use their multi-point interactions to enhance end-effector precision and safety.

Third, successful manipulation tasks require the surgeon to sense forces and moments that the instrument applies to the tissue during surgical procedures [104]. The benefits of force feedback and control in surgery are to be found in surgical tasks that are not currently possible during conventional MIS such as palpation and tissue stiffness estimation. Surgeons often use palpation information during open surgery to detect anatomical features prior to resection or to localize small masses and possibly correspond them to pre-operative images.

This doctoral dissertation addresses these technical challenges while mainly focusing on technical enablers for surgical slave intelligence and safe manipulation. The main topics covered in this work are:

- Control algorithms for improved accuracy, bandwidth, and responsiveness of teleoperated high DoF hybrid continuum surgical robots.
- Algorithmic solutions for collision detection and contact location estimation along multisegment continuum robots suitable for robotic-assisted interventions.
- Algorithms for hybrid motion/force control of continuum robots to enable exploration, palpation, and tissue stiffness estimation in deep surgical sites.

In addition to the aforementioned theoretical contributions, this doctoral work seeks new surgical frontiers to demonstrate the efficacy of these new algorithms. The proposed frameworks will be tested on three robotic platforms for laparoscopy, trans-oral laryngeal surgery, transurethral resection and surveillance, and trans-nasal laryngeal microsurgery. The Insertable Robotic Effectors Platform (IREP) [113, 29]

(Figure I.2(a)) will be used to demonstrate telemanipulation, of hybrid high-DoF systems during laparoscopy and trans-oral laryngeal surgery. Its unique design presents challenges in terms of actuation compensation, coordinated control, and dexterity enhancement. Force control, collision detection, and a novel approach to access-based virtual fixture will be demonstrated on the Rapidly Deployable Platform (RDP) for transurethral resection of bladder tumor (TURBT) shown in Figure I.2(b). In addition to the benefit of force feedback in palpation tasks inside the bladder, this system require a safe interaction of the continuum end-effector with the rigid access constraint due to the urologic resectoscope. Finally, the control algorithms for telemanipulation, motion compensation, and complaint motion control will be evaluated on a novel robotic effector for trans-nasal intervention of the upper airways as shown in Figure I.2(c).

Related Work

This section reports on research related to collision detection, estimation of contact location, control of continuum robots, and hybrid force/motion control.

Motion Control of Continuum Robots

Modeling of continuum robots builds upon the work on hyper-redundant manipulators of Chirikjian and Burdick [20] and Zanganeh and Angeles [119]. The kinematics of single- and multi-segment continuum robots was initially presented by Gravagne and Walker [37], Hannan and Walker [41], and Jones and Walker [49]. Jones and Walker [49] also proposed algorithms for real-time implementation. Simaan et al. [96, 94] proposed a design in which the assumption of circular bending dramatically simplifies the computation of direct and inverse kinematics. Xu and Simaan [116]

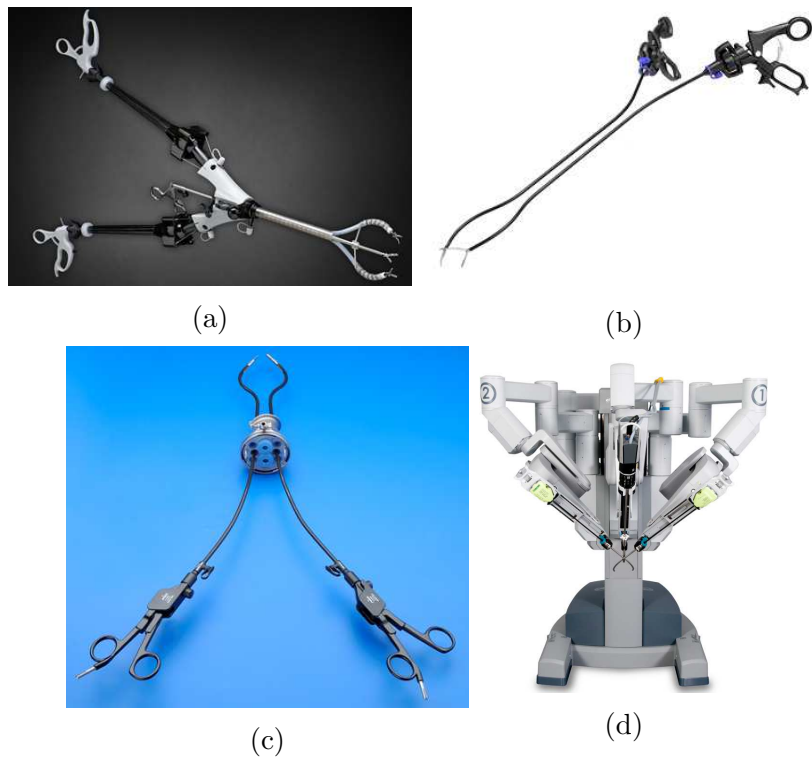


Figure I.1: Commercially available robotic and manual systems for SPAS. (a) The Transenterix Spider hand instruments. (b) The Olympus HiQ LS Curved 5 mm hand instruments. (c) The Storz Endocone hand instruments. (d) The Intuitive daVinci.

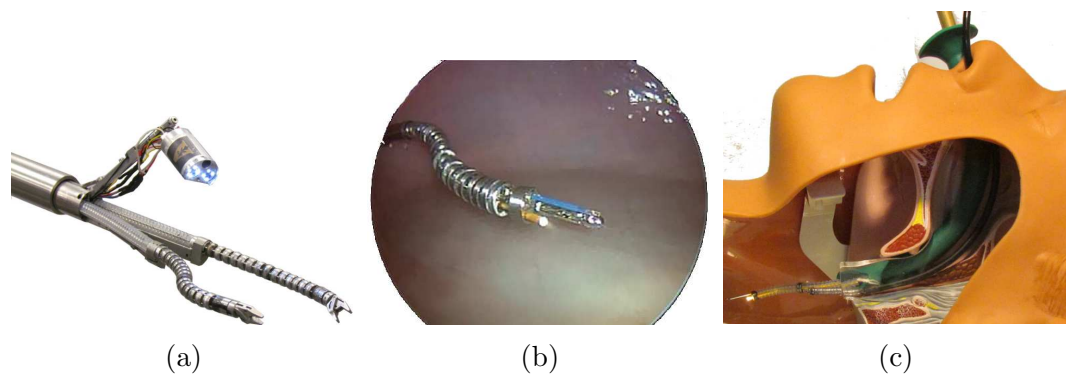


Figure I.2: (a) The Insertable Robotic Effectors Platform (IREP) for Single Port Access Surgery (SPAS). (b) The Rapidly Deployable Robotic Platform (RDRP) for transurethral resection and surveillance. (c) The RDRP for trans-nasal access to the throat.

validated this assumption and proposed and exact kinematics model for continuum robots using elliptic integral. Webster et al. [106] and Dupont et all. [30] presented modeling and control of pre-curved continuum robots. Rucker et al. [85] presented and exact model for externally loaded concentric-tube robots. Furthermore, Rucker and Webster [86] proposed algorithms for real-time control of these type of robots. Xu and Simaan proposed two methods for actuation compensation of multi-backbone continuum robots. The first method involves a closed form compensation derived from theoretical mechanics of solids. The compensation law takes into account the force applied to the actuation lines and their stiffness. The second method consists of a recursive least-square estimator for backlash and model uncertainties. Simaan et al. [97] further refined this approach to compensate for the configurations of multiple segments. Agrawal et al. [2] proposed a smooth backlash inverse for the control of cable actuated devices. Kesner and Howe [55] presented algorithms for friction modeling and compensation in active catheters. Moreover, other researchers tried to use vision to estimate the pose of continuum manipulators. Camarillo et al. [15, 14] presented algorithms for vision-based configuration tracking for continuum robots with couple tendons. Croom et al. [22] used self-organizing maps for estimating the shape of a concentric-tube continuum manipulator. Reiter et al. [81, 80] presented a feature-based algorithm for pose estimation of continuum robots with vertebrae. Penning et al. [73] proposed a catheter design with embedded magnetic sensors for close loop control in task space.

The contribution of this doctoral dissertation in the area of motion control of continuum robots is in proposing the design of a controller that uses both intrinsic and extrinsic online sensory information for improving the configuration tracking and for overcoming modeling uncertainties. We explore the utility of this mixed

feedback controller in enhancing regulation and tracking control of flexible multi-segment continuum robots. The configuration space controller runs on top of the low level, joint-space, PD controller based on the instantaneous inverse kinematics model of the robot.

Constrained Motion Control

As continuum robots reach deeper surgical sites, sensory presence, trajectory planning, and the enforcement of virtual fixtures is crucial for completing complex surgical tasks such as navigation in unstructured environments, suturing, knot tying, and dissection. In [19, 62], the authors investigated obstacle avoidance for hyper-redundant robots using geometric methods. In [51, 52], the authors proposed a library of virtual fixtures for key surgical tasks. In [100], the authors investigated path planning of steerable needles. These methods focus on the end-effector by either solving an optimization problem during path planning or enforcing task-space virtual fixtures. In this paper we propose to enforce virtual fixtures in the configuration space rather than task space and automatically adjusts the redundancy resolution for optimal tracking during constrained motion.

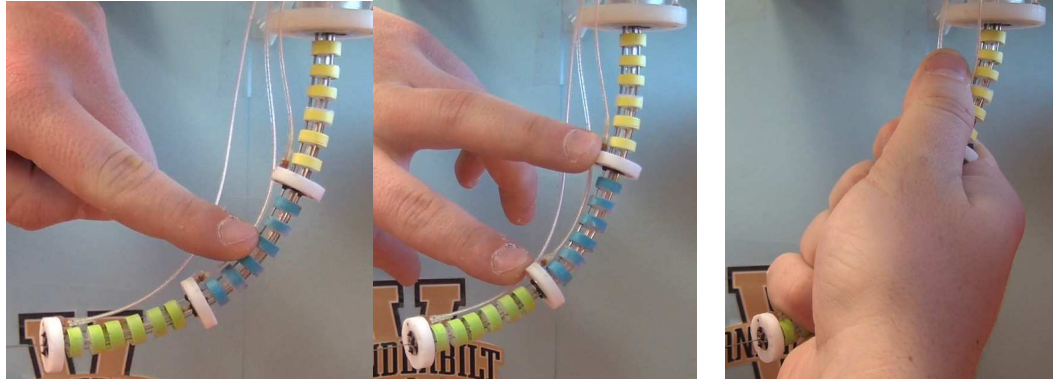
The contribution of this doctoral dissertation is in proposing the enforcement of virtual fixtures in the configuration space of the manipulator rather than in the task space as previously proposed in literature (i.e. [57]). In the case of continuum robots, the burden of safeguarding both the anatomy and the surgical slave can not be left to the surgeon. On the other hand, intelligent surgical slaves should be able to autonomously steer away from access and anatomical constraints and adjust the inversion of the kinematics. The configuration space often provides a lower-order space in which constraints along subsequent segments can be easily and intuitively defined.

Collision Detection and Estimation of Contact Location

Current robotic systems are incapable of fully characterizing their interaction with the environment. Full characterization of the interaction means: discerning collisions, localizing contact constraints, and estimating interaction forces. Although there are mature algorithms for compliant hybrid motion/force control [56, 24, 93, 71, 90], there exists no unified framework for the *impact* and *post-impact* phases. These algorithms require *a priori* knowledge of the environmental constraint geometry via formulation of natural and artificial constraints [78] or motion and constraint screws [67, 59, 32].

Previous works individually focused on collision detection [23, 39], and estimation of constraint locations [31, 25, 74]. De Luca *et al.* [23, 39] used the generalized momentum of serial robots to identify contact incidence and the link at which contact occurs. Eberman and Salisbury [31] proposed a least square method using estimate of contact location from tactile sensors and joint torque measurements to estimate the magnitude and the location of contact force. Petrovskaya *et al.* [74] and Debus *et al.* presented two different probabilistic approaches for contact estimation. Other researchers tried to overcome the limitations of rigid-link robots by developing sensitive robotic skins [61].

The contribution of this doctoral dissertation in the area of contact detection and estimation of contact location is in presenting a general framework for collision detection and contact estimation for an *n-segment* continuum robot. The framework relies only on the relative motion of each segment with respect to its own base. By working in local frames, collision detection and estimation of contact location are generalized for multi-segment continuum robots. A *Screw Motion Deviation* (SMD) is proposed based on the nominal forward kinematics of the robot and extrinsic sensory information. Online calculation of this deviation for each segment enables single- and multi-collision detection at multiple segments. Estimation of contact location is



(a) Single collision (b) Multiple collisions (c) Whole-arm constraint

Figure I.3: A multi-segment continuum robot detecting a single collision (a), multiple collisions (b), and total-arm constraint (c).

carried out by using a constrained kinematics model that describes the constrained motion of the continuum robot. Results demonstrate the ability of estimating the location of contacts, detecting collisions at any point along the robotic structure (Fig. I.3a), multiple collisions acting at different segments (Fig. I.3a), and *total arm* constraint (Fig. I.3c).

Force Sensing and Control

Successful and safe interaction with the environment requires robotic manipulators to simultaneously control motions and forces at the operational point [56]. When contact between the robot's end-effector and the environment occurs, reaction forces prevent motions in normal directions while possibly allowing translation of the contact point in the tangential directions. These directions depend on the type of contact such as point, line, and plane contacts, and the amount of friction between the two bodies [67].

There are mainly two methodologies to control interaction forces and motions: *impedance control* [44] and *hybrid motion/force control* [78]. Impedance control, a generalization of *admittance control* [111] and *stiffness control* [88], aims at regulating

the mechanical impedance of the operational point to contact forces exerted by and onto the environment. As a consequence, directions in which position should be controlled accurately are associated to a large impedance while directions in which the end-effector should comply with the environment are associated with a small impedance. On the other hand, hybrid motion/force control decouples control signals produced by two independent motion and force controllers by projecting them into orthogonal directions in which motions and forces should be independently controlled.

The main difference between the two methodologies is that impedance control indirectly control force via a position feedback while hybrid motion/force control has both position and force loops. The advantage of impedance control is that mode switching at the time of contact and accurate *a priori* knowledge of the geometric constraint and elasticity of the environment are not necessary. On the other hand, hybrid motion/force control require a fairly accurate knowledge of the contact constraint and may produce unstable behaviors during the impact phase because of the intermittent switching in control modes. However, when the robotic manipulator is required to accurately control position and force, the hybrid motion/force control provide better performance. For the interested reader, an exhaustive overview of these two methods, variants, and application are described in [118].

The innate compliance of continuum robots makes them the perfect candidates for medical applications because of their inherent safety [97, 35, 13, 55, 16, 63, 98, 28] and dexterous grasper because of the ability to adapt their shape to unknown objects [49]. However, passive compliance comes with a price of performance degradation in term of position accuracy, payload, and force exchange capabilities.

With this issue in mind, researchers have recently begun investigating algorithms for stiffness control [64], compliance motion control [4], and indirect force control [54] for continuum robots. In [64], the authors proposed a method for combining the

nominal forward kinematics and the deflection of the manipulator due to the external load to solve for the actuator positions required to generate the required tip stiffness. In [4], the authors proposed a method that allows multi-backbone continuum robots to comply to interaction forces acting at unknown locations. The algorithm compares the nominal and actual actuation forces and produces joint-space commands that bring the manipulator to a different configuration that minimizes the interaction force. In [54], the authors proposed an indirect force controller for flexible catheters and demonstrated the possibility to maintain contact with a fast moving object such as a beating heart. To the best of author’s knowledge, there are no algorithms for direct force control of continuum robots. The primary reason for this technological gap is twofold: 1) the lack of force sensors that meet the strict requirements of surgical continuum robots in terms of size, resolution, and sterilization; 2) a framework that ties task space forces, configuration space generalized forces, and joint space actuation forces.

In an effort to provide miniature robotic manipulators with force feedback, researchers have mainly investigated two methodologies: 1) design and manufacturing of miniature sensors for minimally invasive surgery [89, 103, 7]; 2) algorithms for *intrinsic force sensing* [115, 117, 86, 107]. Although the first methodology provides a direct measure of the force at the tip, its wide use is limited by the increasing demand of Magnetic Resonance Imaging (MRI) compatible surgical instruments, sterilizability, miniaturization, and cost. On the other hand, the second methodology views the entire robot as both a multi-axis force sensor and a dexterous end-effector. The advantage of this approach is that sensors (vision or load cells) can be placed away from the tip complying with all surgical requirements. However, the amount of uncertainties due to actuation lines flexibility, friction, and modeling uncertainties influence the resolution and fidelity of the measurement.

The contribution of this doctoral dissertation in the area of force control is in presenting a complete framework for hybrid motion/force control of all types of continuum robots with force sensing. The force feedback can be provided by either a dedicated multi-axis force sensor at the tip or one of the intrinsic force sensing methods. The force and position control outputs are merged in the configuration space of the continuum manipulator via two transformations. The first transformation computes the desired configuration space velocities that achieve the desired task space velocities via the inverse Jacobian matrix. The second transformation computes the desired configuration space velocities that achieve the desired task space forces via the inverse of stiffness matrix of the flexible manipulator. The inverse stiffness matrix provides a mapping between a change in task space forces and a change in configuration space forces. The joint-space control input is then computed using the inverse position solution and a model-based actuation compensation method. The actuation compensation method has a twofold contribution: 1) compensates for actuation line extensions, 2) provide a feed-forward term for the desired task space force to be applied at the tip of the manipulator. The hybrid motion/force control framework for continuum robots is evaluated on a multi-backbone continuum robot with intrinsic force sensing that is suitable for Natural Orifice Endoscopic Transluminal Surgery (NOTES).

Outline

This dissertation proposal is organized as the following.

Chapter 2 summarizes the simplified kinematics and statics model of multibackbone multisegment continuum robots presented in [96, 94, 115, 117, 116] and proposes a new constrained kinematics model that takes into account a point contact acting at any point along the primary backbone of the continuum segment. Furthermore,

results from Xu and Simaan on force sensing [115] and actuation compensation [114]. Close form solution of *compensated* Jacobian is derived in order to be used in real-time control.

Chapter 3 proposes algorithms for motion control of multi-segment continuum robots. First, a tiered controller that uses extrinsic sensory information and model-based actuation compensation techniques for enhanced tracking performance of multi-segment continuum robots. Second, a complete framework for telemanipulation of continuum robots is presented. The framework describes telemanipulation algorithms such as the computation of the desired pose and twist from master input, redundancy resolution for 5, 6, and 7 DoF continuum robots. Third, the concept of configuration space virtual fixtures for safe manipulation in confined spaces is presented. These algorithms improve the telemanipulation framework by autonomously avoiding known constraints along the entire robotic structure. While enforcing the constraint, a method that allows for exploiting the remaining available DoFs is proposed and evaluated.

Chapter 4 proposes algorithms for collision detection and estimation of contact locations along multisegment continuum robots. In particular, two methods are presented for the collision detection problem: the Joint Force Deviation (JFD) method and the Screw Motion Deviation (SMD) method. The former is based on the statics and actuation forces feedback of the manipulator. The latter is a purely kinematics-based method and it relies on extrinsic sensory information. Furthermore, a framework for estimation of contact location is also proposed. The framework is able to estimate contact along multisegment robots using the constrained kinematics model proposed in Chapter 2.

Chapter 5 proposed a framework for hybrid motion/force control of continuum robots. The force force sensing estimation algorithm proposed by Xu and Simaan

[115] is tied with a parallel motion and force controllers. The projected control outputs are merged into the configuration space and a feedforward term is calculated using the statics of the manipulator. The chapter concludes with experimental results demonstrating force regulation, decoupled motion and force regulation, shape estimation, and stiffness estimation of soft tissues.

Chapter 6 presents the integration and evaluation of three surgical systems: the insertable robotic effectors platform IREP and the rapid deployment platform RDP. The IREP system was evaluated on some key surgical tasks such as pick and place, hands exchange of small objects, suturing, and knot tying. The RDRP system was tested for two different surgical applications: transurethral resection and surveillance and trans-nasal microsurgery of the throat. For the urologic procedure, the telesurgical system was evaluated on explanted bovine bladders demonstrating targeting, laser delivery, and biopsy. For the head and neck procedures, the system was first evaluated on a plastic anatomical model and then on cadaveric models.

Chapter 7 presents future research directions and applications enabled by the work proposed in this doctoral dissertation.

CHAPTER II

MODELING OF MULTI-BACKBONE CONTINUUM ROBOTS

This section presents the kinematics, statics, actuation compensation and force sensing of multi-backbone multisegment continuum robots. In particular, two kinematics model are presented. The theoretical one was originally presented in [96, 94] and simplified with a the assumption of circular bending in [115, 116]. The second one is a constrained kinematics model that describes the kinematic behavior of a single segment under a point contact constraints along its central backbone. Statics and actuation compensation were originally presented in [96] and [114]. Force sensing algorithms were originally presented in [115, 117].

Theoretical Kinematics

The multi-backbone continuum robots of Fig. I.2 are composed of multiple segments or stages. Each segment is made from multiple circumferentially located super elastic NiTi secondary backbones and one centrally located super elastic NiTi primary backbone. By controlling the length of the secondary backbones each segment may be independently bent according to the kinematics defined below.

Direct Kinematics

In a n -segment continuum robot, the pose of the end disk of segment k with respect to base disk k (or end disk $k - 1$) can be uniquely parameterized by the configuration space vector (see Figure II.1):

$$\boldsymbol{\psi}_k = \begin{bmatrix} \theta_k & \delta_k \end{bmatrix}^T. \quad (\text{II.1})$$

where θ_k is the angle of the tangent to the primary backbone in the bending plane and δ_k is the right-handed rotation angle from \mathbf{x}_{p_k} about \mathbf{z}_{b_k} to a line pointing from the center of the base and passing through the primary backbone of the i^{th} secondary backbone of segment k .

Assuming circular bending, position $\mathbf{p}_{b_k,g_k}^{B_k}$ and orientation $\mathbf{R}_{b_k,g_k}^{B_k}$ of end disk k with respect to base disk k in $\{B_k\}$ are given by:

$$\mathbf{p}_{b_k,g_k}^{B_k} = \frac{L_k}{\theta_{L_k} - \theta_0} \begin{bmatrix} \cos(\delta_k) (\sin(\theta_{L_k}) - 1) \\ -\sin(\delta_k) (\sin(\theta_{L_k}) - 1) \\ -\cos(\theta_{L_k}) \end{bmatrix} \quad (\text{II.2})$$

$$\mathbf{R}_{b_k,g_k}^{B_k} = \text{Rot}(-\delta_k, \hat{\mathbf{z}}) \text{Rot}(\theta_0 - \theta_L, \hat{\mathbf{y}}) \text{Rot}(\delta_k, \hat{\mathbf{z}}) \quad (\text{II.3})$$

where operator $\text{Rot}(\alpha, \hat{\mathbf{u}})$ returns a rotation matrix of angle α about unit axis $\hat{\mathbf{u}}$.

The desired pose of end disk k can be achieved by controlling the amount of push and pull on the secondary backbones. The joint space variables $q_i = L_i - L$ are related to the configuration space variables as follows:

$$q_i = r \cos(\delta_k + (i-1)\beta) (\theta_0 - \theta_k) \quad (\text{II.4})$$

where β is the division angle by which the secondary backbones are equally distributed around the primary backbone ($\beta = 2\pi/m$). Hence, for a continuum segment having m secondary backbones, we define the following vector of joint space variables:

$$\mathbf{q}_k = \begin{bmatrix} q_1 & \dots & q_m \end{bmatrix}^T \quad (\text{II.5})$$

The direct kinematics of a n -segment continuum robot is obtained by defining the

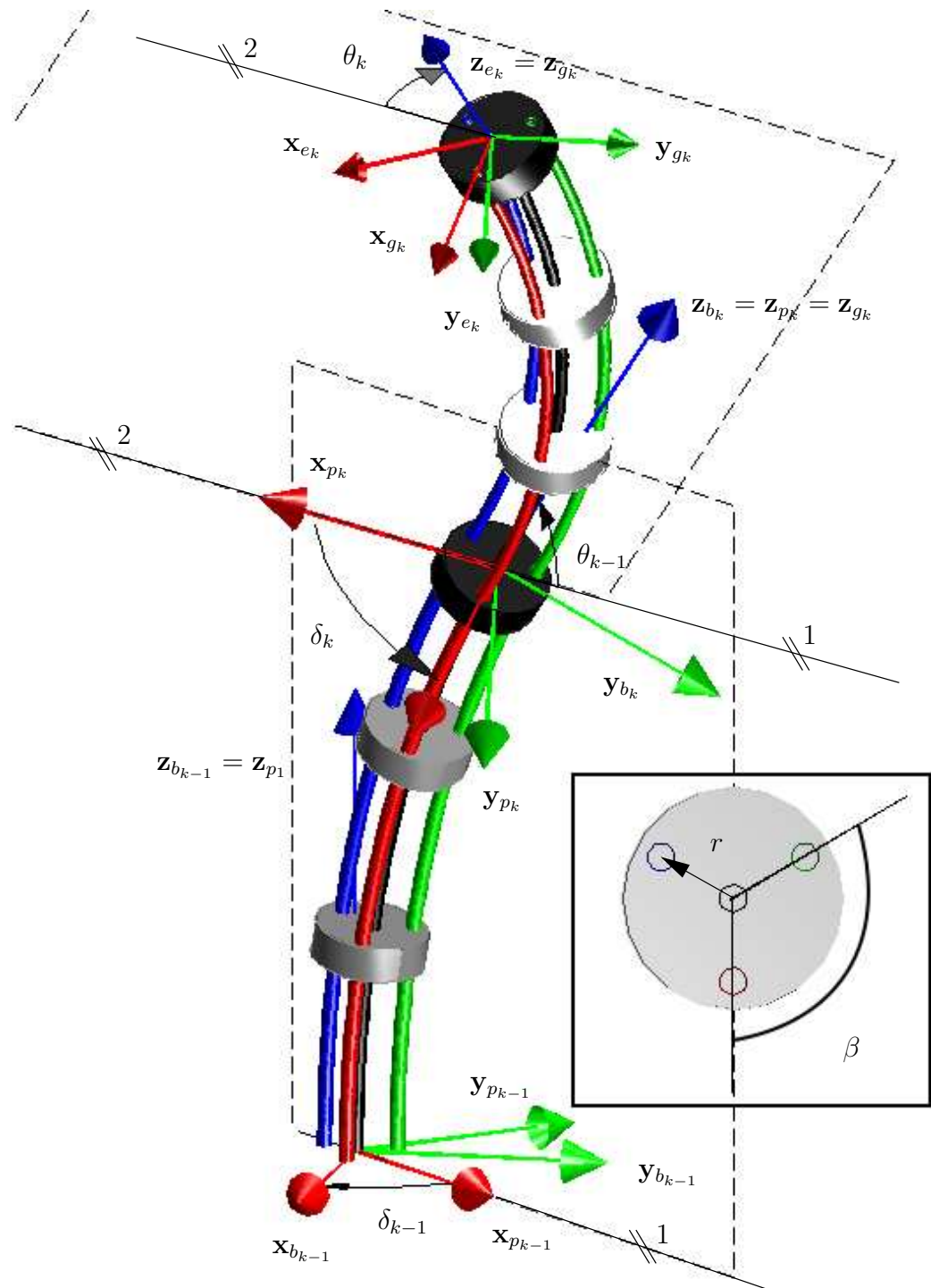


Figure II.1: Kinematic nomenclature of two consecutive segments

following augmented configuration and joint space vectors:

$$\boldsymbol{\Psi} = \begin{bmatrix} \boldsymbol{\psi}_1^T & \dots & \boldsymbol{\psi}_n^T \end{bmatrix}^T \quad (\text{II.6})$$

$$\mathbf{q} = \begin{bmatrix} \mathbf{q}_1^T & \mathbf{q}_2^T & \dots & \mathbf{q}_l^T & \dots & \mathbf{q}_n^T \end{bmatrix}^T \quad (\text{II.7})$$

Using equations II.2, II.3, and II.6, the position and the orientation of the end-effector of a n-segment continuum robot in the base frame $\{B_0\}$ are given by:

$$\mathbf{p}_{ee}^{B_0} = \mathbf{R}_{B_1}^{B_0} \mathbf{p}_{b_1, g_1}^{B_1} + \dots + \mathbf{R}_{b_{k-1}, g_{k-1}}^{B_0} \mathbf{p}_{b_k, g_k}^{B_k} + \dots + \mathbf{R}_{b_{n-1}, g_{n-1}}^{B_0} \mathbf{p}_{b_n, g_n}^{B_n} \quad (\text{II.8})$$

$$\mathbf{R}_{ee}^{B_0} = \mathbf{R}_{B_0}^{B_1} \dots \mathbf{R}_{b_k, g_k}^{B_k} \dots \mathbf{R}_{b_n, g_n}^{B_n} \quad (\text{II.9})$$

where rotation $\mathbf{R}_{B_1}^{B_0}$ is define the transformation between the base frame of segment 1 with respect to robot base frame $\{B_0\}$. Note that, in most cases, the robot base frame coincides with the base frame of the first segment and, therefore, $\mathbf{R}_{B_1}^{B_0}$ is the 3×3 identity matrix.

Direct Instantaneous Kinematics

The twist of end disk k , $\mathbf{t}_{b_k, g_k}^{B_k}$, with respect to base disk k in $\{B_k\}$ is obtained by taking the time derivative of both side of equations II.2 and II.3. The translational velocity, $\mathbf{v}_{b_k, g_k}^{B_k}$ is given by:

$$\mathbf{v}_{b_k, g_k}^{B_k} = \mathbf{J}_{v_k \boldsymbol{\psi}_k} \dot{\boldsymbol{\psi}}_k. \quad (\text{II.10})$$

where

$$\mathbf{J}_{v_k \boldsymbol{\psi}_k} = L_k \begin{bmatrix} \cos \delta_k \frac{(\theta_k - \theta_0) \cos \theta_k - \sin \theta_k + 1}{(\theta_k - \theta_0)^2} & \sin \delta_k \frac{1 - \sin \theta_k}{\theta_k - \theta_0} \\ \sin \delta_k \frac{\sin \theta_k - (\theta_k - \theta_0) \cos \theta_k - 1}{(\theta_k - \theta_0)^2} & \cos \delta_k \frac{1 - \sin \theta_k}{\theta_k - \theta_0} \\ \frac{(\theta_k - \theta_0) \sin \theta_k + \cos \theta_k}{(\theta_k - \theta_0)^2} & 0 \end{bmatrix} \quad (\text{II.11})$$

The angular velocity $\boldsymbol{\omega}_{b_k,g_k}^{B_k} = \begin{bmatrix} \omega_{x_k} & \omega_{y_k} & \omega_{z_k} \end{bmatrix}^T$ can be extracted from the following relationship

$$\begin{bmatrix} 0 & -\omega_{z_k} & \omega_{y_k} \\ \omega_{z_k} & 0 & -\omega_{x_k} \\ -\omega_{y_k} & \omega_{x_k} & 0 \end{bmatrix} = \dot{\mathbf{R}}_{b_k,g_k}^{B_k} \left(\mathbf{R}_{b_k,g_k}^{B_k} \right)^T. \quad (\text{II.12})$$

Hence, angular velocity $\boldsymbol{\omega}_{b_k,g_k}^{B_k}$ is given by:

$$\boldsymbol{\omega}_{b_k,g_k}^{B_k} = \mathbf{J}_{\omega_k \psi_k} \dot{\boldsymbol{\psi}}_k. \quad (\text{II.13})$$

where

$$\mathbf{J}_{\omega_k \psi_k} = \begin{bmatrix} -\sin \delta_k & \cos \delta_k \theta_k \\ -\cos \delta_k & -\sin \delta_k \theta_k \\ 0 & \sin \theta_k - 1 \end{bmatrix} \quad (\text{II.14})$$

By combining equations II.10 and II.13, the twist of end disk k can be written as

$$\mathbf{t}_{b_k,g_k}^{B_k} = \mathbf{J}_{t_k \psi_k} \dot{\boldsymbol{\psi}}_k \quad (\text{II.15})$$

where Jacobian matrix $\mathbf{J}_{t_k \psi_k}$ is given by:

$$\mathbf{J}_{t_k \psi_k} = \begin{bmatrix} \mathbf{J}_{v_k \psi_k} \\ \mathbf{J}_{\omega_k \psi_k} \end{bmatrix} \quad (\text{II.16})$$

The rate of change of configuration space vector, $\dot{\boldsymbol{\psi}}_k$ can be related to the rate of change of the joint space vector $\dot{\mathbf{q}}_k$ by taking the derivative of both side of equation II.5

$$\dot{\mathbf{q}}_k = \mathbf{J}_{q_k \psi_k} \dot{\boldsymbol{\psi}}_k \quad (\text{II.17})$$

where

$$\mathbf{J}_{q_k \psi_k} = r \begin{bmatrix} \cos \delta_k & -(\theta_k - \theta_0) \sin \delta_k \\ \vdots & \vdots \\ \cos(\delta_k + (m-1)\beta) & -(\theta_k - \theta_0) \sin(\delta_k + (m-1)\beta) \end{bmatrix} \quad (\text{II.18})$$

Translation and angular velocity of the end-effector of a n-segment continuum robot can be obtained by taking the time derivative of both side of equations II.8 and II.9 and using the intermediate results for a single segments II.10 and II.13. The time derivative of II.8 yields:

$$\mathbf{v}_{ee}^{B_0} = \mathbf{R}_{B_1}^{B_0} \mathbf{v}_{b_1, g_1}^{B_1} + \dot{\mathbf{R}}_{B_1}^{B_0} \mathbf{p}_{b_1, g_1}^{B_1} + \dots + \mathbf{R}_{b_{n-1}, g_{n-1}}^{B_0} \mathbf{v}_{b_n, g_n}^{B_n} + \dot{\mathbf{R}}_{B_n}^{B_0} \mathbf{p}_{b_n, g_n}^{B_n}. \quad (\text{II.19})$$

Substituting equations II.10 and II.13 into equation II.19 yields:

$$\begin{aligned} \mathbf{v}_{ee}^{B_0} = & \mathbf{R}_{B_1}^{B_0} \mathbf{J}_{v_1 \psi_1} \dot{\psi}_1 + \boldsymbol{\omega}_{b_0, b_1}^{B_0} \times \mathbf{p}_{b_1, g_1}^{B_0} + \dots + \\ & \mathbf{R}_{b_{n-1}, g_{n-1}}^{B_0} \mathbf{J}_{v_n \psi_n} \dot{\psi}_n + \boldsymbol{\omega}_{b_{n-1}, b_n}^{B_0} \times \mathbf{p}_{b_n, g_n}^{B_0}. \end{aligned} \quad (\text{II.20})$$

Similarly, the angular velocity of the end-effector is given by:

$$\begin{aligned} \boldsymbol{\omega}_{ee}^{B_0} = & \boldsymbol{\omega}_{b_0, b_1}^{B_0} + \boldsymbol{\omega}_{b_1, g_1}^{B_0} + \dots + \boldsymbol{\omega}_{b_n, g_n}^{B_0} \\ = & \boldsymbol{\omega}_{b_0, b_1}^{B_0} + \mathbf{R}_{B_1}^{B_0} \mathbf{J}_{\omega_1 \psi_1} \dot{\psi}_1 + \dots + \mathbf{R}_{b_{n-1}, g_{n-1}}^{B_0} \mathbf{J}_{\omega_n \psi_n} \dot{\psi}_n \end{aligned} \quad (\text{II.21})$$

In the case in which the transformation between the robot base and the base of the first segment is fixed, the twist of the end effector can be written as:

$$\mathbf{t}_{ee} = \mathbf{J}_{t\Psi} \dot{\Psi} \quad (\text{II.22})$$

where

$$\mathbf{J}_{t\Psi} = \begin{bmatrix} \mathbf{R}_{B_1}^{B_0} (\mathbf{J}_{v_1\psi_1} - [\mathbf{p}_{b_1,g_1}^{B_1} \times] \mathbf{J}_{\omega_1\psi_1}) & \dots & \mathbf{R}_{b_{n-1},g_{n-1}}^{B_0} (\mathbf{J}_{v_n\psi_n} - [\mathbf{p}_{b_n,g_n}^{B_n} \times] \mathbf{J}_{\omega_n\psi_n}) \\ \mathbf{R}_{B_1}^{B_0} \mathbf{J}_{\omega_1\psi_1} & \dots & \mathbf{R}_{b_{n-1},g_{n-1}}^{B_0} \mathbf{J}_{\omega_n\psi_n} \end{bmatrix} \quad (\text{II.23})$$

Finally, by taking the time derivative of both sides of II.7, it is possible to relate the rate of change of the augmented configuration space vector $\dot{\Psi}$ to the rate of change of the joint space vector $\dot{\mathbf{q}}$ as:

$$\dot{\mathbf{q}} = \mathbf{J}_{q\Psi} \dot{\Psi} \quad (\text{II.24})$$

where

$$\mathbf{J}_{q\Psi} = \begin{bmatrix} \mathbf{J}_{q_1\psi_1} & \mathbf{0} & \dots & \mathbf{0} \\ \vdots & \mathbf{J}_{q_2\psi_2} & \ddots & \mathbf{0} \\ \vdots & \vdots & \ddots & \mathbf{0} \\ \mathbf{J}_{q_1\psi_1} & \mathbf{J}_{q_2\psi_2} & \dots & \mathbf{J}_{q_n\psi_n} \end{bmatrix} \quad (\text{II.25})$$

Constrained Kinematics

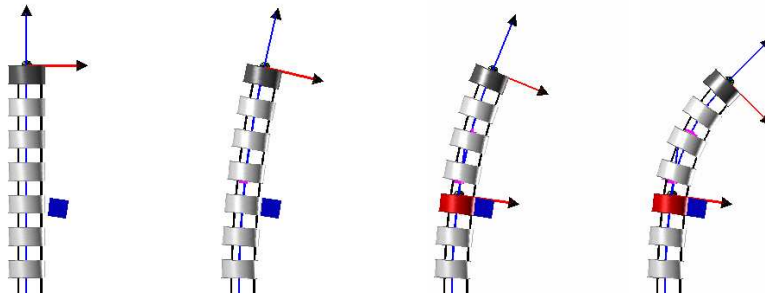


Figure II.2: Simulation sequence of the interaction of a single segment continuum robot with an obstacle according to the proposed constrained kinematics model.

This section presents a modified kinematics model that includes a constraint acting at arbitrary arc-length location $\sigma_k \in [0, L_k]$ along the primary backbone of continuum segment k immediately after the constraint is applied under the following assumptions:

A1: Each CS bends in a circular shape and the gravitational forces are negligible. This assumptions were verified respectively in [116] and [115] for small continuum robots.

A2: After the constraint is applied, the constrained portion of a segment maintains a fixed circular shape and the remainder of the segment continues to bend in the same fashion as a shorter segment as shown by simulation in Figure II.2 and experimentally in Figure II.3.

Figure II.3 shows a single segment continuum robots constrained at its second disk. The image sequence shows how the the shape of the first part of the continuum segment (up to the second disk) does not change while the unconstrained part of the segment bends like a shorter continuum segment having only three disks: one constrained *base* disk, one spacer disk, and the end disk.

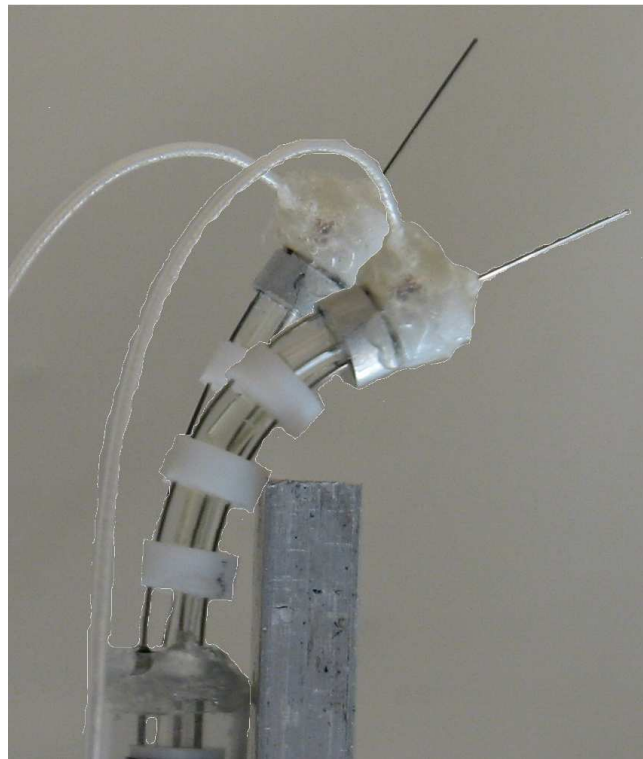


Figure II.3: Overlay of a single continuum segment before and after collision with a static object. The constrained part (bottom) remains fixed while the unconstrained part bends like a shorter continuum segment.

Direct Constrained Kinematics

Immediately after the continuum segment k is constrained, the position $\mathbf{p}_{b_k, c_k}^{B_k}$ and orientation $\mathbf{R}_{b_k, c_k}^{B_k}$ of the contact frame $\{C_k\}$ (Fig. II.4) with respect to a local base frame $\{B_k\}$ is given by:

$$\mathbf{p}_{B_k, C_k}^{B_k} = \mathbf{R}_{B_k, P_k}^{B_k} \frac{L_k}{\theta_0 - \theta_k(t_c)} \begin{bmatrix} 1 - \sin \theta_{\sigma_k} \\ 0 \\ \cos \theta_{\sigma_k} \end{bmatrix} \quad (\text{II.26})$$

$$\mathbf{R}_{B_k, C_k}^{B_k} = \mathbf{R}_{B_k, p_k}^{B_k} \mathbf{R}_{P_k, E_k}^{P_k} \mathbf{R}_{E_k, C_k}^{E_k} \quad (\text{II.27})$$

where $\mathbf{R}_{B_k, p_k}^{B_k} = \text{Rot}(-\delta_k(t_c), \hat{\mathbf{z}})$, $\mathbf{R}_{P_k, E_k}^{P_k} = \text{Rot}(\theta_0 - \theta_{\sigma_k}, \hat{\mathbf{y}})$, and $\mathbf{R}_{E_k, C_k}^{E_k} = \text{Rot}(\delta_k(t_c), \hat{\mathbf{z}})$, $\theta_k(t_c)$ is the bending angle at the time of contact t_c , and θ_{σ_k} is given by:

$$\theta_{\sigma_k} = \theta_0 - \frac{\sigma_k}{L_k} (\theta_0 - \theta_{L_k}(t_c)) \quad (\text{II.28})$$

Using II.26 and II.27, position $\tilde{\mathbf{p}}_{B_k, G_k}^{B_k}$ and orientation $\tilde{\mathbf{R}}_{B_k, G_k}^{B_k}$ of the constrained end disk of segment k is given by:

$$\tilde{\mathbf{p}}_{B_k, G_k}^{B_k} = \mathbf{p}_{B_k, C_k}^{B_k} + \mathbf{R}_{B_k, C_k}^{B_k} \mathbf{R}_{C_k, F_k}^{C_k} \frac{L_k - \sigma_k}{\Theta_k} \begin{bmatrix} 1 - \cos \Theta_k \\ 0 \\ \sin \Theta_k \end{bmatrix} \quad (\text{II.29})$$

$$\tilde{\mathbf{R}}_{B_k, G_k}^{B_k} = \mathbf{R}_{B_k, C_k}^{B_k} \mathbf{R}_{C_k, F_k}^{C_k} \mathbf{R}_{F_k, H_k}^{F_k} \mathbf{R}_{H_k, G_k}^{H_k} \quad (\text{II.30})$$

where $\Theta_k = \theta_{\sigma_k} - \theta_k$ and the rotation matrices in II.30 are defined similarly as in II.27 with rotation angles $\delta_k(t)$, and Θ_k respectively.

Note that when the continuum segment is not in contact, i.e. $\sigma_k = 0$, (II.28)

reads $\theta_{\sigma_k} = \theta_0$, (II.26) and (II.27) reduce to zero, equations (II.29) and (II.30) reduces to (II.2) and (II.3) respectively, and reference frame $\{C_k\}$ coincides with base frame $\{B_k\}$. Therefore, given the contact arc-length σ_k , (II.29) and (II.30) provide both the unconstrained and constrained kinematics model of the continuum segment. Furthermore, $\theta_k(t_c)$ and $\delta_k(t_c)$ denote the configurations of the continuum segment at the time of contact t_c . θ_k and δ_k denote the commanded configurations of the CS for any instant $t > t_c$.

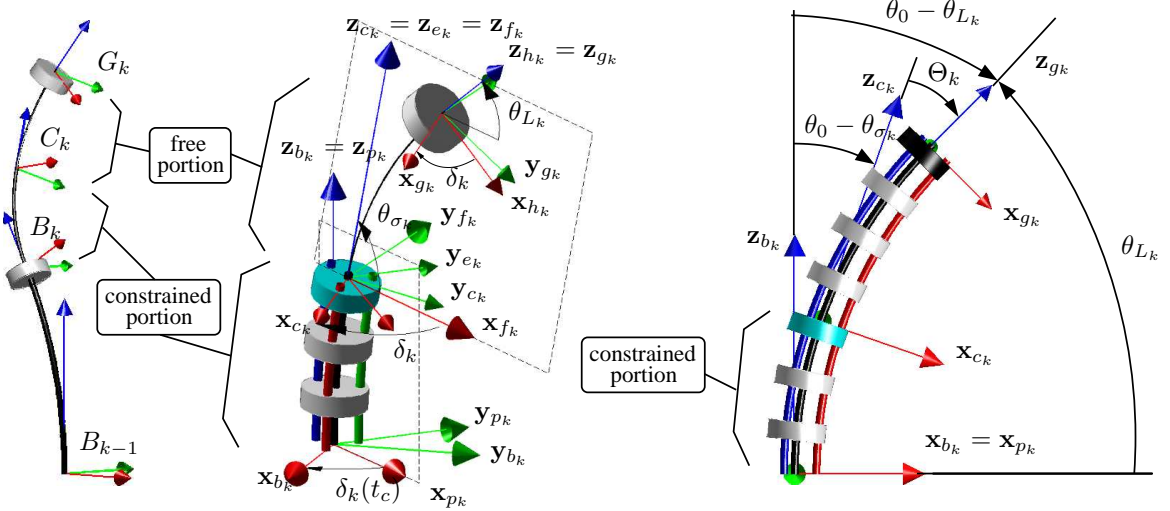


Figure II.4: Constrained kinematic nomenclature. Segment k is constrained at the third disk. Contact frame C_k describes position and orientation of the static portion of the segment. End disk frame G_k describes position and orientation of the end disk of the segment.

Direct Constrained Instantaneous Kinematics

After collision, contact frame $\{C_k\}$ remains fixed (assumption A2) and the forward instantaneous kinematics takes into account the unconstrained portion of the continuum segment. The translational velocity of the constrained end disk is computed by taking the time derivative of both sides of II.29:

$$\tilde{\mathbf{v}}_{g_k/b_k}^{b_k} = \tilde{\mathbf{J}}_{v_k \psi_k} \dot{\boldsymbol{\psi}}_k \quad (\text{II.31})$$

where the *constrained translational Jacobian* $\mathbf{J}_{v_k \psi_k}$ is given by

$$\tilde{\mathbf{J}}_{v_k \psi_k} = \mathbf{R}_{B_k, C_k}^{B_k} \begin{bmatrix} \nu_1 \cos \delta_k & -\nu_3 \sin \delta_k \\ -\nu_1 \sin \delta_k & -\nu_3 \cos \delta_k \\ \nu_2 & 0 \end{bmatrix} \quad (\text{II.32})$$

and

$$\nu_1 = (L_k - \sigma_k) \frac{1 - \Theta_k \sin \Theta_k - \cos \Theta_k}{\Theta_k^2} \quad (\text{II.33})$$

$$\nu_2 = (L_k - \sigma_k) \frac{\sin \Theta_k - \Theta_k \cos \Theta_k}{\Theta_k^2} \quad (\text{II.34})$$

$$\nu_3 = (L_k - \sigma_k) \frac{1 - \cos \Theta_k}{\Theta_k} \quad (\text{II.35})$$

Similarly to (II.3), the angular velocity of the constrained end disk is given by:

$$\tilde{\boldsymbol{\omega}}_{B_k, G_k}^{B_k} = \tilde{\mathbf{J}}_{\omega_k \psi_k} \dot{\boldsymbol{\psi}}_k \quad (\text{II.36})$$

where the *constrained rotational Jacobian* $\tilde{\mathbf{J}}_{\omega_k \psi_k}$ is given by

$$\tilde{\mathbf{J}}_{\omega_k \psi_k} = \mathbf{R}_{B_k, C_k}^{B_k} \begin{bmatrix} -\sin \delta_k & \cos \delta_k \sin \Theta_k \\ -\cos \delta_k & -\sin \delta_k \sin \Theta_k \\ 0 & \cos \Theta_k - 1 \end{bmatrix}. \quad (\text{II.37})$$

Equations (II.32) and (II.37) are ill-defined when $\theta_k = \theta_{\sigma_k} = \theta_0$. This singularity is resolved by applying L'Hôpital's rule as shown in [115].

Statics

Using virtual work arguments we can derived the following first order linear relationship:

$$\mathbf{w}_e^T \Delta \mathbf{x} + \boldsymbol{\tau}^T \Delta \mathbf{q} = \Delta \mathbf{U} \quad (\text{II.38})$$

where $\Delta \mathbf{x}$ is the infinitesimal displacement of the end disk due to the external wrench, $\Delta \mathbf{q}$ is the infinitesimal extension in the actuation lines, and $\Delta \mathbf{U}$ is the change in elastic energy. By noting that $\Delta \mathbf{x} = \mathbf{J}_{t_k \psi_k} \Delta \boldsymbol{\psi}$, $\Delta \mathbf{q} = \mathbf{J}_{q_k \psi_k} \Delta \boldsymbol{\psi}$, and $\Delta \mathbf{U} = \nabla \mathbf{U} \Delta \boldsymbol{\psi}$, equation (II.38) can be rewritten as:

$$\mathbf{J}_{t_k \psi_k}^T \mathbf{w}_e + \mathbf{J}_{q_k \psi_k}^T \boldsymbol{\tau} = \nabla \mathbf{U} \quad (\text{II.39})$$

Actuation Compensation

Xu and Simaan [114] presented the following model based actuation compensation:

$$\tilde{\mathbf{q}} = \mathbf{q} + \boldsymbol{\varepsilon} \quad (\text{II.40})$$

where

$$\boldsymbol{\varepsilon} = \eta \mathbf{K}_d^{-1} \boldsymbol{\tau} + e^{2\mu\phi} \mathbf{K}_c^{-1} (\eta \boldsymbol{\tau} + \mathbf{f}_s) + \boldsymbol{\lambda} \quad (\text{II.41})$$

The time derivative of both sides of (II.41) reads:

$$\dot{\boldsymbol{\varepsilon}} = \eta (\mathbf{K}_d^{-1} + e^{2\mu\phi} \mathbf{K}_c^{-1}) \dot{\boldsymbol{\tau}} \quad (\text{II.42})$$

where

$$\dot{\boldsymbol{\tau}} = \frac{\partial}{\partial t} \left((\mathbf{J}_{q\psi}^T)^{\dagger} \nabla U \right) \quad (\text{II.43})$$

Using the pseudo-inverse property $(A^T)^\dagger = (A^\dagger)^T$ we can write

$$\left(\mathbf{J}_{q\psi}^\dagger\right)^T = \left(\left(\mathbf{J}_{q\psi}^T \mathbf{J}_{q\psi}\right)^{-1} \mathbf{J}_{q\psi}^T\right)^T \quad (\text{II.44})$$

$$\mathbf{J}_{q\psi}^T \mathbf{J}_{q\psi} = r^2 \begin{pmatrix} (c_{\delta_1}^2 + c_{\delta_2}^2 + c_{\delta_3}^2) & \frac{\Theta(s_{(2\delta_1)} + s_{(2\delta_2)} + s_{(2\delta_3)})}{2} \\ \frac{\Theta(s_{(2\delta_1)} + s_{(2\delta_2)} + s_{(2\delta_3)})}{2} & \Theta^2(s_{\delta_1}^2 + s_{\delta_2}^2 + s_{\delta_3}^2) \end{pmatrix} \quad (\text{II.45})$$

The inverse of (II.45) is given by

$$\left(\mathbf{J}_{q\psi}^T \mathbf{J}_{q\psi}\right)^{-1} = \frac{r^2}{d} \begin{pmatrix} \Theta^2(s_{\delta_1}^2 + s_{\delta_2}^2 + s_{\delta_3}^2) & -\frac{\Theta(s_{(2\delta_1)} + s_{(2\delta_2)} + s_{(2\delta_3)})}{2} \\ -\frac{\Theta(s_{(2\delta_1)} + s_{(2\delta_2)} + s_{(2\delta_3)})}{2} & (c_{\delta_1}^2 + c_{\delta_2}^2 + c_{\delta_3}^2) \end{pmatrix} \quad (\text{II.46})$$

where

$$d = r^4 \Theta^2 (s_{(\delta_1 - \delta_2)}^2 + s_{(\delta_1 - \delta_3)}^2 + s_{(\delta_2 - \delta_3)}^2) \quad (\text{II.47})$$

Finally,

$$\left(\mathbf{J}_{q\psi}^T\right)^\dagger = \begin{pmatrix} \frac{r^3 c_{\delta_1} \Theta^2 e}{d} - \frac{r^3 s_{\delta_1} \Theta^2 f}{2d} & \frac{r^3 \Theta(2s_{\delta_1} - 2s_{\delta_2})}{2d} \\ \frac{r^3 c_{\delta_2} \Theta^2 e}{d} - \frac{r^3 s_{\delta_2} \Theta^2 f}{2d} & \frac{r^3 \Theta(2s_{\delta_2} + s_{\delta_3} - s_{\delta_1})}{2d} \\ \frac{r^3 c_{\delta_3} \Theta^2 e}{d} - \frac{r^3 s_{\delta_3} \Theta^2 f}{2d} & \frac{r^3 \Theta(2s_{\delta_3} - s_{\delta_1} + s_{\delta_2})}{2d} \end{pmatrix} \quad (\text{II.48})$$

where

$$e = (s_{\delta_1}^2 + s_{\delta_2}^2 + s_{\delta_3}^2) \quad (\text{II.49})$$

$$f = (s_{2\delta_1} + s_{2\delta_2} + s_{2\delta_3}) \quad (\text{II.50})$$

We now seek an expression for $\dot{\tau}$

$$\frac{d\tau}{dt} = \frac{d}{dt} \left(\mathbf{J}_{q\psi}^T\right)^\dagger \nabla U + \left(\mathbf{J}_{q\psi}^T\right)^\dagger \frac{d}{dt} \nabla U \quad (\text{II.51})$$

$$\frac{d}{dt} \left(\mathbf{J}_{q\psi}^T\right)^\dagger = \dot{\theta} \frac{d}{d\theta} \left(\mathbf{J}_{q\psi}^T\right)^\dagger + \dot{\delta} \frac{d}{d\delta} \left(\mathbf{J}_{q\psi}^T\right)^\dagger \quad (\text{II.52})$$

$$\frac{d}{d\theta} \left((\mathbf{J}_{q\psi}^T)^\dagger \right) = \begin{pmatrix} -\frac{\Theta r^3 (2e c_{\delta_1} - f s_{\delta_1})}{d} & -\frac{r^3 (s_{\delta_1} - s_{\delta_2})}{d} \\ -\frac{\Theta r^3 (2e c_{\delta_2} - f s_{\delta_2})}{d} & -\frac{r^3 (2s_{\delta_2} - s_{\delta_1} + s_{\delta_3})}{2d} \\ -\frac{\Theta r^3 (2e c_{\delta_3} - f s_{\delta_3})}{d} & -\frac{r^3 (s_{\delta_2} - s_{\delta_1} + 2s_{\delta_3})}{2d} \end{pmatrix} \quad (\text{II.53})$$

$$\frac{d}{d\delta} \left((\mathbf{J}_{q\psi}^T)^\dagger \right) = \begin{pmatrix} \frac{\Theta^2 r^3 (s_{\delta_2} - 2s_{\delta_1} + s_{\delta_3})}{2d} & \frac{\Theta r^3 (c_{\delta_1} - c_{\delta_2})}{d} \\ \frac{\Theta^2 r^3 (s_{\delta_1} - 2s_{\delta_2} + s_{\delta_3})}{2d} & \frac{\Theta r^3 (2c_{\delta_2} - c_{\delta_1} + c_{\delta_3})}{2d} \\ -\frac{\Theta^2 r^3 (s_{\delta_2} - s_{\delta_1} + 2s_{\delta_3})}{2d} & \frac{\Theta r^3 (c_{\delta_2} - c_{\delta_1} + 2c_{\delta_3})}{2d} \end{pmatrix} \quad (\text{II.54})$$

Similarly,

$$\frac{d}{dt} \nabla U = \dot{\theta} \frac{d}{d\theta} \nabla U + \dot{\delta} \frac{d}{d\delta} \nabla U = \mathbf{H}_\psi \dot{\psi} \quad (\text{II.55})$$

where the Hessian \mathbf{H}_ψ is given by:

$$\mathbf{H}_\psi = \begin{pmatrix} \frac{EI_p}{L} + \sum_{i=1}^3 \left(\frac{EI_s}{L_i} + \frac{EI_s \Theta r c_{\delta_i}}{L_i^2} \right) & \sum_{i=1}^3 \frac{EI_s \Theta^2 r s_{\delta_i}}{2L_i^2} \\ \sum_{i=1}^3 \frac{3EI_s \Theta^2 r s_{\delta_i}}{2L_i^2} & \sum_{i=1}^3 \frac{EI_s \Theta^2 r c_{\delta_i}}{2L_i^2} \end{pmatrix} \quad (\text{II.56})$$

Hence we can write:

$$\dot{\tau} = \mathbf{J}_{\tau\psi} \dot{\psi} \quad (\text{II.57})$$

where:

$$\mathbf{J}_{\tau\psi} = \left(\frac{d(\mathbf{J}_{q\psi}^T)^\dagger}{d\theta} \nabla U \quad \frac{d(\mathbf{J}_{q\psi}^T)^\dagger}{d\delta} \nabla U \right) + (\mathbf{J}_{q\psi}^T)^\dagger \mathbf{H}_\psi \quad (\text{II.58})$$

CHAPTER III

MOTION CONTROL OF MULTI-BACKBONE CONTINUUM ROBOTS

This Chapter presents algorithms and methods for motion control, telemanipulation, and constrained motion control of multi-segment multi-backbone continuum robots. The first method proposes a tiered control that uses both intrinsic and extrinsic sensory information. The second method proposes a master-slave architecture that does not require velocity inputs from the master console. Instead, it generates velocity profiles based on position and orientation errors and singularity measures. The last method presents a constrained motion control methods for access-based constraints. The algorithm generates dynamic virtual fixtures in the configuration space of the manipulator and adapts the redundancy resolution in order to exploit the remaining degree of freedoms.

Mixed Feedback for Improved Tracking Performance

This section proposes the design of a controller that uses extrinsic information for improving the configuration tracking and for overcoming modeling uncertainties. We explore the utility of this mixed feedback controller in enhancing regulation and tracking control of flexible multi-segment continuum robots. The configuration space controller runs on top of the low level, joint-space, PD controller based on the instantaneous inverse kinematics model of the robot.

Configuration Space Controller (CSC)

Equation (II.24) relates the joint speeds $\dot{\mathbf{q}}$ to the configuration space speeds $\dot{\psi}$. Because of the the robot's flexible elements and coupling between subsequent segments, the continuum robot does not bend as desired. We, therefore, introduce the *configuration space error* \mathbf{e}_ψ as the deviation of the current configuration space vector ψ_c from the desired configuration space vector ψ_d

$$\mathbf{e}_\psi = \psi_d - \psi_c \quad (\text{III.1})$$

The time derivative of (III.1) when accounting for (II.24) becomes

$$\dot{\mathbf{e}}_\psi = \dot{\psi}_d - \eta \mathbf{J}_{q\psi}^\dagger \dot{\mathbf{q}}_{comm} \quad (\text{III.2})$$

where superscript \dagger denotes the pseudo-inverse, $\dot{\mathbf{q}}_{comm}$ is the vector of commanded joint speeds, and η is a positive scalar corresponding to modeling uncertainties. We now prove that the following control law

$$\dot{\mathbf{q}}_{comm} = \mathbf{J}_{q\psi} \left(\dot{\psi}_d + \mathbf{K}_p \mathbf{e}_\psi \right) \quad (\text{III.3})$$

results in a stable system for a diagonal positive-definite matrix \mathbf{K}_p . Define the following Lyapunov function:

$$V(\mathbf{e}_\psi) = \frac{1}{2} \mathbf{e}_\psi^T \mathbf{K}_p \mathbf{e}_\psi \quad (\text{III.4})$$

and its derivative

$$\dot{V} = \mathbf{e}_\psi^T \mathbf{K}_p \dot{\mathbf{e}}_\psi = \mathbf{e}_\psi^T \mathbf{K}_p \dot{\psi}_d - \mathbf{e}_\psi^T \mathbf{K}_p \eta \mathbf{J}_{q\psi}^\dagger \dot{\mathbf{q}}_{comm}. \quad (\text{III.5})$$

Using (III.3), (III.5) results in

$$\dot{V} = \mathbf{e}_\psi^T \mathbf{K}_p \dot{\boldsymbol{\psi}}_d - \eta \mathbf{e}_\psi^T \mathbf{K}_p \mathbf{J}_{q\psi}^\dagger \mathbf{J}_{q\psi} (\dot{\boldsymbol{\psi}}_d + \mathbf{K}_p \mathbf{e}_\psi). \quad (\text{III.6})$$

Noting that $\mathbf{J}_{q\psi} \in \mathbb{R}^{9 \times 6}$, it follows that $\mathbf{J}_{q\psi}^\dagger$ is a *left pseudo-inverse* and, with the assumption of full rank, one obtains:

$$\dot{V} = (1 - \eta) \mathbf{e}_\psi^T \mathbf{K}_p \dot{\boldsymbol{\psi}}_d - \eta \mathbf{e}_\psi^T \mathbf{K}_p \mathbf{K}_p \mathbf{e}_\psi. \quad (\text{III.7})$$

In the case of regulation, $\dot{\boldsymbol{\psi}}_d = \mathbf{0}$, since $\mathbf{e}_\psi^T \mathbf{K}_p \mathbf{K}_p \mathbf{e}_\psi > 0$, it follows that $\dot{V} < 0$ and, therefore, the system in asymptotically stable. In the case of tracking, $\dot{\boldsymbol{\psi}}_d \neq \mathbf{0}$, asymptotic stability cannot be achieved. However, the tracking error \mathbf{e}_ψ is norm-bounded. In fact, as shown in [92], the larger the norm of \mathbf{K}_p , the smaller the norm of the tracking error \mathbf{e}_ψ .

Transient and steady state response of (III.2) can be enhanced by adding a derivative gain as follows

$$\dot{\mathbf{q}}_{comm} = \mathbf{J}_{q\psi} (\dot{\boldsymbol{\psi}}_d + \mathbf{K}_p \mathbf{e}_\psi + \mathbf{K}_d \dot{\mathbf{e}}_\psi) \quad (\text{III.8})$$

and the stability proof can be carried out with similar arguments as for (III.3). Figure III.1 shows a block diagram of the proposed tiered controller. The inner control loop is closed by encoder feedback while the outer one is closed by any sensor capable of measuring the configuration of each segment such as a magnetic tracker or a vision system. The C block implements the pre-compensation proposed in [115].

Experimental Setup

The control algorithm presented in the previous section was tested on the continuum robot of Figure III.2. Dimensional specifications of the robot are reported in

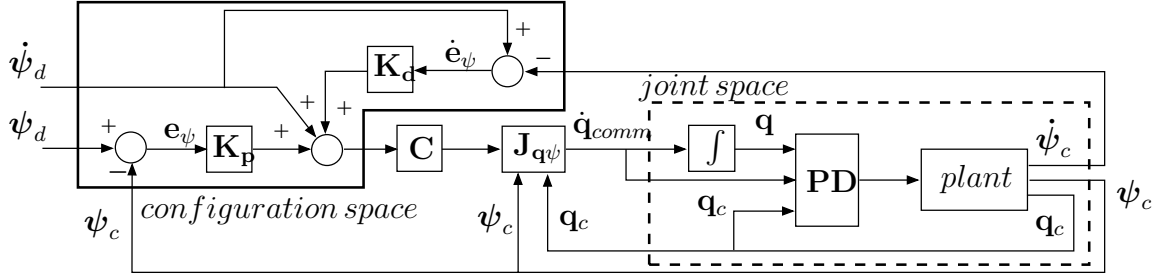


Figure III.1: Block diagram of the proposed tiered mixed feedback controller for multi-segment multi-backbone continuum robots.

Table III.1. Column L gives the segment length. Column r gives the radius of the pitch circle on which the secondary backbones are distributed around the primary backbone. Columns *o.d.* and *i.d.* give the outer and inner diameter of the robot's backbones respectively. The continuum robot is equipped with four 6DOF Model 130 magnetic sensors produced by Ascension Technology with an accuracy (RMS) of 1.4 mm in position and 0.5° in orientation¹. Let \mathbf{T}_0^{MT} , \mathbf{T}_1^{MT} , \mathbf{T}_2^{MT} , and \mathbf{T}_3^{MT} be the homogeneous transformations between the reference frame of magnetic transmitter and the sensors of the robot base, end disk 1, end disk 2, and end disk 3 respectively as shown in Figure III.2. The homogeneous transformation of any end disk with respect to its base disk is given by

$$\mathbf{T}_k^{k-1} = \mathbf{T}_{\text{TM}}^{k-1} \mathbf{T}_k^{\text{TM}} = \begin{bmatrix} \mathbf{R}_k^{k-1} & \mathbf{p}_k^{k-1} \\ \mathbf{0} & 1 \end{bmatrix} \quad (\text{III.9})$$

Using (III.9), the configuration of each segment is given by:

$$\theta_{L_k} = \pi/2 - \text{atan2} \left(\sqrt{r_{13}^2 + r_{23}^2}, r_{33} \right) \quad (\text{III.10})$$

$$\delta_k = \text{atan2} (r_{23}, r_{13}) \quad (\text{III.11})$$

¹RMS accuracy report is available at <http://www.ascension-tech.com/realtime/RTtrakSTAR.php>

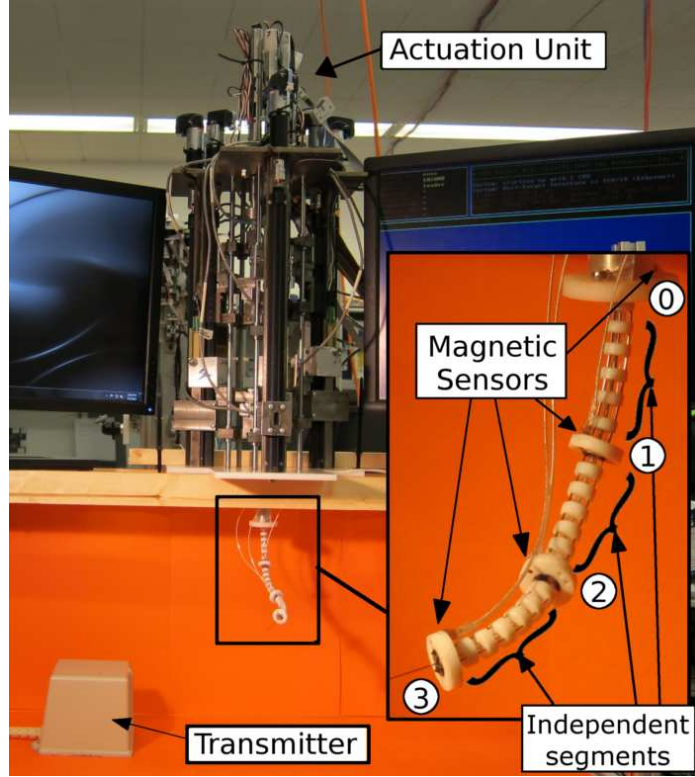


Figure III.2: The experimental setup consist of a nine-axis actuation unit, a 3-segment continuum robot, a magnetic field generator, and four magnetic sensors attached to the robots base (0), the end disk of the first segment (1), the end disk of the second segment (2), and robots end-effector (3).

where elements r_{mn} are the entries of the rotation matrix \mathbf{R}_k^{k-1} .

The control architecture was implemented in Matlab xPC Target 4.2. The joint level control loop ran at 1 KHz while the configuration space feedback loop ran at 125 Hz. The feedback rate included the acquisition time of the tracking device, data packing, and data transmission over a local area network using the UDP.

Table III.1: Dimensional specifications for the continuum robot

Segment	Material	L [mm]	r [mm]	o.d. [mm]	i.d. [mm]
1	NiTi SE508	50	3	0.889	0.762
2	NiTi SE508	49	3	0.635	0.508
3	NiTi SE508	45	3	0.406	n/a (wire)

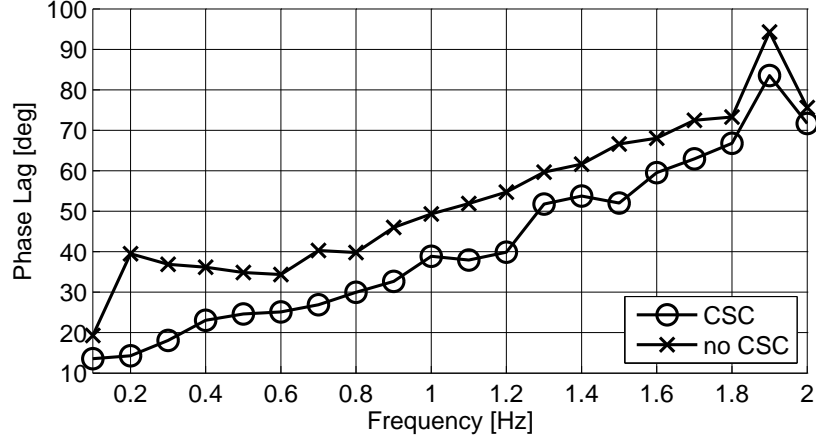
Experimental Evaluation

Effects of the Controller on Phase Lag

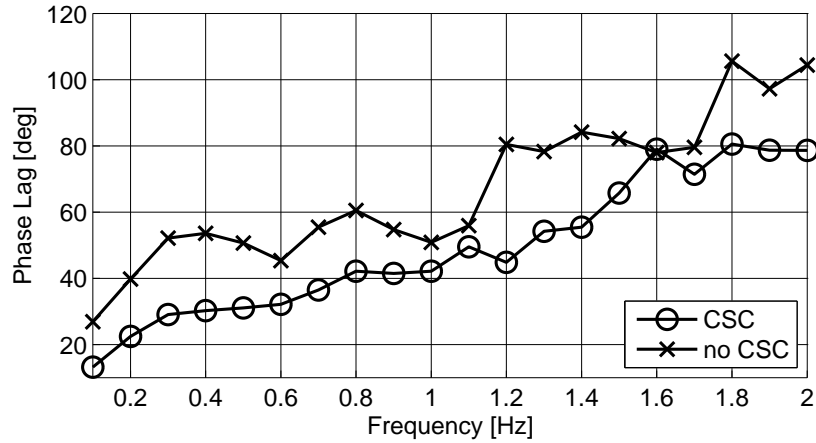
In order to evaluate the performance of the proposed control law, the phase lag was characterized experimentally with and without the CSC. Each segment was controlled in configuration space and the desired configuration variables were individually excited by sinusoidal reference inputs of frequencies ranging between 0.1-2 Hz. Figures. III.3a and III.3b show results associated with the first segment. Figure III.3a clearly shows a reduction in the phase lag when the CSC is applied. The phase angle of configuration variable θ_{L_1} is about 12° at 0.1 Hz and raises up to 82° at 1.9 Hz under compensation. On the other hand, the phase angle is 20° at 0.1 Hz and raises up to 95° when uncompensated. Figure III.3b shows a similar trend for configuration variable δ_1 . Figures. III.4a and III.4b show analogous results for configuration variables θ_{L_2} and δ_2 . The proposed online compensator reduces the phase lag for frequencies between 0.1 Hz and 1.4 Hz for θ_{L_2} and between 0.1 Hz and 1.6 Hz for δ_2 . Finally, Figures. III.5a and III.5b report the behavior of the third segment with and without compensation. The overall performance of the compensated system is clearly better for frequencies between 0.1 Hz and 1.3 Hz. Due to actuation speed limits, past 1.4 Hz the phase angle of the controller grows up to 180° and 140° for θ_{L_3} and δ_3 respectively.

Tracking in Configuration Space and Coupling Effects Between Segments

An evaluation of the benefits of the controller of Figure III.1 in improving tracking in configuration space is next presented. The evaluation is carried out first for a single-CSDoF and then for multi-CSDoF movement in configuration space in order to identify coupling effects between the robot's independently actuated segments and individual segment configuration space DoFs.



(a) Phase lag in θ_{L_1}

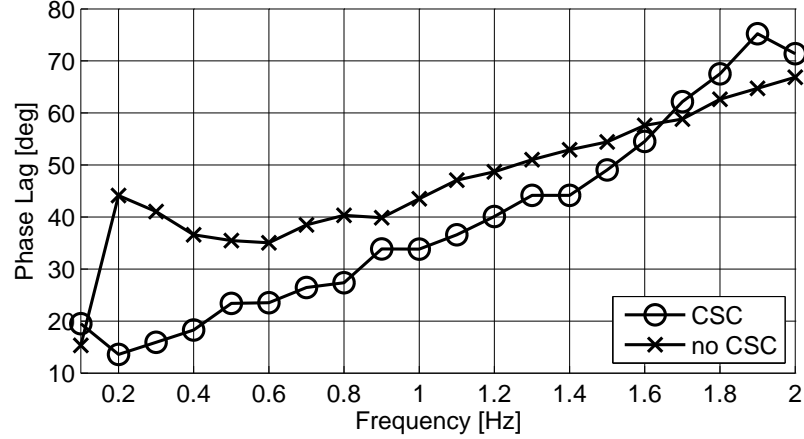


(b) Phase lag in δ_1

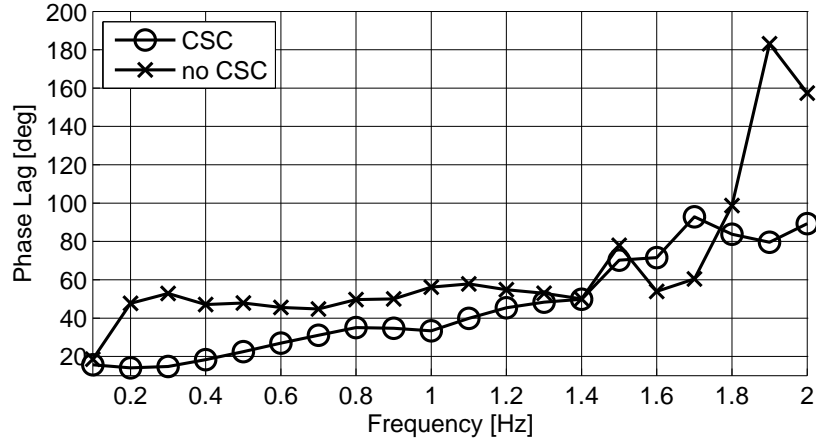
Figure III.3: Phase lag affecting the first segment with and without CSC

Single-DoF Configuration Space Tracking

Experimental data were collected with and without the CSC. After the tuning procedure was completed, the first segment was commanded to bend with a fixed δ_1 and a sinusoidal input in θ_{L_1} with a frequency of 0.5 Hz. Figure III.6 shows a comparison of the tracking performance in θ_{L_1} DoF, with and without the CSC. The system response is affected by a time delay mostly due to the lower frequency of the higher level feedback loop. However, as expected, the response of the system is a sinusoid with the same frequency of the output and a peak-to-peak deviation error



(a) Phase lag in θ_{L_2}



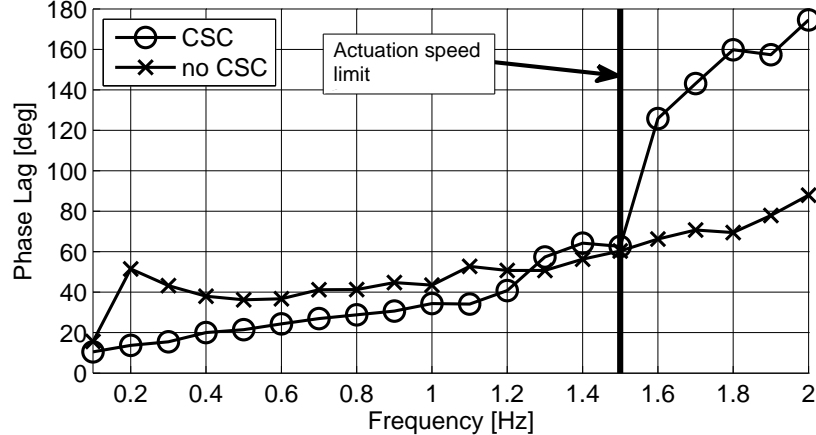
(b) Phase lag in δ_2

Figure III.4: Phase lag affecting the second segment with and without CSC

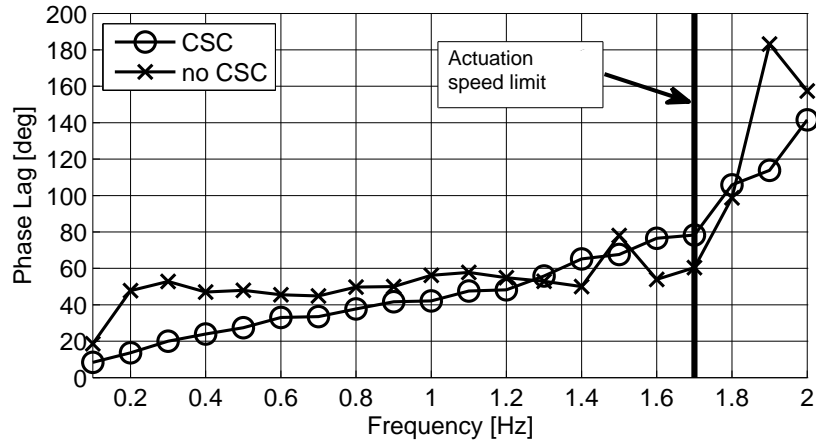
of less than 1° . Figures. III.7, III.8a, III.8b, III.9a, and III.9b show disturbances on all the remaining configuration space variables. The figures show that the use of the CSC reduces the sinusoidal disturbances and drifting phenomena as in the case of conventional joint space control (i.e. without CSC).

Multi-DoF Configuration Space tracking

In order to test the performance of the configuration space controller in the case of concurrent actuation of all the segments, a rest-to-rest quintic polynomial



(a) Phase lag in θ_{L_3}



(b) Phase lag in δ_3

Figure III.5: Phase lag affecting the third segment with and without CSC

trajectory was used to change the robot's configuration from the initial configuration $\psi_0 = \begin{bmatrix} 45^\circ, 0^\circ, 45^\circ, 45^\circ, 45^\circ, -45^\circ \end{bmatrix}^T$ to the final configuration $\psi_f = \begin{bmatrix} 60^\circ, 15^\circ, 60^\circ, 30^\circ, 30^\circ, -30^\circ \end{bmatrix}^T$ with an execution time of 5 seconds. The experimental results for the first, second, and third segment are shown in Figures. III.10, III.11, and III.12 respectively. Figures. III.10a and III.10b show that the pre-compensator factor proposed by Xu and Simaan in [115] is effective only in reducing errors in the configuration space variable θ_{L_1} but not in the configuration space variable δ_1 . Furthermore, Figures. III.11 and III.12 show that efficacy of the

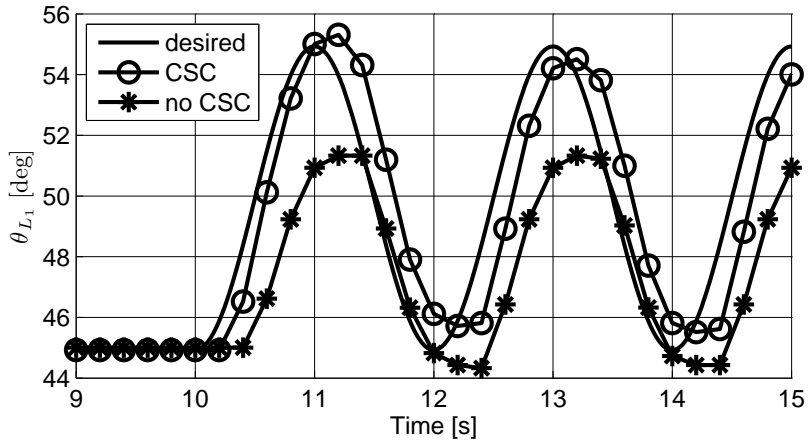


Figure III.6: Tracking performance for θ_{L_1}

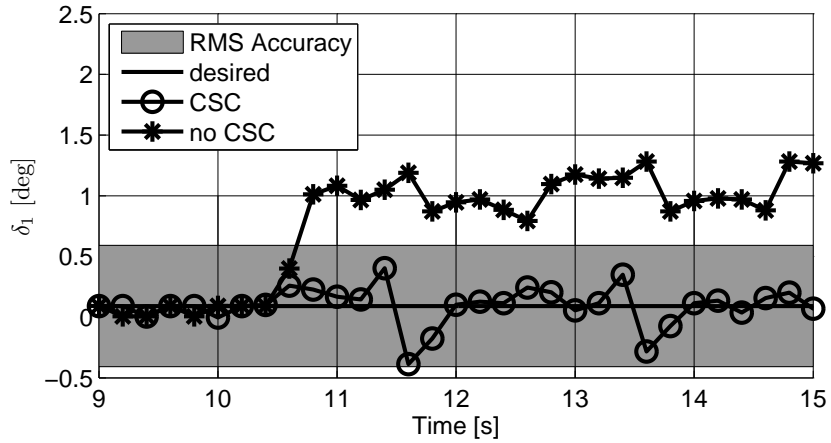
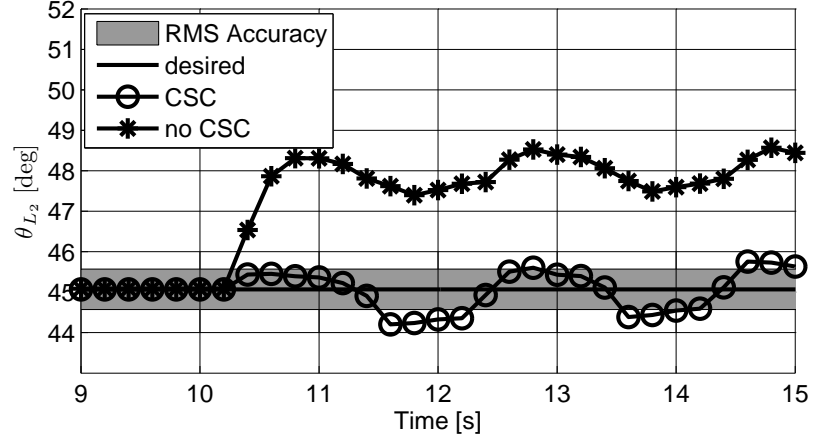
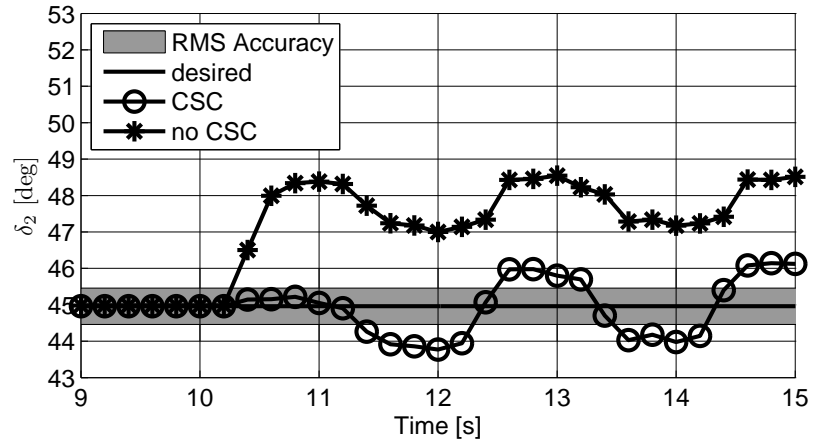


Figure III.7: Coupling effect between δ_1 and θ_{L_1}

pre-compensation deteriorates for the second and last segment. This is due to the fact that the compensation factors are computed by actuating each segment individually with the others in straight configuration. This is not, obviously, the case when all three segments are actuated concurrently and the bending configuration of each segment dynamically modifies the stiffness of the overall structure. The use of the CSC overcomes the deficiencies of the previously proposed pre-compensation. Errors in configuration space are within the RMS accuracy of the magnetic tracking device used for the experiment.



(a) Coupling effect on θ_{L_2}

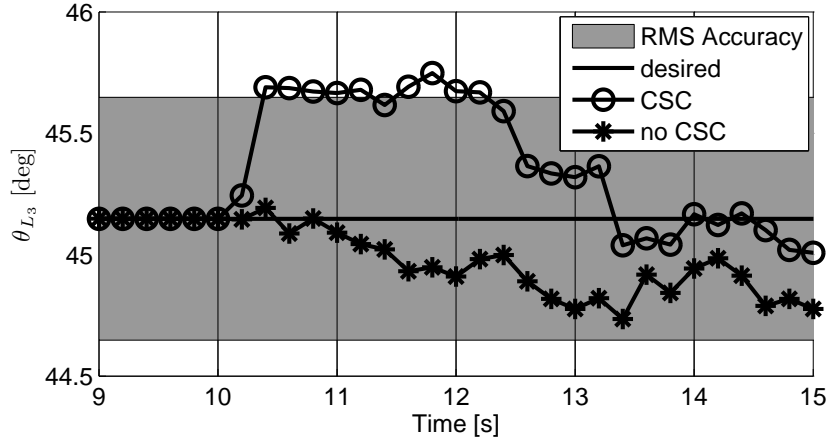


(b) Coupling effect on δ_2

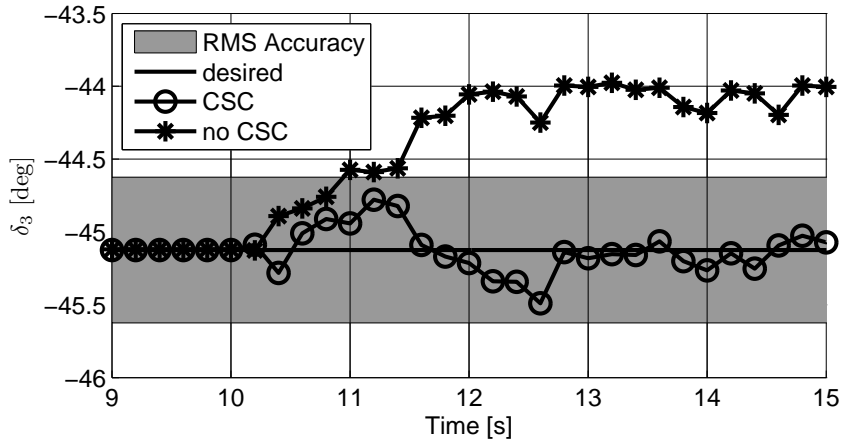
Figure III.8: Coupling effect between the second segment and θ_{L_1}

External Wrench Disturbance

In this section we demonstrate the response of the proposed controller to external wrench disturbances. An external load was applied to the robot end-effector as shown in Figure III.13(a) and the time history of the configuration space angles was recorded. Figure III.14 shows the experimental results. Figure III.14-a shows bending angles θ_{L_1} , θ_{L_2} , and θ_{L_3} while Figure III.14(b) shows plane angles δ_1 , δ_2 , and δ_3 . The results show that the CSC closes errors due to external force disturbances. Although the former graph shows a small change in bending angles θ_{L_1} , θ_{L_2} , and θ_{L_3} , Figure



(a) Coupling effect on θ_{L_3}



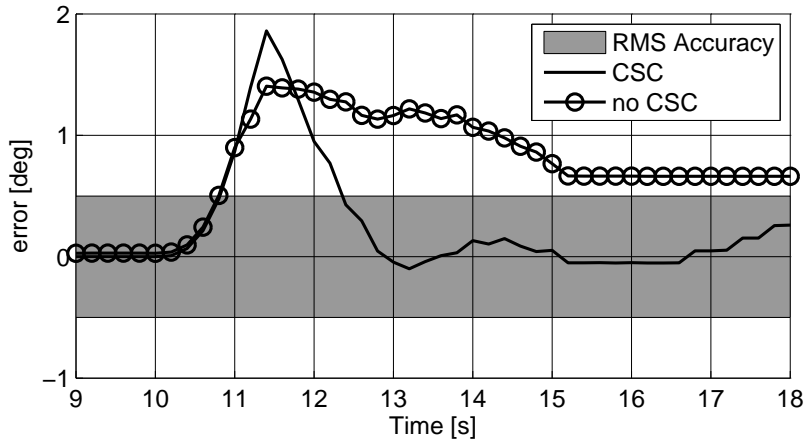
(b) Coupling effect on δ_3

Figure III.9: Coupling effect between the third segment and θ_{L_1}

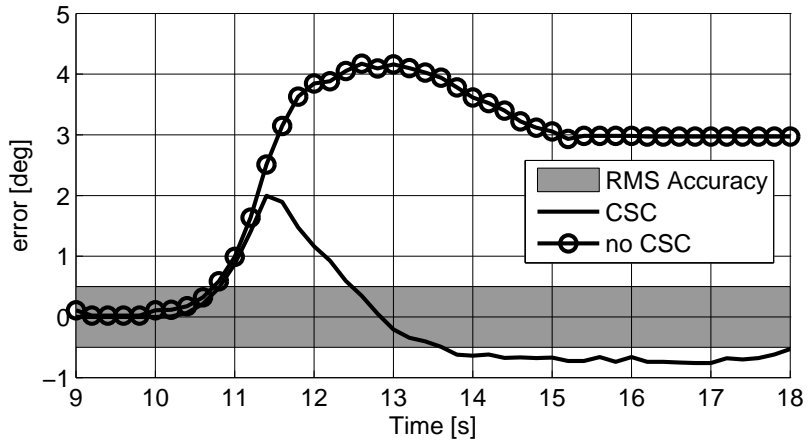
III.13(c) shows the robot's steady-state deformed shape. The perturbable shape is due to torsion about the primary backbones of the segments and to the fact that the orientation of the end disk depends only on the length of the secondary backbones [96].

End-disk Orientation Error

This section reports the task space orientation error of a single segment of the continuum robot by validating its kinematics model. Ideally, the particular structure



(a) Error in θ_{L_1}

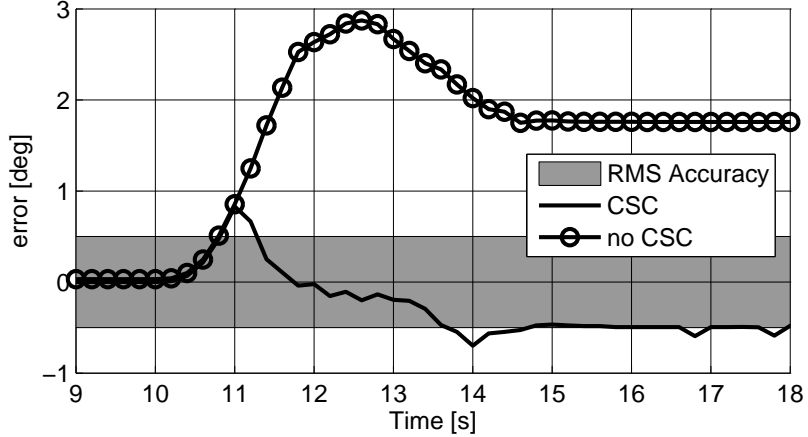


(b) Error in δ_1

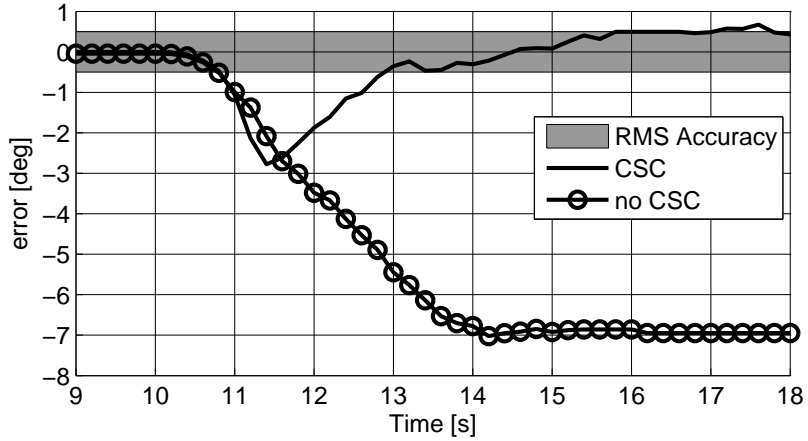
Figure III.10: Errors in the configuration of the first segment

of the robot allows one to fully specify the orientation of the end disk of each continuum segment with only two angles: configuration variables θ_{L_k} and δ_k . Theoretically no rotation about the longitudinal axis of the initially straight segments is allowed during assembly. However, deviations in our assembly caused this *twist* to affect all the orientations of the end disks by an additional rotation about the z-axis. This additional twist is obtained as following

$$\gamma = \text{atan}(\mathbf{r}_{21}, \mathbf{r}_{11}) \quad (\text{III.12})$$



(a) Error in θ_{L_2}

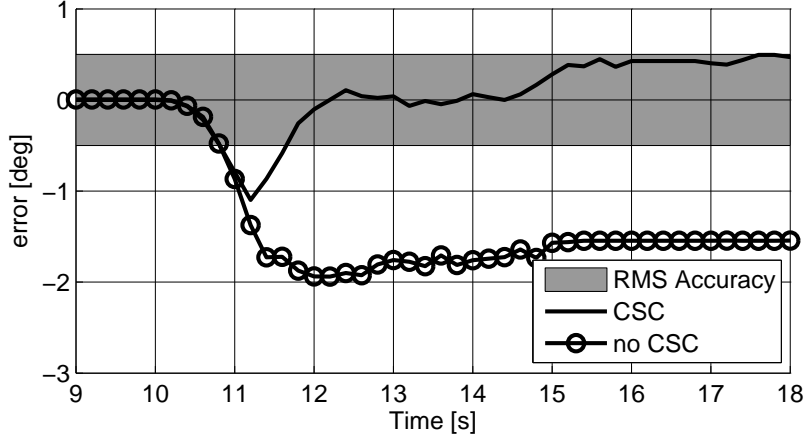


(b) Error in δ_2

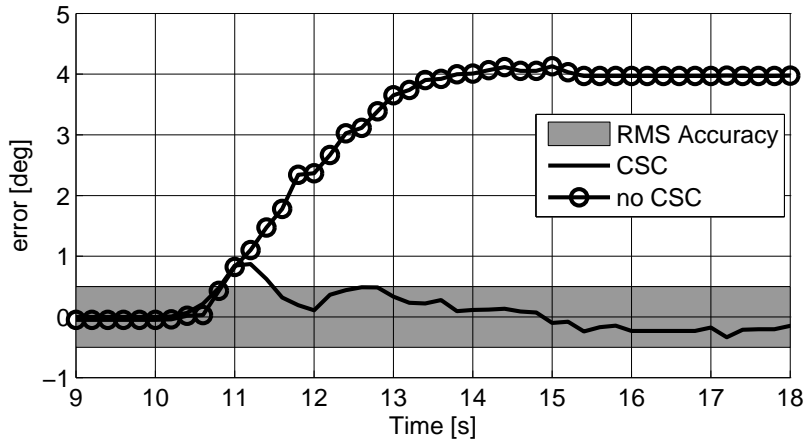
Figure III.11: Errors in the configuration of the second segment

where r_{mn} designates elements m,n of the rotation matrix \mathbf{R}_k^{k-1} as defined in (III.9).

Figure III.15 shows an experimental evaluation of the roll error affecting the third segment. The segment is commanded to bend in a single CDofF (θ_{L_3}) while the second CDofF is fixed at $\delta_3 = 5^\circ, 15^\circ, 25^\circ, 35^\circ$, and 45° respectively. Figure III.15 shows that in an initial straight configuration ($\theta_{L_3} = 90^\circ$) the end disk is twisted by approximately -4° about the primary backbone due to assembly imperfection. The figure also shows that the roll error is more affected by changes in θ_{L_3} and δ_3 .



(a) Error in θ_{L_3}



(b) Error in δ_3

Figure III.12: Errors in the configuration of the third segment

Telemanipulation Architecture

Figure VI.3 shows the proposed telemanipulation architecture. Two computers labeled as *Host* and *Target* are used for querying the master device and controlling the robot. The two machines exchange information over a Local Area Network (LAN) via User Datagram Protocol (UDP).

The telemanipulation is initiated by pressing a foot pedal switch directly wired to the target control machine. At this time, denoted by *init*, the following entities are saved for trajectory planning: slave position and orientation ${}^0\mathbf{p}_{slave,init}$, ${}^0\mathbf{R}_{slave,init}$

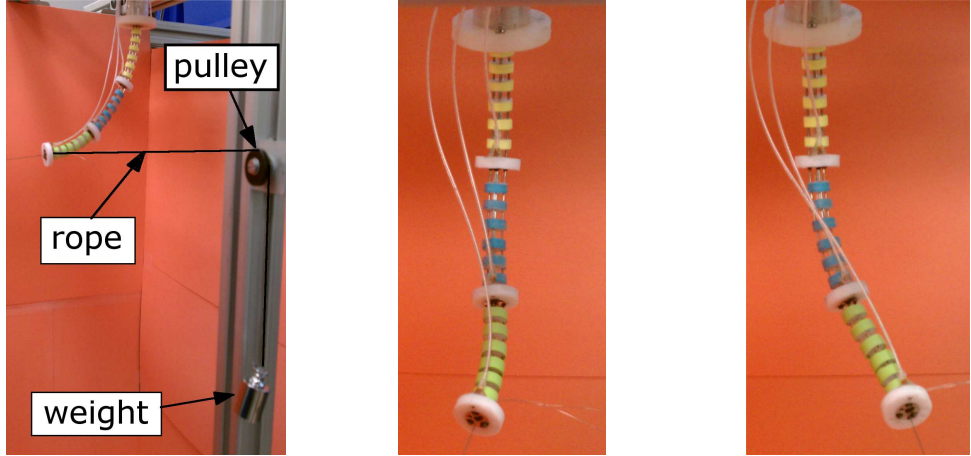


Figure III.13: External wrench disturbance setup. (a) a calibration weight is attached to the end-effector using a rope and a frictionless pulley. (b) the continuum robot with no load applied. (c) the continuum robot with the external load applied.

and the master's stylus position and orientation ${}^{mb}\mathbf{p}_{\text{master},\text{init}}$, ${}^{mb}\mathbf{R}_{\text{master},\text{init}}$. During telemanipulation (pedal foot switch pressed) the change in position and orientation of the master's stylus, ${}^{mb}\mathbf{p}_{\text{master},\text{current}}$ and ${}^{mb}\mathbf{R}_{\text{master},\text{current}}$, is mapped to the change in position and orientation of slave's end-effector, ${}^0\mathbf{p}_{\text{slave},\text{current}}$ and ${}^0\mathbf{R}_{\text{slave},\text{current}}$, as shown in Figure III.16.

Desired slave pose

The desired slave's end-effector position ${}^0\mathbf{p}_{\text{slave},\text{des}}$ and orientation ${}^0\mathbf{R}_{\text{slave},\text{des}}$ are defined as:

$$\mathbf{p}_{\text{des}} = {}^0\mathbf{p}_{\text{slave},\text{init}} + \nu {}^0\mathbf{R}_{mb} \left({}^{mb}\mathbf{p}_{\text{master},\text{current}} - {}^{mb}\mathbf{p}_{\text{master},\text{init}} \right) \quad (\text{III.13})$$

$$\mathbf{R}_{\text{des}} = \begin{cases} \mathbf{R}_{\text{slave},\text{init}} \mathbf{R}_t^T \mathbf{R}_{\text{master},\text{des}} \mathbf{R}_t, & \text{tool frame} \\ \mathbf{R}_t^T \mathbf{R}_{\text{master},\text{des}} \mathbf{R}_t \mathbf{R}_{\text{slave},\text{init}}, & \text{base frame} \end{cases} \quad (\text{III.14})$$

where ${}^0\mathbf{R}_{mb}$ is the rotation matrix between the master interface base frame and the robot base frame $\{0\}$, the scalar ν is the telemanipulation scaling factor between

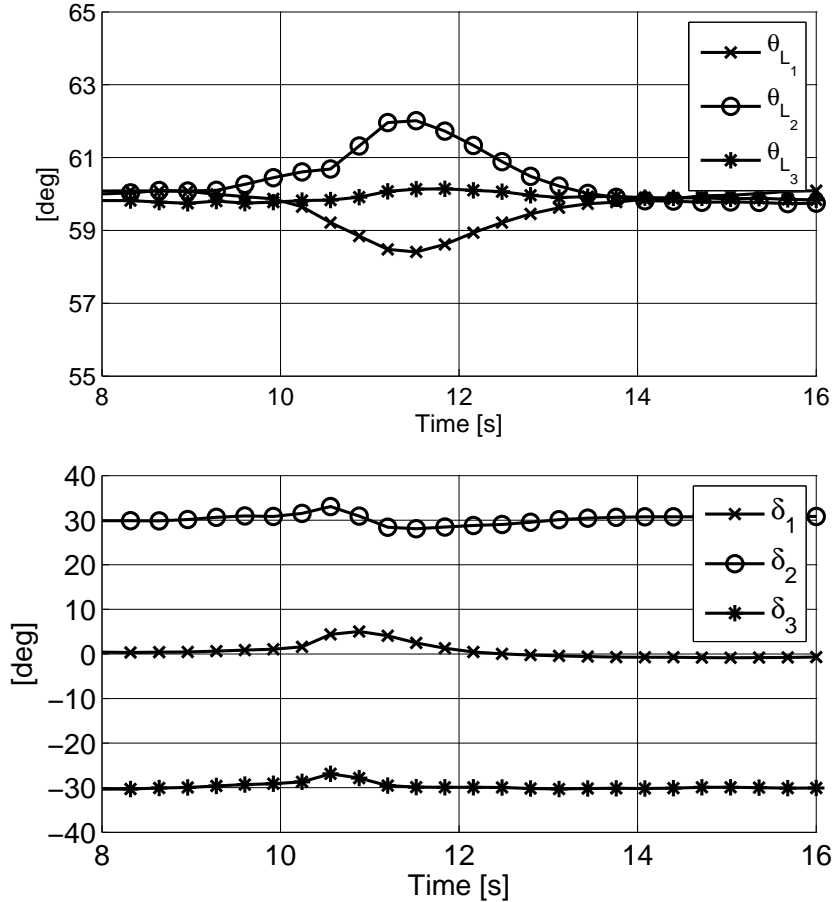


Figure III.14: Response of the controller to an external wrench disturbance. (a) time history of θ_{L_1} , θ_{L_2} , θ_{L_3} . (b) time history of δ_1 , δ_2 , and δ_3

stylus movement and gripper movement, and rotation matrix \mathbf{R}_t aligns the positive z-direction of the robot's end-effector with the positive z-direction of the master's stylus. The two rotation sequences in III.14 allows to rotate the end-effector frame in world frame and tool frame respectively. During surgical teleoperation it is preferable the first rotation sequence (tool frame) since the vision feedback will provide a close-up of the slave's end effector and the operator will unconsciously associate the rotation of the robot's end-effector to his/her own hand.

Algorithm 1 summarizes the steps required to compute the desired pose of the robot's end-effector once the initial and current pose of the master manipulator and

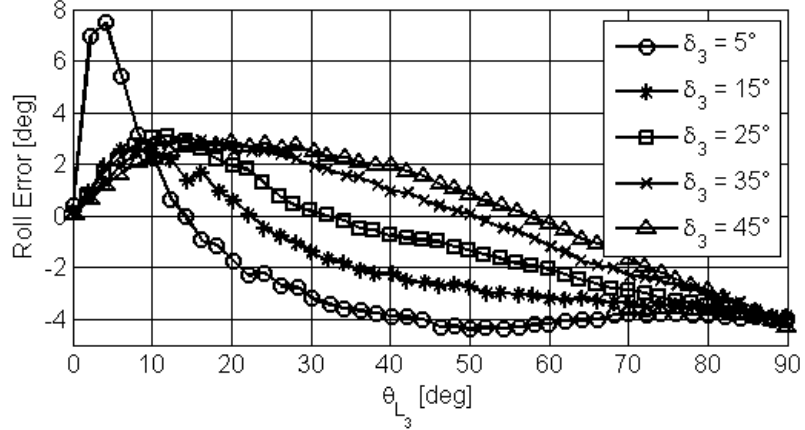


Figure III.15: Roll error affecting the orientation of the third segment as a function of bending angle θ_{L_3}

the initial pose of the slave manipulator are obtained. Algorithm 1 is executed at each time step. The initial poses, if telemanipulation is not interrupted (foot pedal switch open) remain constant while the current pose is constantly updated based on encoder feedback.

Slave Tracking Error

The slave robot position tracking error \mathbf{p}_e is given by

$$\mathbf{p}_e = {}^0 \mathbf{p}_{4_{des}} - {}^0 \mathbf{p}_{4_c} \quad (\text{III.15})$$

while the orientation tracking error ζ is given by:

$$\zeta = \cos^{-1} (\hat{\mathbf{e}}_{1c} \cdot \hat{\mathbf{e}}_{1d} + \hat{\mathbf{e}}_{2c} \cdot \hat{\mathbf{e}}_{2d} + \hat{\mathbf{e}}_{3c} \cdot \hat{\mathbf{e}}_{3d}) \quad (\text{III.16})$$

when all three orientation degrees of freedom (roll, pitch, yaw) are controlled and by:

$$\zeta = \cos^{-1} (\hat{\mathbf{e}}_{3c} \cdot \hat{\mathbf{e}}_{3d}) \quad (\text{III.17})$$

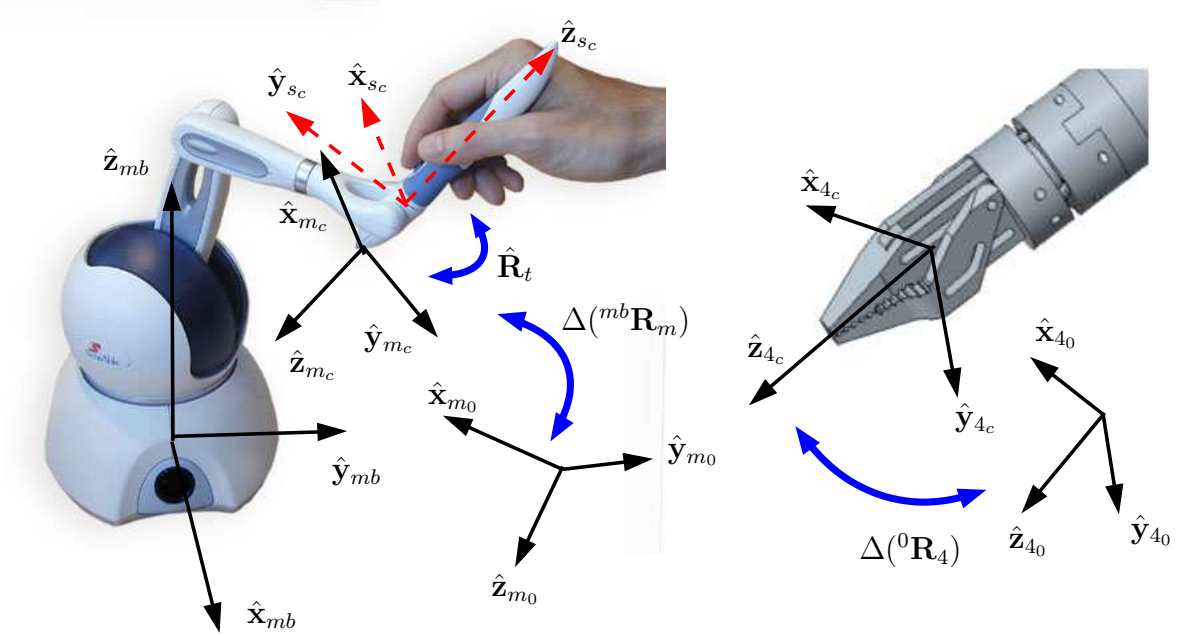


Figure III.16: Definition of end-effector coordinate system of the continuum arm (left) and the Phantom Omni (right)

Algorithm 1 Compute Desired Pose

```

Input:  $\mathbf{p}_{master,curr}$  {Current master position}
Input:  $\mathbf{R}_{master,curr}$  {Current master orientation}
Input:  $\mathbf{p}_{master,init}$  {Initial master position}
Input:  $\mathbf{R}_{master,init}$  {Initial master orientation}
Input:  $\mathbf{p}_{slave,init}$  {Initial slave position}
Input:  $\mathbf{R}_{slave,init}$  {Initial slave orientation}
Input:  $\mathbf{R}_t$  {Rotation matrix between the master'end-effector and the robot's end-effector}

 $\mathbf{p}_{master,des} = \mathbf{p}_{master,curr} - \mathbf{p}_{master,init}$ 
 $\mathbf{p}_{slave,des} = \mathbf{p}_{slave,init} + \mathbf{p}_{master,des}$ 
 $\mathbf{R}_{master,des} = \mathbf{R}_{master,init}^T - \mathbf{R}_{master,curr}$ 
if fixed orientation then
     $\mathbf{R}_{slave,des} = \mathbf{R}_{slave,init}$ 
else
     $\mathbf{R}_{slave,des} = \mathbf{p}_{slave,init} + \mathbf{p}_{master,des}$ 
    if rotation in tool frame then
         $\mathbf{R}_{slave,des} = \mathbf{R}_{slave,init} \mathbf{R}_t^T \mathbf{R}_{master,des} \mathbf{R}_t$ 
    else
         $\mathbf{R}_{slave,des} = \mathbf{R}_t^T \mathbf{R}_{master,des} \mathbf{R}_t \mathbf{R}_{slave,init}$ 
    end if
end if

```

when only two orientation degrees of freedom (pitch, yaw) are controlled. Unit vectors \mathbf{e}_{ic} and \mathbf{e}_{id} are the i^{th} column of the current and desired rotation matrix respectively. Equation III.17 may be used when telemanipulating under-actuated systems like the one proposed in [36].

Slave desired twist

Next, the desired end-effector twist can be computed as follows:

$$\mathbf{t}_{des} = \begin{bmatrix} V\hat{\mathbf{m}} \\ \Omega\hat{\mathbf{r}} \end{bmatrix} \quad (\text{III.18})$$

where

$$\hat{\mathbf{m}} = \frac{\mathbf{p}_e}{\|\mathbf{p}_e\|} \quad (\text{III.19})$$

$$\hat{\mathbf{r}} = \frac{\hat{\mathbf{e}}_{1c} \times \hat{\mathbf{e}}_{1d} + \hat{\mathbf{e}}_{2c} \times \hat{\mathbf{e}}_{2d} + \hat{\mathbf{e}}_{3c} \times \hat{\mathbf{e}}_{3d}}{\|\hat{\mathbf{e}}_{1c} \times \hat{\mathbf{e}}_{1d} + \hat{\mathbf{e}}_{2c} \times \hat{\mathbf{e}}_{2d} + \hat{\mathbf{e}}_{3c} \times \hat{\mathbf{e}}_{3d}\|} \quad (\text{III.20})$$

$$V = \begin{cases} V_{max} & \text{if } \frac{\|\mathbf{p}_e\|}{\epsilon_p} > \lambda_p \\ \eta \frac{(V_{max} - V_{min})}{\epsilon_p(\lambda_p - 1)} + V_{min} & \text{if } \frac{\|\mathbf{p}_e\|}{\epsilon_p} \leq \lambda_p \end{cases} \quad (\text{III.21})$$

$$\Omega = \begin{cases} \Omega_{max} & \text{if } \frac{\zeta}{\epsilon_o} > \lambda_o \\ \mu \frac{(\Omega_{max} - \Omega_{min})}{\epsilon_o(\lambda_o - 1)} + \Omega_{min} & \text{if } \frac{\zeta}{\epsilon_o} \leq \lambda_o \end{cases} \quad (\text{III.22})$$

ϵ_p is the smallest allowable position error, λ_p is a scaling factor that defines the radius of position error beyond which the end-effector moves at maximal linear velocity V_{max} , $\eta = \|\mathbf{p}_e\| - \epsilon_p$, ϵ_o and λ_o are defined similarly to ϵ_p and λ_p respectively, and $\mu = \zeta - \epsilon_o$.

Algorithm 2 Compute Desired Twist

Input: \mathbf{p}_{des} {Desired end-effector position}
Input: \mathbf{R}_{des} {Desired end-effector orientation}
Input: \mathbf{p}_{curr} {Current end-effector position}
Input: \mathbf{R}_{curr} {Current end-effector orientation}
Input: $V_{max}, V_{min}, \epsilon_p, \lambda_p$ {Position trajectory data}
Input: $\Omega_{max}, \Omega_{min}, \epsilon_o, \lambda_o$ {Orientation trajectory data}

```

 $\mathbf{p}_e = \mathbf{p}_{des} - \mathbf{p}_{curr}$ 
 $M = \|\mathbf{p}_e\|$ 
 $\mathbf{R}_e = \mathbf{R}_{curr}^T \mathbf{R}_{des}$ 
if 5 DoF then
     $\zeta = \cos^{-1}(\hat{\mathbf{e}}_{3c} \cdot \hat{\mathbf{e}}_{3d})$ 
else
     $\zeta = \cos^{-1}(\hat{\mathbf{e}}_{1c} \cdot \hat{\mathbf{e}}_{1d} + \hat{\mathbf{e}}_{2c} \cdot \hat{\mathbf{e}}_{2d} + \hat{\mathbf{e}}_{3c} \cdot \hat{\mathbf{e}}_{3d})$ 
end if
if isnan( $\zeta$ ) then
     $\zeta = 0$  {Check if  $\cos^{-1}$  returned real values}
end if
if  $M \leq \epsilon_p \& \zeta \leq \epsilon_o$  then
     $\mathbf{t}_{des} = [ 0 \ 0 \ 0 \ 0 \ 0 \ 0 ]^T$  {Goal pose reached}
else
     $\hat{\mathbf{n}} = \mathbf{p}_e/M$  {Compute desired translational direction}
     $\mathbf{r} = \hat{\mathbf{e}}_{1c} \times \hat{\mathbf{e}}_{1d} + \hat{\mathbf{e}}_{2c} \times \hat{\mathbf{e}}_{2d} + \hat{\mathbf{e}}_{3c} \times \hat{\mathbf{e}}_{3d}$  {Compute desired rotational axis}
    if sum( $\mathbf{r}$ ) then
         $\mathbf{r} = [ 0 \ 0 \ 0 ]^T$  {Check if rotational axis is zero, i.e., no need to rotate}
    else
         $\hat{\mathbf{r}} = \mathbf{r}/\|\hat{\mathbf{e}}_{1c} \times \hat{\mathbf{e}}_{1d} + \hat{\mathbf{e}}_{2c} \times \hat{\mathbf{e}}_{2d} + \hat{\mathbf{e}}_{3c} \times \hat{\mathbf{e}}_{3d}\|$  {Normalize rotation axis}
    end if
    if  $M > \lambda_p \epsilon_p$  then
         $V = V_{max}$ 
    else
         $V = M (V_{max} - V_{min}) / (\epsilon_p (\lambda_p - 1)) + (\lambda_p V_{min} - V_{max}) / (\lambda_p - 1)$ 
    end if
    if  $\zeta > \lambda_o \epsilon_o$  then
         $\Omega = \Omega_{max}$ 
    else
         $\Omega = \zeta (\Omega_{max} - \Omega_{min}) / (\epsilon_o (\lambda_o - 1)) + (\lambda_o \Omega_{min} - \Omega_{max}) / (\lambda_o - 1)$ 
    end if
     $\mathbf{t}_{des} = [ V \hat{\mathbf{n}}^T \ \Omega \hat{\mathbf{r}}^T ]^T$ 
end if

```

Redundancy Resolution

Once the desired twist of the end-effector is obtained as in (III.18), the configuration space velocities and then the joint space velocities of the continuum manipulator are computed.

In the case of full orientation control and a robot manipulator with 6 DoF, the configuration space velocities are given by:

$$\dot{\Psi} = \mathbf{J}_{arm}^\dagger \mathbf{t}_{des} \quad (\text{III.23})$$

where \mathbf{J}_{arm}^\dagger is the robust pseudoinverse [70] of the robot Jacobian:

$$\mathbf{J}_{arm}^\dagger = \mathbf{J}_{arm}^T \left(\mathbf{J}_{arm} \mathbf{J}_{arm}^T + \epsilon \mathbf{I} \right)^{-1}. \quad (\text{III.24})$$

ϵ , if properly chosen, allows the manipulator to get around singularities by damping the inverse of the Jacobian without producing high joint speeds. Several strategies have been proposed to compute ϵ and one of the most common ones is to tie ϵ to the manipulability of the robot manipulator as in [70]. In the case of the continuum robots investigated in this work, a singularity occurs when any of the continuum segments is straight, i.e. $\theta_k = pi/2$. Variable ε is, therefore, defined as:

$$\varepsilon = \begin{cases} 0 & \text{if } \theta_i \leq \theta_* \\ \frac{\alpha}{e^{\xi(\theta_0 - \theta_i)}} & \text{if } \theta_i > \theta_* \end{cases} \quad (\text{III.25})$$

where α and ξ are scalars that define the robust inverse constant at singularity and how quickly the damping is applied passed the safe bending angle θ_* respectively.

In the case of redundant robots, Equation III.23 becomes:

$$\dot{\Psi} = \mathbf{J}_{arm}^\dagger \mathbf{t}_{des} + (\mathbf{I} - \mathbf{J}_{arm}^\dagger \mathbf{J}_{arm}) \dot{\Psi}_0 \quad (\text{III.26})$$

where $\dot{\Psi}_0$ is a configuration space vector of velocities that can be used to accomplish a secondary task, $\mathbf{I} \in \mathbb{R}^{7 \times 7}$ is the identity matrix and

$$\mathbf{J}_{arm}^\dagger = \mathbf{W}^{-1} \mathbf{J}_{arm}^T (\mathbf{J}_{arm} \mathbf{W}^{-1} \mathbf{J}_{arm}^T + \epsilon \mathbf{I})^{-1}, \quad (\text{III.27})$$

matrix $\mathbf{W} \in \mathbb{R}^{7 \times 7}$ is a diagonal positive-definite matrix of weights, and $\epsilon(\Psi)$ avoids robot's singularities [70].

In the case of under-actuated robots, the desired configuration space velocity vector is given by:

$$\dot{\Psi}_{des} = \mathbf{J}_{ee}^\dagger \mathbf{t}_{ee} \quad (\text{III.28})$$

where

$$\mathbf{J}_{ee}^\dagger = \mathbf{J}_{ee}^T (\mathbf{J}_{ee} \mathbf{J}_{ee}^T + \varepsilon \mathbf{I})^{-1} \quad (\text{III.29})$$

$$\mathbf{J}_{ee} = \begin{bmatrix} \mathbf{I}_{5 \times 5} & \mathbf{0}_{5 \times 1} \end{bmatrix} \begin{bmatrix} \mathbf{R}_{ee}^T & \mathbf{0}_{3 \times 3} \\ \mathbf{0}_{3 \times 3} & \mathbf{R}_{ee}^T \end{bmatrix} \mathbf{J}_{arm} \quad (\text{III.30})$$

$$\mathbf{t}_{ee} = \begin{bmatrix} \mathbf{I}_{5 \times 5} & \mathbf{0}_{5 \times 1} \end{bmatrix} \begin{bmatrix} \mathbf{R}_{ee}^T & \mathbf{0}_{3 \times 3} \\ \mathbf{0}_{3 \times 3} & \mathbf{R}_{ee}^T \end{bmatrix} \mathbf{t}_{des}. \quad (\text{III.31})$$

Equations (III.35) and (III.36) are respectively the Jacobian matrix and the end-effector twist expressed in end-effector frame without the angular velocity component about axis $\hat{\mathbf{z}}_3$. By doing so, any commanded twist about that axis is ignored by the redundancy resolution and the continuum manipulator is controlled in 5 DoF.

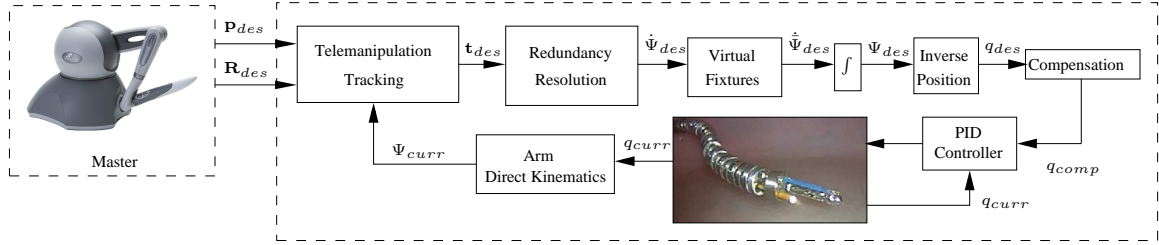


Figure III.17: Control architecture of the surgical robotic system.

Constrained Motion Control

Constrained Redundancy Resolution

The surgical slave is teleoperated using a Sensable Phantom Omni and the master/slave trajectory planner presented in [6]. Once the desired twist of the slave's end-effector, \mathbf{t}_{des} , is obtained, the constrained configuration space velocities, $\dot{\Psi}_{des}$, that approximate the desired motion are computed. As described in Section VI, the surgical slave is only capable to control 3 translational DoFs and two rotational DoFs (point in space). Furthermore, when the first segment is retracted inside the tubular constraint, the controllable DoFs drops to 3 (2 rotational DoFs and insertion along the resectoscope). For these reasons, we defined a primary task and secondary task. The primary task consists of controlling the two rotational DoFs (rotations about $\hat{\mathbf{x}}_0$ and $\hat{\mathbf{y}}_0$) and one translational DoF (along $\hat{\mathbf{z}}_0$) while the secondary task consists of controlling the remaining two translational DoF (along $\hat{\mathbf{x}}_0$ and $\hat{\mathbf{y}}_0$).

Designating \mathbf{t}_{ee} and \mathbf{J}_{ee} as the end effector twist and Jacobian in end-effector frame, one may describe the primary and secondary tasks by:

$$\mathbf{J}_{S_p} \dot{\Psi}_{des} = \mathbf{S}_p \mathbf{t}_{ee}, \quad \mathbf{J}_{S_s} \dot{\Psi}_{des} = \mathbf{S}_s \mathbf{t}_{ee} \quad (\text{III.32})$$

where \mathbf{J}_{S_p} and \mathbf{J}_{S_s} are defined by selecting the corresponding task-specific rows of the

jacobian:

$$\mathbf{J}_{S_p} = \mathbf{S}_p \mathbf{J}_{ee}, \quad \mathbf{J}_{S_s} = \mathbf{S}_s \mathbf{J}_{ee} \quad (\text{III.33})$$

and selection matrices \mathbf{S}_p and \mathbf{S}_s are given by:

$$\mathbf{S}_p = \begin{bmatrix} 0 & 0 & 1 & 0 & 0 \\ 0 & 0 & 0 & 1 & 0 \\ 0 & 0 & 0 & 0 & 1 \end{bmatrix} \quad \mathbf{S}_s = \begin{bmatrix} 1 & 0 & 0 & 0 & 0 \\ 0 & 1 & 0 & 0 & 0 \end{bmatrix} \quad (\text{III.34})$$

The end effector twist and Jacobian are given by:

$$\mathbf{J}_{ee} = \begin{bmatrix} \mathbf{I}_{5 \times 5} & \mathbf{0}_{5 \times 1} \end{bmatrix} \begin{bmatrix} \mathbf{R}_3^{0T} & \mathbf{0}_{3 \times 3} \\ \mathbf{0}_{3 \times 3} & \mathbf{R}_3^{0T} \end{bmatrix} \mathbf{J}_{arm} \quad (\text{III.35})$$

$$\mathbf{t}_{ee} = \begin{bmatrix} \mathbf{I}_{5 \times 5} & \mathbf{0}_{5 \times 1} \end{bmatrix} \begin{bmatrix} \mathbf{R}_3^{0T} & \mathbf{0}_{3 \times 3} \\ \mathbf{0}_{3 \times 3} & \mathbf{R}_3^{0T} \end{bmatrix} \mathbf{t}_{des}. \quad (\text{III.36})$$

The desired configuration space velocity is therefore given by:

$$\dot{\Psi}_{des} = \left(\mathbf{J}_{S_p}^\dagger \mathbf{S}_p + \left(\mathbf{I} - \mathbf{J}_{S_p}^\dagger \mathbf{J}_{S_p}^T \right) \mathbf{J}_{S_s}^\dagger \mathbf{S}_s \right) \mathbf{t}_{ee} \quad (\text{III.37})$$

and superscript \dagger indicates pseudo-inverse. Equation (III.37) partitions the commanded twist, \mathbf{t}_{ee} , into a primary task (defined by selection matrix \mathbf{S}_p) and a secondary task (defined by selection matrix \mathbf{S}_s). Equations (III.35) and (III.36) are respectively the Jacobian matrix and the end-effector twist expressed in end-effector frame without the angular velocity component about axis $\hat{\mathbf{z}}_3$. By doing so, any commanded twist about that axis is ignored by the redundancy resolution and the continuum manipulator is controlled in 5 DoF.

Virtual Fixture Design and Implementation

We now define two orthogonal spaces that partition the configuration space into a subspace of forbidden velocities $\{\bar{V}\}$ and a space of allowed velocities $\{V\}$. We can therefore two projection matrices that project the configuration space velocities of III.37 into forbidden and allowed velocities:

$$\bar{\mathbf{P}} = \bar{\mathbf{V}}(\bar{\mathbf{V}}^T \bar{\mathbf{V}})^\dagger \bar{\mathbf{V}}^T \quad (\text{III.38})$$

$$\mathbf{P} = \mathbf{I} - \bar{\mathbf{P}} \quad (\text{III.39})$$

where \dagger denotes pseudo-inverse for the case where \bar{V} is (column) rank deficient. For example, in the case of a tubular constraint, as the first segment of the continuum manipulator retracts inside the resectoscope, negative $\dot{\theta}_1$ is the forbidden configuration velocity and $\bar{\mathbf{V}}$ is defined as

$$\bar{\mathbf{V}} = \begin{bmatrix} 1 & 0 & 0 & 0 & 0 \end{bmatrix}^T. \quad (\text{III.40})$$

The desired configuration space velocity is therefore given by:

$$\dot{\tilde{\Psi}}_{des} = \mathbf{P}\dot{\Psi}_{des} + k_d \bar{\mathbf{P}}\mathbf{u} \quad (\text{III.41})$$

where $\mathbf{u} = f(\Psi)$ is a signed configuration space distance of the actual configuration Ψ_{curr} to the one imposed by the virtual fixture Ψ_{fix} , and scalar k_d determines how quickly the continuum manipulator is moved to the desired configuration. In the case of tubular constraint, vector \mathbf{u} and projection matrices $\bar{\mathbf{P}}, \mathbf{P}$ depend on the insertion variable q along the tube.

The desired configurations vector Ψ_{des} is then obtained via *Resolved Motion Rate*

[110]:

$$\Psi_{des} = \Psi_{curr} + \Delta_t \dot{\tilde{\Psi}}_{des} \quad (\text{III.42})$$

Once the desired configuration vector is obtained, using the kinematics relationship presented in VI one can compute the desired joint space position to be fed to the actuation compensation subsystem.

The application of virtual fixtures in the configuration space of the robot rather than in the operational space allows for easy correction of the motion of any portion of the continuum manipulator. The computation of projection matrices $\bar{\mathbf{P}}$, \mathbf{P} and vector \mathbf{u} is shown in Algorithm 3. As the robot is commanded to retract inside the resectoscope, the $\dot{\theta}_1$ direction is defined as forbidden and \mathbf{u} depends on the following safe bending angle:

$$\theta_{1,safe} = \theta_{min} + (\theta_0 - \theta_{min}) \frac{\|q_{ins}\|}{L_1}. \quad (\text{III.43})$$

Figure III.17 shows the complete control architecture of the surgical continuum robot. The desired pose is obtained from the master manipulator (Phantom Omni) at 125 Hz over the local area network. The telemanipulation tracking subsystem generates the desired task-space velocities according to the master-slave map as described in [6]. The redundancy resolution subsystem implements the algorithm described in section III while the virtual fixtures subsystems constructs and enforces the configuration space virtual fixtures as described in section III and Algorithm 3. Once the desired configuration space velocities are obtained, the desired joint-space positions are computed via the close-form inverse position analysis of the continuum manipulator and the model-based actuation compensation scheme of [114].

Algorithm 3 Virtual Fixture

Input: $\theta_1, \delta_1, \theta_2, \delta_2, q_{ins}$
Input: $\dot{\theta}_1, \dot{\delta}_1, \dot{\theta}_2, \dot{\delta}_2, \dot{q}_{ins}$

if $q_{ins} \leq 0$ then

$$\bar{V} \leftarrow \begin{bmatrix} \theta_1 & 0 & 0 & 0 & 0 \end{bmatrix}^T$$
$$\bar{P} \leftarrow \bar{V}(\bar{V}^T \bar{V})^\dagger \bar{V}^T$$
$$P \leftarrow I - \bar{P}$$

if $(\dot{q}_{ins} < 0) \& (\theta_1 \leq \theta_{min} + \theta_0 \|q_{ins}\|/L_1)$ then

$$u \leftarrow (\theta_{min} + \theta_0 \|q_{ins}\|/L_1 - \theta_1) \begin{bmatrix} 1 & 0 & 0 & 0 & 0 \end{bmatrix}^T$$

else

$$u \leftarrow \begin{bmatrix} 0 & 0 & 0 & 0 & 0 \end{bmatrix}^T$$

end if

else

$$\bar{P} = 0$$
$$P = I$$
$$u \leftarrow \begin{bmatrix} 0 & 0 & 0 & 0 & 0 \end{bmatrix}^T$$

end if

$$\tilde{\Psi}_{des} \leftarrow P \dot{\Psi}_{des} + k_d \bar{P} u$$

return $\tilde{\Psi}_{des}$

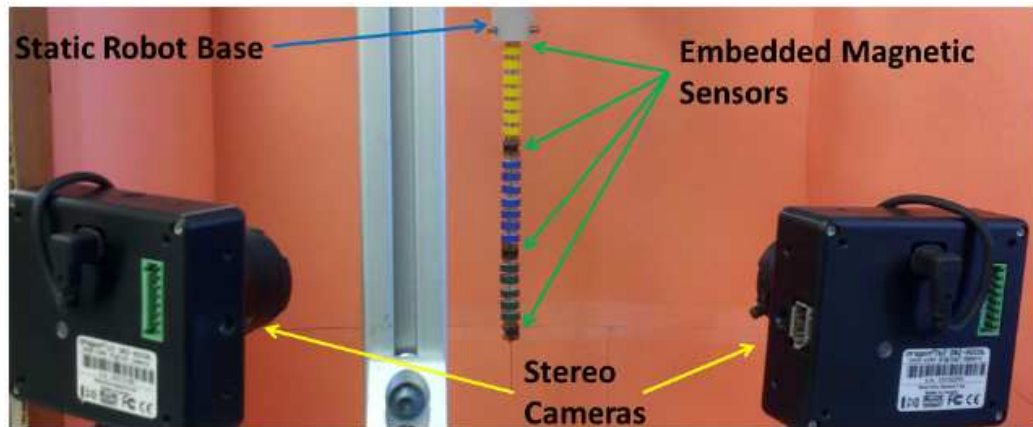


Figure III.18: The configurations of a three-segment continuum robot are estimated by a learning-based algorithm that interpolates a stereo feature descriptor manifold using Radial Basis Functions (Reiter, Bajo *et al.*).

Conclusions

This Chapter presented algorithms for enhanced performance of multisegment continuum robots in configuration and operational space.

The Configuration Space Controller is tiered with model-based actuation compensation and low level control. This hierarchical structure allows for increasing phase lag, tracking performance, multi-segment coupling, and modeling uncertainties. Experiments involved a three-segment continuum robot with magnetic sensors placed at the base, at the first end disk, at the second end disk, and at the end-effector. Recently, Reiter, Bajo, *et al.* [80] presented algorithmic solutions for pose estimation of multisegment continuum robots using vision feedback. Figure III.18 shows the experimental setup. These methods provide an alternative mean for closing the loop in configuration space and use the CSC in hybrid systems with vision feedback such as the IREP.

The telemanipulation framework was tested on two different systems and the results will be presented in Chapter 6. Algorithms for computing the desired pose from the master input are proposed along with all the necessary steps to compute the desired joint-space control input. The telemanipulation architecture can be tiered to the CSC in order to improve tracking performance and reduce telemanipulation bandwidth.

The constrained motion control algorithm enforces virtual fixtures in the configuration space of the continuum manipulator. The configuration space allows to apply constraints along the entire structure of the robot, often provides smaller dimensionality. The algorithms proposed in this Chapter was evaluated on the RDRP during bladder surveillance and targeting. The method is fundamental for complete coverage of the urinary bladder because the robot is required to both retract inside the

resectoscope and accomplish the desired targeting task. Experiments are presented in Chapter 6.

CHAPTER IV

CONTACT DETECTION AND ESTIMATION OF CONTACT LOCATIONS

This Chapter presents algorithmic solutions for collision detection and estimation of contact location along multisegment continuum robots. In particular, two methods for collision detection and one method for estimation of contact locations are proposed. The first method for collision detection is based on actuation force sensing and the statics model of the continuum manipulator. This method is analog to the one proposed by Matsumoto and Kosuge [68] but it has the advantage that only uses the statics of the continuum structure. No numerical derivatives are involved and therefore, it is not affected by numerical noise. The second collision detection method is purely kinematics-based. A motion deviation that takes into account real and theoretical position, orientation, linear and angular velocity of each segment is proposed. This technique allows for problem decoupling and simultaneous detection at multiple segments. Finally, the proposed method for estimation of contact location uses the proposed motion deviation and the constrained kinematics model presented in the previous Chapter. This work was originally published in [5] and [6].

Force-Based Collision Detection

This section presents a strategy for collision detection for continuum robots with actuation sensing capabilities. Actuation sensing capability is possible by placing a load cell between the i^{th} actuator and the i^{th} backbone.

Joint Force Deviation

When the continuum segment is not in contact with the environment, the statics relationship in (V.30) reduces to:

$$\mathbf{J}_{q_k \psi_k}^T \boldsymbol{\tau} = \nabla \mathbf{U} \quad (\text{IV.1})$$

Once contact at any arbitrary location along the segment occurs, a joint force deviation can be defined as:

$$\chi = \sqrt{(\nabla \mathbf{U} - \mathbf{J}_{q_k \psi_k}^T \boldsymbol{\tau}_{lc})^T (\nabla \mathbf{U} - \mathbf{J}_{q_k \psi_k}^T \boldsymbol{\tau}_{lc})} > \xi_{jfd} \quad (\text{IV.2})$$

where ξ_{jfd} is a predetermined contact detection threshold and $\boldsymbol{\tau}_{lc}$ is the force vector measured by the load cells.

Contact Detectability

Ideally, for perfect load cells and a perfect robot, contact detection threshold ξ_{jfd} would be zero and the system would be able to sense any contact. However, in a real situation there is a lower bound for the threshold ξ_{jfd} below which no contact is detectable. If friction forces $\boldsymbol{\tau}_{fri}$ are taken into account, the sensed forces $\boldsymbol{\tau}_{lc}$ might be related to the actual backbone forces as:

$$\boldsymbol{\tau} = \boldsymbol{\tau}_{lc} - \boldsymbol{\tau}_{fri} = (1 - \varepsilon_\tau) \boldsymbol{\tau}_{lc} \quad (\text{IV.3})$$

where ε_τ designates the relative error in the load cell measurements such that $\boldsymbol{\tau}_{fri} = \varepsilon_\tau \boldsymbol{\tau}_{lc}$. Using (IV.3), (IV.2) can be rewritten as:

$$\chi_c = (\nabla \mathbf{U} - \mathbf{J}_{q_k \psi_k}^T (1 - \varepsilon_\tau) \boldsymbol{\tau}_{lc})^T (\nabla \mathbf{U} - \mathbf{J}_{q_k \psi_k}^T (1 - \varepsilon_\tau) \boldsymbol{\tau}_{lc}) \quad (\text{IV.4})$$

For a calibrated system (i.e. $\mathbf{J}_{q_k \psi_k}^T \boldsymbol{\tau}_{lc} = \nabla \mathbf{U}$), (IV.4) becomes:

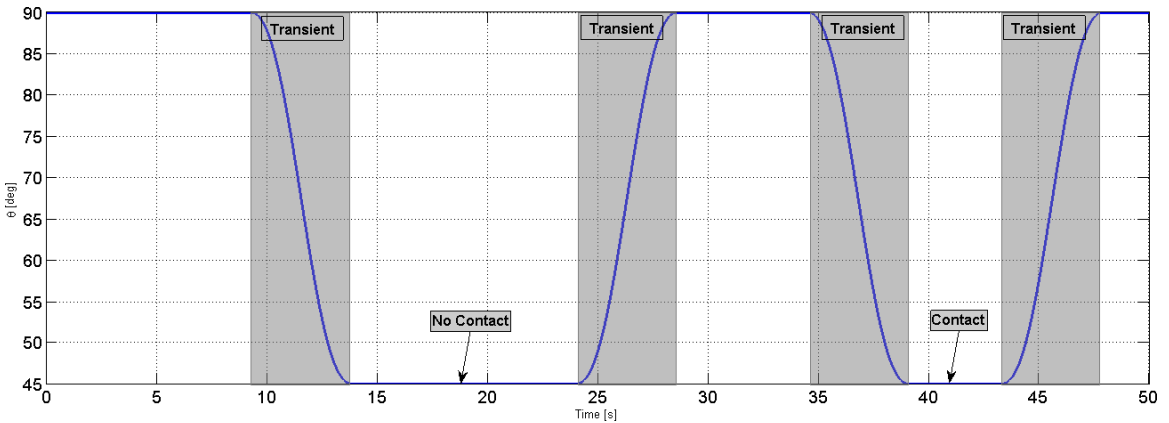
$$\chi_c = \varepsilon_\tau^2 \boldsymbol{\tau}_{lc}^T \mathbf{J}_{q_k \psi_k} \mathbf{J}_{q_k \psi_k}^T \boldsymbol{\tau}_{lc}. \quad (\text{IV.5})$$

Equation (IV.5) provide a relationship between the minimum threshold that allows contact detection, amount of friction in the system, kinematics design (Jacobian matrix $\mathbf{J}_{q_k \psi_k}$ includes radius r of the pitch circle on which the secondary backbone are equally distributed), and bending angle θ_k .

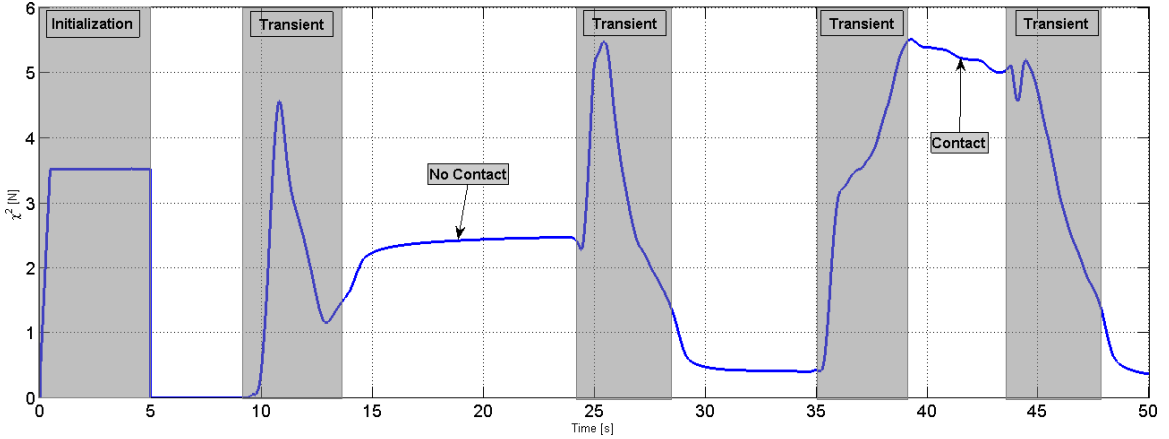
Experimental Results

Preliminary experiments have been conducted on a the two-segment continuum robot of Figure I.2(a). The second segment was bent according to the desired trajectory of Figure IV.1(b). In particular, the second segment was commanded twice to bend to desired configuration $\theta_2 = 45^\circ, \delta = 0$. During the first motion no contact is applied and the collision detection residual ξ shows two error peaks during transition and a steady state error of approximately 2.4 N. The transition error is due to unmodelled dynamic friction effect. The steady state error is due to unmodeled static friction effect. The segment is then straightened and bent again to the desired configuration. During this second motion a contact is applied at the second segment. The second half of graph IV.1(b) shows how the collision detection residual ξ is appreciably bigger than the first half of trajectory (no contact applied). The residual error is approximately 5.1 N. This discrepancy allows for detecting collisions using joint force information.

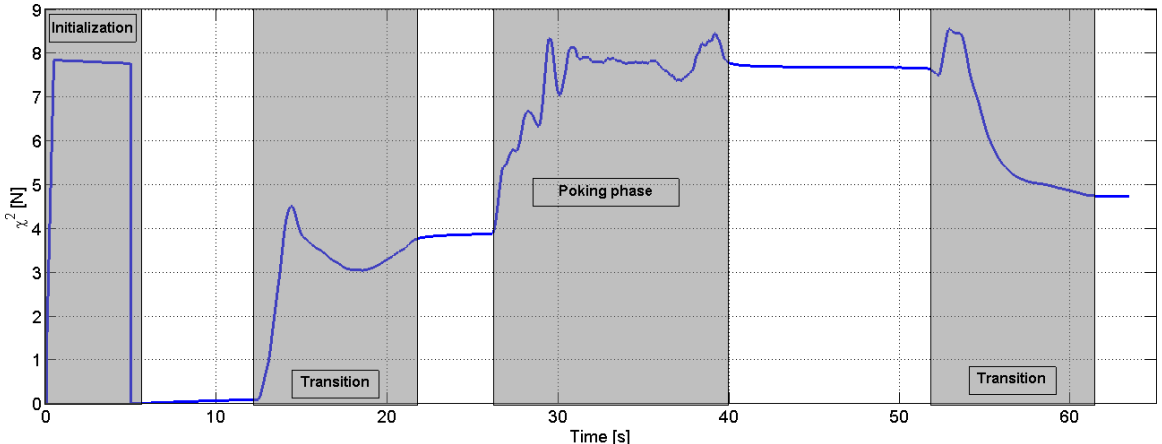
Additional experiments are reported in Figure IV.1(c) where the second segment is bent to $\theta_2 = 45^\circ, \delta = 0$ and underwent a *poking phase*. In particular, the entire robot was poked repeatedly to demonstrate the ability of the algorithm to detect collisions while at rest. The figure shows that after the interaction is ended (approximately



(a) Desired trajectory of the second segment



(b) Collision detection during motion



(c) Collision detection at rest

Figure IV.1: Force-based collision detection experiments using a two-segment continuum robot equipped with load cells. Difference in ξ (a) with and without contact during a pre-determined motion (b).

$t = 40s$) the friction has built up into the system and the residual error does not return back to the initial value (4N between $t = 20$ and $t = 25$).

Future experiments experiments will investigate the detection of collision in more realistic scenarios such as minimally invasive surgery of the throat and of the bladder.

Kinematics-Based Collision Detection

This section presents a kinematics-based collision detection for any single and multisegment continuum robot. The collision detection strategy is based on a motion deviation that captures the difference between the true motion of the robot obtained from extrinsic sensors and the theoretical kinematics model of the robot. The algorithm computes the motion deviation for each section of the robot in local frames attached at the base of each continuum segment. This strategy allows for segment decoupling and for the detection of individual contacts acting on different segments.

Screw Motion Deviation

This section defines a motion deviation using screw theory. In the following, the mathematical entities that constitute the instantaneous screw of motion of a rigid body are summarized from [3, 11]. As a consequence of Chasles's theorem [11], the instantaneous motion of a rigid body is fully described by the *Plücker line coordinates* [11] of the Instantaneous Screw Axis (ISA) and the screw pitch. Thus, the following three entities describe the motion of end disk k with respect to local base frame $\{B_k\}$:

$$\mathbf{r}_k = \frac{\boldsymbol{\omega}_{g_k/b_k}^{b_k} \times \left(\mathbf{v}_{g_k/b_k}^{b_k} + p_{g_k}^{b_k} \times \boldsymbol{\omega}_{g_k/b_k}^{b_k} \right)}{\|\boldsymbol{\omega}_{g_k/b_k}^{b_k}\|^2} \quad (\text{IV.6})$$

$$\hat{\boldsymbol{\omega}}_k = \frac{\boldsymbol{\omega}_{g_k/b_k}^{b_k}}{\|\boldsymbol{\omega}_{g_k/b_k}^{b_k}\|} \quad (\text{IV.7})$$

$$\lambda_k = \frac{\hat{\omega}_k^T (\mathbf{v}_{g_k/b_k}^{b_k} + p_{g_k}^{b_k} \times \boldsymbol{\omega}_{g_k/b_k}^{b_k})}{\|\boldsymbol{\omega}_{g_k/b_k}^{b_k}\|} \quad (\text{IV.8})$$

where vector \mathbf{r}_k locates the closest point on the screw axis relative to the origin, $\hat{\omega}_k$ is the unit vector along the axis, and λ_k is the screw pitch.

Note that the general case of rigid body motion, (IV.6), (IV.7), and (IV.8) are ill-defined when $\|\boldsymbol{\omega}_{g_k/b_k}^{b_k}\| = 0$. The screw axis lies along the direction of translational velocity and $\lambda_k = 0$. However, because of the constrained bending shape of continuum robots, $\mathbf{v}_{g_k/b_k}^{b_k}$ and $\boldsymbol{\omega}_{g_k/b_k}^{b_k}$ always vanish simultaneously. This means that during motion $\|\boldsymbol{\omega}_{g_k}^{b_k}\|$ is never equal to zero and the special case can be excluded.

A better way to compute vector \mathbf{r}_k is given by the following least-square approximation [3]:

$$\mathbf{r}_k = \mathbf{A}^\dagger \mathbf{b} \quad (\text{IV.9})$$

where superscript \dagger indicates the left pseudo-inverse and

$$\mathbf{A} = \begin{bmatrix} \boldsymbol{\Omega}_{g_k/b_k}^T & \boldsymbol{\omega}_{g_k/b_k}^{b_k T} \end{bmatrix}^T \quad (\text{IV.10})$$

$$\mathbf{b} = \begin{bmatrix} \boldsymbol{\Omega}_{g_k/b_k} \mathbf{p}_{g_k}^{b_k} - \boldsymbol{\Lambda} \mathbf{v}_{g_k}^{b_k} & 0 \end{bmatrix}^T, \quad (\text{IV.11})$$

$\boldsymbol{\Lambda} = \mathbf{I} - \boldsymbol{\omega}_{g_k/b_k}^{b_k} \boldsymbol{\omega}_{g_k/b_k}^{b_k T} / \|\boldsymbol{\omega}_{g_k/b_k}^{b_k}\|^2$, and \mathbf{I} is the 3×3 identity matrix.

Using (IV.7) and (IV.9) one obtains the *axode* of motion [10] associated with the motion of the k^{th} end disk. As a consequence of a collision, the axode of motion suddenly shifts as shown in Fig. IV.2. The figure shows the abrupt gap between *pre-contact* ISAs and *post-contact* ISAs when applying the constraint at the third SD. The constrained portion of the segment remains fixed while the unconstrained portion bends as a shorter segment with nominal length $L_k - \sigma_k$. The concept of screw motion deviation is also shown in Figures IV.3 and IV.4 where the axode of motion

obtained by experimental data is compared to its counterpart based on theoretical kinematics. Figure IV.3 shows a sequence of images depicting a continuum segment in free motion. The true axode of motion (magenta), after initial noise due to low twist magnitude, converges to the theoretical axode of motion (green). On the other hand, Figure IV.4 shows the motion deviation due to a contact acting at the third disk of the continuum segment. The true axode of motion (magenta) deviates from the theoretical one (green) shifting toward the end disk of the continuum segment.

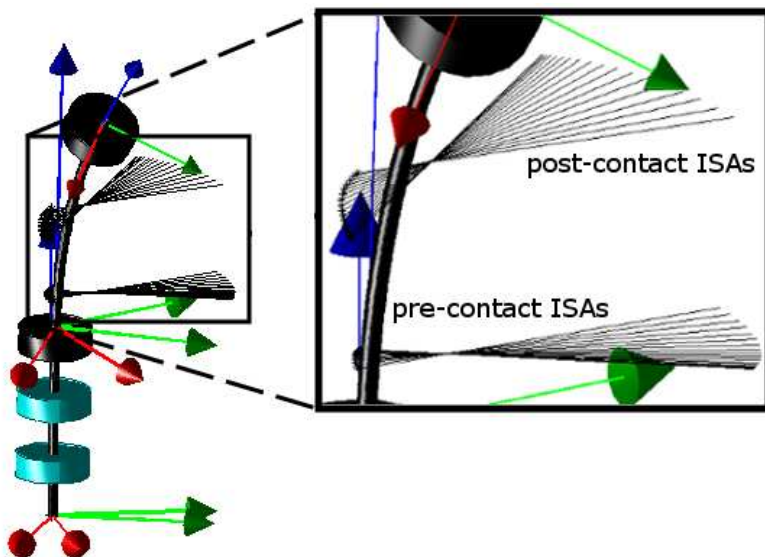


Figure IV.2: The group of ISAs after the contact is appreciably shifted toward the ED of the segment because of the smaller radius of curvature of the unconstrained portion of the segment. The closer the disk in contact is to the end disk, the closer the post-contact ISAs will be to the end disk.

Various approaches can be used to quantify the difference between two infinitesimally separated screws. Since the screw axis is essentially a line, one possible way is to use a Riemannian metric as described in [120]. For spatial motion, the natural generalization of the curve of centrododes used in [5] is given by what is called the *striction curve* [77]. An approximation of the striction curve is obtained by concatenating the closest points between infinitesimally separated screw axes. These pairs of points are obtained by the intersection of two consecutive screw axes and their common

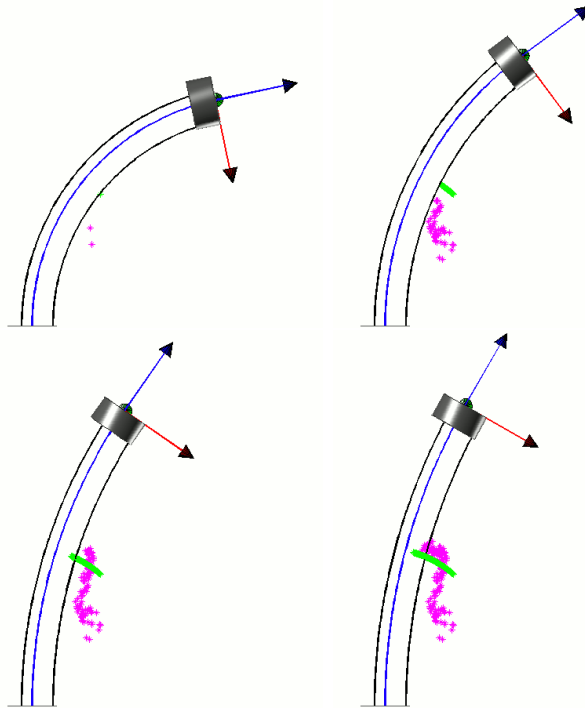


Figure IV.3: Comparison between the theoretical axode of motion (green) and the real one (magenta) obtained by extrinsic sensory information when no contact is applied to the continuum segment.

normal. The striction curve was used in [112] to classify knee pathologies. However, the striction curve is ill-defined when the CS bends in a fixed plane. In fact, during planar motion, the ISA's are all perpendicular to the bending plane and there are infinite pairs of points that define the minimum distance between the axes. In this case, the striction curve is no other than the curve of centrodes used in [5]. In order to eliminate this special case and decrease computation effort, we investigate the use of a Cartesian metric between the closest points from the origin on the expected ISA based on the kinematics model and on the sensed ISA as obtained from an extrinsic sensor.

Although it could be possible to detect a motion discrepancy between the theoretical and actual kinematics by separately monitoring position deviation, orientation

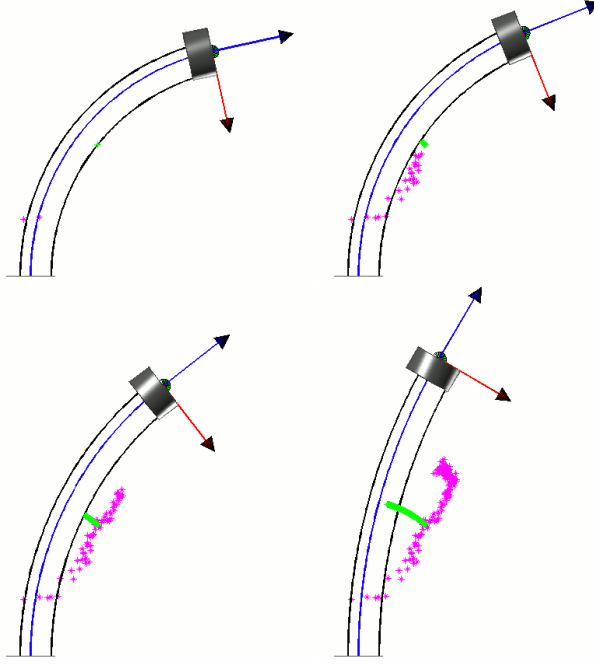


Figure IV.4: Comparison between the theoretical axode of motion (green) and the real one (magenta) obtained by extrinsic sensory information when a contact is applied to the continuum segment.

deviation, and twist deviation, it would not be possible to find a single metric with homogeneous units.

Assume that an extrinsic sensor provides the position $\bar{\mathbf{p}}_{g_k}^W$ and orientation $\bar{\mathbf{R}}_{g_k}^W$ of the ED of each segment with respect to a world reference frame $\{W\}$. Without loss of generality, we assume that $\{W\}$ is aligned with $\{B_1\}$. The relative position and orientation of the k^{th} ED with respect to the previous one is given by

$$\bar{\mathbf{p}}_{g_k}^{b_k} = \bar{\mathbf{R}}_W^{g_{k-1}} \left(\bar{\mathbf{p}}_{g_k}^W - \bar{\mathbf{p}}_{g_{k-1}}^W \right) \quad (\text{IV.12})$$

$$\bar{\mathbf{R}}_{g_k}^{g_{k-1}} = \bar{\mathbf{R}}_{g_k}^{b_k} = \bar{\mathbf{R}}_W^{g_{k-1}} \bar{\mathbf{R}}_{g_k}^W. \quad (\text{IV.13})$$

where all entities marked with a bar (i.e. \bar{p}) are based on sensor measurements.

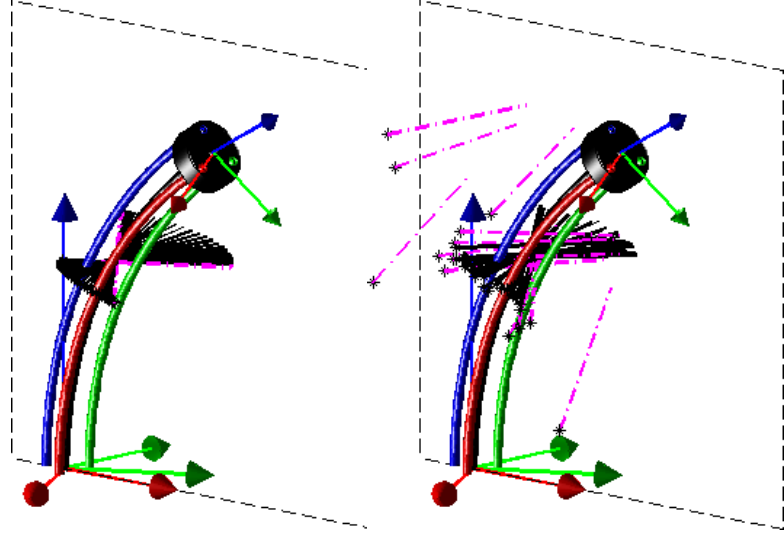


Figure IV.5: Comparison of the ISA's for a perfect sensor (a) and for a noisy sensor (b). The dashed ISA's indicates that the magnitude of the angular velocity is smaller than 0.1 rad/s

Equations (IV.12) and (IV.13) provide the decoupled motion of each segment. Using the constrained kinematic model in (II.29) and (II.30) with $\sigma_k = 0$ (i.e. no contact) the theoretical relative position $\mathbf{p}_{g_k}^{b_k}(\sigma_k = 0)$ and orientation $\mathbf{R}_{g_k}^{b_k}(\sigma_k = 0)$ are obtained. The theoretical linear and angular velocities $\mathbf{v}_{g_k/b_k}^{b_k}$ and $\boldsymbol{\omega}_{g_k/b_k}^{b_k}$ are obtained using (II.31) and (II.36) respectively. On the other hand, the sensed linear and angular velocities $\bar{\mathbf{v}}_{g_k/b_k}^{b_k}$ and $\bar{\boldsymbol{\omega}}_{g_k/b_k}^{b_k}$ are obtained by numerical differentiation of respectively (IV.12) and (IV.13) along with the definition of angular velocity. These theoretical and sensed relative poses and velocities are used to define the following Screw Motion Deviation (SMD):

$$\mu_k = \|\mathbf{r}_k(\sigma_k = 0) - \bar{\mathbf{r}}_k\| \quad (\text{IV.14})$$

where $\bar{\mathbf{r}}_k$ is calculated using (IV.6).

The use of relative motion data for μ_k decouples the SMD's and provides the basis for collision detection and estimation of contact location along any segment of the continuum robot independently.

Collision detection

Ideally, for a perfect robot, a perfect controller, and a perfect sensor, one would obtain $\mu_k = 0$. However, because of uncertainties due to kinematic model approximations, an uncalibrated robot, extension of the actuation lines, and sensor noise, μ_k will be bounded by a certain distance threshold ϵ_k during unconstrained motion. Collision is therefore independently detected for any segment when $\mu_k > \epsilon_k$ for $k = 1, 2, \dots, n$.

In the case of electromagnetic tracking devices, threshold ϵ_k is time, position, and velocity dependent because the accuracy varies depending on the workspace and the proximity to ferro-magnetic and conductive metals. Although it is possible to improve the accuracy of these devices by recalibrating the device [9, 46], we can assume that non-static ferro-magnetic objects are present in the proximity of the robot. Furthermore, if a low-order difference method is used for differentiating (IV.12) and (IV.13) with respect to time, low velocities amplify the noise components [121] and increase the variance of the SMD. For this reason the algorithm needs to filter out false positive due to noise ratio when $\|\omega_{g_k/b_k}^{b_k}\| < \zeta_k$ where ζ_k is a threshold with units of rad/s .

This phenomenon is reproduced in simulation and shown in Fig. IV.5. Fig. IV.5a shows an unconstrained CS following a quintic polynomial trajectory in configuration space with its compact axode of motion (i.e. the group of infinitesimally separated ISA's). The dashed ISA's are associated with $\|\omega_{g_k/b_k}^{b_k}\| < \zeta_k$. Since the motion is generated with a quintic polynomial, the dashed ISA's are associated with the beginning and the end of the motion. Figure IV.5b shows the CS following the same trajectory but the position and twist of its ED are perturbed with white Gaussian noise. When the magnitude of the noise is comparable to the magnitude of the linear and angular velocities, the screw of motion obtained with (IV.7) and (IV.9) loses any physical significance.

If a sensor with resolution ε_s [rad] collects data with frequency f_s [Hz], then the value of ζ_k must meet the following constraint for trustworthy velocity measurements:

$$\zeta_k > \alpha \varepsilon_s f_s \quad (\text{IV.15})$$

where $\alpha > 1$ (ideally 2 or 3). The threshold value ζ_k is proportional to sensor resolution ε and sample frequency f_s and defines the lowest angular velocity of each end disk under which no contact can be reliably detected. There are two ways to reduce the critical angular velocity magnitude ζ_k : increase sensor resolution or decrease sampling frequency. Although the latter solution also decreases threshold ζ_k , it also degrades the responsiveness of the collision detection algorithm by introducing lag into the system. However, since the minimal and maximal allowable twist is generally known once a task is defined, threshold ζ_k can be tuned accordingly.

Thus, we define the following binary function

$$\mathcal{F}(t) = \begin{cases} 1 & \boldsymbol{\mu}_k > \epsilon_k \\ 0 & \boldsymbol{\mu}_k \leq \epsilon_k \end{cases} \quad (\text{IV.16})$$

Once $\boldsymbol{\mu}_k > \epsilon_k$ and $\left\| \boldsymbol{\omega}_{g_k/b_k}^{b_k} \right\| > \zeta_k$, collision is detected when

$$\sum_{t=t_c}^{t_c+Q\Delta_t} \mathcal{F}(t) = Q \quad (\text{IV.17})$$

where t_c is the first instant in which $\boldsymbol{\mu}_k > \epsilon_k$, Δ_t is time step constant of the contact detection algorithm, and Q is the width of the collision detection window that allows to filter out false positives.

The collision detection strategy is described in Algorithm 4. Its inputs are: the nominal length of the segment, L_k , the closest point from the origin on the sensed

ISA, $\bar{\mathbf{r}}_k(t)$, the commanded configuration space orientation, $\psi(t)$, its time derivative, $\dot{\psi}(t)$, a counter variable c_{t-1} , a binary variable d_{t-1} , and the time step Δ_t . The algorithm initializes the contact arc-length $\sigma_k = 0$ so that the unconstrained model of the CS is used. Thus, it checks if the magnitude of the angular velocity is high enough to have meaningful sensor data. If this is the case, the motion residual is obtained using (II.29), (II.32), (II.37), (II.31), (II.36), and (IV.9). Next, it checks for $\mu_k > \epsilon_k$. In the case of detection, the algorithm checks if the collision detection window was previously started. If so, the counter variable c_{t-1} is incremented and used for future iterations. When the condition in (IV.17) is met, collision is detected.

Experimental Results

This section presents experiments of single-contact collision detection, multi-contact collision detection, collision detection repeatability, and estimation of contact location. In all experiments, the robot of Figure IV.9 was commanded from starting configuration $\psi_s = \begin{bmatrix} 72^\circ & 0^\circ & 72^\circ & 0^\circ & 72^\circ & 45^\circ \end{bmatrix}^T$ to final configuration $\psi_f = \begin{bmatrix} 45^\circ & 45^\circ & 45^\circ & -45^\circ & 45^\circ & 45^\circ \end{bmatrix}$ using a quintic polynomial trajectory with zero initial and final velocity, zero initial and final acceleration, and accomplishment time of five seconds in configuration space.

Single-Contact Collision Detection

The first set of experiments demonstrate the ability of the collision detection algorithm to detect a single collision acting along the continuum robot. Results are presented in Figures. IV.6, IV.7, and IV.8. The vertical lines labeled *detection enabled* and *detection disabled* designate beginning and end of the portion of the motion with the angular velocity magnitudes bigger than $\zeta_k = 0.1\text{rad/s}$ as described in Algorithm 1.

Algorithm 4 Collision detection

Input: L_k {length of k^{th} segment}
Input: $\psi(t)$ {commanded configuration space}
Input: $\dot{\psi}(t)$ {commanded configuration space velocity}
Input: $\bar{r}_k(t)$ {point from the origin on sensed ISA}
Input: Δ_t {time step}
Input: c_{t-1} {counter variable}
Input: d_{t-1} {collision detection flag at $t - \Delta_t$ }

$\sigma_k = 0$
if $\|\omega_{g_k/b_k}^{b_k}\| > \zeta_k$ **then**
 $\mathbf{p}_{g_k}^{b_k} \leftarrow$ equation (II.2) {position of gripper}
 $\mathbf{J}_{v\psi} \leftarrow$ equation (II.11) {translational Jacobian}
 $\mathbf{J}_{\omega\psi} \leftarrow$ equation (II.14) {rotational Jacobian}
 $\mathbf{v}_{g_k/b_k}^{b_k} \leftarrow \mathbf{J}_{v\psi} \dot{\psi}_d(t)$ {linear velocity}
 $\omega_{g_k/b_k}^{b_k} \leftarrow \mathbf{J}_{\omega\psi} \dot{\psi}_d(t)$ {angular velocity}
 $\mathbf{r}_k \leftarrow$ equation (IV.9) {point on expected ISA}
 $\mu_k(t) = \|\mathbf{r}_k - \bar{r}_k(t)\|$ {SMD}
 if $\mu_k > \epsilon_k$ **then**
 $c_t = c_{t-1} + 1$
 if $d_{t-1} == 1$ **then**
 if $c_t >= Q$ **then**
 return 1 {Collision detected}
 end if
 else
 $d_t = 1$ {start detection window}
 end if
 else
 $c_t = 0, d_t = 0$
 return 0 {No collision}
 end if
 else
 $c_t = 0, d_t = 0$
 return 0 {No Collision}
 end if

First, the first segment of the continuum robot is constrained during the motion. The time histories of SMD's μ_1 , μ_2 , and μ_3 as defined in IV.14 are presented in Figure IV.6. The SMD of the first segment (Fig. 7a) rises above the threshold at approximatively $t = 15s$. After a detection window of half second, collision is successfully triggered. The SMD's associated with the second and third segments (Figures IV.6b and IV.6c respectively) are not affected by the constraint.

Secondly, the second segment of the continuum robot is constrained during the motion. The time histories of SMD's μ_1 , μ_2 , and μ_3 are presented in Figure IV.7. Collision is detected at the second segment (Fig. IV.7b) at approximatively $t = 14.9s$ after a collision detection window of half second. The SMD μ_1 associated with the first segment is also affected by the contact and rises above the threshold at approximatively $t = 14.8s$. This delay is due to the compliance of the segments and allows to distinguish between single and multiple collisions as shown later in this section. Also in this case, the SMD μ_3 associated with the third segment remain unaffected.

Thirdly, the third segment of the continuum robot is constrained during the motion. The time histories of SMD's μ_1 , μ_2 , and μ_3 are presented in Figure IV.8. Collision is detected at the third segment at $t = 14.95s$ (Figure 9c). Similar to the previous case the two proximal segment are also affected by the contact as shown by their respective SMD's (Figures IV.8a and IV.8b).

These experiments are shown in Figure Figure:Collision:Detection:Experiemnts. The picture sequence demonstrate the ability of the collision detection algorithm to successfully detect collisions with a soft constraint and other continuum arms. This capability is of primary importance when the algorithm is implemented on surgical continuum robots and surgical robotic systems with continuum end-effectors [29]. The

collision detection algorithm would be able to prevent inadvertent trauma to delicate surrounding tissues by triggering a reaction strategy as in [23].

Multi-Contact Collision Detection

The second set of experiments demonstrate the ability of the collision detection algorithm to detect multiple collisions. We assume that the constraints act on different segments of the robot and that in the case of a two-contact collision, the proximal segment collides first. This is possible by using one of the reaction strategies proposed in [23]: once the collision is detected, the motion of the constrained segments is stopped while the unconstrained segments continue the pre-planned trajectory. Figure IV.10 shows the time histories of the SMD's μ_1 , μ_2 , and μ_3 . Collision with the first segment is detected at approximately $t = 14.2s$ (Figure IV.10a). The detection window is initiated immediately after the collision detection is enabled. Collision at the second segment is detected at approximately $t = 15s$ (Figure IV.10b). The main difference between Figure IV.10 and Figure IV.7 is the order in which collisions are detected. In Figure IV.7 collision is first detected at the second segment and then at the first segment. On the other hand, in Figure IV.10 collision is first detected at the first segment and then at the second segment. The order in which the collisions are detected allows for discerning between a single contact acting at the second segment and multiple contacts acting at the first and second segment. Similarly to the previous case studies, the SMD associated with the third segment is not affected and no collision is detected (Figure IV.8c).

Figure IV.11 shows the multi-segment continuum robot detecting multiple collisions acting at multiple segments and on the entire flexible structure.

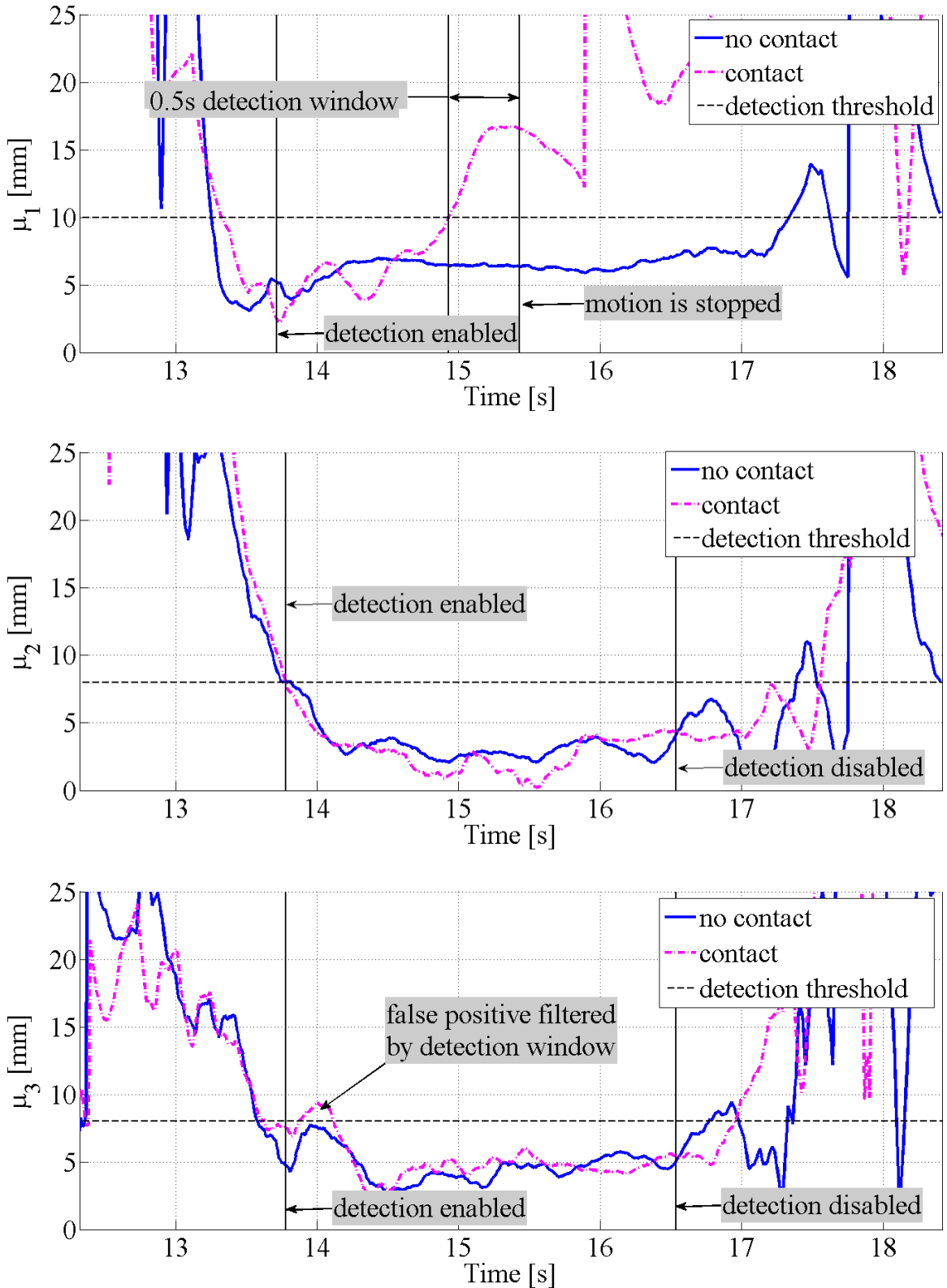


Figure IV.6: Constraint acting at the first segment. (a) time history of μ_1 , (b) time history of μ_2 , (c) time history of μ_3 .

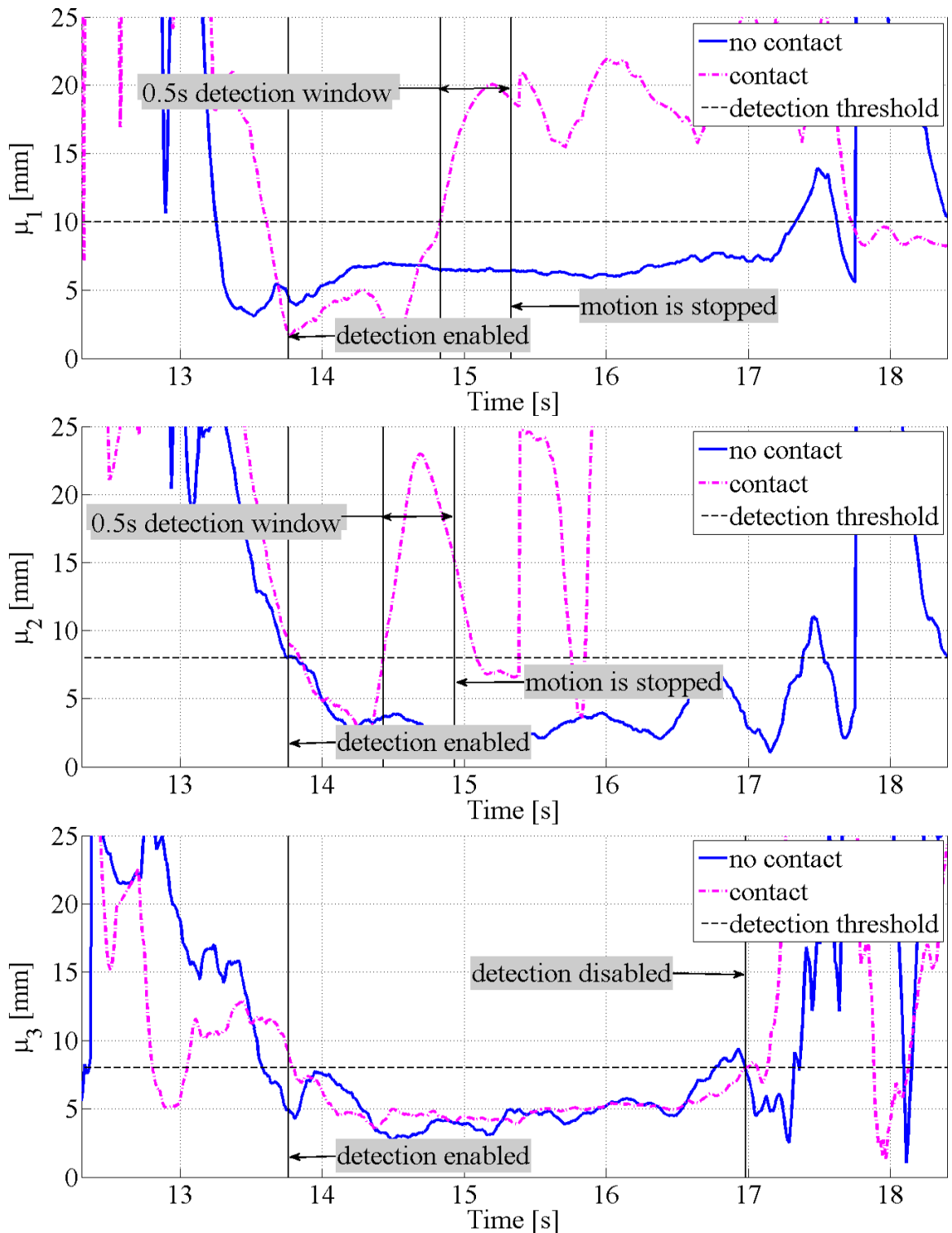


Figure IV.7: Constraint acting at the second segment. (a) time history of μ_1 , (b) time history of μ_2 , (c) time history of μ_3 .

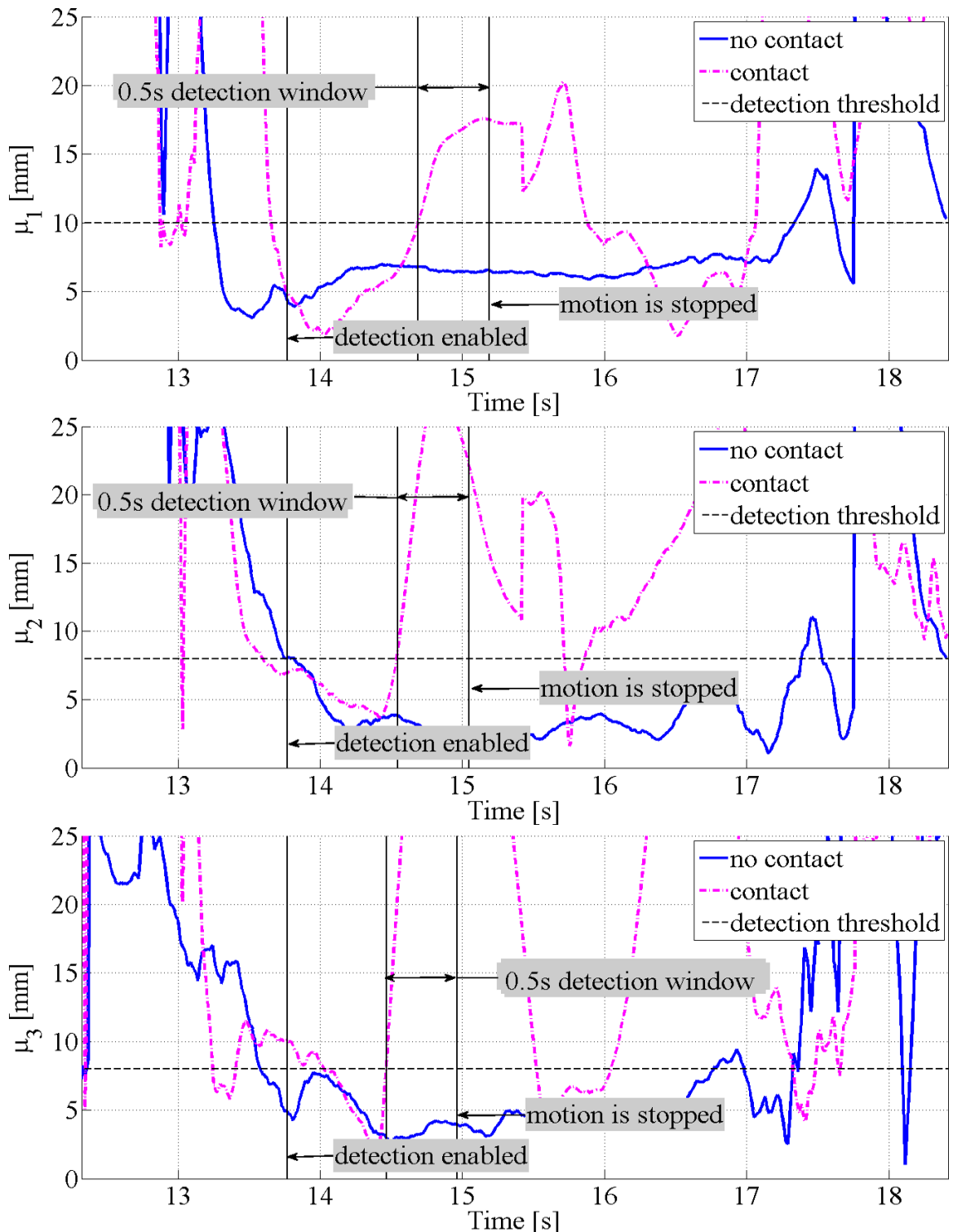
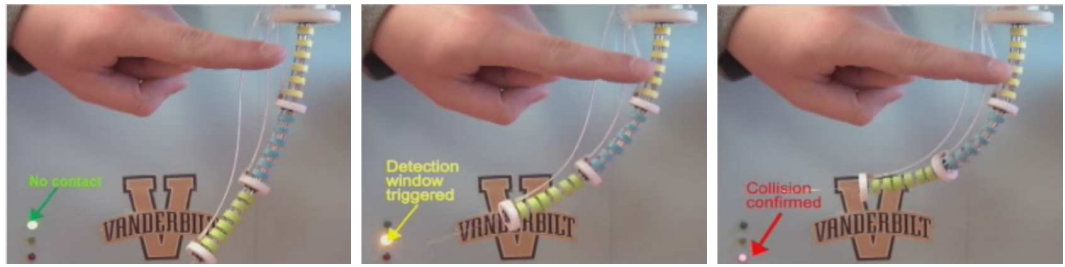
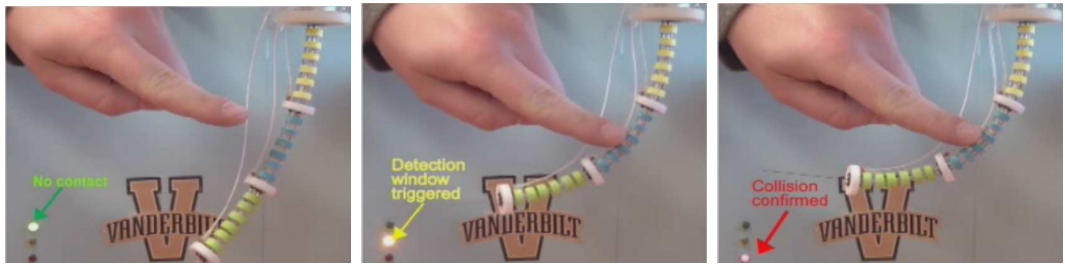


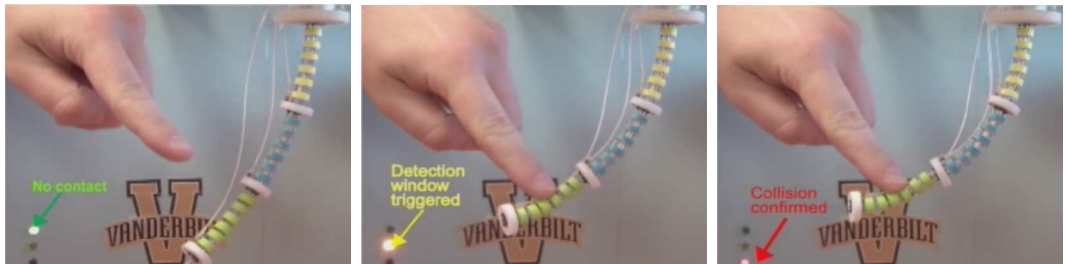
Figure IV.8: Constraint acting at the third segment. (a) time history of μ_1 , (b) time history of μ_2 , (c) time history of μ_3 .



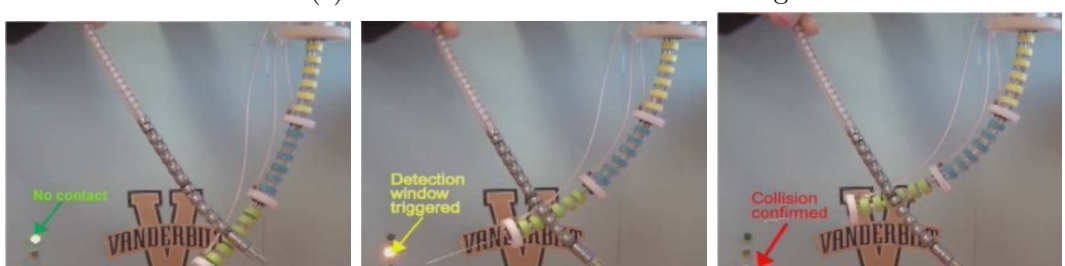
(a) Collision detected at the first segment



(b) Collision detected at the second segment



(c) Collision detected at the third segment



(d) Collision detected with another continuum arm

Figure IV.9: Collision detection experiments using a three-segment continuum robot equipped with magnetic sensors. (a) Constraint acting at the first segment. (b) Constraint acting at the second segment. (c) Constraint acting at the third segment. (d) Collision with another flexible arm.

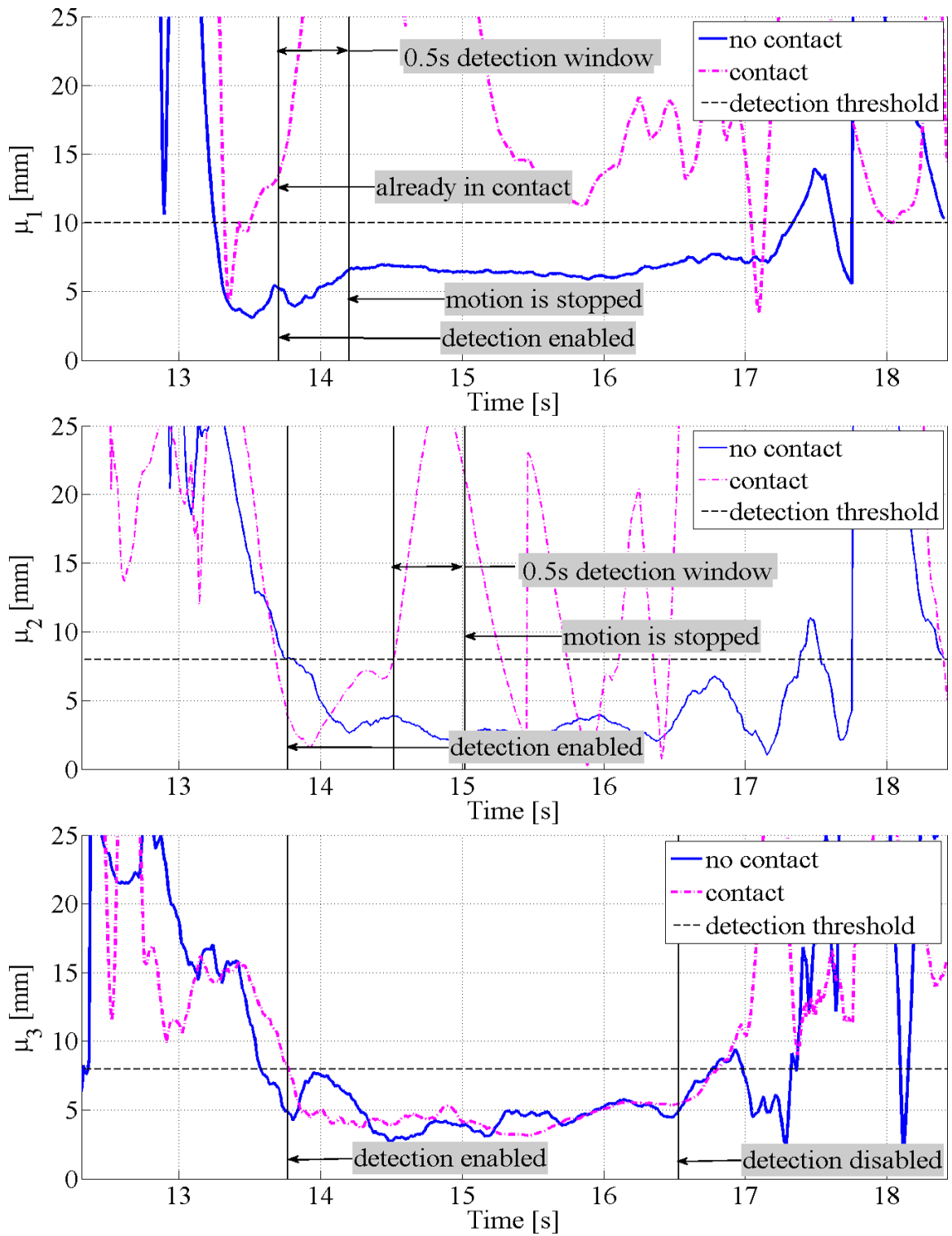
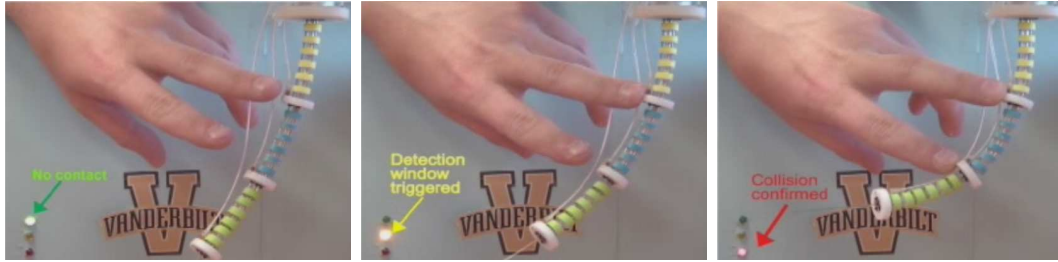
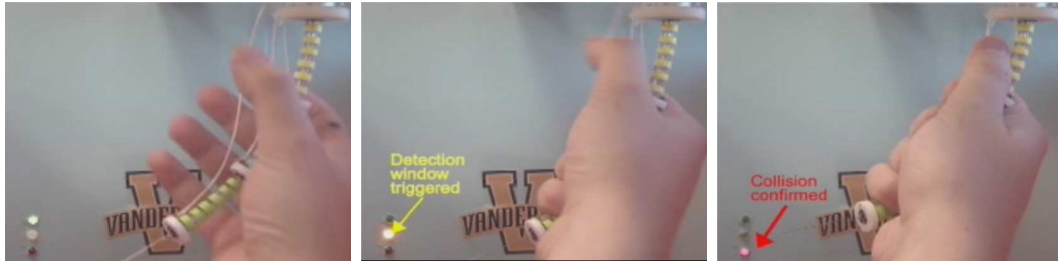


Figure IV.10: Detection of multiple collisions: (a) time history of μ_1 , (b) time history of μ_2 , (c) time history of μ_3



(a) Collision detected at the first segment



(b) Collision detected at the second segment

Figure IV.11: Multiple collision detection experiments using a three-segment continuum robot equipped with magnetic sensors. (a) Dual collision detection with detected at the first and second segment. (b) Total constraint acting at all segment simultaneously.

Repeatability of Collision Detection

Additional experiments were conducted to quantify the repeatability of the collision detection algorithm. The second segment of the continuum robot impacted a static, rigid object ten times. The constraining object is a carbon fiber tube covered with silicon material to increase friction at the contact point and reduce slippage. The time history of the SMD μ_2 for all ten trials is shown in Figure IV.12. The instant of collision varies by only 0.07s demonstrating a very high repeatability.

Kinematic-Based Estimation of Contact Location

For an n -segment continuum robot, the collision detection algorithm presented in the previous section already identifies which segments are constrained by the environment. We therefore propose a second algorithm that narrows down the estimation

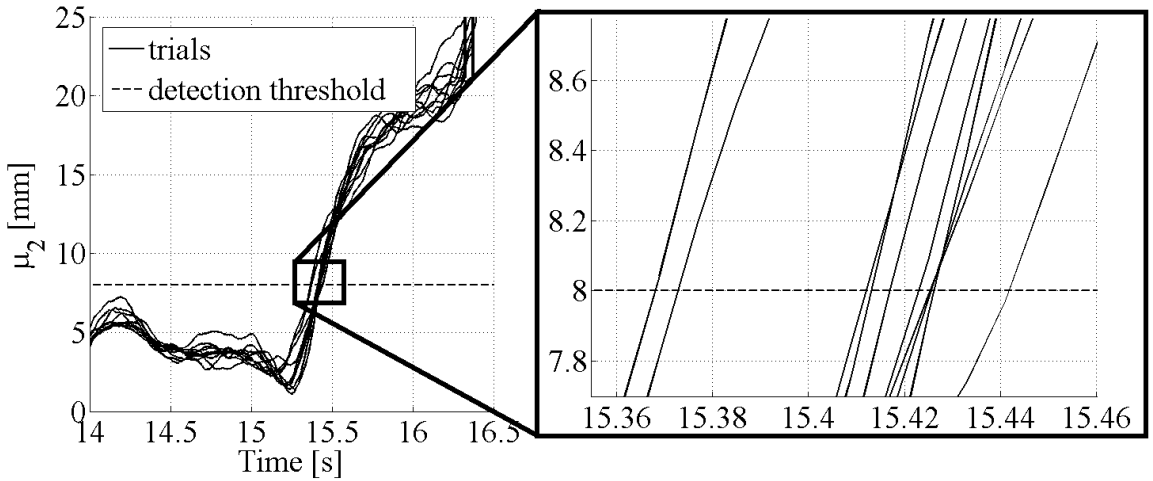


Figure IV.12: Repeatability analysis of contact detection. Time history of μ_2

Algorithm 5 Estimation of Contact Location

Input: L_k {length of k^{th} segment}
Input: N {number of disks}
Input: Δ_t {time step}
Input: t_c {instant of contact}
Input: t_f {end of detection window}
Input: $\psi(t_c : t_f)$ {trajectory for $t = t_c, \dots, t_f$ }
Input: $\dot{\psi}(t)$ {commanded configuration space velocity}
Input: $\bar{r}_k(t_c : t_f)$ {point on sensed ISA for $t = t_c, \dots, t_f$ }

for $\sigma_k = 0 : L_k/N : L_k$ **do**

- $\mathbf{p}_{c_k}^{b_k} \leftarrow$ equation (II.26) {compute position of C_k }
- $\mathbf{R}_{c_k}^{b_k} \leftarrow$ equation (II.27) {compute orientation of C_k }
- $\theta_{\sigma_k} \leftarrow$ equation (II.28) {compute angle at contact location}
- for** $t = t_c : \Delta_t : t_f$ **do**

 - $\mathbf{p}_{g_k}^{b_k} \leftarrow$ equation (II.29) {position of gripper}
 - $\mathbf{J}_{v\psi} \leftarrow$ equation (II.32) {translational Jacobian}
 - $\mathbf{J}_{\omega\psi} \leftarrow$ equation (II.37) {rotational Jacobian}
 - $\mathbf{v}_{g_k/b_k}^{b_k} \leftarrow \mathbf{J}_{v\psi} \dot{\psi}_d(t_c)$ {linear velocity}
 - $\boldsymbol{\omega}_{g_k/b_k}^{b_k} \leftarrow \mathbf{J}_{\omega\psi} \dot{\psi}_d(t)$ {angular velocity}
 - $\mathbf{r}_k \leftarrow$ equation (IV.9) {closest point on expected ISA}
 - $\mu_k(t) = \|\mathbf{r}_k - \bar{r}_k(t)\|$ {SMD}

- end for**
- $\tilde{\mu}_k \leftarrow \frac{1}{\Delta_t(t_f-t_c)} \sum \|\mu_k\|_{\sigma_k, t}$ {median of the SMD's}

end for

return σ_k with smallest $\tilde{\mu}_k$

of contact location at the segment level. The main assumption is that, immediately after collision, the constrained segment behaves according to assumption A2 of Chapter 2. This assumption was experimentally verified in [5] for a single segment with a fixed base during planar motion. In the case of multiple segments this assumption is still valid if the stiffness of two subsequent segments is comparable. The stiffness of constrained segment $k+1$ needs to be high enough to prevent the motion of segments $k = 1, \dots, k$. This assumption is experimentally evaluated in this work where the algorithm is used with a three-segment continuum robot in which the distal segment is very compliant. Results show that the estimation of the location at the third segment is less effective because assumptions A1 and A2 are violated.

The estimation method is described in Algorithm 5. Input N is the parameter that defines the level of discretization for the estimation. In the case of the continuum robot used in this work the contact is most likely to occur at any of the SD that are placed L_k/N apart from each other. Input Δ_t is the time step associated with the extrinsic sensor. Inputs t_c and t_f are the first and last instants of the detection window initiated by Algorithm 4. Inputs $\psi(t_c : t_f)$ and $\bar{\mathbf{r}}_k(t_c : t_f)$ are respectively the the desired configuration space trajectory and the time history of closest point on the sensed ISA. Once the algorithm is initialized, the algorithm collects the SMD's associated with each guessed σ_k and finds the arithmetic mean of the SMD for instants of time included into the detection window. The method finally returns the contact arc-length σ_k associated with the smallest SMD.

The accuracy of the estimation of contact location algorithm not only depends on the modeling arguments described in Chapter 2 but it is also affected by the discretization parameter N . The smaller this value is the finer the minimization problem is. For the robot used in this work, N is equal to the number of spacer disks. This means that the algorithm will only return the disk at which the contact is most likely

to occur. Contacts in between two adjacent spacer disks will be associated with one of the two disks. This phenomenon will be shown in remainder of this section.

Experimental Results

The last set of experiments evaluates the performance of the estimation algorithm. Each experiment is repeated five times and the obstacle is adjusted to constrain one of the spacer disks of the continuum robot. However, because of the small size of the robot, contact can occur at any location along the disk's height.

Results are reported in Tables IV.1, IV.2, and IV.3. Column d_i indicates which disk is impacted and column T indicates the experiment trial number. The remaining eight columns d_0, \dots, d_7 report the arithmetic average of the SMD associated with each guessed constrained disk locations as described in Algorithm 5. In particular, d_0 represents the base disk (i.e. no contact) and d_7 represents the end disk (i.e. segment completely constrained). In each row, the entry associated with the smallest SMD is highlighted in gray.

Experimental results of the estimation of contact location on the proximal segment of the continuum robot are presented in Table IV.1. Very small SMD's for two consecutive disks (3.64 mm apart from each other) are reported. This discrepancy in estimating the location of contact corresponds to a worst-case-scenario error of at most the height of two SD's and the space between two adjacent disks. The sources of uncertainty and the possible slippage of the robot with respect to the rod indicate that the error in estimating the contact location within one disk error is indeed expected.

Experimental results of the estimation of contact location on the second segment of the continuum robot are presented in Table IV.2. The success rate of the algorithm is appreciably higher than the previous case study. The improvement is due to better noise/signal ratio and a smaller collision threshold as shown in Figures IV.7a and

IV.7b. The third disk is successfully identified four out of five times and the fourth disk is successfully identified five out of five times . In the case of the second and fifth disks, the algorithm reports a very small deviation between consecutive disks 1,2 and 5,6.

Experimental results of the estimation of contact location on the second segment of the continuum robot are presented in Table IV.3. The performance of the estimation algorithm appear to be more problematic because Assumption A2 is violated as shown Figure IV.13. The lower stiffness of the third continuum segment results in dramatic deformation of the segment invalidating the constrained kinematic model presented in Chapter 2.

Table IV.1: Contact estimation along the first segment. Units of mm

d_i	T	d_0	d_1	d_2	d_3	d_4	d_5	d_6	d_7
3	1	9.2	6.0	3.4	3.6	6.3	9.6	13.0	16.5
	2	7.7	4.7	3.0	4.7	7.8	11.1	14.6	18.0
	3	9.8	6.4	3.5	2.9	5.4	8.7	12.2	15.7
	4	9.8	6.6	4.1	3.9	6.2	9.4	12.7	16.1
	5	10.4	7.1	4.2	3.2	5.3	8.4	11.8	15.2
4	1	11.7	8.4	5.6	4.1	5.2	7.9	11.1	14.5
	2	11.9	8.7	6.0	4.5	5.4	8.0	11.0	14.4
	3	11.7	8.6	6.0	4.6	5.7	8.3	11.4	14.7
	4	11.7	8.5	5.7	4.7	5.2	7.9	11.1	14.4
	5	11.3	8.1	5.2	3.7	5.1	7.9	11.2	14.6
5	1	14.6	11.3	8.2	5.4	3.8	5.0	7.7	10.8
	2	15.0	11.6	8.3	5.3	3.1	4.0	6.9	10.1
	3	15.6	12.4	9.2	6.3	4.3	4.7	7.0	10.0
	4	16.2	12.9	9.7	7.1	5.3	5.4	7.4	10.2
	5	15.6	12.5	9.7	7.5	6.4	7.1	9.1	11.8

Table IV.2: Contact estimation along the second segment. Units of mm

d_i	T	d_0	d_1	d_2	d_3	d_4	d_5	d_6	d_7
2	1	7.0	5.8	6.3	8.4	11.0	14.1	17.2	20.4
	2	5.9	4.7	5.7	8.1	11.1	14.3	17.6	20.9
	3	6.3	4.5	5.0	7.4	10.4	13.7	17.0	20.4
	4	7.8	6.5	6.7	8.4	10.9	13.8	16.9	20.0
	5	6.1	3.9	4.1	6.7	9.8	13.1	16.5	19.9
3	1	11.8	10.4	9.9	10.5	12.0	14.0	16.5	19.3
	2	13.1	11.2	10.0	9.7	10.6	12.3	14.6	17.2
	3	13.2	11.3	10.1	9.9	10.7	12.3	14.7	17.3
	4	13.0	11.0	9.6	9.2	10.0	11.7	14.1	16.8
	5	13.1	11.1	9.8	9.5	10.4	12.1	14.4	17.1
4	1	18.1	15.8	13.8	12.4	11.7	11.9	13.0	14.8
	2	17.9	15.4	13.3	11.8	10.9	11.1	12.2	14.0
	3	17.6	15.2	13.2	11.7	11.1	11.4	12.6	14.4
	4	18.7	16.3	14.2	12.6	11.6	11.6	12.4	14.0
	5	17.8	15.2	13.2	11.6	10.9	11.1	12.2	14.1
5	1	20.3	17.1	13.9	10.7	7.8	5.6	5.1	6.7
	2	22.2	19.2	16.4	13.7	11.4	9.7	9.0	9.5
	3	21.6	18.7	16.0	13.5	11.4	10.0	9.6	10.4
	4	22.0	19.0	16.3	13.7	11.5	10.0	9.5	10.1
	5	21.0	18.1	15.3	12.7	10.5	9.1	8.9	9.9

Conclusions

Preliminary results have been presented to validate the theory and feasibility implementation of both algorithms for collision detection along multisegment continuum robots.



Figure IV.13: Effects on shape deviation when assumption A2 is violated.

Table IV.3: Contact estimation along the third segment. Units of mm

d_i	T	d_0	d_1	d_2	d_3	d_4	d_5	d_6	d_7
2	1	7.6	5.1	3.8	4.8	7.3	10.1	13.2	16.2
	2	8.7	7.3	7.0	8.1	10.0	12.5	15.2	18.0
	3	5.1	3.4	4.2	6.7	9.7	12.7	15.8	18.9
	4	5.3	4.4	5.5	7.9	10.7	13.6	16.6	19.7
	5	7.2	6.7	7.4	9.3	11.7	14.4	17.2	20.1
3	1	12.2	9.4	6.9	5.1	4.9	6.6	9.0	11.8
	2	15.7	13.2	10.9	9.0	8.0	8.1	9.2	11.1
	3	14.8	12.6	10.7	9.4	9.0	9.6	11.0	13.0
	4	15.3	12.4	9.6	7.0	5.2	5.0	6.5	8.9
	5	15.1	12.6	9.3	6.4	5.8	6.2	7.1	11.2
4	1	12.0	10.2	9.1	9.0	9.8	11.4	13.6	16.0
	2	14.5	11.8	9.3	7.2	6.0	6.3	7.9	10.3
	3	12.6	10.7	9.5	9.0	9.5	10.9	12.9	15.2
	4	13.6	10.9	8.6	6.9	6.3	7.1	9.0	11.4
	5	11.6	9.6	7.6	6.8	7.3	8.9	11.1	13.6

The JFD-based algorithm was tested on a single segment continuum robot without proper estimation of Young's modulus and friction. Although the experiments were conducted with an uncalibrated robot, results show the potential of this algorithm in detecting collisions. Goldman *et al.* used the idea behind the JFD-based algorithm to trigger compliant motion control and proposed the use of a support vector machine to estimate non-linear friction effects along the actuation lines. The authors demonstrated that even without a model for friction, it is possible to compensate for uncertainties and, therefore, accurately tune the collision detection threshold. This algorithm can be straightforwardly implemented on surgical continuum robots with actuation force sensing such as the system presented in [36]. In future investigations, the aforementioned system will be equipped with the JFD-based collision detection and use in surgical scenarios will be demonstrated. In particular, the JFD-based algorithm will be used to construct virtual fixtures in real-time without *a priori* knowledge of the environment ensuring safety during telemanipulation.

The SMD-base algorithm is able to detect multiple collision along multiple segments. Experiments demonstrated the ability of the algorithm to sense collision with soft environments and other continuum arms. The SMD-based algorithm has also been integrated with a constrained Kalman filter in [101] for the registration of continuum surgical robots to compliant environments. The constrained Kalman filter uses only meaningful data provided by the collision detection algorithm. This strategy can also be applied to blind exploration of environment in extreme conditions where vision and other sensory information are not available. The collision detection algorithm my be integrated with a search strategy in order to efficiently explore a portion of the robot workspace.

The kinematics-based estimation algorithm uses a simplifies constrained model in which the base of the segment is assumed fixed or quasi static. Although proper filter need to be applied to the magnetic tracker data, experiments demonstrated that when the requirements in term of stiffness of two consecutive segments are met, the estimation algorithm is able to estimate contact better than 20% of the segment length.

CHAPTER V

HYBRID MOTION/FORCE CONTROL OF MULTI-BACKBONE CONTINUUM ROBOTS

This section presents a general framework for hybrid motion/force control of continuum robots. We assume that the kinematic model is known and that the robot is equipped with a device for measuring or estimating environmental interaction forces. This information can be provided by a dedicated miniature multi-axis force sensor placed at the tip of the robot or by an intrinsic wrench estimator of the types described in [115, 86, 107]. In this work, a multi-backbone continuum robot with intrinsic wrench estimation capabilities is used to demonstrate the hybrid motion/force control framework. The following assumptions specifically apply to multi-backbone continuum robots with intrinsic force sensing. Different assumptions are necessary for different types of robots but the fundamental control framework remain invariant.

Assumption 1 The continuum robot bends in a circular shape and gravitational forces are negligible. These assumptions were verified in [115] and [116] for small robots such as the one used in this work.

Assumption 2 The continuum robot is able to sense actuation forces via load cells placed between each actuation line and its actuator. Examples of actuation units with force sensing capabilities are provided in [115] and [35].

Assumption 3 The geometric constraint is known and the environment is rigid. This information is used for both the hybrid motion/force controller and the intrinsic wrench estimation. However, because of the innate compliance of continuum robots

and as demonstrated by experimental results, an exact knowledge of the geometric constraint is not necessary.

Figure V.1 shows the classical hybrid motion/force controller for rigid-link robot manipulators as proposed in [56]. Motion and force controllers provide two separate control signals that are first projected into allowable motion and force directions (using projection matrices Ω and $\bar{\Omega}$) and then merged into the joint-space of the manipulator. Motion commands are first transformed into task-space wrenches using the inverse of the inertia matrix \mathbf{B} and then into joint-torque commands using the transpose of the Jacobian matrix \mathbf{J} . The desired joint-torque vector Γ is then added to the feedback linearization term that compensates for non-linearities (e.g. coriolis/centrifugal and gravitational effects) and fed to the joint-space PID controller.

Figure V.2 shows the proposed hybrid motion/force controller for multi-backbone continuum robots with intrinsic force sensing. As in the classic architecture in Figure V.1, two separate controllers produce motion and force commands that are then projected into allowable motion/force directions using projection matrices Ω and $\bar{\Omega}$. Hence, the motion and force commands are projected into the configuration space velocity of the continuum manipulator using respectively the inverse of the Jacobian matrix $\mathbf{J}_{t\psi}$ and a composition of the transpose of the matrix $\mathbf{J}_{t\psi}$ and the configuration space compliance matrix \mathbf{K}_ψ^{-1} . The configuration space compliance matrix provides a mapping between the change in task-space wrenches and the change in configuration space velocities. Finally, using the closed-form inverse position of the manipulator, the theoretical desired joint-space positions \mathbf{q}_{des} are obtained. Similar to the feedback linearization term in Figure V.1, an additional term is obtained through the statics of the continuum manipulator and the stiffness of the actuation lines. This term include both an actuation compensation term for the applied wrench at the tip of the robot and a compensation term for extension and friction in the actuation lines.

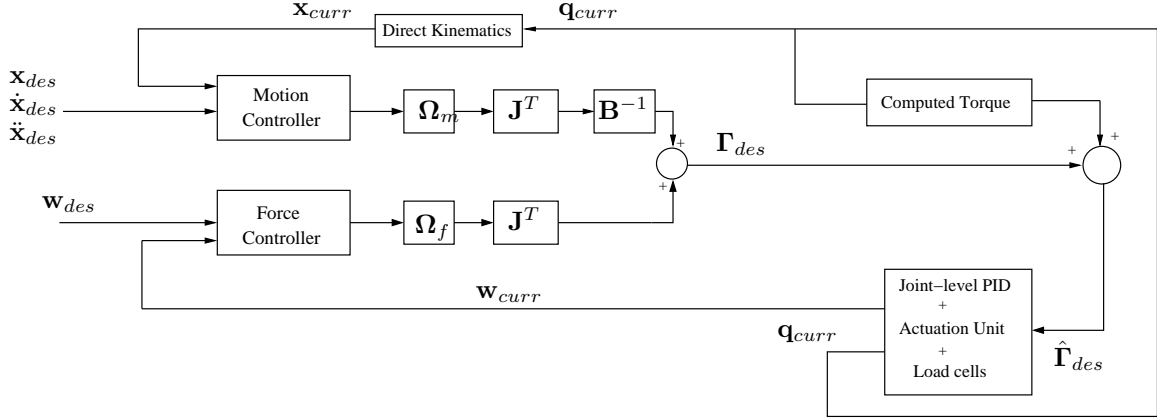


Figure V.1: Classic hybrid motion/force control of rigid-link industrial manipulators [56]. Ω and $\bar{\Omega}$ are projection matrices, \mathbf{J} is the Jacobian matrix of the manipulator, \mathbf{B} is the inertia matrix of the manipulator, $\boldsymbol{\Gamma}_{des}$ is the joint torques vector that accomplishes the desired motion and force tasks, and $\hat{\boldsymbol{\Gamma}}_{des}$ is the joint torque vector that includes the feedback linearization term.

In the reminder of this chapter, the foundations of hybrid motion/force control are summarized and the proposed adaptation for continuum robots is presented, analyzed, and evaluated.

Control Architecture

A First-order Model of Contact

Hybrid motion/force control aims at controlling the interaction of two rigid bodies by decoupling control inputs into allowable *relative motions* and *constraining wrenches*¹. The control inputs are specifically generated to maintain contact between the two bodies by simultaneously generating motion directions that do not break the contact state and apply the desired interaction wrench. For example, in the case of frictionless point contact (see Figure V.3), body 1 can translate along axes x and y ,

¹Here we adopt the notation of axis coordinates for motion screws ($T = [\mathbf{v}_0^T, \boldsymbol{\omega}^T]^T$) where \mathbf{v}_0 is the linear velocity and $\boldsymbol{\omega}$ is the angular velocity. We also adopt the ray coordinate representation for wrenches ($F = [\mathbf{f}^T, \mathbf{M}^T]^T$) where \mathbf{f} is a force vector and \mathbf{M} is a moment.

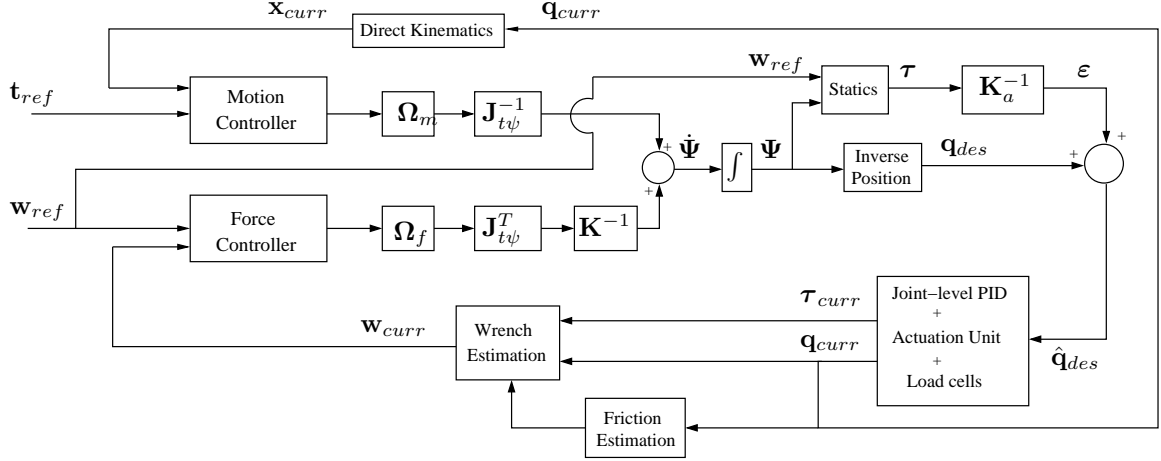


Figure V.2: Proposed hybrid motion/force control of multi-backbone continuum robots with intrinsic force sensing. Ω and $\bar{\Omega}$ are projection matrices, $\mathbf{J}_{t\psi}$ is the Jacobian matrix, \mathbf{K} is the configuration-space stiffness matrix, Ψ is the configuration space vector, \mathbf{K}_a is the joint-space stiffness matrix.

rotate about axes \hat{x} , \hat{y} , and \hat{z} , and apply a force along axis \hat{z} , i.e. the normal vector between body 1 and body 2.

Regardless of the type of contact, it is always possible to define two dual vector sub-spaces, one containing wrenches \mathbf{F}^6 , and the other containing motion screws \mathbf{M}^6 [59, 32]. The reciprocal product between these two spaces is defined as the rate of work done by a wrench f_i acting on a motion screw m_j . In the case of rigid bodies, under conservative contact, the bases of the two spaces must satisfy the reciprocity condition [33]. At any given time, the type of contact [67] between the two rigid bodies defines two vector sub-spaces: a n -dimensional space of normal vectors $N \subseteq \mathbf{F}^6$ and a $(6-n)$ -dimensional space of tangent vectors $T \subseteq \mathbf{M}^6$, where n is the degree of motion constraint. The bases of these two spaces can be defined by a $6 \times n$ matrix \mathbf{N} and a $6 \times (6 - n)$ matrix \mathbf{T} . The columns of \mathbf{N} and \mathbf{T} are respectively any n linearly independent wrench in N and any $6 - n$ linearly independent motion screw in T . As a consequence of the reciprocity condition and the contact constraint, the scalar

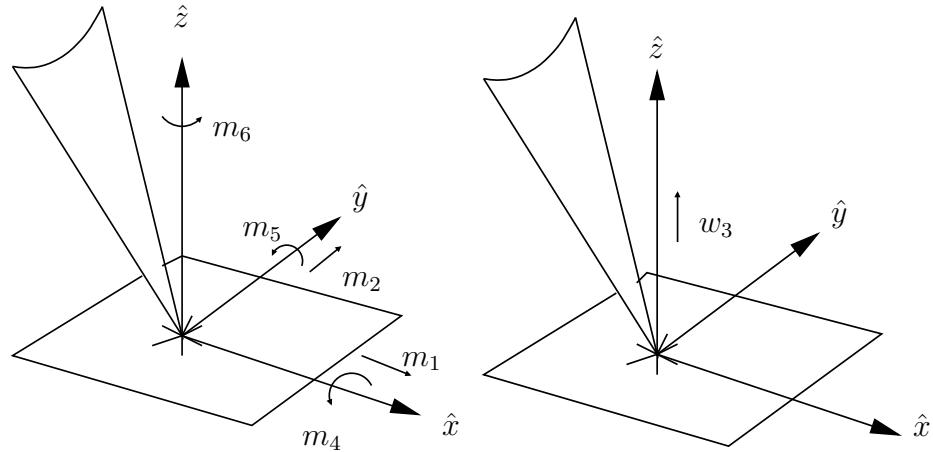


Figure V.3: Wrench and twist screw bases corresponding with a frictionless point contact (adapted from [67])

product of any column of \mathbf{N} with any column of \mathbf{T} is zero, i.e.

$$\mathbf{N}^T \mathbf{T} = \mathbf{0} \quad (\text{V.1})$$

For example, for the contact constraint depicted in Figure V.3, matrices \mathbf{N} and \mathbf{T} are given by:

$$\mathbf{N} = \begin{bmatrix} 1 & 0 & 0 & 0 & 0 \\ 0 & 1 & 0 & 0 & 0 \\ 0 & 0 & 0 & 0 & 0 \\ 0 & 0 & 1 & 0 & 0 \\ 0 & 0 & 0 & 1 & 0 \\ 0 & 0 & 0 & 0 & 1 \end{bmatrix}, \mathbf{T} = \begin{bmatrix} 0 \\ 0 \\ 1 \\ 0 \\ 0 \\ 0 \end{bmatrix} \quad (\text{V.2})$$

Although in many situations matrices \mathbf{N} and \mathbf{T} are simply the composition of canonical vectors in \mathbb{R}^6 and can be obtained by inspection [66], this is not the case when dealing with complex interaction tasks and multi-point contacts [59, 32].

Projection Matrices

The efficacy of hybrid motion/force control stems from its ability to produce adequate motion and force control inputs that do not violate the reciprocity condition (Equation V.1). The reciprocity of the control inputs is enforced by projecting each control input into the correct subspace by pre-multiplication of a projection matrix. We, therefore, define two projection matrices Ω_f and Ω_m that project any control input into consistent wrenches and twists respectively:

$$\Omega_f = \mathbf{N}(\mathbf{N}^T \mathbf{N})^{-1} \mathbf{N}^T \quad (\text{V.3})$$

$$\Omega_m = \mathbf{T}(\mathbf{T}^T \mathbf{T})^{-1} \mathbf{T}^T = \mathbf{I} - \Omega_f. \quad (\text{V.4})$$

It is worth noticing that equations V.3 and V.4 provide only two particular projection matrices. A general formulation that expresses general projections consistent with the given contact is discussed in [33, 8].

Control Architecture

According to the classical formulation of hybrid motion/force control, the framework inputs are defined by the desired twist $\mathbf{t}_{ref} = \begin{bmatrix} \mathbf{v}_{ref}^T & \boldsymbol{\omega}_{ref}^T \end{bmatrix}^T$ and the desired interaction wrench at the operational point $\mathbf{w}_{ref} = \begin{bmatrix} \mathbf{f}_{ref}^T & \mathbf{m}_{ref}^T \end{bmatrix}^T$.

At any given time, the pose error is obtained using the strategy presented in Chapter III while the wrench error is given by:

$$\mathbf{w}_e = \mathbf{w}_{ref} - \mathbf{w}_{curr} \quad (\text{V.5})$$

where \mathbf{w}_{curr} is the sensed wrench.

The output of the motion controller, \mathbf{t}_{des} , that can be obtained as in III.18, is

first projected onto the allowed motion space M^6 via projection matrix Ω_m as defined in V.4 and then onto the configuration space velocity of the manipulator via the pseudo-inverse of the *Jacobian* matrix $\mathbf{J}_{t\psi}^\dagger$ as defined in III.24:

$$\dot{\Psi}_m = \mathbf{J}_{t\psi}^\dagger \Omega_m \mathbf{t}_{des}. \quad (\text{V.6})$$

One the other hand, the output of the motion controller \mathbf{w}_{des} can be obtained with a conventional PI control schemes:

$$\mathbf{w}_{des} = \mathbf{K}_{f,p} \mathbf{w}_e + \mathbf{K}_{f,i} \int \mathbf{w}_e. \quad (\text{V.7})$$

Similarly to the motion controller, the desired wrench \mathbf{w}_{des} is first projected into the allowed wrench space F^6 via projection matrix Ω_f as defined in V.3, then into the generalized force space via the transpose of the *Jacobian* matrix $\mathbf{J}_{t\psi}$. The generalized force is the projection of the task-space wrench acting at the end effector into the configuration space of the manipulator. The relationship between task and configuration spaces is formulated using virtual work arguments as originally presented in [95] and summarized in Chapter II. Finally into the configuration velocity space of the continuum manipulator via the configuration space compliance matrix \mathbf{K}_Ψ^{-1} :

$$\dot{\Psi}_f = \mathbf{K}_\Psi^{-1} \mathbf{J}_{t\psi}^T \Omega_f \mathbf{w}_{des}. \quad (\text{V.8})$$

Using equations V.6 and V.8 the motion and force control inputs are merged into a configuration space velocity vector $\dot{\Psi}$ that does not violate the contact constraint:

$$\dot{\Psi} = \dot{\Psi}_m + \dot{\Psi}_f. \quad (\text{V.9})$$

Once the desired configuration space velocity vector is obtained, a resolved motion

rate approach [110] is used to obtain the desired configuration and exploit the inverse pose solution:

$$\dot{\Psi} = \Psi_{t-1} + \Delta t \dot{\Psi} \quad (\text{V.10})$$

Equation V.10 provides the desired configuration of the continuum manipulator that accomplishes both the desired motion and force tasks without violating the contact constraint. The next step in the control architecture is to generate joint-level commands to accomplish the desired tasks. Because of the flexibility of the arm, actuation compensation is required for both achieving the desired pose and applying the desired wrench at the end-effector. Using the statics model proposed in V.30, the desired actuation forces τ_{des} are obtained as follows:

$$\tau_{des} = (\mathbf{J}_{q\psi}^T)^{\dagger} (\nabla \mathbf{U} - \mathbf{J}_{t\psi}^T \boldsymbol{\Omega}_f \mathbf{w}_{ref}) \quad (\text{V.11})$$

According to the model-based actuation compensation scheme proposed in [114] and summarized in Chapter II, the desired joint-space compensation is given by:

$$\epsilon = \mathbf{K}_a^{-1} \tau_{des} \quad (\text{V.12})$$

where \mathbf{K}_a^{-1} designates the compliance matrix of the actuation lines.

By combining equations II.4, V.10, and V.12, the desired joint-space control input is obtained as follows:

$$\mathbf{q}_{des} = \hat{\mathbf{q}}_{des}(\Psi) + \epsilon \quad (\text{V.13})$$

where $\hat{\mathbf{q}}_{des}(\Psi)$ is the joint's positions associated with configuration (Ψ) according to the theoretical inverse position analysis.

The hybrid motion/force control architecture for continuum robots with intrinsic

force sensing is summarized in Figure V.2. According to the classical hybrid motion/force control scheme [78, 56, 59], two independent controllers provide high-level control commands for both motion and force regulation. These commands are projected into adequate force-vectors and velocity-vectors that do not violate the contact constraint and then they are projected into the configuration space of the continuum manipulator. The motion commands are projected using the inverse of the Jacobian matrix $\mathbf{J}_{t\psi}$, while the force commands are projected using first the transpose of the Jacobian matrix $\mathbf{J}_{t\psi}$ and then the configuration space compliance matrix \mathbf{K}_ψ^{-1} . The configuration space stiffness matrix describes how a change in the external wrench direction and magnitude is related to a change in the configuration of the continuum manipulator. Once the desired configuration space vector is obtained, a model-based actuation compensation scheme is used to produce the required joint-space displacements for both configuration compensation and the acting wrench. Note that, equation V.11 includes two terms: the first compensate for actuation line extension, friction, and model uncertainties, while the second term is a feedforward term that produces the desired wrench at the end-effector by actuation the manipulator in joint-space. Finally, The control input \mathbf{q}_{des} is fed into the low-level PID controller. In the case of continuum robots with intrinsic wrench estimation, there are two additional components: the friction compensation/estimation block, and the wrench estimator. These components are described in the next section.

Compensation of Uncertainties

During control of the real continuum robot there will be a deviation $\boldsymbol{\lambda}$ between the desired actuation force vector $\boldsymbol{\tau}_{des}$ and the sensed actuation force vector $\boldsymbol{\tau}_{curr}$. This deviation is due to friction and extension in the actuation lines, perturbation of the bending shape from the ideal circular configuration, and geometric and static

parameters. Thus, the sensed actuation force vectors is as follows:

$$\boldsymbol{\tau}_{curr} = \boldsymbol{\tau}_{des} + \boldsymbol{\lambda}. \quad (\text{V.14})$$

In [4], the authors showed that the force deviation $\boldsymbol{\lambda}$ is a function of the configurations Ψ of the manipulator and the joint-space velocities $\dot{\mathbf{q}}$. Several methods have been proposed in order to characterize friction and uncertainties. For example, in [65], the authors proposed a discrete Dahl model for friction compensation in a master console. In [73], the authors included a Dahl friction model into the control architecture of steerable catheters. In [60], the authors proposed a method for friction estimation and compensation in concentric tube robots. In [36], the authors used a non-linear regression via Support Vector regressors to compensate for lumped uncertainties in multi-backbone multi-segment continuum robots.

In this work, without loss of generality, we experimentally evaluate uncertainties vector $\boldsymbol{\lambda}$ across the robot's workspace and populate a lookup table for real-time control.²

Wrench Estimation

Continuum robots with actuation force sensing allow to estimate external wrenches acting at the tip. Xu and Simaan investigated this capabilities in [115] where the authors presented a minimization algorithm for estimating forces with a single segment and presented the full estimation in [117]. This section summarizes the results from [115, 117] while assuming point contact at the tip of the robot. Using the statics model in V.30, the external wrench acting at the tip of the continuum robot is given

²Ideally, two look-up tables are required in order to characterize friction uncertainties due to direction of motion, i.e. one for $\dot{q} > 0$ and one for $\dot{q} < 0$.

by:

$$\mathbf{w}_{curr} = (\mathbf{J}_{t\psi}^T)^\dagger (\nabla \mathbf{U} - \mathbf{J}_{q\psi}^T (\boldsymbol{\tau}_{curr} - \boldsymbol{\lambda})) + (\mathbf{I} - (\mathbf{J}_{t\psi}^T)^\dagger \mathbf{J}_{t\psi}^T) \eta \quad (\text{V.15})$$

where

$$\eta = \mathbf{D}^\dagger \mathbf{F}^T \mathbf{S}_e \left(\mathbf{w}_{se} - (\mathbf{J}_{t\psi}^T)^\dagger (\nabla \mathbf{U} - \mathbf{J}_{q\psi}^T (\boldsymbol{\tau}_{curr} - \boldsymbol{\lambda})) \right) \quad (\text{V.16})$$

$$\mathbf{D} = \left(\mathbf{I} - (\mathbf{J}_{t\psi}^T)^\dagger \mathbf{J}_{t\psi}^T \right)^T \mathbf{S}_e \left(\mathbf{I} - (\mathbf{J}_{t\psi}^T)^\dagger \mathbf{J}_{t\psi}^T \right) \quad (\text{V.17})$$

$$\mathbf{F} = \left(\mathbf{I} - (\mathbf{J}_{t\psi}^T)^\dagger \mathbf{J}_{t\psi}^T \right) \quad (\text{V.18})$$

$$\mathbf{S}_e = \begin{bmatrix} (\hat{\mathbf{n}}_t \times \hat{\mathbf{n}}_n) (\hat{\mathbf{n}}_t \times \hat{\mathbf{n}}_n)^T & \mathbf{0}_{3 \times 3} \\ \mathbf{0}_{3 \times 3} & \mathbf{I}_{3 \times 3} \end{bmatrix} \quad (\text{V.19})$$

$$\mathbf{W}_{se} = \begin{bmatrix} c_t \hat{\mathbf{n}}_t + n_t \hat{\mathbf{n}}_n \\ \mathbf{0}_{3 \times 1} \end{bmatrix}. \quad (\text{V.20})$$

\mathbf{S}_e and \mathbf{W}_{se} contains *a priori* knowledge of the contact constraint and guide the estimation algorithm. The *a priori* knowledge is defined by contact normal vector $\hat{\mathbf{n}}_n$ and contact tangential vector $\hat{\mathbf{n}}_t$. These two vectors define the plane in which the sensable component of the external wrench lies.

Experimental Results

In order to validate the proposed framework, the control algorithms were implemented on the one-segment multi-backbone continuum robot of Figure V.4. The continuum segment is able to translate along the $\hat{\mathbf{z}}_0$ axis providing the end-effector with a total of 3 DoFs: q_{ins} and angles θ and δ . The continuum segment is equipped with three load cells that monitor the forces acting on the three secondary backbones. According to the algorithm proposed in [115], estimation of the \hat{x} and \hat{y} component of a force acting at the tip of the manipulator is possible. In the remainder of this

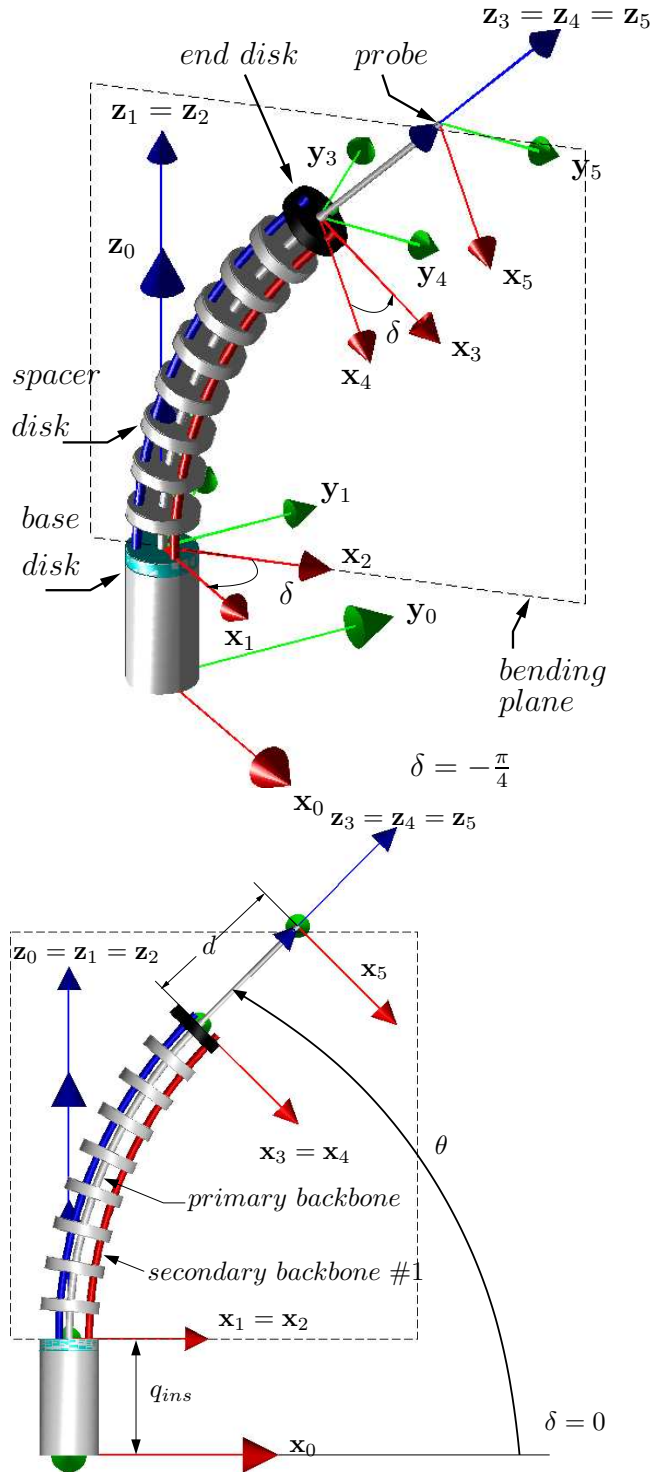


Figure V.4: Kinematics nomenclature used in this paper.

section, multiple experiments are presented to validate the efficacy and usefulness of the proposed framework. While the motion controller always controls motion in z direction (the estimation algorithm is not able to sense forces in the \hat{z} direction [115]), the force controller switches between regulating a force in the \hat{x} or \hat{y} directions depending on the task.

The remainder of this section is organized as follows. First, the experimental setup is presented. The continuum robot manipulator and required equipment are described. Second, the estimation of uncertainties such as friction and un-modeled actuation forces are presented. Finally, three experiments are presented: force regulation in the \hat{x} and \hat{y} direction, shape estimation, and stiffness characterization.

The Continuum Manipulator

Direct Kinematics The surgical slave of Fig. V.4 is the composition of a linear stage and a two Degree of Freedom (DoF) continuum manipulator. The continuum segment has three *push-pull* backbones that allows for bending its end disk in space. A complete derivation of the direct and differential kinematics of these continuum structures are given in [97]. For the ease of presentation, in the remainder of this section, the kinematics and statics of the manipulator is summarized. Six coordinate systems are defined (Figure V.4): 1) world frame $\{\hat{\mathbf{x}}_0, \hat{\mathbf{y}}_0, \hat{\mathbf{z}}_0\}$, 2) segment's base disk frame $\{\hat{\mathbf{x}}_1, \hat{\mathbf{y}}_1, \hat{\mathbf{z}}_1\}$, 3) segment's bending plane frame $\{\hat{\mathbf{x}}_2, \hat{\mathbf{y}}_2, \hat{\mathbf{z}}_2\}$, 4) segment's end-disk frame $\{\hat{\mathbf{x}}_3, \hat{\mathbf{y}}_3, \hat{\mathbf{z}}_3\}$, 5) segment's gripper frame $\{\hat{\mathbf{x}}_4, \hat{\mathbf{y}}_4, \hat{\mathbf{z}}_4\}$, and 6) segment's tool frame $\{\hat{\mathbf{x}}_5, \hat{\mathbf{y}}_5, \hat{\mathbf{z}}_5\}$. The position, \mathbf{p}_3^0 , and the orientation, \mathbf{R}_3^0 , of the tool in reference frame is given by:

$$\mathbf{p}_5^0 = \mathbf{p}_1^0 + \mathbf{R}_1^0 \mathbf{p}_3^1 + \mathbf{R}_4^0 \mathbf{p}_5^4 \quad (\text{V.21})$$

$$\mathbf{R}_5^0 = \mathbf{R}_4^0 = \text{Rot}(-\delta, \hat{\mathbf{z}}) \text{Rot}(\Theta, \hat{\mathbf{y}}) \text{Rot}(\delta, \hat{\mathbf{z}}) \quad (\text{V.22})$$

where $\mathbf{R}_1^0 = \mathbf{I}$, $\mathbf{p}_1^0 = \begin{bmatrix} 0 & 0 & q_{ins} \end{bmatrix}^T$, $\mathbf{p}_3^2 = \begin{bmatrix} 0 & 0 & d \end{bmatrix}^T$, d is the distance between frames $\{4\}$ and $\{5\}$ (see Figure V.4), \mathbf{p}_3^1 is the position of the end disk of the continuum segment as in II.2, $\Theta = \theta - \theta_0$, L is the nominal length of the continuum segment, $\theta_0 = \pi/2$, and operator $Rot(\phi, \hat{\mathbf{w}})$ returns a rotation of angle ϕ about axis $\hat{\mathbf{w}}$. As shown in Chapter II, the pose of the tool is uniquely defined by configuration variables θ , δ , and q_{ins} . We, therefore, define the configuration space vector $\Psi \in \mathbb{R}^3$ as:

$$\Psi = \begin{bmatrix} \theta & \delta & q_{ins} \end{bmatrix}^T. \quad (\text{V.23})$$

In order to achieve configuration Ψ , the secondary backbones of the continuum robot ($i = 1, 2, 3$) are shortened or lengthened as follows:

$$q_i = r \cos(\delta_i)(\theta - \theta_0). \quad (\text{V.24})$$

where $\delta_i = \delta + (i-1)\beta$, $\beta = 2/3\pi$, and r is the radial distance of each secondary backbone from the centrally-located backbone (Figure II.1). Similarly to the configuration space, we define the augmented joint-space vector $\mathbf{q} \in \mathbb{R}^4$ as:

$$\mathbf{q} = \begin{bmatrix} q_1 & q_2 & q_3 & q_{ins} \end{bmatrix}^T. \quad (\text{V.25})$$

Differential Kinematics The tool twist $\mathbf{t}^T = \begin{bmatrix} \mathbf{v}^T & \boldsymbol{\omega}^T \end{bmatrix}$ is given by:

$$\mathbf{t} = \mathbf{J}_{t\psi} \dot{\Psi} \quad (\text{V.26})$$

where $\dot{\Psi}$ is the rate of change of the configuration space vector Ψ and

$$\mathbf{J}_{t\Psi} = \begin{bmatrix} -dc_\Theta c_\delta - \frac{Lc_\delta c_\theta}{\Theta} - \frac{A_2}{\Theta^2} & -ds_\Theta s_\delta + \frac{A_1}{\Theta} & 0 \\ dc_\Theta s_\delta + \frac{Ls_\delta c_\theta}{\Theta} + \frac{A_1}{\Theta^2} & -ds_\Theta c_\delta + \frac{A_2}{\Theta} & 0 \\ ds_\Theta + \frac{Lc_\theta}{\Theta^2} - \frac{Ls_\theta}{\Theta} & 0 & 1 \\ -s_\delta & c_\delta c_\theta & 0 \\ -c_\delta & -s_\delta c_\theta & 0 \\ 0 & -1 + s_\theta & 0 \end{bmatrix}, \quad (\text{V.27})$$

where $c_y = \cos(y)$, $s_y = \sin(y)$, $A_1 = L \sin(\delta)(\sin(\theta) - 1)$, and $A_2 = L \cos(\delta)(\sin(\theta) - 1)$. Similarly, the configuration space velocities are related to the configuration space velocities as:

$$\dot{\mathbf{q}} = \mathbf{J}_{q\Psi} \dot{\Psi} \quad (\text{V.28})$$

where

$$\mathbf{J}_{q\Psi} = \begin{bmatrix} r \cos(\delta_1) & -r\Theta \sin(\delta_1) & 0 \\ r \cos(\delta_2) & -r\Theta \sin(\delta_2) & 0 \\ r \cos(\delta_3) & -r\Theta \sin(\delta_3) & 0 \\ 0 & 0 & 1 \end{bmatrix}. \quad (\text{V.29})$$

Statics Using virtual work arguments presented in Chapter II we can derived the following first order linear relationship:

$$\tilde{\mathbf{J}}_{t\Psi}^T \mathbf{w}_e + \tilde{\mathbf{J}}_{q\Psi}^T \boldsymbol{\tau} = \nabla \mathbf{U} \quad (\text{V.30})$$

where

$$\tilde{\mathbf{J}}_{t\Psi} = \mathbf{J}_{t\Psi} \begin{bmatrix} 1 & 0 \\ 0 & 1 \\ 0 & 0 \end{bmatrix}, \quad (\text{V.31})$$

$$\tilde{\mathbf{J}}_{q\Psi} = \mathbf{J}_{q\Psi} \begin{bmatrix} 1 & 0 \\ 0 & 1 \\ 0 & 0 \end{bmatrix}, \quad (\text{V.32})$$

and

$$\nabla U = E_Y I \begin{bmatrix} \frac{\Theta}{L} + \sum_{i=1}^3 \frac{\Theta}{L+q_i} - \frac{\Theta^2}{2} r \sum_{i=1}^3 \frac{\cos(\delta_i)}{(L+q_i)^2} \\ \frac{\Theta^3}{2} r \sum_{i=1}^3 \frac{\sin(\delta_i)}{(L+q_i)^2} \end{bmatrix}. \quad (\text{V.33})$$

Configuration Space Stiffness The configuration space stiffness was presented in [4] and used for compliant motion control. In the remainder of this paragraph, results from [4] are summarized. Let the wrench acting on the end disk that is projected into the configuration space of the k^{th} segment be given as the generalized force vector

$$\mathbf{f}_{(k)} = \mathbf{J}_{\mathbf{t}\psi_{(k)}}^T \mathbf{w}_{e,(k)}. \quad (\text{V.34})$$

Applying (V.30) to the generalized force expression, the i^{th} row of the generalized force $\mathbf{f}_{(k)}$ can be written as³

$$\mathbf{f}_i = \nabla U_i - [\mathbf{J}_{\mathbf{q}\psi}^T]_i \boldsymbol{\tau} = \nabla U_i - [\mathbf{J}_{\mathbf{q}\psi}^{[i]}]^T \boldsymbol{\tau}. \quad (\text{V.35})$$

where $\mathbf{J}_{\mathbf{q}\psi}^{[i]}$ denotes the i^{th} column of $\mathbf{J}_{\mathbf{q}\psi}$.

For small perturbations from an equilibrium configuration, the stiffness of the individual continuum segment can be posed in the configuration space as

$$\delta \mathbf{f} = \mathbf{K}_\psi \delta \boldsymbol{\psi} \quad (\text{V.36})$$

where the stiffness is given by the Jacobian of the generalized force with respect to

³The subscripted (k) denoting the k^{th} segment will be dropped for (V.35) through (V.44) for ease of notation although it is understood that these equations are defined for the individual segment.

configuration space perturbation. Thus, the elements of \mathbf{K}_ψ are given by:

$$\frac{\partial \mathbf{f}_i}{\partial \boldsymbol{\psi}_j} = [\mathbf{K}_\psi]_{ij} = \frac{\partial}{\partial \boldsymbol{\psi}_j} \left[\nabla U_i - \left[\mathbf{J}_{\mathbf{q}\psi}^{[i]} \right]^T \boldsymbol{\tau} \right]. \quad (\text{V.37})$$

The elements of the stiffness matrix (V.37) can be expanded as

$$[\mathbf{K}_\psi]_{ij} = [\mathbf{H}_\psi]_{ij} - \left[\frac{\partial}{\partial \boldsymbol{\psi}_j} \left(\mathbf{J}_{\mathbf{q}\psi}^{[i]} \right) \right]^T \boldsymbol{\tau} - \left[\mathbf{J}_{\mathbf{q}\psi}^{[i]} \right]^T \frac{\partial \boldsymbol{\tau}}{\partial \boldsymbol{\psi}_j}. \quad (\text{V.38})$$

The first term of the configuration space stiffness, \mathbf{H}_ψ , is the Hessian of the elastic energy of the segment given by

$$\mathbf{H}_\psi = \begin{bmatrix} \frac{\partial^2 U}{\partial \theta^2} & \frac{\partial^2 U}{\partial \theta \partial \delta} \\ \frac{\partial^2 U}{\partial \delta \partial \theta} & \frac{\partial^2 U}{\partial \delta^2} \end{bmatrix}. \quad (\text{V.39})$$

The axial stiffness along the length of a given actuation line can then be expressed as

$$\frac{1}{k} = \frac{1}{k_c} + \frac{1}{k_b} \quad (\text{V.40})$$

where $k_c = \frac{E_Y A}{L_c}$ and $k_b = \frac{E_Y A}{L_b}$, and A denotes the cross-sectional area of the backbone.

For continuum robotic systems with remote actuation designed to access deep confined spaces, e.g. [114] and [97], the lengths of the non-bending regions of the actuation lines far exceed that of the bending regions, $L_c \gg L_b$. The stiffness will therefore be dominated by the non-bending regions of the actuation lines. Local perturbations of the backbones at the actuation unit can be expressed as

$$\frac{\partial \boldsymbol{\tau}}{\partial \mathbf{q}} = \mathbf{K}_a \quad (\text{V.41})$$

r [mm]	L [mm]	β [$^\circ$]	d [mm]	E_Y [N/mm^2]	o_d [mm]	I [mm^4]
1.8	17.5	120	13.5	$6.5 \cdot 10^4$	0.3	$3.9761 \cdot 10^{-04}$

Table V.1: Kinematic and static parameters of the continuum robot used for the experiments

where

$$\mathbf{K}_q \cong \begin{bmatrix} \frac{E_Y A}{L_c} & 0 & 0 \\ 0 & \ddots & 0 \\ 0 & 0 & \frac{E_Y A}{L_c} \end{bmatrix} \in \mathbb{R}^{m \times m} \quad (\text{V.42})$$

Expanding terms by applying the chain rule and using the instantaneous inverse kinematics, $\frac{\partial \boldsymbol{\tau}}{\partial \boldsymbol{\psi}}$ is given by

$$\frac{\partial \boldsymbol{\tau}}{\partial \boldsymbol{\psi}} = \frac{\partial \boldsymbol{\tau}}{\partial \mathbf{q}} \frac{\partial \mathbf{q}}{\partial \boldsymbol{\psi}} \cong \mathbf{K}_a \mathbf{J}_{\mathbf{q}\boldsymbol{\psi}} \quad (\text{V.43})$$

The configuration space stiffness therefore reduces to

$$[\mathbf{K}_\boldsymbol{\psi}]_{ij} = [\mathbf{H}_\boldsymbol{\psi}]_{ij} - \left[\frac{\partial}{\partial \boldsymbol{\psi}_j} \left(\mathbf{J}_{\mathbf{q}\boldsymbol{\psi}}^{[i]} \right) \right]^T \boldsymbol{\tau} - \left[\mathbf{J}_{\mathbf{q}\boldsymbol{\psi}}^{[i]} \right]^T \mathbf{K}_a \mathbf{J}_{\mathbf{q}\boldsymbol{\psi}}^{[j]} \quad (\text{V.44})$$

Kinematic and Static Parameters The numerical value of the kinematic and static parameters defined in the previous sections are reported in Table V.1. r is the radial distance from the secondary backbone to the central backbone, L is the nominal length of the continuum segment, β is the division angle between secondary backbones, E_Y is the Young's modulus of the NiTi backbones, o_d is the outer diameter of the backbones, and

$$I = \frac{\pi}{64} o_d^4 \quad (\text{V.45})$$

is the second area moment of each backbone.

Estimation of Uncertainties

Uncertainties are due to: 1) deviation of the kinematic and static parameters from the nominal ones reported in Table V.1, 2) unmodeled friction along the actuation lines, 3) statics and kinematics modeling assumptions, and 4) actuation unit assembly. The algorithm presented in [115] was evaluated on a much bigger continuum robot (\varnothing 9mm) with very short actuation lines in order to minimize modeling and setup uncertainties. The robot used in this work is a \varnothing 5mm continuum robot with a cone that re-route the actuation lines and an actuation line length of more than 300 mm. In this work, we calibrate actuation uncertainties by populating a look-up table that depends on the configuration of the continuum manipulator.

Methods

The continuum manipulator of Figure V.4 is commanded to scan its workspace between $\delta = \pi/2$ and $\delta = -\pi/2$ with intervals of $5^\circ \simeq 0.098rad$. At each δ configuration the manipulator is bent from $\theta = \pi/2$ to $\theta = 0$ with constant velocity and accomplishment time of 10s. The discrepancy between the expected actuation forces and the sensed actuation forces was recorded.

Results

Figures V.5, V.6, and V.7 show the actuation force errors on backbone one, two, and three respectively. The graphs show a plot of the actuation force error versus the bending angle θ for different values of δ .

Figure V.5 shows the actuation force error, τ_{e_1} , associated with the first backbone. The graphs shows how the actuation force error depends on both θ and δ and, therefore, on the configuration of the manipulator. The error on backbone one reaches its minimum at $\delta = \pi/2$ and $\delta = -\pi/2$. In these two configurations backbone one

is neither extended nor shortened and the load on it is, therefore, zero. In all other configurations, the error mainly increases as a function of θ but also as a function of δ .

Figure V.6 shows the actuation force error, τ_{e_2} , associated with the second backbone. In this case, the minimum is reached for $\delta = -\pi/6$. In this configuration the second backbone is neither extended nor shortened and, therefore, the resultant load is zero. In all other configurations, τ_{e_2} is non-zero and mainly depends on the bending angle θ . In this case, it is possible to see the effect of friction along the line. For configurations with a negative δ , backbone two is extended while for configurations with positive δ , backbone two is shortened. This phenomenon is not seen in backbone one because between $\delta \in [-\pi/2, \pi/2]$ the backbone is only shortened.

Figure V.7 shows the actuation force error, τ_{e_3} , associated with the third backbone. Similarly to backbone $n^{\circ}2$, because of symmetry, the actuation force error τ_{e_3} is zero at $\delta = \pi/6$, negative for $\delta \in (\pi/6, \pi/2]$, and positive for $\delta \in [-\pi/2, \pi/6)$.

Several methods can be used to characterize friction and uncertainties as in [65, 53, 4]. In this work, we populated a lookup table using the data shown in Figures V.5, V.6, and V.7. The table has a size of 36×18 and linearly interpolates over δ and θ with increments of 5° . In the current implementation, the table is only populated with data associated with negative $\dot{\theta}$, i.e. the continuum segment bends from $\theta = \pi/2$ (straight configuration) to $\theta = 0$. For this reason, the compensation is not effective when the motion is reversed; thus affecting the force estimation. Although it is possible to produce velocity-dependent lookup tables, this is excluded from the scope of this work.

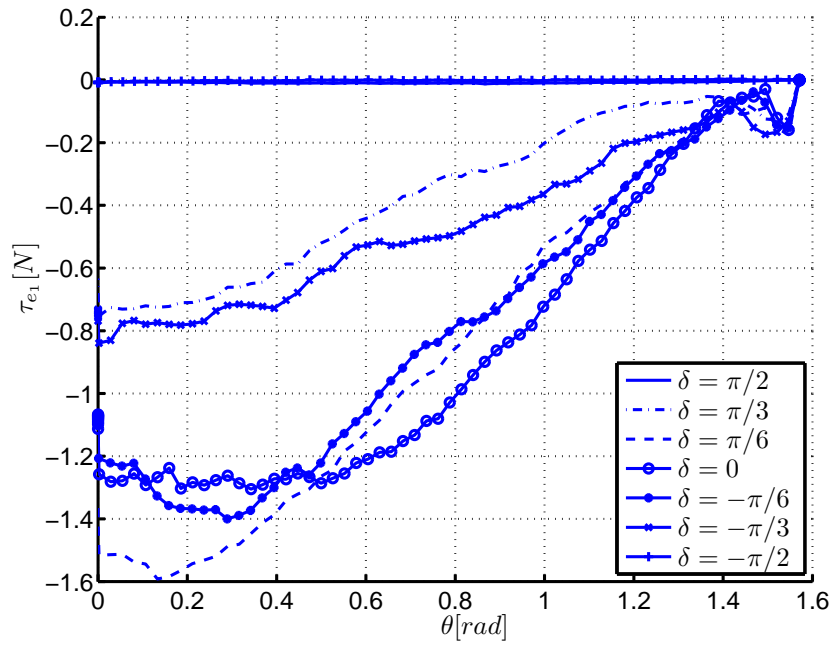


Figure V.5: Error between the expected and actual actuation force on backbone 1 versus bending angle θ for different values of δ .

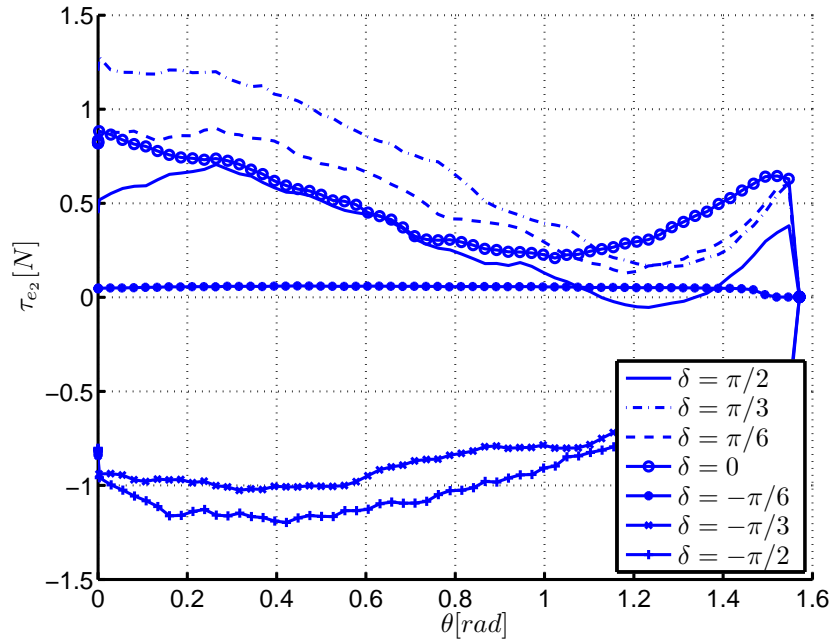


Figure V.6: Error between the expected and actual actuation force on backbone 2 versus bending angle θ for different values of δ .

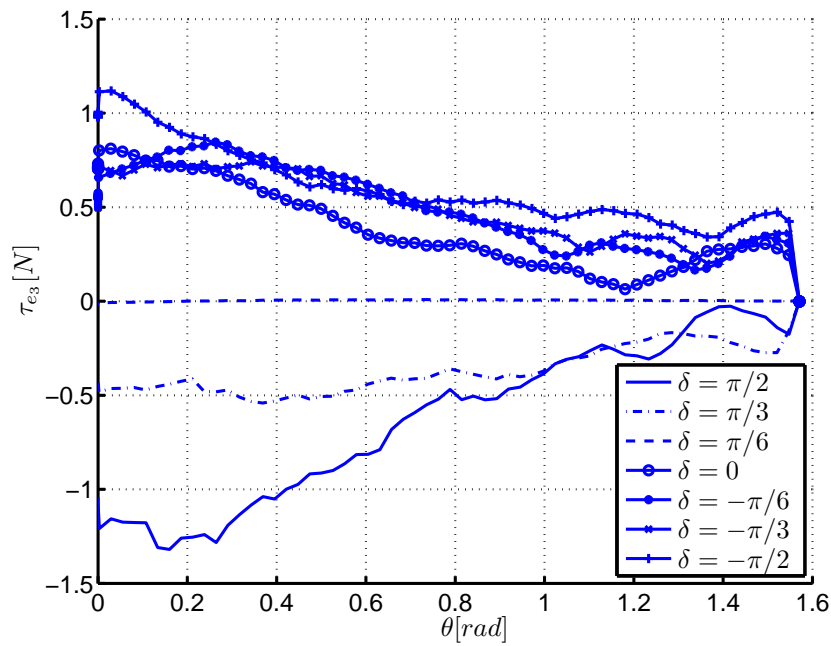


Figure V.7: Error between the expected and actual actuation force on backbone 3 versus bending angle θ for different values of δ .

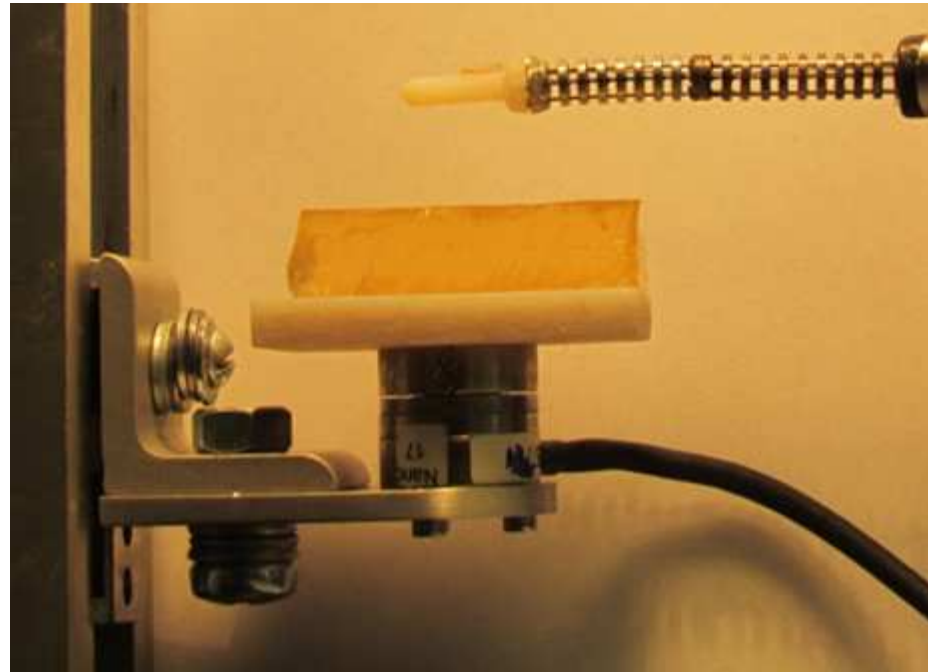


Figure V.8: Experimental setup for force regulation experiments. The setup consist of the continuum manipulator, the ATI Nano 17 force/torque sensor, and a hand-controlled linear actuator for the placement of the sensor at different heights.

Force regulation

This section presents force regulation experimental results. The goal of these experiments is to demonstrate the ability of the controller to regulate a predetermined force in both x and y directions at different configurations. The experimental setup (Figure V.8) consists of a \varnothing 5mm continuum robot, an interaction probe with a spherical tip of \varnothing 5mm radius, an aluminum block, and an ATI Nano 17 for ground truth.

Methods

In order to test the force estimation and force controller efficacy in the \hat{x} direction the continuum robot is bent to the following three configurations: 1) $\theta = 80^\circ$, $\delta = 0^\circ$, 2) $\theta = 60^\circ$, $\delta = 0^\circ$, and 3) $\theta = 40^\circ$, $\delta = 0^\circ$. At each configuration, a reference force magnitude of 5 gr, 10 gr, and 15 gr were commanded. Data from the force estimator and the ATI Nano 17 were compared and the rise time and steady state error computed.

In order to test the force estimation and force controller efficacy in the \hat{y} direction the continuum robot is bent to the following configurations: 1) $\theta = 80^\circ$, $\delta = 0^\circ$, 2) $\theta = 60^\circ$, $\delta = 0^\circ$, and 3) $\theta = 40^\circ$, $\delta = 0^\circ$. At each configuration, a reference force magnitude of 10 gr is tested. Data from the force estimator and the ATI Nano 17 are compared and the rise time and steady state error are computed.

Results

Figures V.9, V.10, and V.11 show the step response for force magnitudes 5 gr, 10 gr, and 15 gr in the \hat{x} direction at $\theta = 80^\circ$, $\theta = 60^\circ$, and $\theta = 40^\circ$ respectively. Each graph shows the time history of three quantities: desired force (black), sensed force

$\theta [^\circ]$	Force [gr]	Rise Time [s]	Steady State Error [gr]
80	5	1.11	-0.30
	10	1.09	0.60
	15	1.04	1.50
60	5	1.03	1.30
	10	0.77	3.00
	15	0.88	3.00
40	5	1.35	1.35
	10	1.03	4.30
	15	0.67	4.20

Table V.2: Experimental result of force regulation in the \hat{x} direction for three configurations $\theta = 80^\circ, 60^\circ, 40^\circ$, and three force magnitudes 5 gr, 10 gr, and 15 gr.

$\theta [^\circ]$	Force [gr]	Rise Time [s]	Steady State Error [gr]
80	10	0.75	1.90
60	10	2.72	4.10
40	10	1.63	8

Table V.3: Experimental result of force regulation in the \hat{y} direction for three configurations $\theta = 80^\circ, 60^\circ, 40^\circ$, and an applied force of 10 gr.

by the ATI Nano 17 (red), and sensed force by the intrinsic force estimator (blue).

These results are summarized in Table V.2.

Figure V.12 show the step response for a force magnitude of 10 Gr in \hat{y} direction at $\theta = 80^\circ, \theta = 60^\circ$, and $\theta = 40^\circ$. The results are summarized in Table V.3.

The experimental results demonstrate both that the hybrid motion/force control is able to regulate forces of different magnitudes in different directions and that the accuracy depends on the configuration of the manipulator. Steady state error in the x direction between the force sensed by the ATI Nano 17 and the intrinsic force estimator are mainly due to residual un-modeled uncertainties as the more energy is stored into the system ($\theta = \pi/2$ zero energy, $\theta = 0$ maximum energy). These uncertainties are static and dynamic friction, bending shape, and extension/contraction of the actuation lines. Steady state error in the y direction is due to uncompensated uncertainties for side motions $\dot{\delta} \neq 0$ and the much more compliance of the continuum

manipulator in the δ direction at this particular configuration. As shown in Figures V.5, V.6, and V.7, uncertainties are symmetric depending on the configuration of the backbones. The efficacy of the intrinsic force estimator and, therefore, the force controller is definitely weaker in the δ direction. However, depending on such configuration, the x and y directions are consecutively affected in different ways. It is worth noting that the experiments were conducted on a non-calibrated robot in which geometric parameters (nominal length, distance between backbones, bending shape) and static parameters (Young's modulus, actuation line stiffness, and second moment area of all backbones) were set to the nominal value. Furthermore, the intrinsic force estimator could also undergo proper calibration as in any force/torque sensor. However, this is beyond the scope of this work in which we aim to demonstrate force control schemes for continuum robots and their use in several scenarios.

Force Regulated Shape Estimation

This section presents environment's shape estimation experimental results. The goal of these experiments is to demonstrate simultaneous force and motion control. The hybrid motion/force controller was integrated into the telemanipulation architecture presented in Chapter VI. The user is able to control the end-effector while free of contact and engage the force control in pre-determined directions when in contact with the environment. The experimental setup (Figure V.13) consists of a $\varnothing 5$ mm continuum robot, a diamond-shape silicon phantom, an Ascension Technologies trakSTAR 2 with flat transmitter placed under the silicone phantom, and a Force Dimension Omega 7.

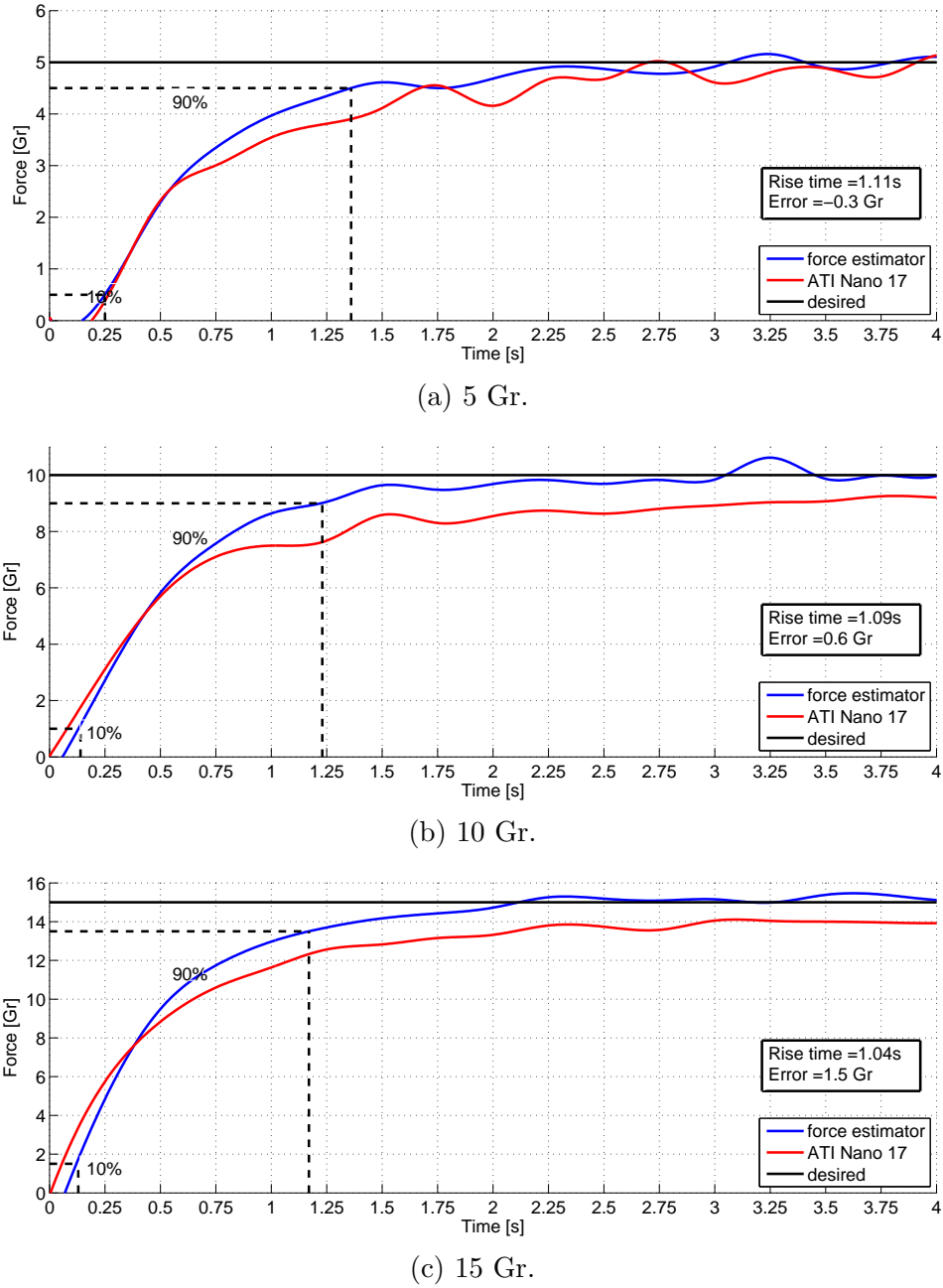


Figure V.9: Force step response on a silicone block in the \hat{x} direction from starting configuration $\theta = 80^\circ$, $\delta = 0^\circ$.

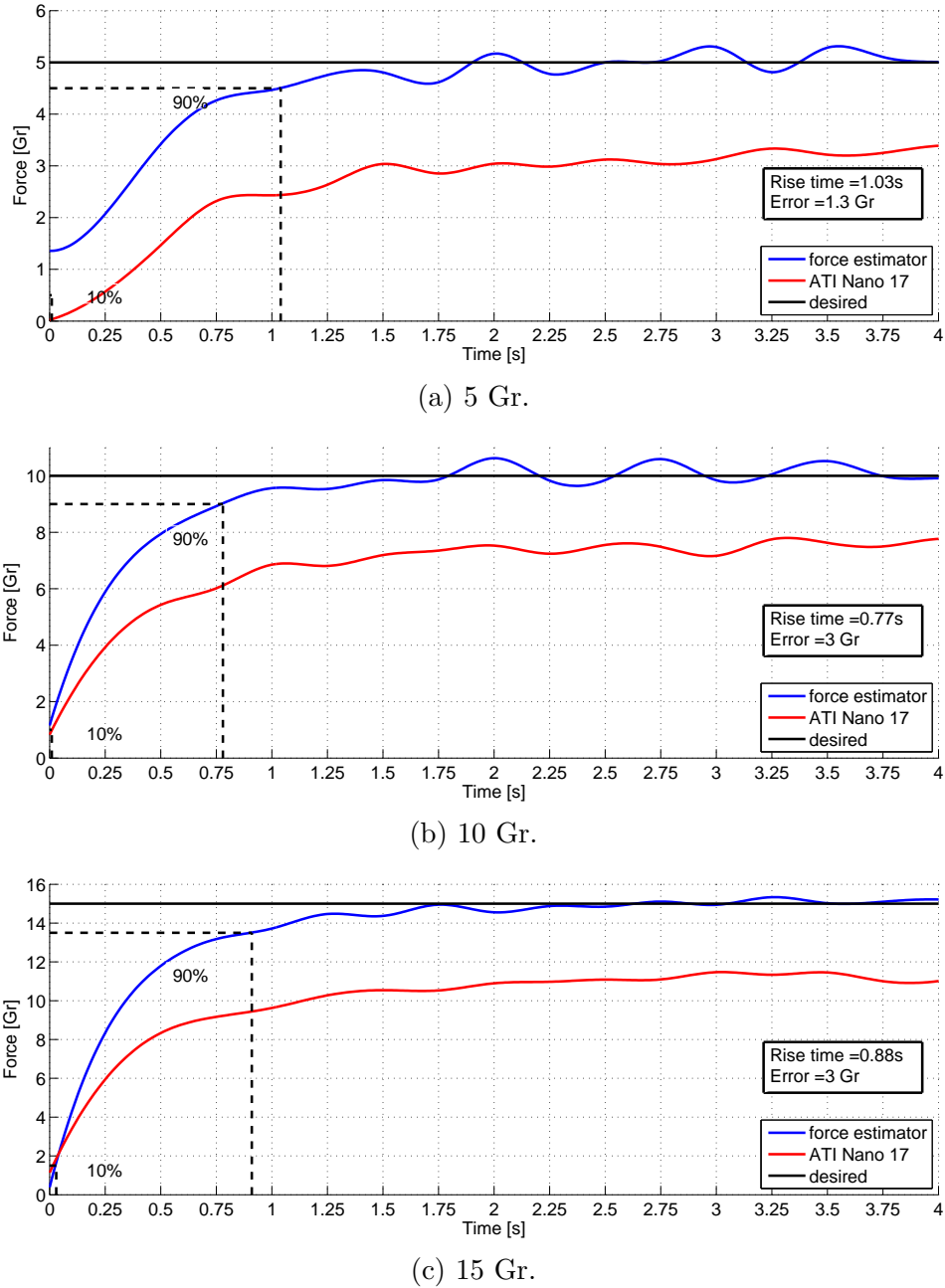


Figure V.10: Force step response on a silicone block in the \hat{x} direction from starting configuration $\theta = 60^\circ$, $\delta = 0^\circ$.

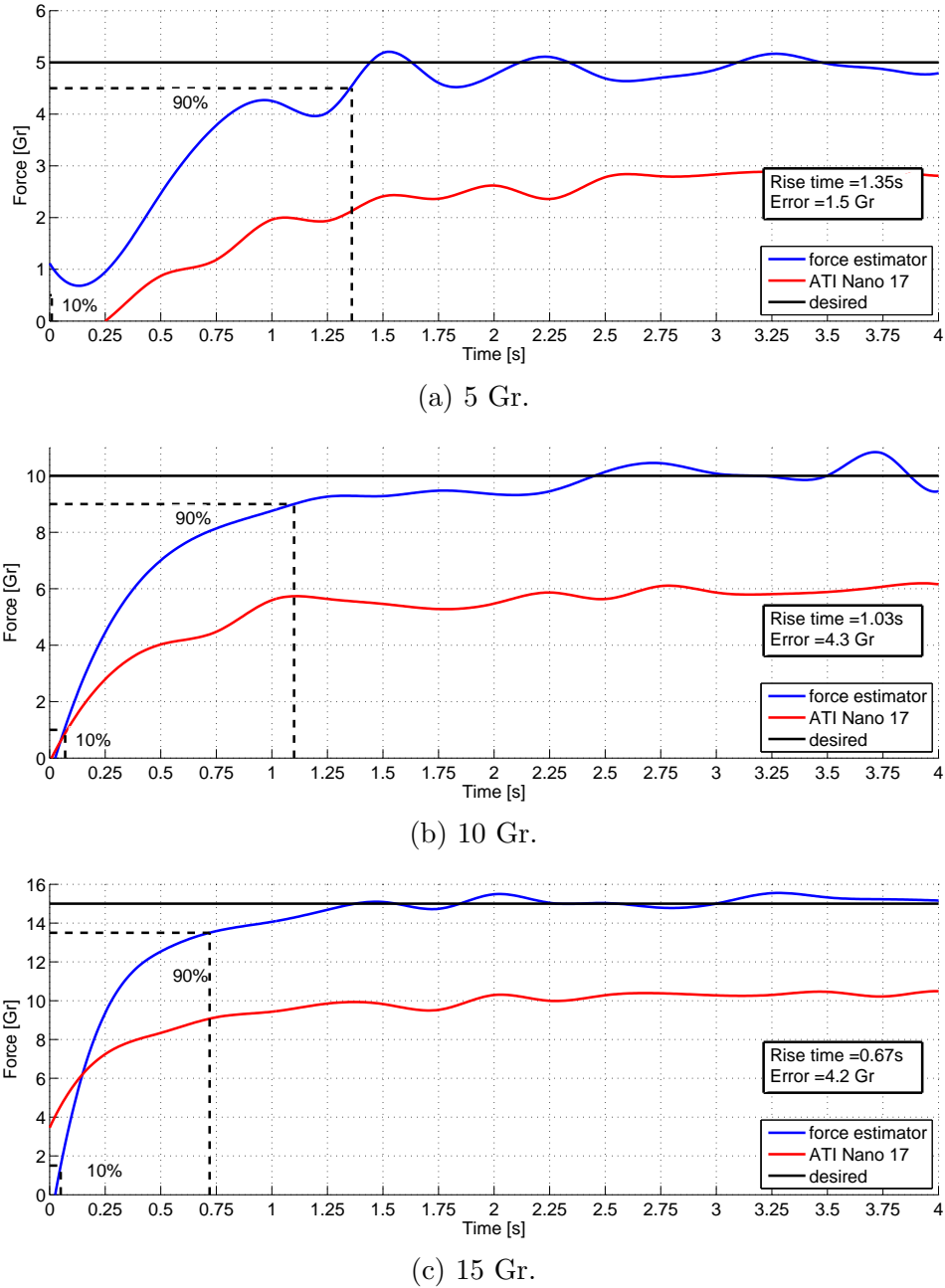


Figure V.11: Force step response on a silicone block in the \hat{x} direction from starting configuration $\theta = 40^\circ$, $\delta = 0^\circ$.

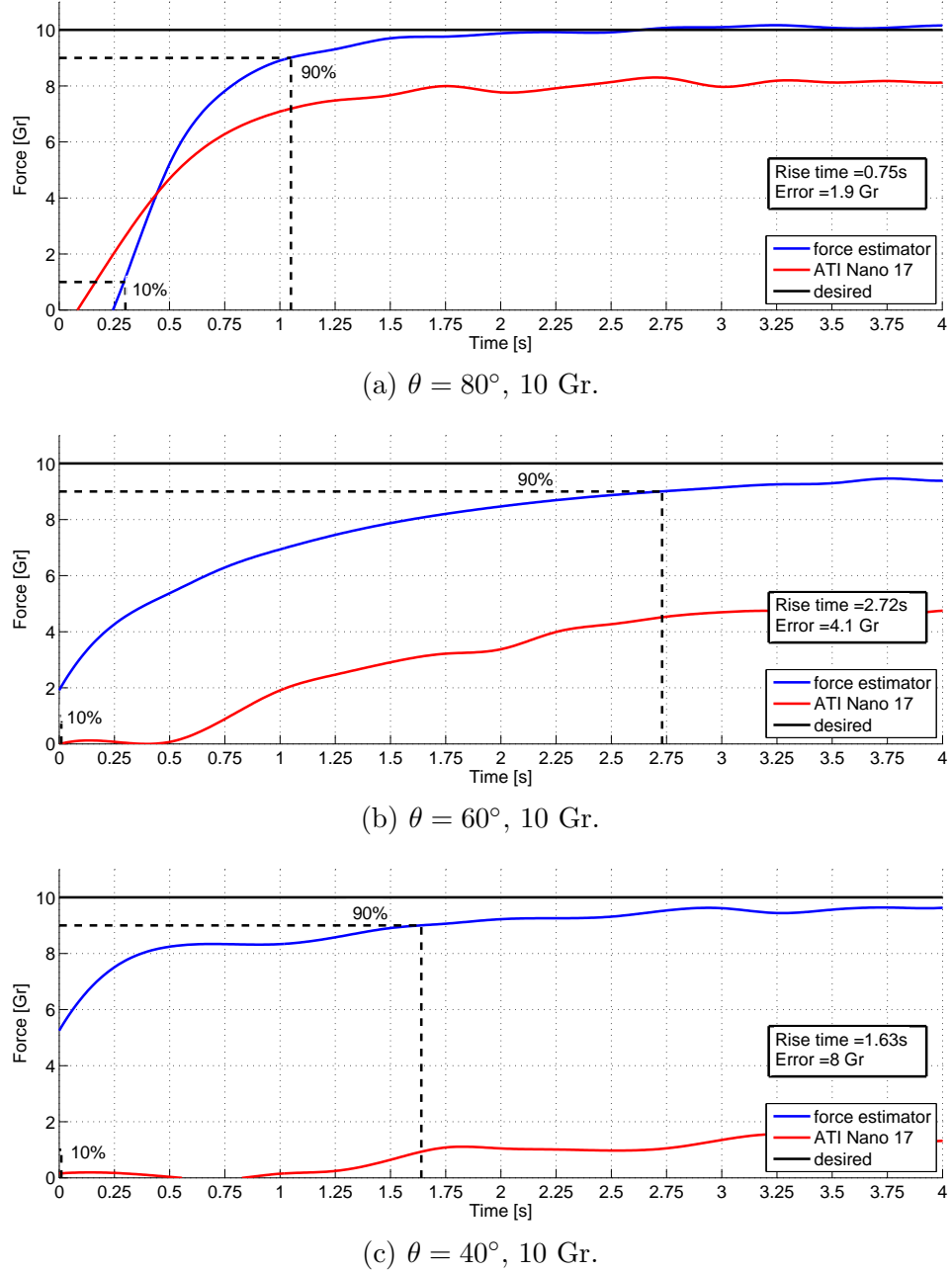
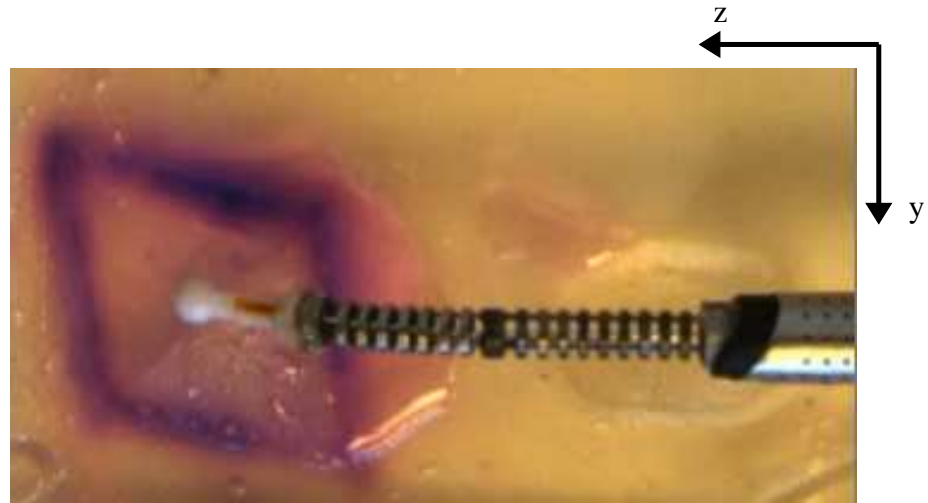
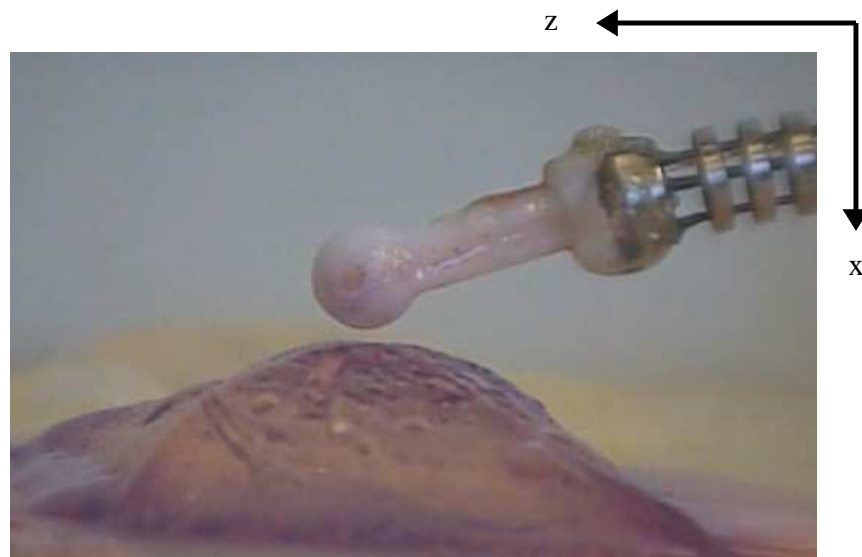


Figure V.12: Force step response on a silicone block in the \hat{y} direction from three starting configurations: 1) $\theta = 80^\circ$, $\delta = 0$, 2) $\theta = 60^\circ$, $\delta = 0$, and 3) 1) $\theta = 40^\circ$, $\delta = 0^\circ$.



(a) Top view (YZ plane).



(b) Side view (XZ plane)

Figure V.13: Experimental setup for shape estimation of a silicon diamond-shaped extrusion (a). The base plane of the extrusion is placed at approximately 18 mm from the origin along the x direction (b). The user actively controlled motion of the probe in the y and z directions. The force controller regulates a force with a magnitude of 0.1 N in the x direction.

Methods

The \varnothing 5 mm continuum robot is equipped with a plastic probe having a 5 mm radius sphere at the interaction point. The sphere reduces the impingement of the probe into the soft tissue. A \varnothing 0.9 mm magnetic coil is delivered through one of the robot's working channels and secured to the probe. A silicon diamond-shaped extrusion is placed in a YZ plane at a distance of approximately 18 mm from the robot's reference frame as shown in Figures V.13a (top view) and V.13b (side view).

End-effector's motions in the \hat{y} and \hat{z} directions were commanded via a Force Dimension Omega 7 with 3-axis force feedback. Position commands were sent over the Local Area Network (LAN) using User Datagram Protocol (UDP) at 100 Hz. The end-effector's position was acquired at 125 Hz using the Ascension Technology trakSTAR 2 and sent over the LAN using UDP at 100 Hz. The high-level motion and force controllers and the wrench estimator run at 200 Hz while the low-level joint controller run at 1 kHz. Switching between full motion control and hybrid motion/force control was enabled using the 7th axis of the Omega 7 (gripper).

The continuum robot, under full motion telemanipulation mode, is guided to reach a point on the silicon phantom. Once hybrid motion/force control is enabled, the continuum robot autonomously regulates a force of -0.1 N in the \hat{x} direction. Position data of the probe were only collected when the sensed force in the \hat{x} direction was smaller or equal to -0.05 N and the hybrid motion/force controller was engaged. These conditions ensured that each data point was actually on the surface of the silicon phantom. Switching between full motion/force control and hybrid motion/force control allowed to cover a workspace of 18 mm \times 30 mm \times 40 mm.

Ground truth shape data was obtained using a second probe equipped with another \varnothing 0.9 mm magnetic coil as shown in Figure V.14. The probe was manually swept over the silicon phantom and data collected. The use of an identical probe

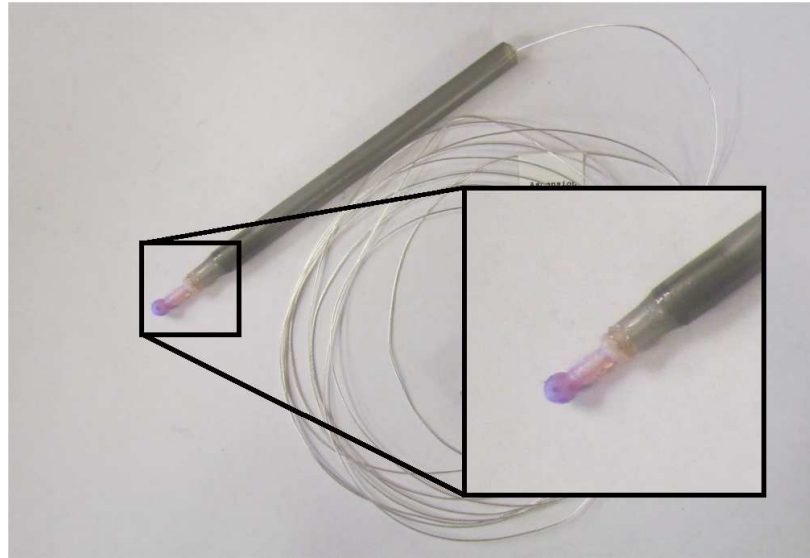


Figure V.14: Probe for the manual scan of the phantom tissue. A similar probe is attached to a non-magnetic rod. A $\varnothing 0.9$ mm is secured to the probe.

equipped with a similar sensor ensures comparison of data having the same accuracy, repeatability, noise, and uncertainties.

Position data from the electro-magnetic tracker were stored and linearly interpolated using Matlab function *griddata*. This function interpolates the surface at query points on the YZ plane and returns the interpolated value along the \hat{x} direction. Multiple data points are automatically averaged during the interpolation.

Results

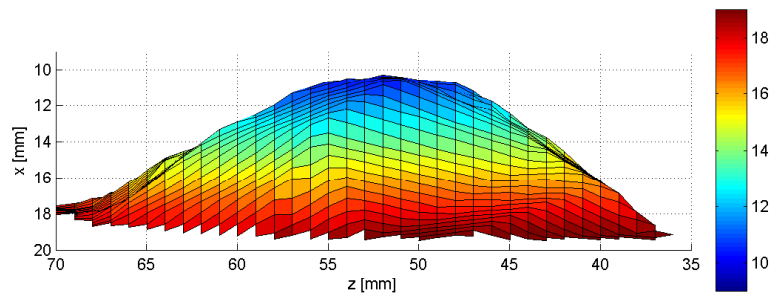
The estimated shape using the continuum robot is shown in Figures V.15a, V.15b, and V.15c while the ground truth data obtained with the manual scan is shown in Figures V.16a, V.16b, and V.16c. A color map (blue to red) identifies different surface heights. The error between the estimate shape and the ground truth shape is presented in Figure V.17. As expected, the maximum deviation is found at the boundaries of the robot's workspace along the \hat{y} axis. In fact, in order for the continuum segment to stretch along the \hat{y} axis the bending angle θ decreases considerably and

the δ angle decreases (positive \hat{y}) or increases (negative \hat{y}). As shown in the force regulation experiments reported in the previous section, the sensitivity of the force estimation in the \hat{x} direction decreases considerably while the sensitivity in the \hat{y} direction increases. Although the controller is unable to regulate the requested amount of force due to the force estimator, the continuum manipulator does not lose contact with the surface. This phenomenon is not seen at the boundaries of the workspace along the \hat{z} direction because the insertion stage provide most of the displacement.

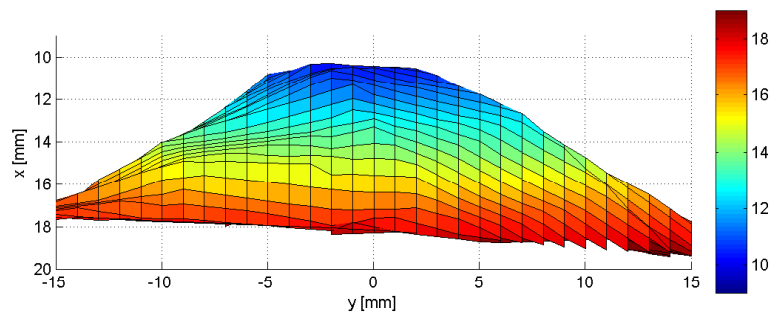
The very small inertia of the continuum manipulator allows the force controller to maintain contact with the unknown surface without perfect knowledge of the tangent and normal vectors at the contact point. These experiments demonstrate the efficacy of the proposed hybrid motion/force control scheme to perform independent motion and force regulation. The intrinsic compliance of the continuum manipulator also makes the impact phase stable allowing for safe and smooth transitions between full motion control and hybrid motion/force control.

Stiffness Imaging

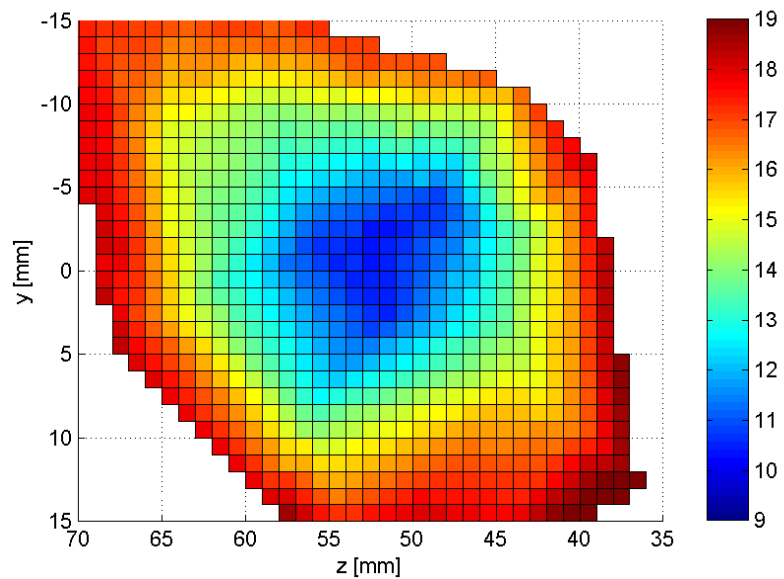
This section presents experimental results on stiffness characterization of soft tissues using the proposed hybrid motion/force controller. The goal of the experiment is to build a stiffness image of the surrounding environment using both position and force data. One way to build such image is to repetitively scan the surface applying different force and recording the displacement of each point between scans. The experimental setup (Figure V.18) consists of a $\varnothing 5$ mm continuum robot, a plastic probe with a spherical tip of 5 mm radius, a $\varnothing 0.9$ mm electro-magnetic sensor, and a silicone phantom with embedded rubber tubes.



(a) Side view.

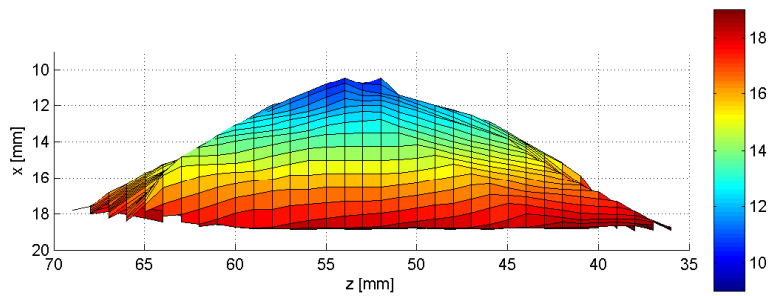


(b) Front view.

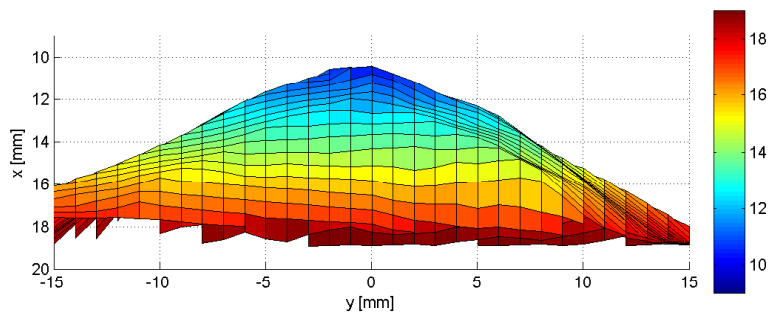


(c) Top view.

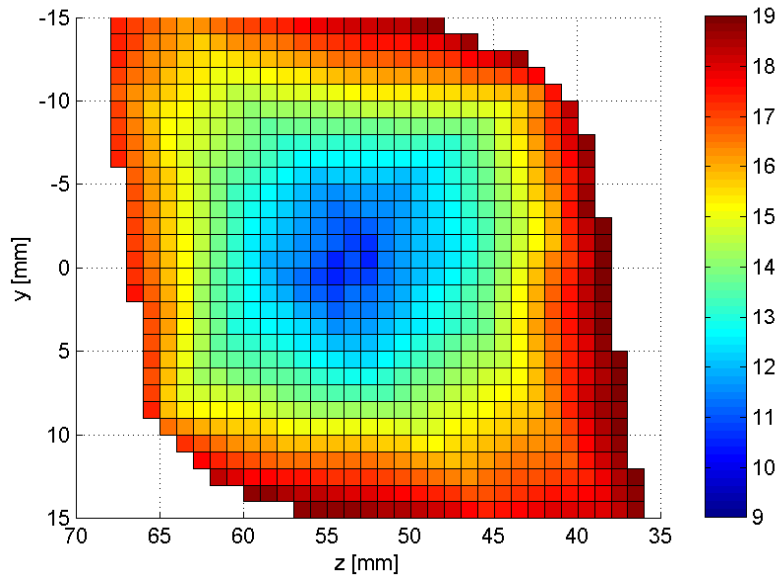
Figure V.15: Estimate shape under force-regulated scan.



(a) Side view.

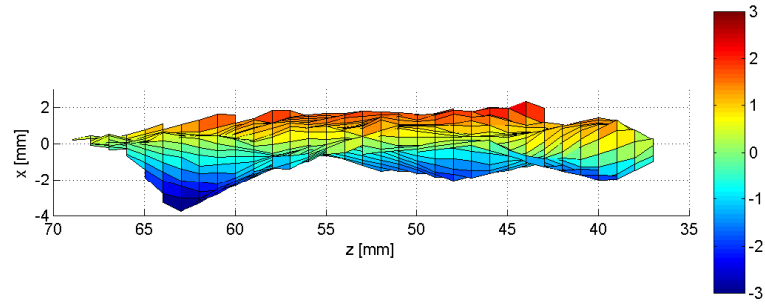


(b) Front view.

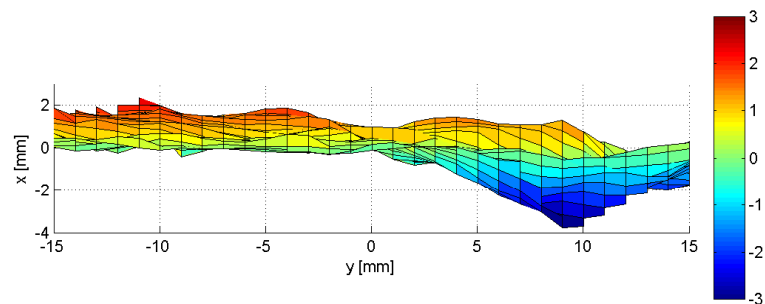


(c) Top view.

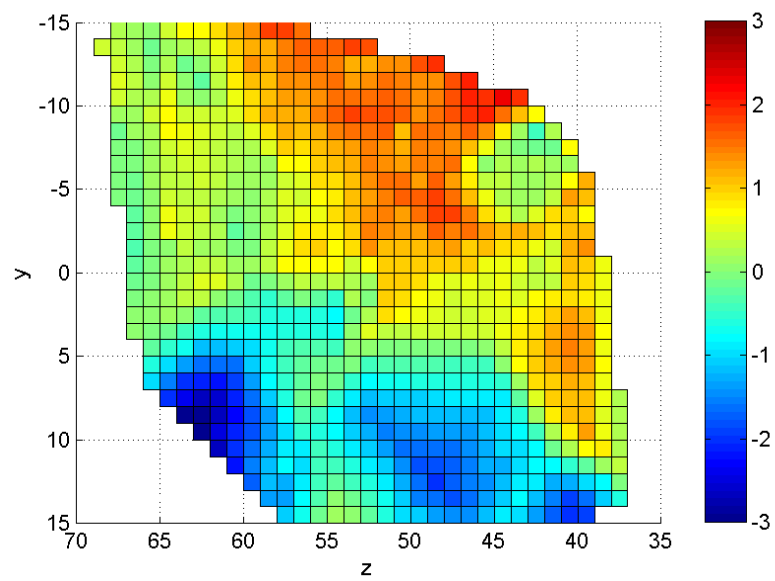
Figure V.16: Ground truth shape.



(a) Side view.



(b) Front view.



(c) Top view.

Figure V.17: Shape estimation error.

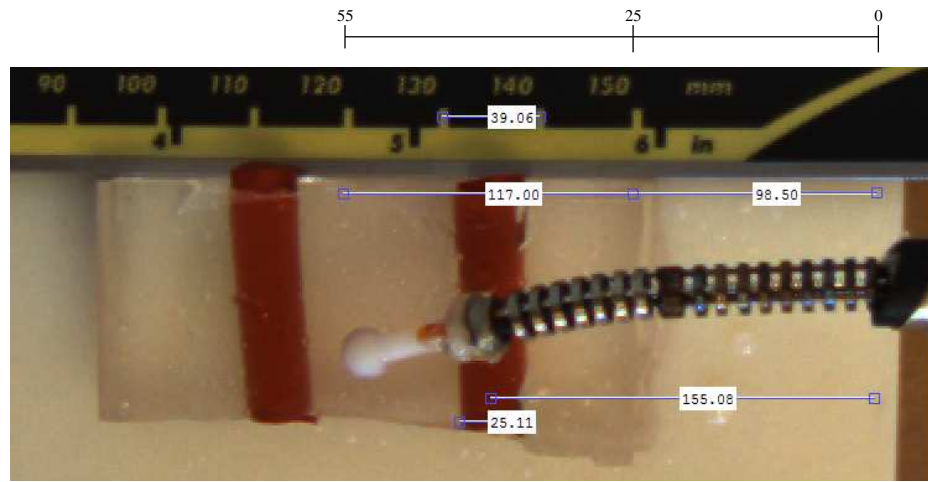


Figure V.18: Setup measurements to localize the mockup blood vessel. The image shows the setup, a ruler, and pixel measurements taken with the Matlab Image Processing Toolbox. From the image is possible to define a scaling factor that relates pixels to mm, the distance of the centerline of the blood vessel from the base of the robot and its width.

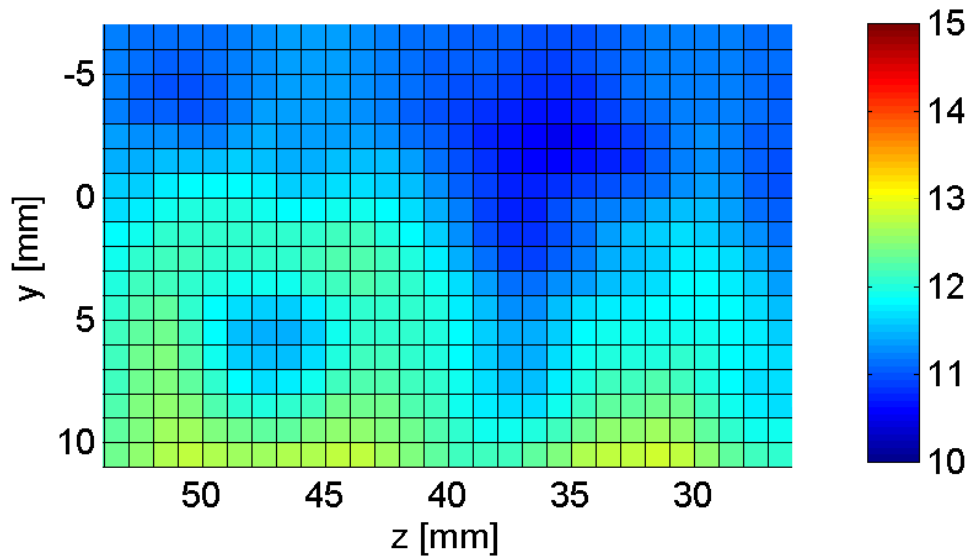


Figure V.19: Colormap of the estimated surface during the first scan (5 gr).

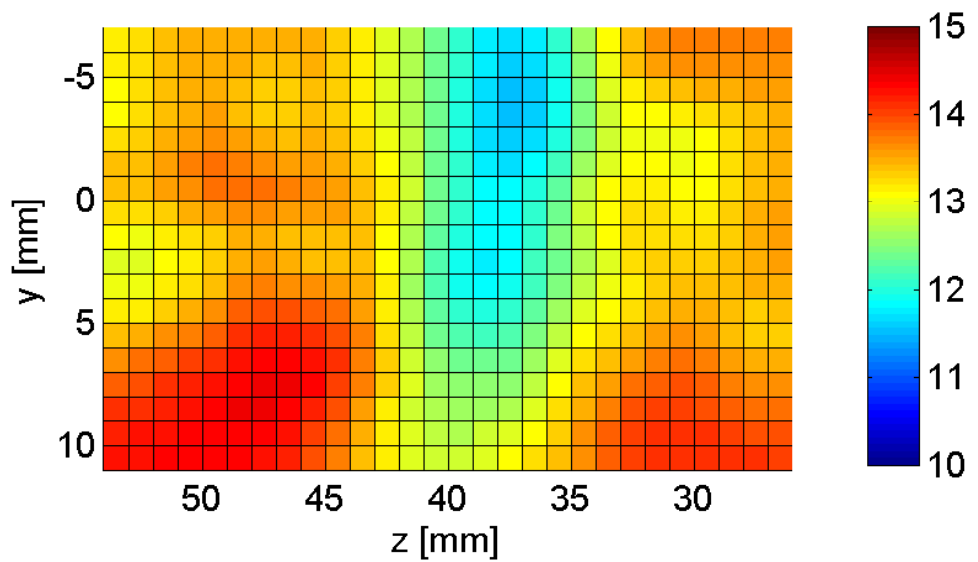


Figure V.20: Colormap of the estimated surface the last scan (25 gr).

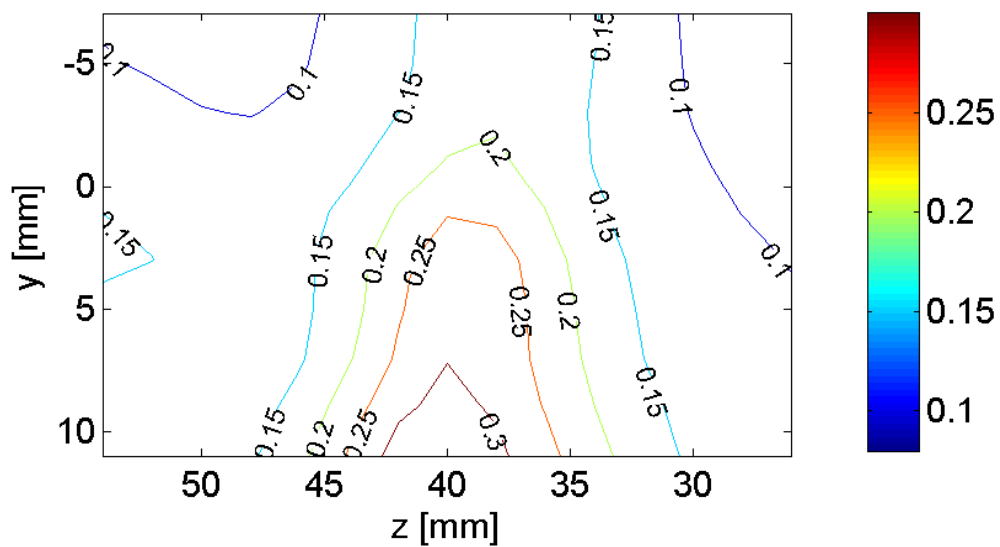


Figure V.21: Stiffness imaging

Methods

Five consecutive surface scans were completed under hybrid motion/force control applying respectively 5 gr, 10 gr, 15 gr, 20 gr, and 25 gr. After selecting the desired force magnitude, the operator guides the robot to cover the designated area (Figure V.18). A rubber tube is embedded at approximately 155 pixels (px) from the base of the robot. Using the ruler shown in Figure V.18, it is possible to define a scaling factor between image pixels and mm. In this case, $39px = 10mm$. Using this scaling ratio, the position of the rubber tube is identified at approximately 39.7 mm from the base of the manipulator. The operator was asked to scan a rectangular area of approximately 20×30 mm.

Position data during each scan were recorded from the electro-magnetic sensor placed at the tip along with the sensed force in the \hat{x} direction and smoothed by spline interpolation. Because of the position RMS of the Ascension Technologies trakSTAR 2 it was chosen to use the first and the last scan in order to obtain a better noise/signal ratio.

Results

The estimated surfaces under 5 Gr force control and 25 Gr force control are shown in Figures V.19 and V.20. Figure V.19 shows a color map of the estimated surface with points between 10 mm and 13 mm along the x direction. Figure V.20 shows a color map of the estimated surface with points between 12 mm and 15 mm along the x direction.

In order to characterize the difference in stiffness along the surface (not the absolute stiffness) a linear spring-model is used. Figure V.21 shows the estimated stiffness values across the scanned area. The graph shows a peak of 0.3 N/mm at approximately 40 mm from the base of the robot. The estimated stiffness decreases to 0.25

N/mm, 0.2 N/mm, and 0.15 N/mm respectively along both positive z direction and negative z direction. Lower stiffness is estimated at the boundaries of the scanned surface ($z = 55$ and $z = 25$). Figure V.18 shows that the rubber tube lays along the y axis at approximately $155px = 39.7mm$ from the base of he robot. The stiffness map clearly identifies high stiffness along that same axis as shown in Figure V.21.

CHAPTER VI

CLINICAL APPLICATIONS

This Chapter presents the implementation of several of the algorithms presented in Chapter 3 on state-of-the-art robotic systems developed at the Advanced Robotics Mechanism Applications Laboratory at Vanderbilt University. In particular, three systems are presented: 1) the dual arm insertable robotic effectors platform (IREP) for abdominal general surgery, the rapid deployment platform RDP for transurethral resection and surveillance, and a variation of the RDP for trans-nasal microsurgery of the throat. The variation includes a completely flexible stem with embedded localization sensors.

A Telesurgical System for Single Port Access Surgery

This section presents the integration and the preliminary evaluation of the IREP system shown in Fig. VI.1. To the best of the authors' knowledge the IREP is the smallest surgical robotic platform for SPAS. We present the complete direct and inverse kinematics formulation, integration with a dual-arm master interface, resolved-rates telemanipulation control, redundancy resolution, workspace enlargement using an additional insertion stage, and actuation compensation. Experimental results demonstrate that the IREP meets workspace and dexterity requirements for basic abdominal MIS procedures.

Clinical Motivations

Robotic end-effectors reinstate dexterity [38], enhance accuracy, filter hand tremor [108, 99], and safeguard delicate anatomy by creating virtual fixtures [84, 43]. For

these reasons, robotic-assisted Minimally Invasive Surgery (MIS) has been progressively accepted in many disciplines of surgery such as urologic, cardiothoracic, and gynecologic surgery. Although traditional MIS procedures reduce patient's trauma, multiple (typically 3-5) access ports [50] are required for a minimal set of surgical instruments or approaches. Each incision increases the risk of infection, lengthen the patient's convalescence, and increase post-operative pain. New surgical paradigms such as Single Port Access Surgery (SPAS) and Natural Orifice Trans-luminal Endoscopic Surgery (NOTES) aim to reduce or completely eliminate skin incisions. In SPAS procedures, the surgical site is reached through a single trocar while in NOTES procedures natural orifices are used. Both these surgical paradigms require a shift in the way robotic slaves are designed, built, and controlled.

In recent years, both industry [27] and academic groups [47, 72, 26, 1, 75, 113, 97, 76, 13] tried to further improve and expand the set of robotic-assisted procedures by proposing a variety of telesurgical systems for SPAS and NOTES. Designs vary from purely rigid-link effectors, to wire-actuated rigid link effectors, and continuum arms [105].

Successful telemanipulation and control of hybrid platforms including continuum robots requires present additional challenges such as kinematic modeling, real-time implementation of direct and inverse kinematics, backlash compensation, friction estimation, and extensions of the actuation lines. Several approaches have been proposed to address these problems and limitations. The mathematical foundations for modeling and analysis of hyper-redundant robots were laid out in [20, 119] while subsequent works addressed practical implementation and specific modeling issues. For example, in [49], the authors presented a simplified kinematic model for multi-segment continuum robots suitable for real-time control. In [114], a recursive estimation framework

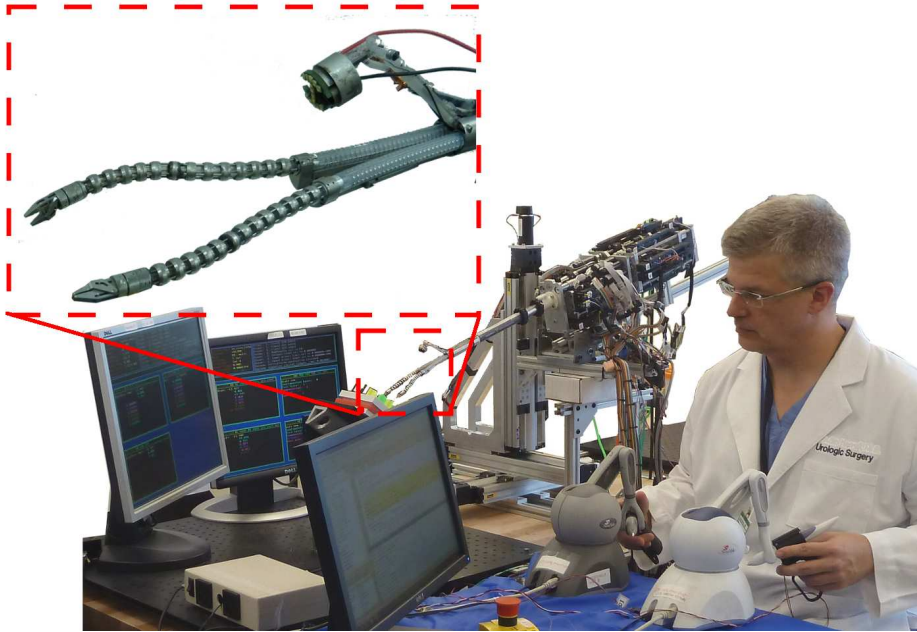


Figure VI.1: The Insertable Robotic Effectors Platform (IREP) with two continuum arms, wrists, grippers, stereo vision camera head, and illumination system

for actuation compensation was proposed. In [42], intra-corporeal knot tying using a dual-arm continuum robot system for laryngeal surgery was demonstrated. In [97], the authors proposed a recursive method for overcoming coupling, backlash, and extension of multi-segment multi-backbone continuum robots while in [14], configuration tracking for tendon-driven catheters was presented. Other works such as [2, 53] focused on backlash and friction compensation for wire-actuated robots and tendon-driven catheters. In [30, 105], a modeling and control framework for concentric tube continuum robots was proposed.

Surgical Slave System

Figure VI.1 shows the integrated surgical system for SPAS. The system is composed of 24 controlled axes: 18 for the IREP’s hybrid arms, 3 for the stereo camera

system, and 3 for the Cartesian stage. The Cartesian robot provides additional motion along the insertion axis for gross manipulation.

Each arm is composed of 9 controlled axes ($q_1 \dots q_9$): an insertion linear stage q_1 , a planar 2 DoF parallel mechanism (q_2, q_3), two continuum arms (q_4, q_5, q_6 and q_7), a 1 DoF wrist q_8 , and a gripper jaw q_9 . The role of the parallel linkage is to increase the lateral movement of the arm and to improve dual-arm triangulation. The insertion stage q_1 coordinates the insertion of the passively bending stem when the parallel linkage deploys. Each continuum segment is composed of four circumferentially located super elastic NiTi secondary backbones and 1 centrally located super elastic NiTi primary backbone. The particular design of the actuation unit couples opposing secondary backbones; thus, reducing the controlled axes from four to two for each continuum segment [29]. By controlling the length of the secondary backbones, each segment may be actively bent in 2 DoF.

Four coordinate systems are defined as shown in Fig. VI.2. Frame $\{0\}$ is the fixed base frame attached to the end of long insertion stem. Frame $\{1\}$ is attached to the moving ring of the parallelogram and always maintains the same orientation of frame $\{0\}$. Frames $\{2\}$ and $\{3\}$ are attached at the end disk of the first and second continuum arm respectively. Frame $\{4\}$ captures the additional wrist rotation.

Direct Kinematics

The direct kinematics of each arm may be described by the following augmented configuration space vector:

$$\Psi = \begin{bmatrix} b_x & b_z & \psi_1^T & \psi_2^T & \gamma \end{bmatrix}^T \quad (\text{VI.1})$$

where b_x and b_z (Fig. VI.2) denote the x and z coordinates of frame $\{1\}$ with respect to base frame $\{0\}$, $\psi_1 = \begin{bmatrix} \theta_1 & \delta_1 \end{bmatrix}^T$ and $\psi_2 = \begin{bmatrix} \theta_2 & \delta_2 \end{bmatrix}^T$ define the shape of the

first and second continuum segments and, therefore, the position and the orientation of frame $\{2\}$ with respect to frame $\{1\}$ and frame $\{3\}$ with respect to frame $\{2\}$ respectively. Angle θ_k is the bending angle of segment $k = 1, 2$, δ_k is the angle defining the plane in which segment k bends, and γ (Fig. VI.2) is the roll angle about axis $\hat{\mathbf{z}}_3$ that defines frame $\{4\}$.

The position and orientation of the end-effector is given by:

$$\mathbf{p}_4^0 = \mathbf{p}_1^0 + \mathbf{R}_1^0 (\mathbf{p}_2^1 + \mathbf{R}_2^1 \mathbf{p}_3^2 + \mathbf{R}_2^1 \mathbf{R}_3^2 \mathbf{p}_4^3) \quad (\text{VI.2})$$

$$\mathbf{R}_4^0 = \mathbf{R}_1^0 \mathbf{R}_2^1 \mathbf{R}_3^2 \mathbf{R}_4^3 \quad (\text{VI.3})$$

where $\mathbf{p}_1^0 = [b_x \ 0 \ b_z]^T$, $\mathbf{p}_4^3 = [0 \ 0 \ z_0]^T$, $\mathbf{R}_1^0 = \mathbf{I} \in \mathbb{R}^{3 \times 3}$, $\mathbf{R}_4^3 = \text{Rot}(\gamma, \hat{\mathbf{z}})$, and the remaining offsets and orientations due to the two continuum segments ($k = 1, 2$) are given by equations II.2 and II.3.

By taking the time derivative of (VI.2) and (VI.3) one obtains the 6×7 Jacobian matrix that relates the rate of change of the augmented configuration space vector $\dot{\Psi}$ and the linear and angular velocities of the end-effector:

$$\mathbf{J}_{\text{arm}} = \begin{bmatrix} \mathbf{e}_1 & \mathbf{e}_3 & \mathbf{S}_1 \mathbf{J}_1 & \mathbf{S}_2 \mathbf{J}_2 & \mathbf{S}_3 \mathbf{e}_6 \end{bmatrix} \quad (\text{VI.4})$$

where $\mathbf{e}_i \in \mathbb{R}^6$ is the i^{th} canonical basis vector, \mathbf{J}_1 and \mathbf{J}_2 are the Jacobian matrices of the first and second continuum segment respectively obtained from equation II.16 and

$$\mathbf{S}_1 = \begin{bmatrix} \mathbf{I} & [-\mathbf{R}_2^0 (\mathbf{p}_3^2 - \mathbf{R}_3^2 \mathbf{p}_4^3)] \times \\ \mathbf{0} & \mathbf{I} \end{bmatrix} \quad (\text{VI.5})$$

$$\mathbf{S}_2 = \begin{bmatrix} \mathbf{R}_2^0 & [-\mathbf{R}_3^0 \mathbf{p}_4^3] \times \\ \mathbf{0} & \mathbf{R}_2^0 \end{bmatrix} \quad (\text{VI.6})$$

$$\mathbf{S}_3 = \begin{bmatrix} \mathbf{0} & \mathbf{0} \\ \mathbf{0} & \frac{1}{4}\mathbf{R}_0 \end{bmatrix} \quad (\text{VI.7})$$

where $\mathbf{I} \in \mathbb{R}^{3 \times 3}$ is the identity matrix, $\mathbf{0} \in \mathbb{R}^{3 \times 3}$ is a matrix of zeros, and operator $[\mathbf{u}] \times$ constructs a 3×3 skew-symmetric matrix from vector \mathbf{u} .

Joint-Space Kinematics

The augmented configuration space vector $\Psi \in \mathbb{R}^7$ is related to the joint space vector $\mathbf{q} = \begin{bmatrix} q_1 & \dots & q_8 \end{bmatrix}^T$ as following:

$$q_1 = L(b_x, b_z) - L_0 \quad (\text{VI.8})$$

$$q_2 = b_z - d_1 \cos(\alpha) - d_5 - q_1 \quad (\text{VI.9})$$

$$q_3 = q_2 - d_8 + d_3 \cos(\xi) - d_4 \cos(\beta) - q_1 \quad (\text{VI.10})$$

$$q_4 = r\Theta_1 \cos(\delta_1) \quad (\text{VI.11})$$

$$q_5 = -r\Theta_1 \sin(\delta_1) \quad (\text{VI.12})$$

$$q_6 = r(\Theta_1 \cos(\delta_1) + \Theta_2 \cos(\delta_2)) \quad (\text{VI.13})$$

$$q_7 = -r(\Theta_1 \sin(\delta_1) + \Theta_2 \sin(\delta_2)) \quad (\text{VI.14})$$

$$q_8 = q_4 - q_5 + q_6 - q_7 + r_w \gamma \quad (\text{VI.15})$$

where $\Theta_k = \theta_k - \theta_0$, $L(b_x, b_z)$ and L_0 are respectively the arc-length of the passive stem when the parallelogram is open and when it is closed at a home position ($\alpha = 0$, $q_2 = 0$), r and r_w are the kinematic radii of the continuum segments (Fig. VI.2) and the wrist mechanism respectively. Kinematic parameters $\alpha, \beta, \xi, d_1, d_4, d_5$, and d_8 are shown in Fig. VI.2. Arc-length $L(b_x, b_z)$ of the passive stem depends on the position

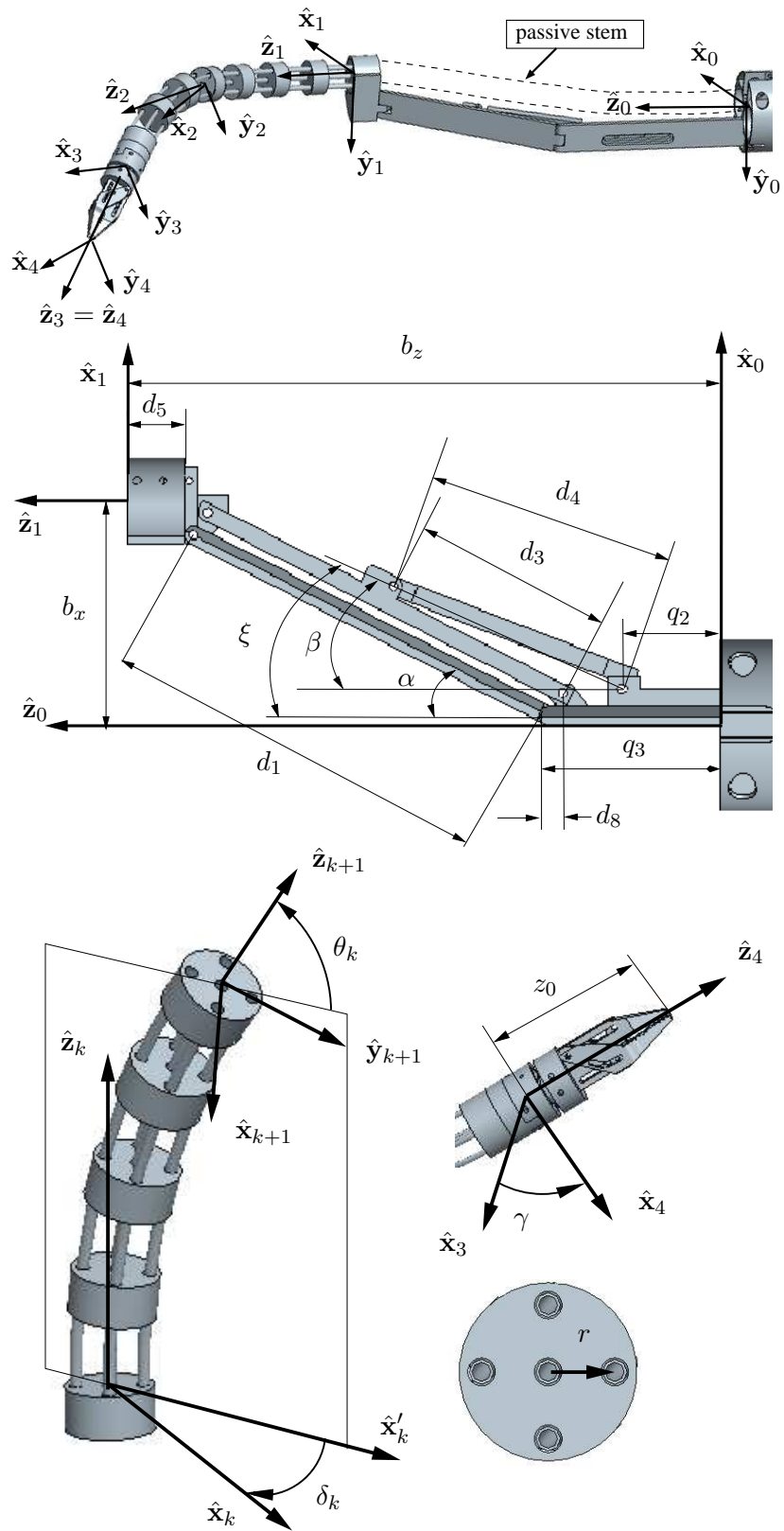


Figure VI.2: Kinematics nomenclature for one arm of the IREP

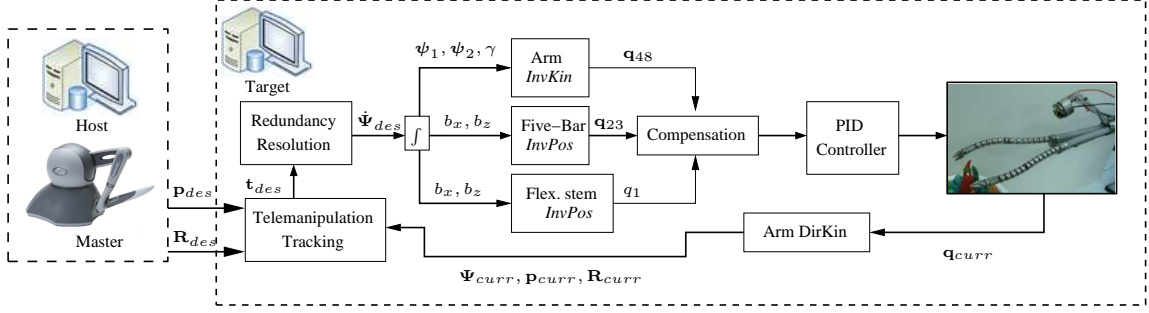


Figure VI.3: Telemanipulation integration architecture of the IREP. The notation q_{ij} is used as shorthand notation to vector $q_i \dots q_j$

of the moving base ring and can be obtained using the pseudo-rigid body method proposed in [45]. The derivative of (VI.11), (VI.12), (VI.13), (VI.14), and (VI.15) yields the instantaneous inverse kinematics Jacobian matrix that relates configuration space velocities $\dot{\psi}_1, \dot{\psi}_2, \dot{\gamma}$ and joint space velocities $\dot{\mathbf{q}}_{48} = \begin{bmatrix} \dot{q}_4 & \dot{q}_5 & \dot{q}_6 & \dot{q}_7 & \dot{q}_8 \end{bmatrix}^T$ such that:

$$\dot{\mathbf{q}}_{48} = \begin{bmatrix} \mathbf{J}_{q_1} & 0 & 0 \\ \mathbf{J}_{q_1} & \mathbf{J}_{q_2} & 0 \\ \mathbf{J}_{w_1} & \mathbf{J}_{w_2} & r_w \end{bmatrix} \begin{bmatrix} \dot{\psi}_1 \\ \dot{\psi}_2 \\ \dot{\gamma} \end{bmatrix} \quad (\text{VI.16})$$

where, for $k = 1, 2$,

$$\mathbf{J}_{q_k} = r \begin{bmatrix} c_{\delta_k} & -\Theta_k s_{\delta_k} \\ -s_{\delta_k} & -\Theta_k c_{\delta_k} \end{bmatrix} \quad (\text{VI.17})$$

$$\mathbf{J}_{w_k} = \begin{bmatrix} -(c_{\delta_k} + s_{\delta_k}) & \Theta_k (s_{\delta_k} - c_{\delta_k}) \end{bmatrix} \quad (\text{VI.18})$$

Telemanipulation

Telemanipulation Architecture

The telemanipulation framework of the IREP (Fig. VI.3) is subdivided as follows: *master-slave tracking error*, *redundancy resolution*, *configuration-to-joint space mapping*, and *direct kinematics*. The master-slave tracking error subsystem receives

V_{max}	V_{min}	ϵ_p	λ_p	Ω_{max}	Ω_{min}	ϵ_o	λ_o
15 mm	0.5 mm	0.5 mm	3	30°	1°	1°	3

Table VI.1: Slave telemanipulation parameters

data from the master manipulator and computes the desired twist of the end-effector. The redundancy resolution subsystem inverts the kinematics avoiding joint-limits and Jacobian singularities. The third subsystem provides the desired joint-space values that achieve the desired motion as described in the *InvPos* solution of (VI.8), (VI.9), (VI.10), and *InvKin* solution of (VI.16).

Since the IREP is a redundant manipulator, all 6 DoF are controlled and the master-slave tracking errors (position and orientation) are given by equations III.15 and III.16. The desired twist is computed according to equations III.18, III.21, III.22, and the telemanipulation parameters are reported in Table VI.1.

The desired configuration space velocities are computed according to III.26. In the case of the IREP, the primary goal of the weighted inverse is to prevent the continuum segments from reaching the minimum ($\theta_k = 0$) and maximum ($\theta_k = \theta_0 = \pi/2$) bending angles by exploiting redundancy as in [18]. The weights for the θ DoF can be computed as follows:

$$w = 1 + \left(\frac{\theta_0}{\theta_k \Theta_k^2} + \frac{\theta_0}{\theta_k^2 \Theta_k} \right) \quad (\text{VI.19})$$

Additionally, matrix \mathbf{W} can be used to guide the inversion of the Jacobian in order to favor the movement of the parallel mechanism or the insertion stage for some Cartesian directions.

Once the configuration space velocities are obtained, a resolved-rate approach [110] is used for both the parallel mechanism and the continuum arm. The position of frame $\{1\}$ is obtained as

$$b_x(t_{k+1}) = b_x(t_k) + \dot{b}_x(t_k) \Delta t \quad (\text{VI.20})$$

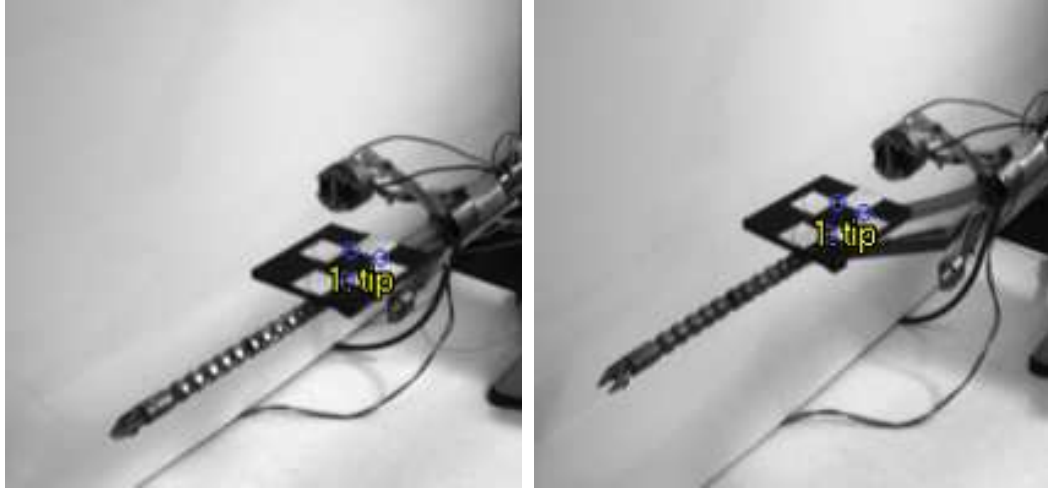


Figure VI.4: Snapshots taken from the vision tracker during data collection

$$b_z(t_{k+1}) = b_z(t_k) + \dot{b}_z(t_k) \Delta t \quad (\text{VI.21})$$

while, using (VI.17) and (VI.18), the rest of the configuration space vector is obtained as

$$\mathbf{q}_{48}(t_{k+1}) = \mathbf{q}_{48}(t_k) + \dot{\mathbf{q}}_{48}(t_k) \Delta t \quad (\text{VI.22})$$

where \mathbf{q}_{48} denotes $[q_4, \dots, q_8]$.

Compensation

Equations (VI.8), (VI.9), (VI.10), and (VI.22) provide the theoretical joint values that accomplish the commanded motion of the end-effector. However, because of backlash, friction, coupling between subsequent continuum segments, and extension of the actuation lines, the responsiveness of the IREP system is degraded. In particular, the main deficit of the parallel mechanism is backlash while the extension of the long actuation lines affects the continuum segments.

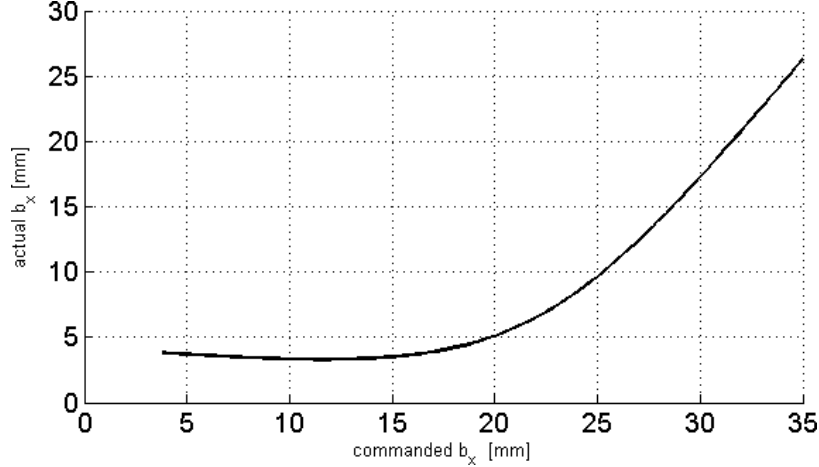


Figure VI.5: current versus commanded x position of the moving ring

Backlash Compensation

Experiments using a Claron Micron Tracker (Figure VI.4) were conducted to characterize the backlash affecting the parallel mechanism. Figure VI.5 shows a graph of the actual versus the commanded x position of the moving ring of the parallelogram while opening the mechanism. The figure shows a deadband between $x = 3.8$ mm (five-bar closed) and $x = 15$ mm. A reverse spline was numerically evaluated and its coefficients used during operation.

Actuation Compensation

Actuation compensation for multi-backbone continuum robots was presented in [114, 97]. Xu and Simaan [114] proposed the following compensation law:

$$\tilde{\mathbf{q}}_{47} = \mathbf{q}_{47} + \mathbf{K}^{-1}\boldsymbol{\tau} \quad (\text{VI.23})$$

where

$$\mathbf{K} = \begin{bmatrix} E_{ys}A/L_a & 0 \\ 0 & E_{ys}A/L_a \end{bmatrix}, \quad (\text{VI.24})$$

$$\boldsymbol{\tau} = \begin{bmatrix} \mathbf{J}_{q_1} & \mathbf{J}_{q_1} \\ 0 & \mathbf{J}_{q_2} \end{bmatrix}^\dagger \nabla U, \quad (\text{VI.25})$$

E_{ys} is the Young's modulus of the secondary backbones, A is the cross-sectional area of the backbones, L_a is the length of the actuation lines, and ∇U is the gradient of the elastic energy $U = U_1 + U_2$ of a two segment continuum robot [97] with respect to $\boldsymbol{\psi}_1$, and $\boldsymbol{\psi}_2$.

Augmenting the Workspace

The robotic system presented in Section VI was augmented with two additional Cartesian axes as shown in Fig. VI.1. Coordinated motion of the x and z axes allows the IREP to translate along the central stem axis. This additional DoF turned out to be essential for increasing the reachable workspace of the dual-arm system. The configuration space vector of the leading arm in (VI.1) is then augmented as the following

$$\bar{\boldsymbol{\Psi}} = \begin{bmatrix} \bar{b}_z & \boldsymbol{\Psi}^T \end{bmatrix}. \quad (\text{VI.26})$$

The inversion of the kinematics presented in Chapter 4 is modified as follows. The augmented arm Jacobian $\bar{\mathbf{J}}_{arm}$ is given by

$$\bar{\mathbf{J}}_{arm} = \begin{bmatrix} \mathbf{J}_{xz} & \mathbf{J}_{arm} \end{bmatrix} \quad (\text{VI.27})$$

where \mathbf{J}_{arm} is given in (VI.4) while

$$\mathbf{J}_{xz} = \begin{bmatrix} -\sin(\varphi) & 0 & \cos(\varphi) & 0 & 0 & 0 \end{bmatrix}^T \quad (\text{VI.28})$$

In order to use the Cartesian manipulator when the IREP reaches upper and lower

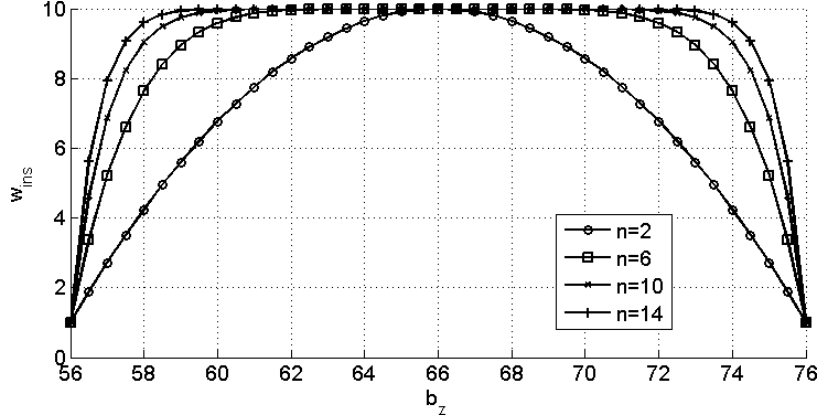


Figure VI.6: Weight profile for the insertion stage and different values of n

limits of its workspace, the following weight w_{ins} is associated with the insertion stage:

$$w_{ins} = w_{min} + w_{max} \left(1 - \left(\frac{b_z - b_{z,mid}}{b_{z,amp}} \right)^n \right) \quad (\text{VI.29})$$

where $b_{z,mid}$ is the middle of the range in the z direction and $b_{z,amp}$ is the mechanical travel of the insertion stage. Weight w_{ins} depends on the z -component of the position of the tip of the parallelogram. By choosing exponent n (Figure VI.6), it is possible to guide the inversion of the kinematics in (III.27) and use the insertion stage only when b_z approaches the upper and lower joint limits of the five-bar linkage.

Preliminary Evaluations

The integrated telemanipulation system of Fig. VI.1 was qualitatively evaluated for ability to complete key surgical tasks. The capabilities of this system were evaluated in stringent conditions that do not rely on using the standard four DoFs of laparoscopic surgery (translation along the insertion axis and three tilting angles). We evaluated the system with only one additional translational DoF provided by the coordinated motion of the Cartesian robot. The insertion DoF allowed for sufficient

workspace reachability to complete some of the surgical tasks described by the Fundamentals of Laparoscopic Surgery (FLS) [34]. The addition of the insertion DoF was crucial to place the IREP near the target surgical zone and successfully complete the tasks.

We set forth to evaluate the ability of the IREP to complete the following tasks: 1) pick and place, 2) hand exchange of rings, 3) passing circular needles, 4) completing knot tying. To achieve these goals we used the *dexterity peg board* provided by FLS, the *Robotic Sea Spikes Pod* training model available from The Chamberlain Group, a suturing goretex model by FLS, and standard circular needles used in abdominal surgery.

Pick and place and hand exchange

Experiments for pick and place included manipulation of plastic triangular-shaped objects as shown in Figs. VI.7 and VI.8. The experiments show that the tasks were completed successfully with minimal experience by novice users (all users in these experiments with the exception of the lead author had no experience with the telemomanipulation system and had only minimal familiarization periods totalling less than 30 minutes of continuous test driving of the system). The experiments for FLS required the users to manipulate size large objects by picking them from the left 6 pegs and then placing them on the right 6 pegs. The peg diameters in the FLS training model is 3.2 mm, the diameter of hole in the manipulated triangular cross section objects is 6.34 mm. We found out that 1) exchange of objects between hands was possible despite the small side of the IREP gripper; 2) some difficulties were observed due to limited depth perception when trying to guide the objects to slide on the pegs. This stemmed from the fact that we were unable to use real 3D stereo vision but instead, the user observed the robot while standing as shown in Figure VI.1; 3)

the accuracy of the IREP was suitable for successful completion of the experiments by both the surgeon author and the non-surgeon authors; 4) the reach of the IREP arms allowed it to cover the entire workspace of 64 mm × 103 mm of the FLS board without exchange of the manipulated object between hands.

Passing surgical needles and knot tying

In addition we evaluated the ability of the IREP to pass circular sutures and tie surgeon's knots. We used standard V-shaped 26 mm needle and a 2-0 size suture. The passage of circular needles was not easy due to the limited rotation range of the distal wrist of ± 60 degrees. Though it was possible to pass a circular suture using a long series of needle re-grasping, we deem the performance of the IREP for this task as deficient and new designs to allow full turn rotation in each direction will be considered. Knot tying was completed after manually placing the circular needle in a goretex tube. The IREP was able to easily triangulate to its target zone and the knot tying was achieved easily. The grippers were also able to exchange the needle successfully despite the limited rotation of the wrist. Figures VI.7, VI.8, and VI.9 show sequences of images depicting the experiments.

Conclusions

SPAS presents challenges that require unique designs of surgical devices with large workspace and enhanced dexterity in small and confined spaces. The IREP system meets these requirements and, to the best of authors' knowledge is the smallest existing robotic system for SPAS that requires a single incision of $\varnothing 15$ mm. The IREP's 24 controlled axes are able to deploy two 7 DoF continuum manipulators equipped with wrists and grippers and a 3 DoF stereo vision module.

This paper presented the telemanipulation framework, kinematic modeling, and

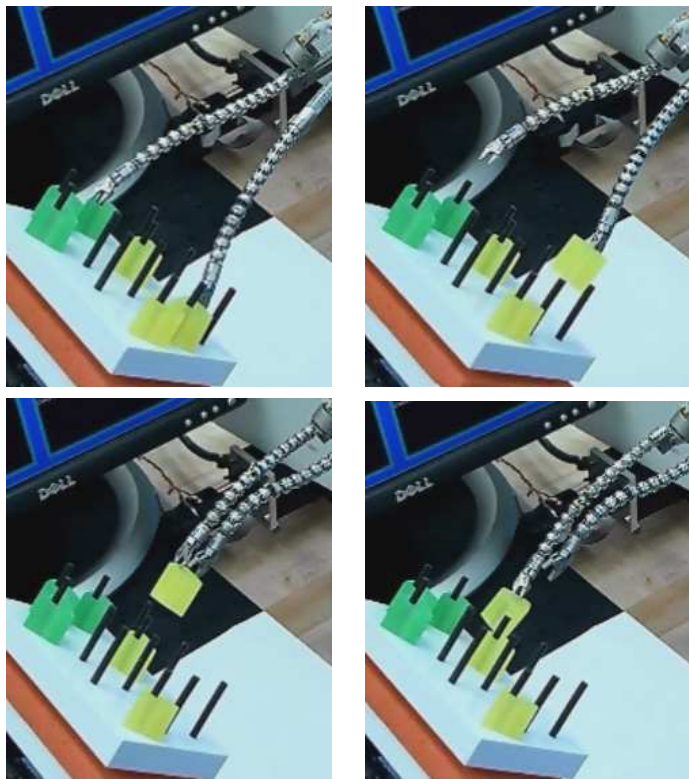


Figure VI.7: Sequence of pick and place using the dexterity peg board

redundancy resolution of the IREP system. The qualitative evaluation and demonstration revealed that the current integrated system is capable of completing key laparoscopic tasks. Because the IREP is compact, it can be locked to the surgical bed facilitating quick reorientation of the patient during surgery. This capability

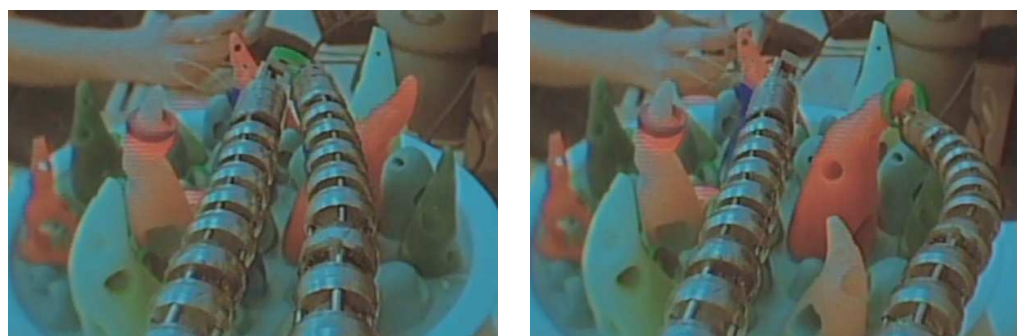


Figure VI.8: Sequence of pick soft object swap between hands

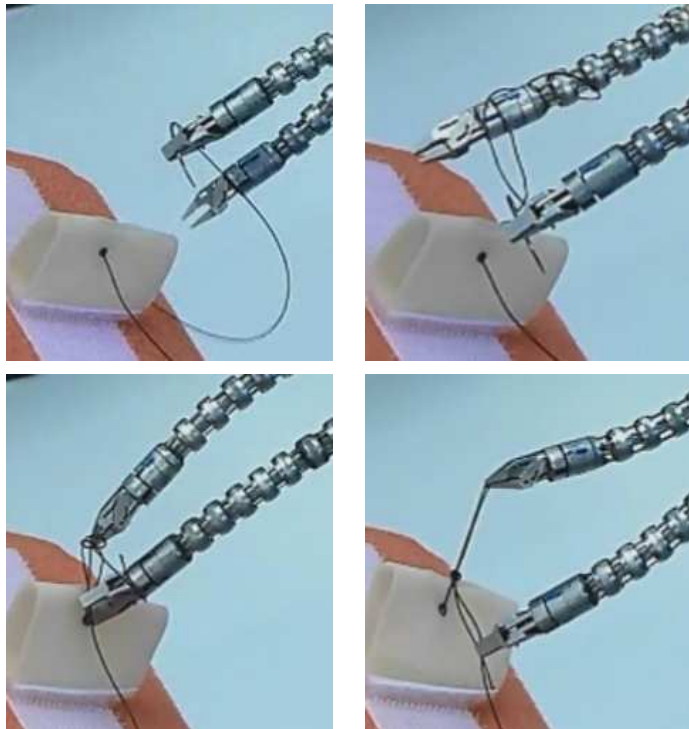


Figure VI.9: Sequence of knot tying under bimanual telemanipulation

eludes existing commercial systems, which use stand-alone slave robots next to the surgical bed. The IREP thus offers key advantages in terms of setup time, dexterity, reduced operating room footprint and ease of changing the patient's surgical pose. Because it requires only one small $\varnothing 15\text{mm}$ incision, the IREP is expected to minimize patient trauma, pain, recovery time and complications such as wound infection and incisional hernia. These benefits remain to be validated in future clinical evaluations.

Experiments demonstrated successful completion of knot tying, exchange of small and large objects between hands, and delicate pick and place tasks. The experiments revealed that the limited axial rotation of the wrists $\pm 60^\circ$ hindered successful completion of circular suture passing. In future designs, the wrists will allow for full rotation of the grippers.

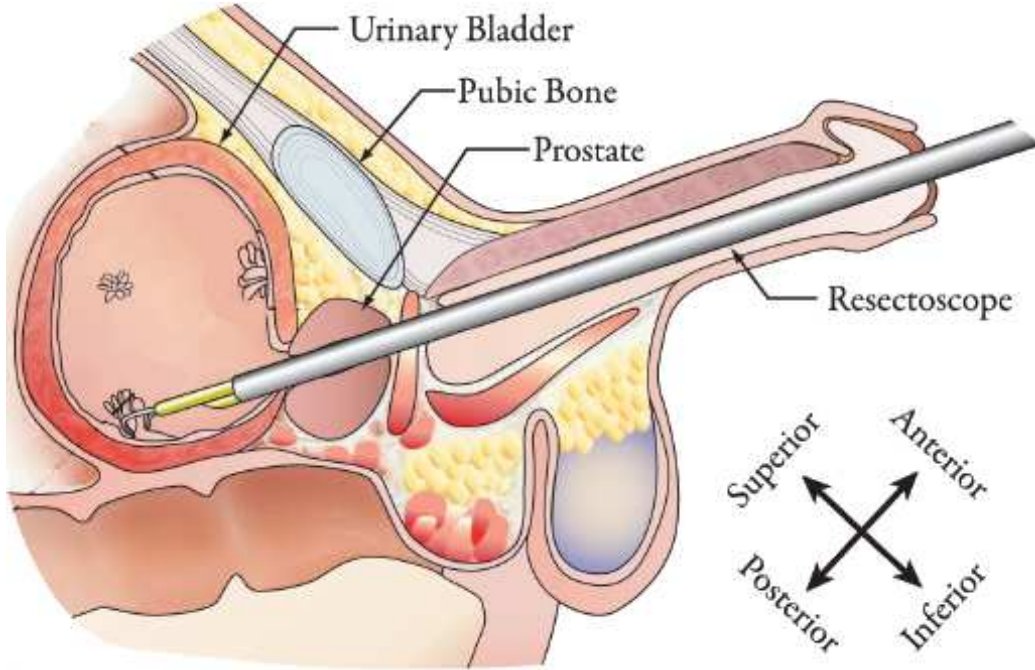


Figure VI.10: Overview of the TURBT procedure. The resectoscope is inserted through the urethra to access the bladder.

A Telesurgical System for Transurethral Resection of Bladder Tumors (TURBT)

This section presents the integration and preliminary ex-vivo evaluation of a system for bladder surveillance and intervention. The design presented in [35] is, to the best of the author's knowledge, the first robotic slave for TURBT surveillance and intervention. Experimental results include laser delivery, grasping, and biopsy inside a bovine bladder. Future experiments will evaluate telemanipulation bandwidth, repeatability, and accuracy of the system.

Clinical Motivations

Transurethral Resection of Bladder Tumor (TURBT) is an endoscopic surgical procedure that aims for resecting non-invasive tumors inside the urinary bladder. In

2012, the number of newly diagnosed bladder cancer patients and deaths were 73,510 and 14,880 respectively [48]. TURBT procedures provide access to the bladder via the urologic resectoscope, a device that consists of multiple telescoping and interlocking parts. The inner diameter that is used to deliver instruments and visualization is typically between 7 and 8 mm. The resectoscope is inserted through the urethra to access the bladder as shown in Fig. VI.10. A long, straight instrument and a laparoscope are inserted through the resectoscope to perform the tumor removal.

The long straight access channel dramatically reduce dexterity at the tool tip. The access constraint only allows for insertion along the resectoscope and limited lateral movement that is usually achieved by shifting the resectoscope itself and the surrounding anatomy. Coverage of the posterior and superior quadrant is difficult but possible. Accuracy of the resection highly depends on the particular anatomy and surgeon skills. Coverage of the anterior and inferior quadrant is achieved by pushing on the pubic bone in order to deform the urinary bladder internal wall. Note that this procedure is completely helpless in obese patients where the abdominal fat prevent for reaching the desired shifting. Moreover, one perplexing drawback of current practice of TURBT is that tumor resection is carried out piecemeal and, therefore, possibly contributing to seeding other cancer sites [79]. Typically, suspicious tissues is resected in one piece (en-block) to prevent spread of malignant cells. Although en-block TURBT was recently demonstrated clinically [102], en-block resection remains challenging or impossible depending on lesions location and surgeon's technical expertise [87]. Current devices and techniques prevent the validation of a clinical standard for en-bloc resection and acceptance by the Urologic community [17]. Instruments limitations such as reduced resection accuracy, lack of intracavitory tool-tip dexterity, and lack of in-vivo feedback do not allow for TURBT treatment improvements and make TURBT outcomes highly dependable on surgical skills.

In order to address these challenges, we proposed a telesurgical system [36] and evaluated deployment, laser delivery, and biopsy inside an explanted bovine bladder. Posterior and superior quadrants of the urinary bladder were easily reached and key surgical tasks were performed. On the other hand, the anterior and inferior quadrants were not easily accessed under telemanipulation control because of the inability of the operator to safely retract the continuum arm inside the resectoscope and accomplish the desired movement with the deployed portion of the manipulator. In order to perform any surgical procedure in these areas of the bladder, the surgical slave should actively assist the surgeon by avoiding the tubular constraint without *a priori* knowledge of the task while allowing full control of the remaining DoF. Traditional virtual fixture methods that constraint the robot's end-effector may not easily exploited in this scenario because of the fact that the virtual fixtures need to be applied to section of the manipulator only (in this case the first segment). Furthermore, these virtual fixtures do not only depend on the particular access channel used but also on the insertion depth along the tubular constraint.

Surgical Slave System

The surgical slave of Figure VI.11 is the composition of a linear stage and a dexterous four Degree of Freedom (DoF) continuum manipulator. The continuum manipulator has two multi-backbone segments that provide two DoF each. Each segment has three *push-pull* backbones that allows for bending each segment in space. A complete derivation of the direct and differential kinematics of these continuum structures are given in [94]. For the ease of presentation, in the remainder of this section, the kinematics of the two segments and the insertion stage is unified without explicit derivation.

Direct Kinematics

Five coordinate systems are defined: 1) base frame $\{\hat{\mathbf{x}}_0, \hat{\mathbf{y}}_0, \hat{\mathbf{z}}_0\}$, 2) first segment base disk frame $\{\hat{\mathbf{x}}_1, \hat{\mathbf{y}}_1, \hat{\mathbf{z}}_1\}$, 3) second segment base disk frame $\{\hat{\mathbf{x}}_2, \hat{\mathbf{y}}_2, \hat{\mathbf{z}}_2\}$, 4) end-effector frame $\{\hat{\mathbf{x}}_3, \hat{\mathbf{y}}_3, \hat{\mathbf{z}}_3\}$, and 5) tool frame $\{\hat{\mathbf{x}}_4, \hat{\mathbf{y}}_4, \hat{\mathbf{z}}_4\}$. The position and the orientation of the end-effector in base frame is given by:

$$\mathbf{p}_3^0 = \mathbf{p}_1^0 + \mathbf{R}_1^0 (\mathbf{p}_2^1 + \mathbf{R}_2^1 \mathbf{p}_3^2) \quad (\text{VI.30})$$

$$\mathbf{R}_3^0 = \mathbf{R}_1^0 \mathbf{R}_2^1 \mathbf{R}_2^3. \quad (\text{VI.31})$$

where

$$\mathbf{p}_1^0 = \begin{bmatrix} 0 & 0 & q_{ins} \end{bmatrix}^T \quad (\text{VI.32})$$

and position and orientation of the continuum segments, \mathbf{p}_{1+k}^k and \mathbf{R}_{k+1}^k , are given by equations II.2 and II.3.

The direct kinematics of the surgical slave can be easily updated if a tool is deployed through one of its access channels. In this case, the position of the tools is given by:

$$\mathbf{p}_4^0 = \mathbf{p}_3^0 + \mathbf{R}_3^0 \begin{bmatrix} r_c \cos \beta & r_c \sin \beta & d_3 \end{bmatrix}^T \quad (\text{VI.33})$$

We now define two vectors $\Psi \in \mathbb{R}^5$ and $\mathbf{q} \in \mathbb{R}^7$. The former is called *configuration space* vector and includes all the independent variables of the kinematics equations (VI.30) and (VI.31):

$$\Psi = \begin{bmatrix} \theta_1 & \delta_1 & \theta_2 & \delta_2 & q_{ins} \end{bmatrix}^T \quad (\text{VI.34})$$

The latter is called *joint space* vector and it is defined as:

$$\mathbf{q} = \begin{bmatrix} q_{1,1} & q_{1,2} & q_{1,3} & q_{2,1} & q_{2,2} & q_{2,3} & q_{ins} \end{bmatrix}^T \quad (\text{VI.35})$$

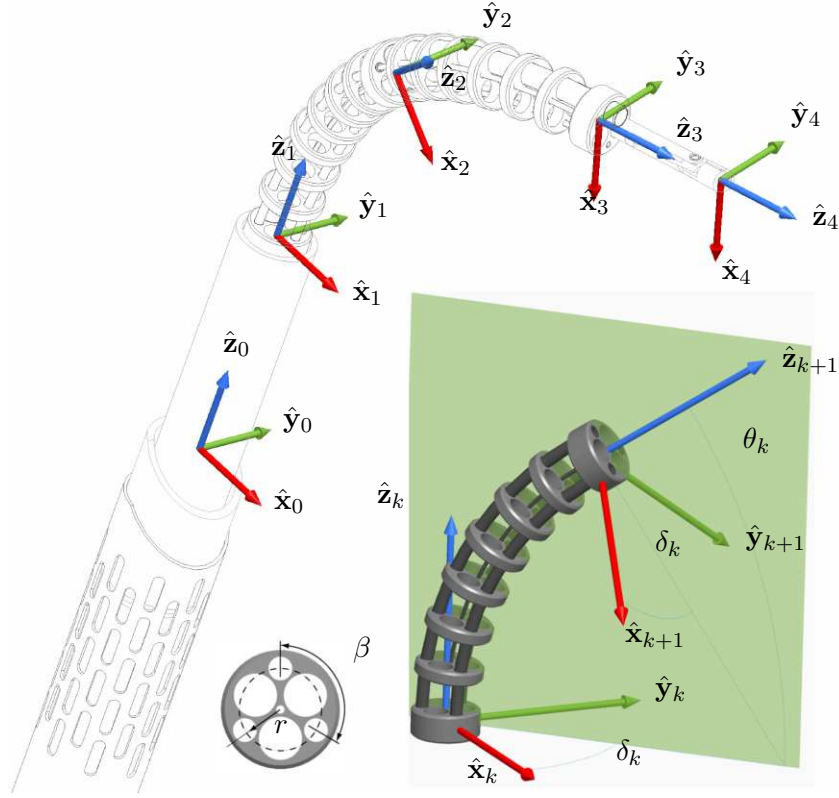


Figure VI.11: Kinematics nomenclature of the surgical system. Five coordinate systems are defined: 1) base frame $\{\hat{x}_0, \hat{y}_0, \hat{z}_0\}$, 2) first segment base disk frame $\{\hat{x}_1, \hat{y}_1, \hat{z}_1\}$, 3) second segment base disk frame $\{\hat{x}_2, \hat{y}_2, \hat{z}_2\}$, 4) end-effector frame $\{\hat{x}_3, \hat{y}_3, \hat{z}_3\}$, and 5) tool frame $\{\hat{x}_4, \hat{y}_4, \hat{z}_4\}$.

where, for segments $k = 1, 2$ and backbones $i = 1, 2, 3$, $q_{k,i}$ is given by equation II.4.

Differential Kinematics

The end-effector translational and rotational velocities can be found as:

$$\mathbf{v}_{0,3}^0 = \mathbf{v}_{0,1}^0 + \mathbf{R}_1^0 (\mathbf{v}_{1,2}^1 + \mathbf{R}_2^1 \mathbf{v}_{2,3}^2 + \boldsymbol{\omega}_{1,2}^1 \times \mathbf{R}_2^1 \mathbf{p}_3^2) \quad (\text{VI.36})$$

$$\boldsymbol{\omega}_{0,3}^0 = \mathbf{R}_1^0 \boldsymbol{\omega}_{1,2}^1 + \mathbf{R}_2^0 \boldsymbol{\omega}_{2,3}^2 \quad (\text{VI.37})$$

where $\mathbf{v}_{a,b}^c$ and $\omega_{a,b}^c$ are the translational and rotational velocities of frame b with respect to frame a written in frame c . The translational velocity of frame $\{1\}$, $\mathbf{v}_{0,1}^0$, is given by differentiating (VI.32) with respect to time while the translational velocities of the first, $\mathbf{v}_{1,2}^1$, and second end disk, $\mathbf{v}_{2,3}^2$, in local coordinate frames is given by II.10 for $k = 1, 2$. Similarly, angular velocities $\omega_{1,2}^1$ and $\omega_{2,3}^2$ are given by equation II.13.

$$\omega_{k-1,k}^{k-1} = \dot{\theta}_k \hat{\mathbf{y}}_k^{k-1} + \dot{\delta}_k (\hat{\mathbf{z}}_k^{k-1} - \hat{\mathbf{z}}_{k-1}^{k-1}). \quad (\text{VI.38})$$

By defining $\dot{\Psi}$ as the rate of change of the configuration space vector Ψ , one can rewrite the twist of the end-effector (i.e. (VI.36) and (VI.37)) as:

$$\begin{bmatrix} \mathbf{v}_{0,3}^0 \\ \omega_{0,3}^0 \end{bmatrix} = \mathbf{J}_{arm} \dot{\Psi}. \quad (\text{VI.39})$$

The geometrical arm Jacobian \mathbf{J}_{arm} is the result of three contributions: the insertion linear stage, and the two continuum segments:

$$\mathbf{J}_{arm} = \begin{bmatrix} \mathbf{S}_1 \mathbf{J}_1 & \mathbf{S}_2 \mathbf{J}_2 & \mathbf{e}_3 \end{bmatrix} \quad (\text{VI.40})$$

where $\mathbf{e}_3 = \begin{bmatrix} 0 & 0 & 1 & 0 & 0 & 0 \end{bmatrix}^T$, Jacobian J_k is given by equation II.16 and transformation matrices \mathbf{S}_1 and \mathbf{S}_2 are given by:

$$\mathbf{S}_1 = \begin{bmatrix} \mathbf{I} & [-{}^0\mathbf{R}_2 {}^2\mathbf{p}_3] \times \\ \mathbf{0} & \mathbf{I} \end{bmatrix} \quad (\text{VI.41})$$

$$\mathbf{S}_2 = \begin{bmatrix} {}^0\mathbf{R}_2 & \mathbf{0} \\ \mathbf{0} & {}^0\mathbf{R}_2 \end{bmatrix}. \quad (\text{VI.42})$$

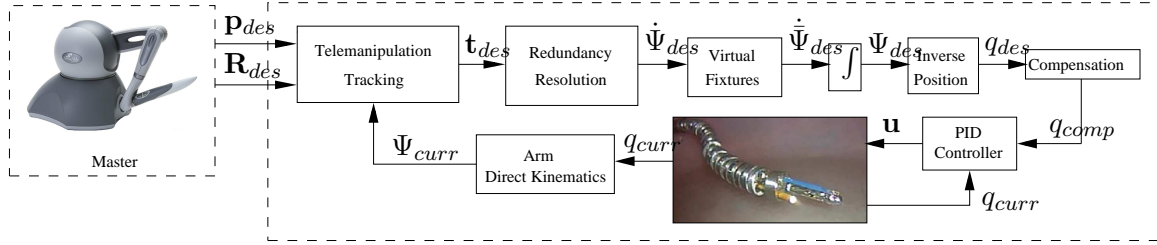


Figure VI.12: Telemanipulation architecture.

Table VI.2: Slave linear velocity parameters

V_{max}	V_{min}	ϵ_p	λ_p	Ω_{max}	Ω_{min}	ϵ_o	λ_o
15 mm	0.5 mm	0.5 mm	3	30°	1°	1°	3

Telemanipulation Architecture

Figure VI.12 shows the telemanipulation architecture of the RDP robot. The software architecture is composed of telemanipulation tracking error, redundancy resolution, configuration space virtual fixtures, inverse position analysis, actuation compensation, and the joint-space controller. The architecture is analogous to the one presented for the IREP in the previous sections. Most of the algorithms and functions apply to the RDP robot except of the master-slave tracking error, the redundancy resolution, and the addition of the configuration space virtual fixtures.

Since the RDP has 5 DoF, the master slave tracking errors for position and orientation are given by equations III.15 and III.17. Table VI.2 reports the telemanipulation parameters for the RDP robot.

Once the desired twist is obtained, the configuration space velocity vector is obtained using equation III.28 and the configuration space virtual fixtures are applied as in equation III.42. Finally, the instantaneous joint space position are found similarly as in VI.22.

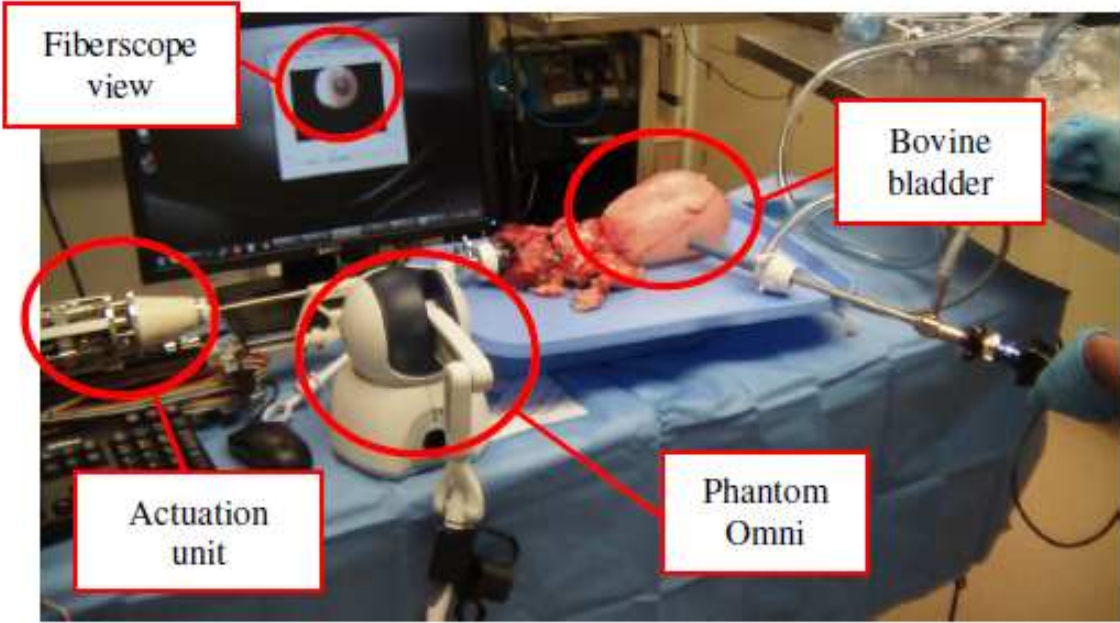


Figure VI.13: The experimental setup consists of an explanted bovine bladder, an external 30° scope, a 6 DoF Sensable Phantom Omni, the robot's actuation unit, and control computer that also provide the vision feedback from the on-board fiberscope.

Experimental Results

Ex-Vivo Bovine Bladder

The experimental setup is shown in Figure VI.13. Using a resectoscope and a trocar to regulate inflation, the robot is inserted through the bovine urethra and deployed inside the bladder. An HD fiberscope is deployed through the additional trocar to facilitate telemanipulation and guiding of the robot via a 6 DoF Phantom Omni. Three tasks were performed in order to demonstrate the capabilities of the surgical device: 1) laser delivery, 2) biopsy.

Laser delivery

Laser delivery was performed in four different areas of the bladder: 1) left side, 2) right side, 3) top, and 4) bottom. The experiments are shown in Figure VI.14. The

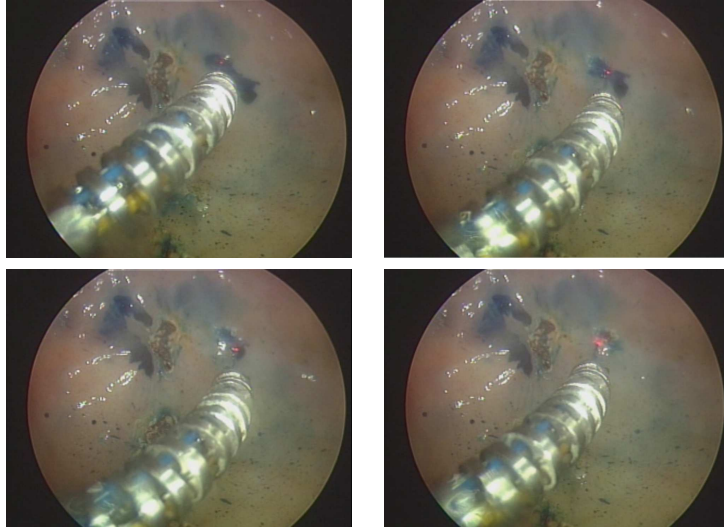


Figure VI.14: Picture sequence of laser delivery. The laser fiber is deployed through the continuum manipulator and the end-effector commanded via the master manipulator.

figure shows a fiberscope view of the surgical slave delivering surgical energy on the left side of the bladder. Multiple areas of the bladder were marked with indigo blue dye and then targetted with a \varnothing 0.66mm laser. The picture sequence shows how the target area (in blue) is progressively reduced by laser delivery. Close-up pictures of the target areas are shown in Fig. VI.15. The pictures show that the marked areas were circumscribed by laser delivery.

Biopsy

Additional experiments were carried out to demonstrate the feasibility of cancer resection and biopsy. A \varnothing 1.8 mm disposable biopsy forceps were delivered through the third access channel. Tissue was gripped and laser was delivered to resect the sample as shown in Figure VI.16. The dexterity of slave allows for pivoting about the contact point and successfully completing en-block biopsy/resection. The sample tissue was successfully extracted from inside the bovine bladder and examined as shown in Figure VI.17.

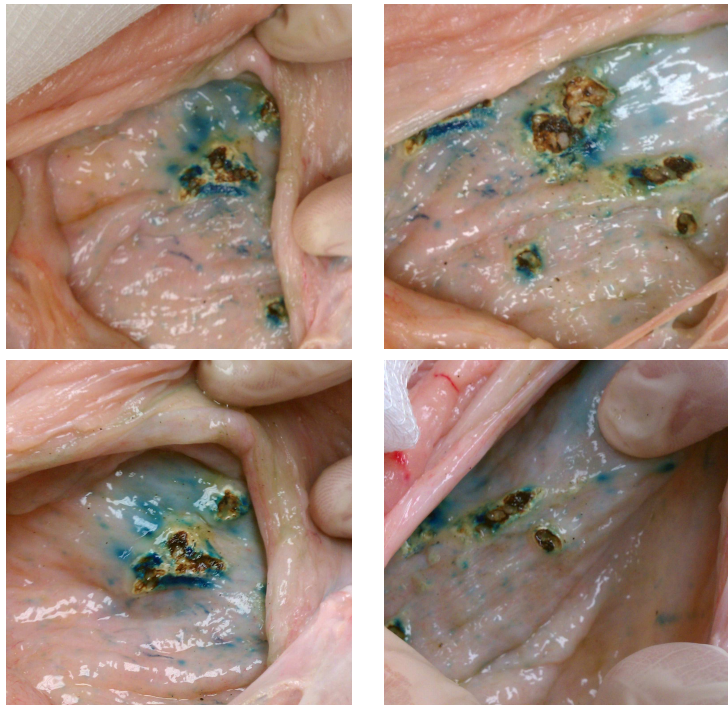


Figure VI.15: Picture sequence of laser delivery result. The bovine bladder wall was cut and the target area inspected.



Figure VI.16: En-block resection demonstration.



Figure VI.17: En-block resection results. The tissues was successfully extracted from inside the bladder and examined.

Constrained Motion Control

The experimental setup of Fig. VI.28 consists of a 7-axes actuation unit, a 2-segment $\oslash 5$ mm continuum robot, a 250 ml beaker, and Sensable Phantom Omni (not shown). The beaker approximates an inflated average-sized urinary bladder. Target points on the outer surface of the beaker were marked for targeting experiments. These points are placed in the *interior* and *anterior* quadrants, the areas of the bladder that are not easily reached with conventional urologic instruments and the robot in normal telemanipulation mode.

CSVF Demonstration In order to validate the efficacy of the resectoscope-based virtual fixture, Algorithm 3 was implemented on the surgical robot of Figure VI.11 and results are shown in Figure VI.18. Figure VI.18 shows the time history of the configuration space vector Ψ . Between $t = 5s$ and $t = 10s$ the surgical slave is deployed via configuration space control to initial configuration $\Psi_s = \begin{bmatrix} 60 & 0 & 60 & 180 & 0 \end{bmatrix}^T$. At $t = 15s$ the telemanipulation is engaged and the continuum manipulator is moved forward and no virtual fixture is applied. At $t = 25s$ the slave is commanded to

retract inside the resectoscope $q_{ins} < 0$. The virtual fixture algorithm engages and θ_1 increases according to III.43. Accordingly, the resolved rate control algorithm increases θ_2 to maintain the desired orientation specified by the master manipulator. The virtual fixture algorithm keeps increasing θ_1 until the insertion direction is inverted ($t = 35s$).

Constrained Targeting In order to test the configuration space virtual fixtures and the constrained redundancy resolution presented in Section III, the robot was commanded to reach predetermined points inside the *interior* quadrant of the glass bladder. Points vary between configurations in which the robot is fully deployed inside the bladder (points close to the bladder *equator*) and points in which the continuum arm is partially inserted into the urologic resectoscope (points close to entry point). Figure VI.20 shows the continuum manipulator guided from one target point on the left of the interior quadrant to the right side of the interior quadrant in a partially deployed configuration. The picture sequence of Fig. VI.20 shows how the proximal segment (partially inserted into the resectoscope) automatically complies its motion to the tubular constraint while allowing the primary task to be accomplished. During the motion, the θ_1 degree-of-freedom is autonomously adjusted in order not to violate the tubular constraint while the δ_1 degree-of-freedom is freely exploited to accomplish the primary task.

Constrained Targeting Accuracy In order to evaluate constrained targeting accuracy, the operator was asked to insert a $\varnothing 0.55$ mm laser into a $\varnothing 2.4$ mm, $\varnothing 1.62$ mm, and $\varnothing 0.9$ mm tubes respectively. The user was able to target all tubes. The clearance between the outer diameter of the laser fiber and inner diameter of the smallest tube gives a constrained targeting accuracy of better than 0.35 mm.

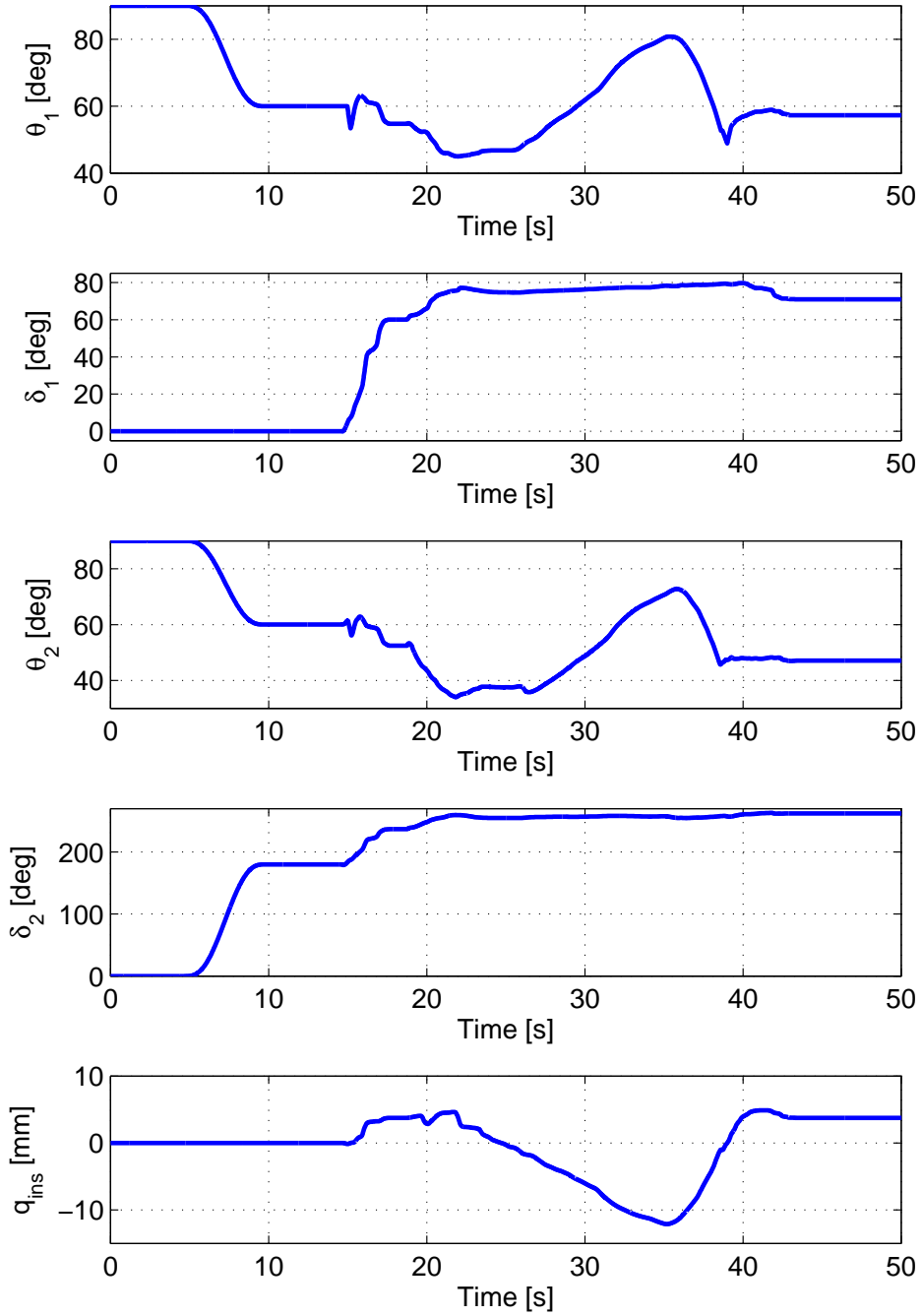


Figure VI.18: Constrained motion experiment. The surgical slave is commanded to retract into the resectoscope ($q_{ins} < 0$). The virtual fixture law automatically straightens the continuum robot (θ_1 and θ_2 grow).

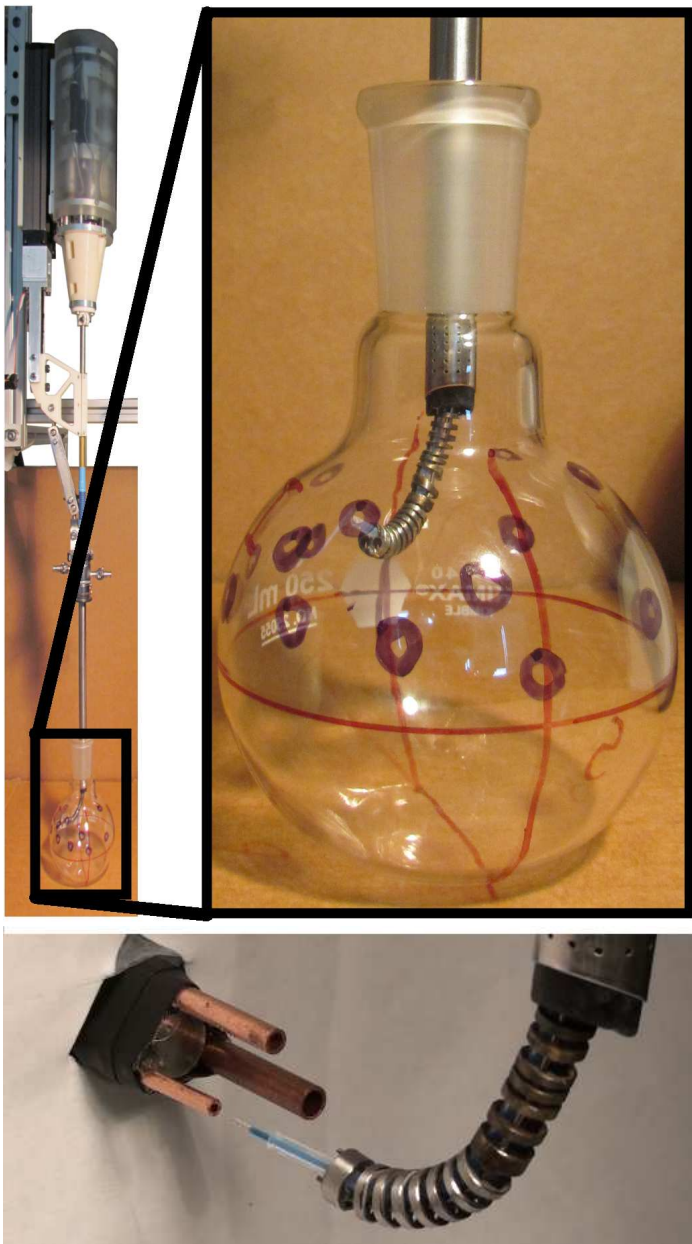


Figure VI.19: The experimental setup consists of a 7-axes actuation unit, a urologic resectoscope, a 2-segment continuum robot, a 250 ml beaker, and three tubes with various diameters. The beaker approximates the size of an average-sized bladder when inflated while the tubes were used for testing targeting accuracy.

Coverage In order to evaluate the ability of the surgical slave to reach the whole urinary bladder additional telemanipulation experiments were conducted. The robot was deployed inside the glass bladder model and guided to *sweep* the posterior and the interior quadrants. A picture sequence is shown in Fig. VI.21. From left to right, each frame shows the continuum manipulator covering progressively the posterior and interior quadrant. The posterior quadrant is reached with the robot fully deployed and the insertion stage at its maximum insertion depth. In this case both segments are free to move in any direction and both primary and secondary tasks can be accomplished.

Conclusions

The preliminary results demonstrated the ability of the proposed robot to complete critical surgical tasks required during TURBT. These tasks include: surveillance, energy delivery, biopsy, and resection of cancerous areas. At the current state, the main limitation of the robot is the on-board 1.2 mm fiberscope prototype with embedded light source. The limited cross section requires a tradeoff between fibers used for visualization and fibers used for illumination. Although, the fiberscope was useful to examine tissue and maneuver the end-effector locally on the tissue, its short focal distance does not allow one to use it for gross motion. Energy delivery to the superior, anterior, and posterior quadrants was successfully carried out. Figure 5 shows pictures of some of the targeted area. The bovine bladder was cut after the experiments and the targeted areas examined. The slave manipulator allows for the delivery of a standard 1.8 mm biopsy forceps. The biopsy forceps allows for grasping and removing large areas of tissue using the laser. By pivoting about the contact point, it is possible to ablate larger areas than using the forceps only. Figure VI.17 shows the slave manipulator grasping the resected tissue outside the bovine bladder.



Figure VI.20: Image sequence of constrained targeting in the interior quadrant. The first continuum segment is partially retracted inside the resectoscope. Its motion is autonomously limited by the configuration space virtual fixture while allowing for the completion of the task.

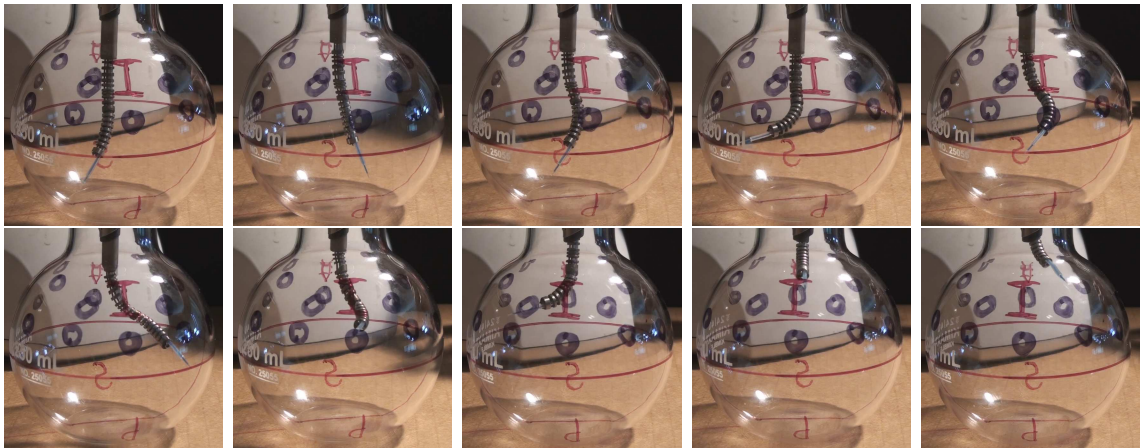


Figure VI.21: Picture sequence of bladder coverage. The slave manipulator, under telemansipulation control, is guided to cover progressively the posterior and interior quadrants. The manipulator goes from a completely deployed configuration to a completely folded configuration into the urologic resectoscope.

The tissue sample was pulled out along with the slave manipulator at the end of the procedure. The size of the resected tissue is larger than conventional samples that can be obtained with biopsy forceps alone. The size of the tissue is compared next to a one dime of 18 mm. Future designs will improve dexterity in the inferior quadrant by adding a wrist at the end-effector. Additional research will focus on depth controlled resection, enforcement of safety telemansipulation zones (virtual fixtures/active constraints), and on detailed clinical evaluation of the benefits of robotic assistance for transurethral resection and surveillance.

A Telesurgical System for Transnasal Microsurgery of the Throat

Introduction

Minimally invasive surgery (MIS) of the throat demands innovative devices capable to harmoniously conform to the narrow and elongated anatomy of the upper airways. The benefits of MIS of the throat, however, come at a price of limited access, visualization, and depth perception, lack of tool dexterity, reduced precision, and amplified tremor due to elongated surgical tools [42]. To improve tool dexterity, researchers and surgeons investigated the use of robotic assistance. In [97], the authors presented a dual-arm robotic system that fits conventional laryngoscopes. In [40, 58, 109], the authors investigated the use of the daVinci surgical system (Intuitive Surgical, Sunnyvale, CA) to treat tumors in the upper airways. Recently, in [82], the authors presented a highly-articulated flexible robot with embedded vision and tool-delivery channels.

All the aforementioned robotic systems access the larynx trans-orally using either a retractor, a laryngoscope, or a curved guiding channel. These devices limit the robot's workspace, prevent optimal triangulation, and are associated with complications such as tongue edema, nerve injuries, and sore throat [40, 69, 58]. Furthermore, TO access imposes the use of general anesthesia during any surgical procedure, thus, increasing the risk of additional complications (i.e. delirium and cardiac infarcts [58]) and preventing some patients from undergoing surgery [21, 91]. The mandatory use of an operating room (OR) also prevents cost reduction for several simple, highly recurrent procedures that could be performed in-clinic under local anesthesia in favor of lower cost and patient's comfort.

In this section, we propose a robotic system (Fig. VI.22) for trans-nasal (TN)

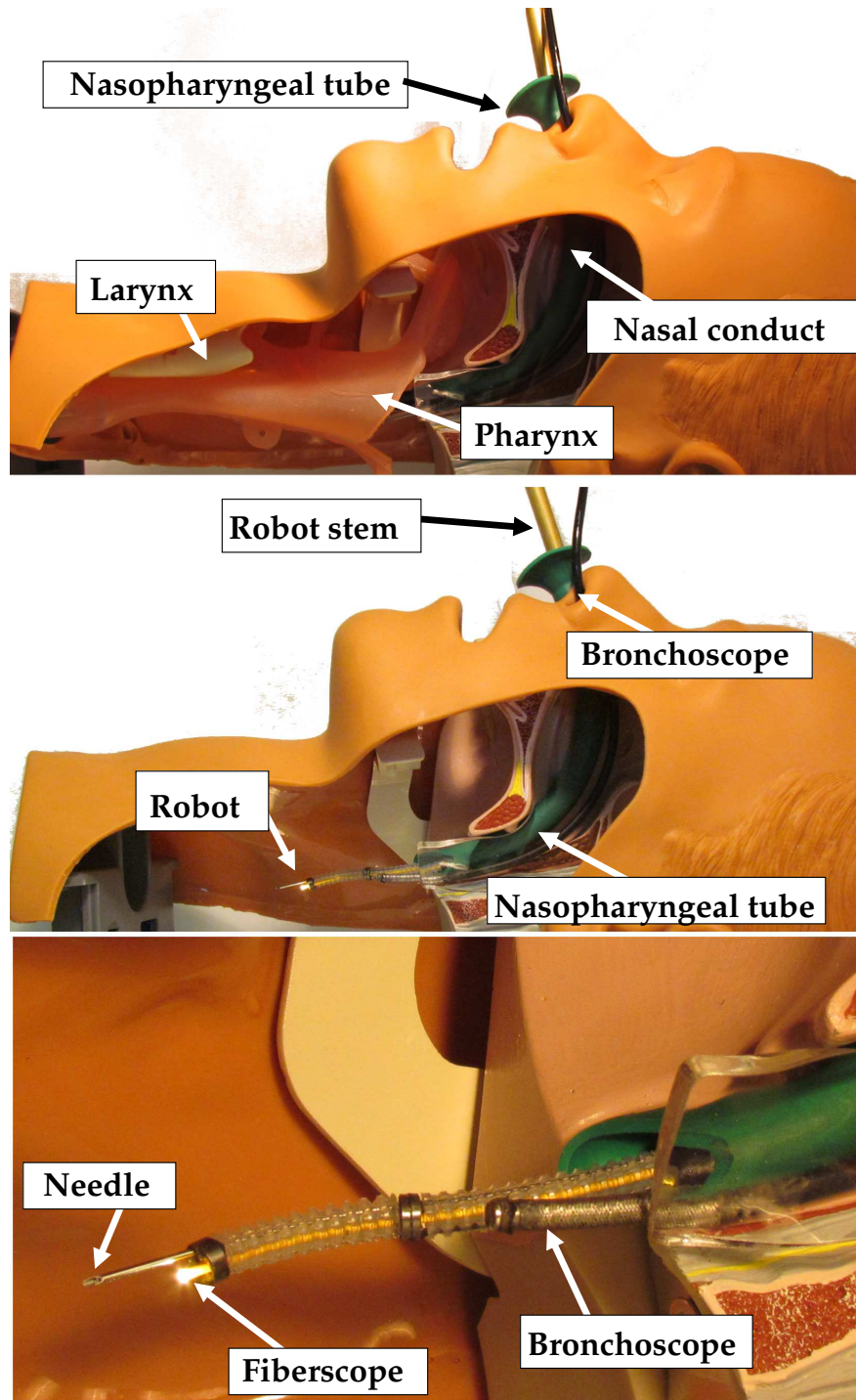


Figure VI.22: Top: overview of the anatomy. Middle: The flexible robotic stem and a 4 mm bronchoscope are deployed to the larynx through the nasal cavity. Bottom: The robotic end-effector carries a needle for vocal fold repair and a 1.2mm fiberscope.

access to the throat. This approach eliminates most of the shortcomings of TO surgery. To the best of the authors' knowledge, the earliest work on robotic TN access was presented in [47] where the authors proposed a flexible wire-actuated end-effector. The present work builds upon this idea and proposes a complete solution to fundamental challenges such as safe and rapid access into the anatomy [4], enhanced intra-corporal dexterity [97], force feedback [117], tool delivery, and visualization.

The contribution of this section is in presenting the design, the control architecture, and a pilot evaluation of a dexterous tele-operated end-effector for office-based TN micro-surgery of the throat. The end-effector is composed of both active and passive multi-backbone continuum segments. We propose the modified kinematics and actuation compensation required to control the passive and active segments. A hybrid motion/compliance controller assists the surgeon during the insertion phase by actively complying to the unknown environment while allowing the operator to control the insertion depth and speed. The robot is evaluated in an anatomically correct model and a mockup vocal nerve paralysis treatment is performed. We believe that this system will enable low-cost office-based treatment of common head and neck surgical procedures.

Clinical Motivation

Trans-oral MIS of the throat is preferred over open surgery because it preserves the integrity of the laryngeal framework, eliminates visible scars, promotes faster recovery, and in many cases overcomes the need for tracheostomy. However, these advantages come at a price of limited access, visualization, and depth perception, lack of tool distal dexterity, amplified tremor due to manual elongated surgical tools, limited precision, and a requirement for advanced hand-eye coordination.

The use of the endotracheal tube and the laryngoscope has also been associated

with several complications such as airway stenosis, coughing, gagging, laryngospasm, hypertension, and tachycardia [40, 69, 58] and require the mandatory use of general anesthesia. General anesthesia is associated with additional complications such as postoperative delirium, myocardial depression, and temporary renal dysfunction. Additional attention is required for patients with heart, circulatory, or nervous system problems and elderly patients [21, 91] that often are not considered safe candidates for the surgical procedure.

The mandatory use of the OR prevents cost reduction for some simple and recurrent head and neck procedures. For example, laryngeal nerve paralysis, which is the injury of one or both of the nerves that allow the vocal fold to close, is a common complication of the use of organ suspension devices. As a result, the patient has difficulty to speak and swallow. The most common treatment is the injection of collagen (Fig. VI.23) into the paralyzed side of the larynx. The treatment, however, is only temporary since the collagen is absorbed in about 6 to 12 months and the patient needs to undergo surgery repeatedly. The injection can be achieved either through a laryngoscope or percutaneously. The former approach allows precise targeting of the paralyzed vocal fold since the surgeon is able to guide the needle tip under a microscope. The latter approach requires the vocal fold to be punctured through the side of the neck and the cartilages making needle targeting difficult and imprecise (and sometimes requiring multiple needle punctures in order to reach the target). The reimbursement cost of vocal nerve paralysis treatment via injection of collagen in the OR is estimated as \$2,505 as opposed to \$496 when using an office-based percutaneous approach [12].

Robot-assisted TN treatment of vocal fold paralysis would benefit: 1) the surgeon (providing sub-millimetric precision, enhanced visualization, patient's feedback, and

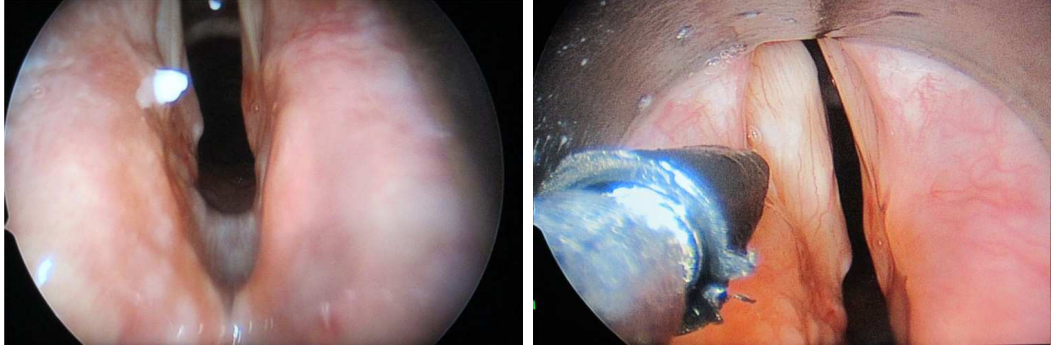


Figure VI.23: Procedure overview for the treatment of vocal fold nerve paralysis. Collagen is injected into the paralyzed side of the vocal fold in order to close the gap between the vocal fold lips and allows for proper speech and swallowing.

an ergonomic console), 2) the patient (leading to fewer complications, faster recovery time, and more comfortable office-base environment), 3) the healthcare system (allowing higher throughput while reducing cost). This approach is consistent with conventional practice of TN deployment of fiber nasopharyngeal laryngoscopes, local anesthesia, and vaso-constricting agents that reduce patient's discomfort and risk of bleeding.

The Telerobotic System

The robotic system is composed of a dexterous 5 DoF continuum manipulator (Fig VI.22), an actuation unit (Fig. VI.24), a Sensable Phantom Omni, an Ascension 3D Guidance trakSTAR 2 with flat *metal immune* transmitter, a $\varnothing 4$ mm bronchoscope, and a $\varnothing 1.2$ mm fiberscope (Fig. VI.22). The actuation unit has seven controlled axes (Fig. VI.24) of which six control the two continuum segments and one controls the insertion depth into the nasopharyngeal tube (Fig. VI.22). Additional sensors include load cells for monitoring actuation forces and potentiometers for redundant positioning information.

The system can operate in both *passive* and *semi-active* modes. The passive

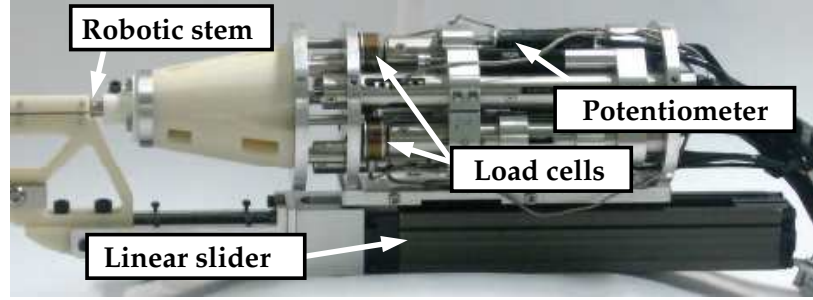


Figure VI.24: The actuation unit consists of a linear stage for stem insertion, six pistons for the continuum segments actuation, potentiometers for homing and redundant positioning information, and load cells for force sensing and compliant insertion.

mode is based on a standard telemanipulation architecture where the operator guides the end-effector via a master manipulator (the Phantom Omni) while observing endoscopic images provided by the *in-hand* fiberscope. The semi-active mode is used to reach the surgical site. During the semi-active mode the surgeon commands the insertion depth while the continuum manipulator autonomously complies with the anatomy using a variation of the compliance motion controller first presented by Goldman et al. [4].

The Surgical Slave

The surgical slave is composed of a flexible passive stem and two active segments (Fig. VI.25). Each $\varnothing 5$ mm segment is composed of four super-elastic NiTi backbones (one central and three secondary ones) that provide two DoF for bending in any direction. An additional DoF is provided by the linear stage (Fig. VI.24), which controls the insertion of the base of continuum arm. The robotic arm has three $\varnothing 1.8$ mm lumens that allow for the deployment of surgical instruments. In order to compensate for the unknown shape of the passive segment constrained by the nasopharyngeal tube (Fig. VI.22), a $\varnothing 0.9$ mm 6 DoF electro-magnetic sensor is attached to the base of the two-segment continuum robot. The metal immune flat

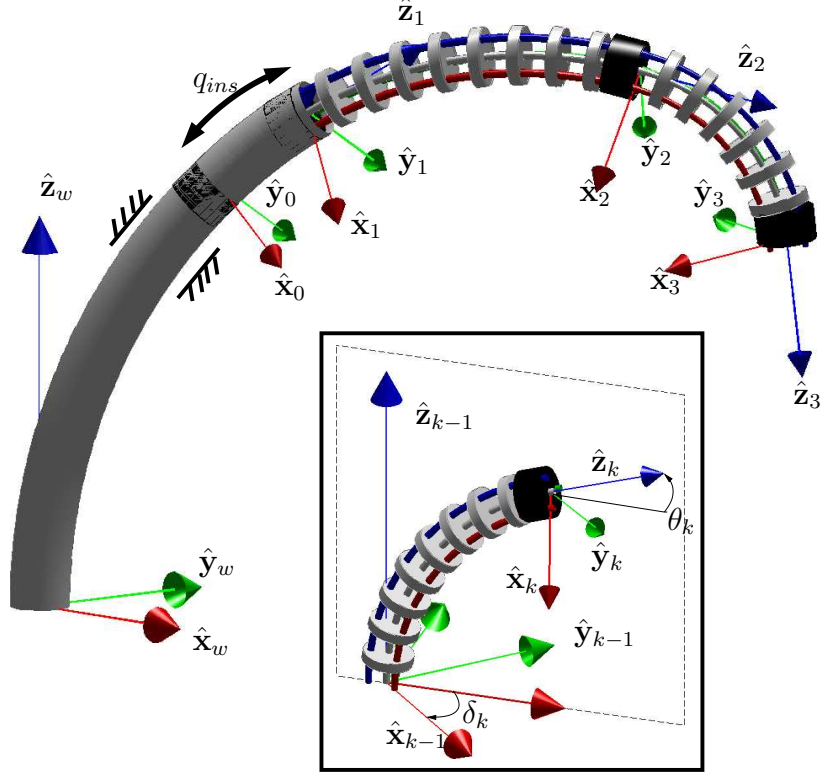


Figure VI.25: Kinematics nomenclature used in this section.

transmitter makes the system robust to surrounding metal and easy to place under the patient's head.

Five coordinate systems (Fig. VI.25) are defined to describe the direct kinematics of the surgical slave: the world frame B_w defined by vectors $\{\hat{x}_w, \hat{y}_w, \hat{z}_w\}$, the frame attached to the exit of the nasopharyngeal tube B_0 defined by vectors $\{\hat{x}_0, \hat{y}_0, \hat{z}_0\}$, the base frame of the actively bending continuum robot B_1 defined by vectors $\{\hat{x}_1, \hat{y}_1, \hat{z}_1\}$, the base frame of the second segment B_2 defined by vectors $\{\hat{x}_2, \hat{y}_2, \hat{z}_2\}$, and the end effector frame B_3 defined by vectors $\{\hat{x}_3, \hat{y}_3, \hat{z}_3\}$.

The position and orientation of end-effector frame B_3 in B_0 may be described by the following augmented configuration space vector:

$$\Psi = \begin{bmatrix} \theta_1 & \delta_1 & q_{ins} & \theta_2 & \delta_2 & \theta_3 & \delta_3 \end{bmatrix}^T \quad (\text{VI.43})$$

where, q_{ins} is the insertion depth and angles θ_k and δ_k are defined similarly for the passive segment ($k = 1$) and active segments ($k = 2, 3$) as depicted in Fig. VI.25. Using Ψ , the position and orientation of frame B_3 in B_0 is given by:

$${}^0\mathbf{p}_3 = {}^0\mathbf{p}_1 + {}^0\mathbf{R}_1 ({}^1\mathbf{p}_2 + {}^1\mathbf{R}_2 {}^2\mathbf{p}_3) \quad (\text{VI.44})$$

$${}^0\mathbf{R}_3 = {}^0\mathbf{R}_1 {}^1\mathbf{R}_2 {}^2\mathbf{R}_3 \quad (\text{VI.45})$$

where

$${}^{k-1}\mathbf{p}_k = \frac{L_k}{\Theta_k} \begin{bmatrix} \cos(\delta_k) (\sin \theta_k - 1) \\ -\sin(\delta_k) (\sin \theta_k - 1) \\ -\cos \theta_k \end{bmatrix} \quad (\text{VI.46})$$

$${}^{k-1}\mathbf{R}_k = \text{Rot}(-\delta_k, \hat{\mathbf{z}}) \text{Rot}(-\Theta_k, \hat{\mathbf{y}}) \text{Rot}(\delta_k, \hat{\mathbf{z}}). \quad (\text{VI.47})$$

with: $L_1 = q_{ins}$, L_2 and L_3 being the lengths of the first and second active segments, $\Theta_k = \theta_k - \frac{\pi}{2}$, and operator $\text{Rot}(a, b)$ being the rotation matrix about axis b by angle a . Note that, since the first segment is passive, θ_1 and δ_1 are not directly controllable. In the remainder of this work we assume that θ_1 and δ_1 and the origin of frame B_1 are measured by a magnetic tracker (the position and the orientation frame B_1 is known). Hence, the forward kinematics is easily calculated using θ_1 and δ_1 and B_1 along with joint values $q_i, i = 1..6$.

The configuration space vector Ψ relates to the joint space vector as

$$\mathbf{q}(\Psi) = \left[q_{ins} \quad \mathbf{q}_2(\Psi)^T \quad \mathbf{q}_3(\Psi)^T \right]^T \quad (\text{VI.48})$$

where \mathbf{q}_2 and \mathbf{q}_3 are the amount of pushing-pulling on the secondary backbones of

active segments 2 and 3 [96]. In particular:

$$\mathbf{q}_2 = r \begin{bmatrix} \Theta_1 \cos(\delta_2) - \Theta_0 \cos(\delta_0) \\ \Theta_1 \cos(\delta_2 + \beta) - \Theta_0 \cos(\delta_0 + \beta) \\ \Theta_1 \cos(\delta_2 + 2\beta) - \Theta_0 \cos(\delta_0 + 2\beta) \end{bmatrix} \quad (\text{VI.49})$$

$$\mathbf{q}_3 = r\Theta_2 \begin{bmatrix} \cos(\delta_2) \\ \cos(\delta_2 + \beta) \\ \cos(\delta_2 + 2\beta) \end{bmatrix} \quad (\text{VI.50})$$

$$\theta_0 = \pi/2 - \text{atan2}\left(\sqrt{R_{13}^2 + R_{23}^2}, R_{33}\right) \quad (\text{VI.51})$$

$$\delta_0 = -\text{atan2}(R_{23}, R_{13}) \quad (\text{VI.52})$$

where $\beta = 2\pi/3$, r is the radial distance of the secondary backbone from the center of the base disk, $\Theta_0 = \theta_0 - \pi/2$, $\Theta_1 = \theta_1 - \pi/2$, and R_{ij} is element ij of rotation matrix ${}^w\mathbf{R}_1$ obtained from the magnetic sensor placed at the base of first active segment. Note that angles θ_0 and δ_0 allows us to work in local frame B_0 decoupling the kinematics of the distal active and passive segments from shape variations of the passive stem.

Control Architecture

Figure VI.27 shows the complete control architecture of our telesurgical system. Control inputs and electro-magnetic orientation information are both received at 125 Hz over the Local Area Network while encoder and actuation force signals are sampled at 1 kHz and 5 kHz respectively. The conventional hybrid motion/compliance control is adopted in which two separate controllers independently provide motion and compliance control commands. However, the hybrid motion/compliance control approach

is adapted to our continuum robot by decomposing the control task in configuration space rather than in task space. The projection matrices Ω and $\bar{\Omega}$ ensure that the control commands are projected into sub-spaces for motion and compliance control. Joint-level commands to the actuators are then obtained through the inverse position of the continuum manipulator and the required model-based actuation compensation. The following details describe the specific implementation of our approach.

Compliance Control Compliance Motion Control (CMC), as first presented in [4], allows multi-backbone continuum robots with intrinsic actuation sensing to autonomously steer away from constraints without *a priori* knowledge of the contact nor the external wrench. In the following, the CMC control law proposed in [4] is modified in order to use only information about actuation forces sensed on the most distal segment. This control law allows the robot to actively comply to the circle-shaped nasopharyngeal tube. If actuation force information on the second active segment is available, the actuation force error is defined as:

$$\boldsymbol{\tau}_{e_3} = \boldsymbol{\tau}_3 - \bar{\boldsymbol{\tau}}_3 \quad (\text{VI.53})$$

where $\boldsymbol{\tau}_3$ are the expected actuation forces [95] and $\bar{\boldsymbol{\tau}}_3$ are the sensed actuation forces acting on the third segment respectively. We now project the actuation force error, $\boldsymbol{\tau}_{e_3}$, into the configuration space of the distal segment obtaining the generalized force error [4]:

$$\mathbf{f}_{e_3} = \mathbf{J}_{q\psi}^T \boldsymbol{\tau}_{e_3} \quad (\text{VI.54})$$

where $\mathbf{J}_{q\psi}$ is the Jacobian matrix that relates the configuration space velocities to the joint space velocities [96].

Hence, the desired configuration space velocity vector that steers the robot away

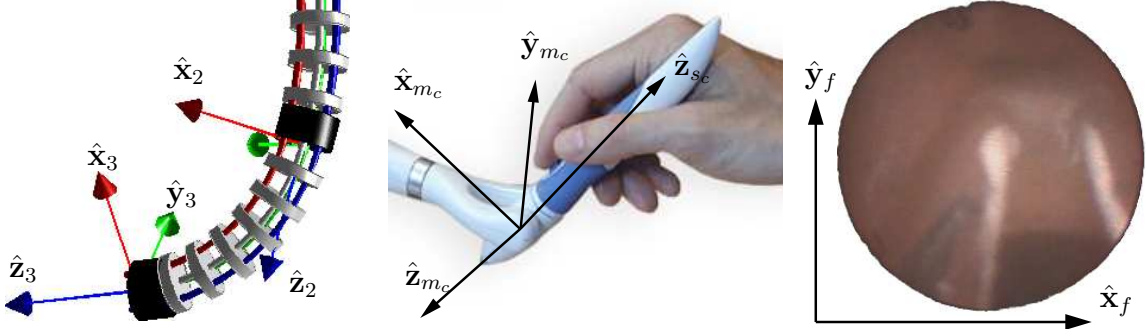


Figure VI.26: Telemanipulation mapping between the robot's end-effector, the master manipulator and the fiberscope view.

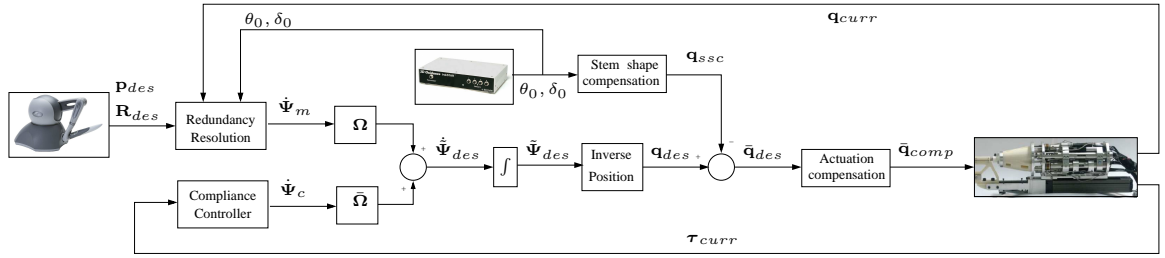


Figure VI.27: Control architecture of the telesurgical system.

from the unknown contact is:

$$\dot{\Psi}_c = \Phi \mathbf{K}_{\psi_2}^{-1} \mathbf{f}_{e_3} \quad (\text{VI.55})$$

where \mathbf{K}_{ψ_2} is the configuration space stiffness matrix of the second segment [4] and

$$\Phi = \begin{bmatrix} 0 & 1 & 0 & 1 & 0 \\ 0 & 0 & 1 & 0 & 1 \end{bmatrix}^T. \quad (\text{VI.56})$$

Note that, (VI.55) is a simplification of the algorithm presented in [4] for multiple segments. In the case of TN insertion, assuming an overall circular shape of the entire manipulator, both segments need to bend by the same angle in order pass through the nasopharyngeal tube. The efficacy of this control law is demonstrated in Section VI.

Motion Control Telemanipulation of the surgical slave is achieved by defining a mapping between the movement of the master’s end-effector and the desired motion directions in the fiberscope image space as shown in Fig. VI.26. Because of the difficulties in accurately controlling the two active segments and the long unknown-shaped passive stem, it was chosen to map the movement of the Phantom Omni to only 3 DoF of the most distal segment: 1 DoF of insertion and 2 DoF of bending (as in a conventional bronchoscope). Therefore, once the robot is inserted, the first segment is bent ($\theta_1 = 60^\circ$) in the direction of the vocal folds ($\delta_1 = 0^\circ$). The user advances the robot in the direction of $\hat{\mathbf{z}}_f$ (insertion) and tilts about axes $\hat{\mathbf{x}}_f$ and $\hat{\mathbf{y}}_f$ in fiberscope-attached frame. The fiberscope-attached frame is related to B_3 by a known fixed rotation. This movement in image space is first mapped to the movement of the master stylus $\{\hat{\mathbf{x}}_{m_s}, \hat{\mathbf{y}}_{m_s}, \hat{\mathbf{z}}_{m_s}\}$ and then to the movement of the distal segment frame $\{\hat{\mathbf{x}}_3, \hat{\mathbf{y}}_3, \hat{\mathbf{z}}_3\}$ (Fig. VI.26).

The desired position and orientation of distal segment are given as follows:

$${}^2\mathbf{p}_{3,des} = {}^2\mathbf{p}_{3,curr} + {}^2\mathbf{R}_{3,curr}\mathbf{p}_{des,master} \quad (\text{VI.57})$$

$${}^2\mathbf{R}_{3,des} = {}^2\mathbf{R}_{3,curr}\mathbf{R}^T\mathbf{R}_{des,master}\mathbf{R} \quad (\text{VI.58})$$

where matrix \mathbf{R} defines the transformation between the camera-attached frame and the master’s stylus (Fig. VI.26). Once the desired pose is computed, the desired twist \mathbf{t}_{des} is computed as described in [6] and the desired configuration space velocities are obtained as follows:

$$\begin{bmatrix} \dot{q}_{ins} \\ \dot{\theta}_2 \\ \dot{\delta}_2 \end{bmatrix} = (\boldsymbol{\Gamma}\boldsymbol{\Sigma}\mathbf{J}_2)^{-1} \boldsymbol{\Gamma}\boldsymbol{\Sigma}\mathbf{t}_{des}. \quad (\text{VI.59})$$

In (VI.59), \mathbf{J}_2 is the Jacobian matrix of the distal segment [115]:

$$\mathbf{J}_2 = \begin{bmatrix} 0 & L_2 c_{\delta_2} \frac{\Theta_2 c_{\theta_2} - s_{\theta_2} + 1}{\Theta_2^2} & -\frac{L_2 s_{\delta_2} (s_{\theta_2} - 1)}{\Theta_2} \\ 0 & -L_2 s_{\delta_2} \frac{\Theta_2 c_{\theta_2} - s_{\theta_2} + 1}{\Theta_2^2} & -\frac{L_2 c_{\delta_2} (s_{\theta_2} - 1)}{\Theta_2} \\ 1 & L_2 \frac{\Theta_2 s_{\theta_2} + c_{\theta_2}}{\Theta_2^2} & 0 \\ 0 & -s_{\delta_2} & c_{\delta_2} c_{\theta_2} \\ 0 & -c_{\delta_2} & -s_{\delta_2} c_{\theta_2} \\ 0 & 0 & -1 + s_{\theta_2} \end{bmatrix}, \quad (\text{VI.60})$$

matrix Σ transforms the desired twist into gripper frame

$$\Sigma = \begin{bmatrix} {}^2\mathbf{R}_{3,curr}^T & \mathbf{0} \\ \mathbf{0} & {}^2\mathbf{R}_{3,curr}^T \end{bmatrix} \quad (\text{VI.61})$$

and selection matrix Γ defines a desired subtask

$$\Gamma = \begin{bmatrix} 0 & 0 & 1 & 0 & 0 & 0 \\ 0 & 0 & 0 & 1 & 0 & 0 \\ 0 & 0 & 0 & 0 & 1 & 0 \end{bmatrix}. \quad (\text{VI.62})$$

In this case, matrix Γ selects the third, fourth, and fifth rows of the Jacobian matrix allowing to control only 3 DoF: translation along \mathbf{z}_3 and tilting about $\mathbf{x}_3, \mathbf{y}_3$. As a result, we only invert a square 3×3 matrix and control only the desired DoFs.

Finally, the augmented desired configuration space velocity vector is given as follows:

$$\dot{\Psi}_m = \begin{bmatrix} \dot{q}_{ins} & 0 & 0 & \dot{\theta}_2 & \dot{\delta}_2 \end{bmatrix}^T \quad (\text{VI.63})$$

Projection Matrices Depending on the operational mode (insertion or telemanipulation) the configuration space Ψ can be partitioned in directions in which motion

needs to be controlled, T , and directions in which compliance needs to be controlled, C . Similar to wrench and twist systems in the hybrid motion/force control formulation, [33], these two spaces, T and C , are orthogonal and their sum returns the configuration space Ψ ($T \oplus C = \Psi$). It is, therefore, possible to construct two projection matrices, Ω and $\bar{\Omega}$, that project desired configuration space velocities into the motion space T and into the compliance space C :

$$\Omega = \mathbf{T} (\mathbf{T}^T \mathbf{T})^\dagger \mathbf{T}^T \quad (\text{VI.64})$$

$$\bar{\Omega} = \mathbf{I} - \Omega \quad (\text{VI.65})$$

where \mathbf{T} is a $5 \times m$ matrix in which its columns define a base of T and superscript \dagger indicate the pseudo-inverse. For example, in the case of compliant insertion, configuration variables q_{ins} , δ_2 , and δ_3 will be position-controlled while variables θ_2 , and θ_3 will be compliance-controlled allowing the segment to adapt to the shape of the nasal conduit. Hence, matrix \mathbf{T} is defined as:

$$\mathbf{T} = \begin{bmatrix} 1 & 0 & 0 & 0 & 0 \\ 0 & 0 & 1 & 0 & 0 \\ 0 & 0 & 0 & 0 & 1 \end{bmatrix}^T \quad (\text{VI.66})$$

Actuation Compensation The desired joint variables are computed using the theoretical kinematics model and the model-based actuation compensation of Xu et al. [114] is used.

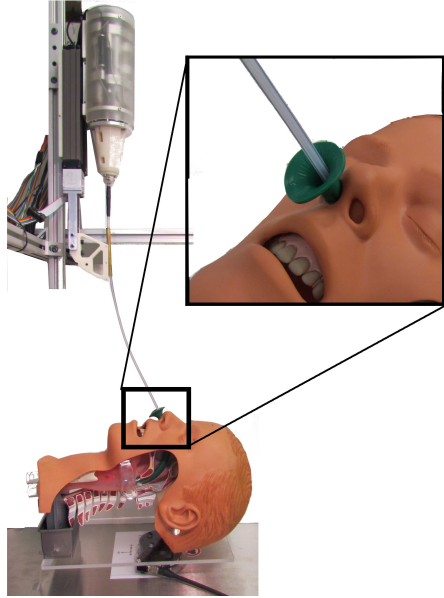


Figure VI.28: The experimental setup consists of a $\varnothing 5$ mm continuum robot with flexible actuation lines, a 34Fr nasopharyngeal tube, a Nasco AMBU intubation trainer, an Ascension Technology trakSTAR 2 with flat transmitter, one $\varnothing 0.9$ mm magnetic coil, and an ATI Gamma force/torque sensor.

Experimental Evaluation

Rapid Deployment

Rapid deployment of the surgical end-effector was evaluated with the experimental setup shown in Fig. VI.28. The setup consists of a $\varnothing 5$ mm continuum robot with flexible actuation lines, a 34Fr nasopharyngeal tube, a Nasco AMBU intubation trainer, an Ascension Technology trakSTAR 2 with flat transmitter, one $\varnothing 0.9$ mm electro-magnetic sensor placed at the base disk of the continuum robot, and an ATI Gamma force/torque sensor. The Nasco trainer provides a realistic anatomical model of the upper airways with a clear side to allow for inspection. The nasopharyngeal tube is inserted through the right nostril.

Ten insertions were performed and insertion time and forces exerted on the manikin were recorded. The robot was guided to straight configuration prior to each

experiment and the stem was lubricated in order to reduce friction as shown in the Multimedia Extension.

The average insertion time to reach the pharynx was 5.87 s (range 4.32 s - 11.05 s). The start and final times of the insertion were manually extracted for each trial from the time history of the forces exerted on the ATI Gamma sensor as shown in Fig. VI.29. The average maximum insertion forces in the x, y, and z directions were 0.855 N (range 0.648 N - 1.219 N), 2.685 N (range 2.407 N - 3.144 N), and 4.551 N (range 3.743 N - 5.396 N) respectively.

Targeting in Deep Surgical Sites

In order to evaluate the ability to perform a teleoperated injection of the vocal folds, the robotic end-effector was inserted into the Nasco trainer and six predetermined points on the true vocal folds were targeted.

The surgeon was given the onboard fiberscope view and was asked to guide the robot using a Phantom Omni as shown in Fig. VI.30. The end-effector needle was directed to touch three points on the right fold and three point on the left fold as shown in Fig. VI.31. The surgeon had no previous experience using our telemanipulation system. The experiment was conducted after only a 15-minute training where the surgeon was introduced to the instrumentation and the telemanipulation mapping.

As shown in Fig. VI.31 and in the Multimedia Extension, the surgeon was able to direct the needle toward all the predetermined points, reaching the targets without prolonged readjustments of the robot end-effector's orientation. The most challenging points were the bottom right and left areas of the true vocal fold because of the unnatural high stiffness of the epiglottis. However, by inserting both the needle and the fiber further and re-orienting the robot both targets were successfully reached.

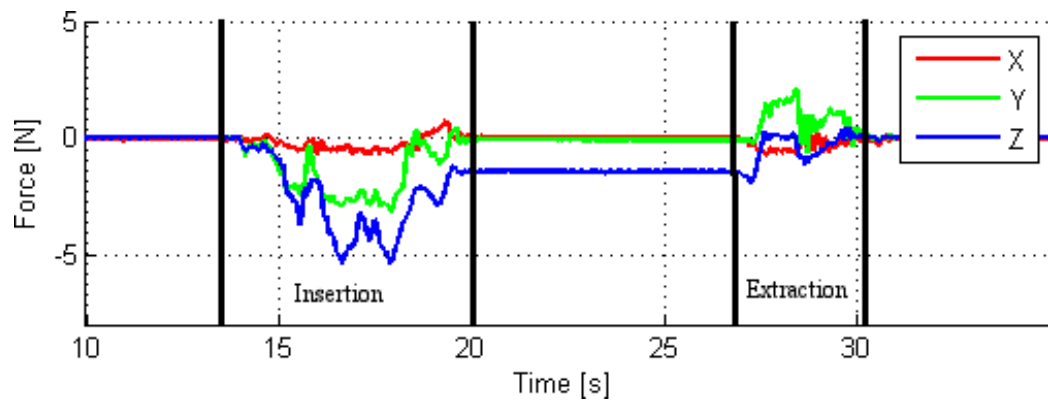


Figure VI.29: Experiment #1's time history of the insertion and extraction forces exerted on the ATI Gamma sensor.

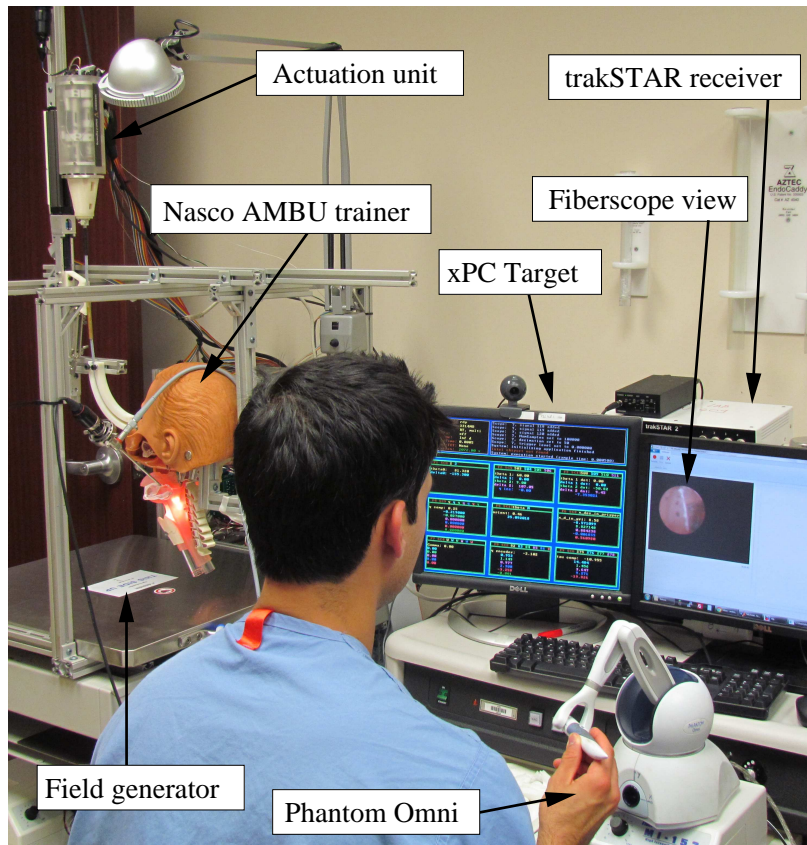


Figure VI.30: Experimental setup for the targeting evaluation. The surgeons guided the surgical slave using a Sensable Phantom Omni and the image provided by the onboard fiberscope.

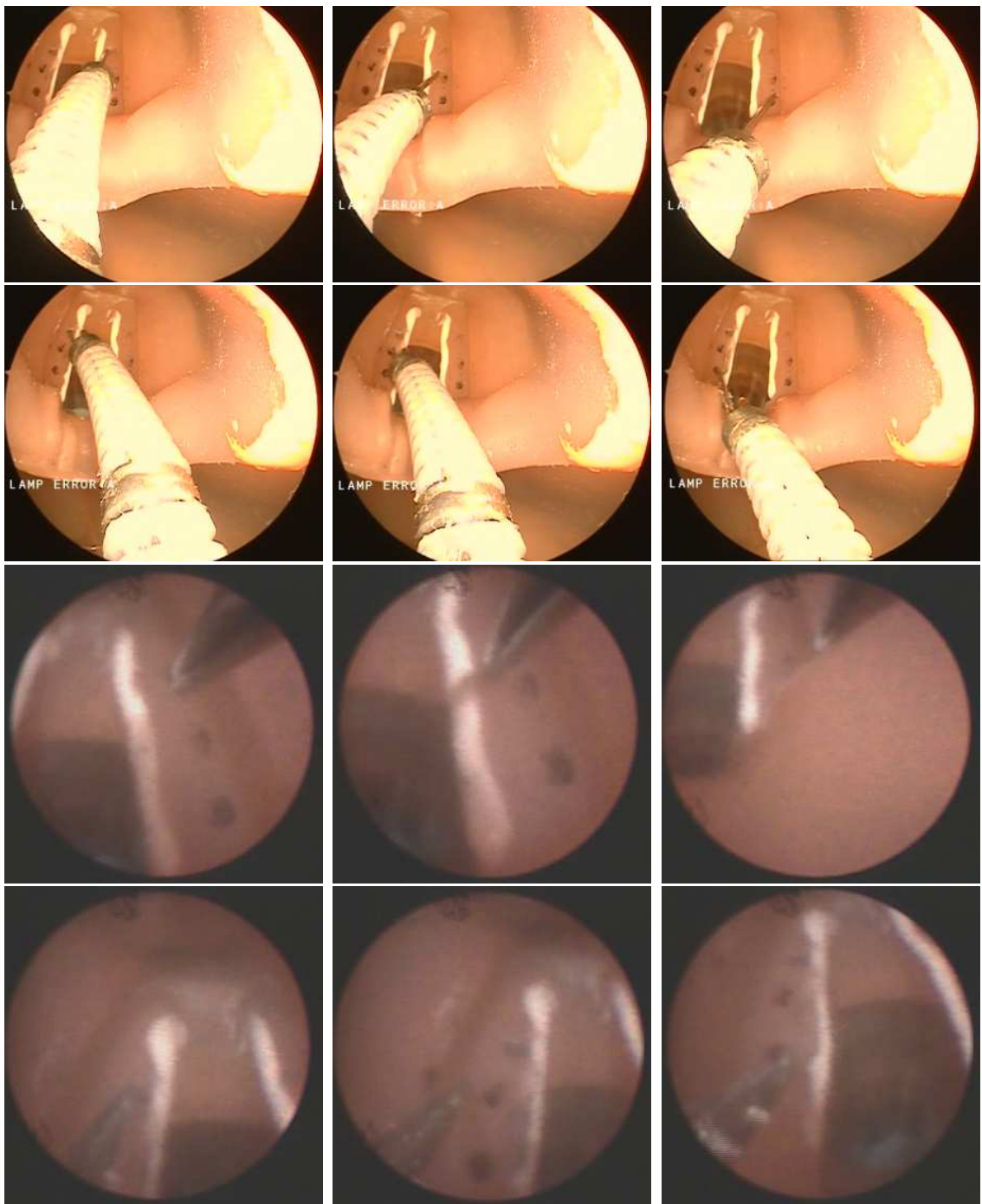


Figure VI.31: Picture sequence of the surgeon targeting pre-determined points on the true vocal folds using 2D vision through the onboard fiberscope. Top row: view from the additional HD endoscope. Bottom row: view from the onboard fiberscope.

Cadaveric Evaluation

This section presents a cadaveric evaluation of the insertion procedure and feasibility of reaching the voice box in human anatomy. The experimental setup (Figure VI.31) consists of the continuum robot, a female cadaver, a 34 Fr nasopharyngeal tube, the trakSTAR 2 flat transmitter, a \varnothing 4 mm bronchoscope, a \varnothing 1.2 mm on-board fiberscope, and a visualization tower. The control architecture run at 1 kHz while the commands from the master manipulator are sent at 125 Hz using UDP over LAN. Five cadavers were obtained through the Vanderbilt Anatomical Donation Program, 3 females and 2 males. After the inspection of the nasal conduct, pharynx, and larynx, only one cadaver was selected for the study. The other four were discarded because the internal organs were not well preserved or the nasal conduct was obstructed. The cadavers upper airways were then irrigated using water and all debris was then removed using a suction device. The nasal conduit was sequentially expanded using different sizes of a nasopharyngeal rubber tube up to 34 Fr. The continuum robot was then inserted through the nasopharyngeal tube after proper lubrication of the teflon stem. Under compliant motion control, the continuum manipulator easily reached the end of the nasopharyngeal tube (Figure VI.32) and entered the larynx right in front of the epiglottis. The controller was then switched to telemanipulation control and the tip of the continuum manipulator was steered on the left. Manual insertion allowed the robot to pass the epiglottis. Using visual information through the bronchoscope, the end-effector was first directed toward the voice box and then inserted further to reach the vocal folds. Figure VI.33 shows the voice box from the on-board fiberscope. Independent insertion of the scope allowed to examine the vocal folds. A flexible needle was then deployed through the remaining working channel and the left fold was punctured as shown in Figure VI.34



Figure VI.32: Experimental setup of the cadaveric evaluation of insertion and targeting of the voice box: 1) robots actuation unit, 2) cadavers head, 3) traksSTAR 2 flat transmitter, 4) bronchoscope, 5) visualization station, 6) surgeon.

Discussion

The pilot experiments described in this section demonstrate safe trans-nasal access to the throat, the ability to reach the voice box, and the feasibility of some micro-surgical procedures. Future experiments will focus on demonstrating key microsurgical procedures in cadavers and other commonly used anatomical models in head and neck surgery.

The flexible robotic effector was easily inserted through the nasal cavity using a hybrid motion/compliance controller with an average insertion time of 5.87 s (range 4.32 s - 11.05 s). Following proper lubrication of the nasopharyngeal tube, minimal forces are exerted onto the anatomy allowing safe and conformable deployment of the surgical robot. The compliance insertion algorithm originally proposed in [4] and applied in this paper to reach the voice box through the nasal cavity, demonstrates the need for intelligent surgical slaves able to assist the surgeon using a new set of sensory information that state-of-the-art surgical robotic systems do not provide.

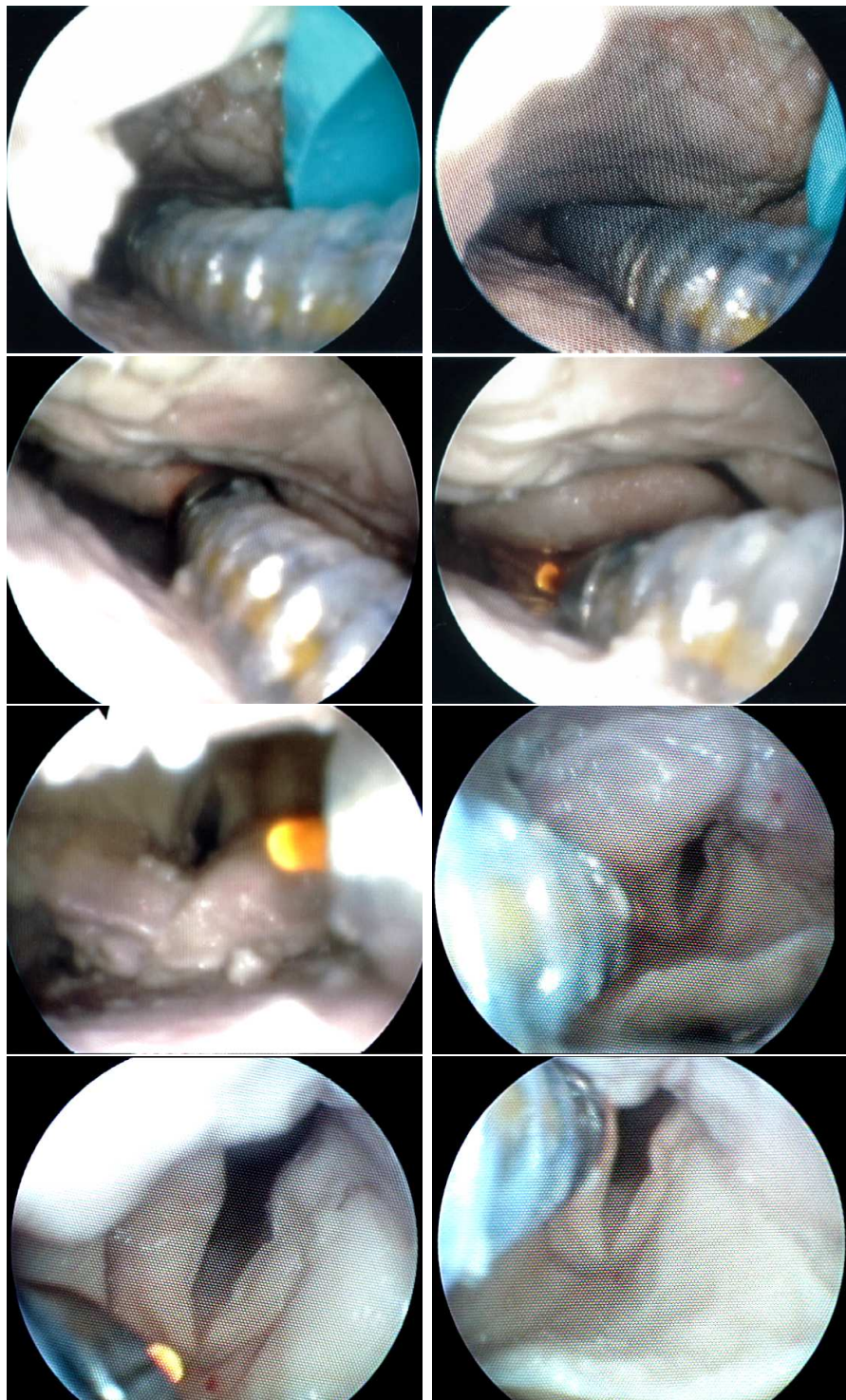


Figure VI.33: Image sequence of the insertion from the auxiliary bronchoscope inserted through the second nostril. The tip of the robot emerges from the nasopharyngeal tube, bends down to avoid the epiglottis, and continues the navigation of the upper airway cavity to reach the voice box.



Figure VI.34: Image of robots needle puncturing the left vocal fold.

The deployment of needles, flexible fiberscopes, laser fibers, and biopsy forceps already provide a minimal set of surgical instruments that could enable selected in-office surgical procedures such as collagen and steroid injection, biopsies, and laser energy delivery. The surgeon is provided with a multi-purpose platform for both diagnosis and intervention. The proposed surgical end-effector is suitable in size for operating in narrow spaces such as the larynx and its capabilities can be augmented with the installation of distal grippers and wrists [97]. Furthermore, the insertion of an additional arm through the second nostril would enable dual-arm operations such as resection and suturing in confined space.

Although the preliminary evaluation presented in this paper shows the promising use of continuum robots for deep surgical intervention, it also opens new technological challenges in terms of design, modeling, and control of these robots. Optimization algorithms are needed for the design of such robots in order to maximize the reachable workspace in unstructured environments. An accurate model of active and passive

segments in whole contact with flexible environments would improve telemanipulation accuracy and bandwidth. Although the human-in-the-loop architecture allows for successful maneuvering, control algorithms that use both intrinsic and extrinsic sensory information such as the one proposed in Chapter II are needed to compensate for unknown contacts, friction, and calibration uncertainties.

The goal of the cadaveric evaluation was to demonstrate the insertion procedure on real human anatomy and the feasibility of reaching the voice box. Although some of the organs were collapsed (i.e. the epiglottis) and the surrounding tissues stiff because of the preservation process, the continuum manipulator was able to navigate the upper airways and reach the vocal folds. Once there, instruments such as a fiberscope and a flexible needle were deployed and operated. This experiment demonstrate the efficacy of the compliant insertion algorithm in assisting the surgeon during the deployment phase and the flexibility of the control architecture in switching between semi-active and passive modes in order to steer away from anatomy.

The mobility of the end-effector remains, however, limited due to inadequate travel of the actuation pistons. As already shown by the inanimate model, the large deflection of the teflon stem require consist compensation along the actuation lines. However, as shown in the last two photographs of Figure VI.32 the end-effector was able to cover the entire length of the vocal fold

Conclusions

In this section, we presented the first integrated system for trans-nasal micro-surgical intervention of the throat. This approach has several advantages over the traditional TO minimally invasive techniques in terms of complications, cost, and setup time. The TN approach does not require devices such as the laryngoscope or a retractor and allows the procedure to be conducted under local rather than

general anesthesia. The elimination of general anesthesia reduces complications and allows more patients to be considered for minor and major head and neck surgeries. Furthermore, some surgical procedures could be performed in an office-based setting rather than in a fully equipped OR decreasing reimbursements by almost 80%. The proposed system demonstrated rapid and safe insertion into unknown anatomy and the ability to perform key surgical task such as drug delivery and tool deployment (needles, fiberscopes, biopsy forceps, laser fibers). The evaluation presented in this work provides critical design parameters for future revisions such as required actuator stroke, optimized segments lengths, and actuation compensation.

CHAPTER VII

CONCLUSIONS

Summary of Findings

Pioneering surgical paradigms such as Single Port Access Surgery and Natural Orifice Translumenal Surgery demand for intelligent surgical slaves that are both an extension of the surgeon's hand and an enhancement of the surgeon's senses. Traditional rigid-link robotic structures are unable to provide scarless access to the body while providing operators with enhanced intracorporeal dexterity, sensory presence, situation awareness, and methods to handle access and anatomical constraints. Continuum robots offer an opportunity to overcome these limitations because of their innate flexibility and ability to conform to unstructured environments, improve dexterity, sense forces, and reach deep surgical sites along tortuous paths. Future surgical continuum robots designed to meet the challenges of NOTES and SPAS will require intelligent algorithms and methods to allow for safe interaction with the anatomy along their entire structure, detect collisions, estimate contacts, avoid or exploit constraints, and exchange forces while guaranteeing responsiveness, accuracy, and maneuverability.

This doctoral dissertation proposed methods that address the aforementioned technological and theoretical gaps. These algorithms were evaluated on state-of-the-art surgical systems for single-port laparoscopy, transurethral bladder intervention, and trans-nasal microsurgery of the throat. These robotic systems were evaluated on key surgical tasks in plastic, ex-vivo, and cadaveric models.

In Chapter III algorithms for motion control of multi-segment continuum robots were presented and evaluated. Firstly, a tiered controller that uses both intrinsic and

extrinsic sensory information was discussed. The dual-feedback architecture (configuration and joint space) allowed to conventional PID controllers and model-based actuation compensation. The control law was implemented and evaluated on a three-segment multi-backbone continuum robot. Secondly, a complete master-slave telemanipulation framework was presented. The framework includes different master/robot mappings, pose-to-pose interpolation with error-based velocity profiles, redundancy resolution for three, two, and one segment continuum robots, configuration resolved motion rate, and different actuation compensation schemes. The control architecture was implemented on the Insertable Robotic Effectors Platform (IREP) and the Rapidly Deployable Robotic Platform (RDRP). These control schemes were used in multiple evaluations in ex-vivo and cadaveric models. Finally, a constrained motion control algorithm is proposed to address telemanipulation in confined spaces and access-based constraints. We proposed the enforcement of virtual fixtures in the configuration space of the robot manipulator exploiting lower dimensionality and allowing to constraint different sections. The constrained motion algorithm was evaluated on the RDRP demonstrating complete coverage of the urinary bladder otherwise impossible with conventional control schemes.

In Chapter IV algorithms for collision detection and estimation of contact locations along multi-segment continuum robots were presented and evaluated. Firstly, a collision detection method that uses actuation force sensing and a first order static model of the continuum is discussed. The deviation between the nominal and the current actuation forces allows to discern dynamic and static collisions. Secondly, a kinematics-based method for collision detection is presented. The method uses both extrinsic sensory information and the kinematic model of single- and multi-segment continuum robots. Collision is detected by monitoring the deviation between the theoretical and the actual screw motion of each end disk. This method allows to discern

multiple collisions, applies to n-segment continuum robots, and automatically reveals which segment is in contact with the environment. Finally, a kinematics-based estimation of contact location is proposed. The use of extrinsic sensory information and a constrained kinematic model allows to estimate the arc-length location of the contact along the primary backbone via a minimization strategy. Experiments demonstrated that the algorithm is able to identifies contact with an uncertainty equals to 20 % of the segment length.

In Chapter V an adaptation of the classic hybrid motion/force controller for continuum robots is presented and evaluated. The dual control inputs (force and motion) are merged in the configuration space of the manipulator using both differential inverse kinematics (motion) and the configuration space compliance matrix (force). By producing consistent configuration space commands, the inverse position of the manipulator is used along with model-based actuation compensation methods and feed-forward force-inputs. The framework was evaluated on a single segment continuum robots suitable for NOTES surgery. Firstly, force regulation experiments were conducted. The experiments demonstrated the ability to estimate and regulate forces at the tip of the robot. The controller's performances are tied to the intrinsic force estimator's sensitivity and accuracy. Secondly, force-regulated shape estimation of unknown flexible environments was demonstrated. The hybrid motion/force controller was embedded into the telemanipulation framework of Chapter III and unknown shapes were estimated using both force and position information obtained from the force estimator and an electro-magnetic sensors placed at the tip of the robot. The force controller ensured that the probe maintained contact with the tissue phantom. Finally, force-regulated stiffness estimation of unknown flexible environments was conducted. Force and position data from subsequent scans with different forces were compared and a linear stiffness model was used to produce a stiffness image of

the explored workspace. The experiments demonstrated that this strategy allows to discern change in stiffness.

Future Research Directions

This doctoral dissertation complements previous works that provide continuum robots with the ability to act as sensors as well as surgical intervention platforms. Simaan et al. [96] proposed a novel design, the kinematics, and the statics of a multi-backbone continuum robot. Xu investigated the intrinsic force sensing capabilities of these devices along with the validity of the circular bending-shape assumption and model-based actuation compensation. Goldman proposed algorithm for shape and stiffness estimation in compliant environments and a method for compliant insertion of multi-backbone continuum robots.

This doctoral work lays the foundation for future research on situation awareness and exploration of surgical continuum robots in compliant environments. The collision detection algorithm was paired with a constrained Extended Kalman filter for registration of surgical continuum robots to compliant environments [101]. Future work will integrate information from the contact estimation algorithm and the force-regulated shape and stiffness exploration. This additional information will improve the performance of the probabilistic registration to pre-operative model. In future developments, the stiffness imaging will be used to construct online virtual fixtures in order to improve safety and resection of tumors accuracy. Hybrid motion/force control based stiffness characterization will enable autonomous or semi-automated palpation in deep surgical sites, exploration of hidden cavities, and localization of vital features such as veins, arteries, or conduits.

REFERENCES

- [1] ABBOTT, J., MARAYONG, P., AND OKAMURA, A. M. Haptic virtual fixtures for robot-assisted manipulation. *Robotics Research* 28, August (2007), 49–64.
- [2] AGRAWAL, V., PEINE, W. J., YAO, B., AND CHOI, S. Control of Cable Actuated Devices using Smooth Backlash Inverse. In *2010 IEEE International Conference on Robotics and Automation* (Anchorage, AK, 2010), pp. 1074–1079.
- [3] ANGELES, J. Automatic Computation of the Screw Parameters of Rigid-Body Motions. Part II: Infinitesimally- Separated Positions. *Journal of Dynamic Systems, Measurement, and Control* 108, March (1986), 32–38.
- [4] BAJO, A., GOLDMAN, R. E., AND SIMAAN, N. Compliant Motion Control for Continuum Robots with Intrinsic Actuation Sensing. In *2011 IEEE International Conference on Robotics and Automation* (Shanghai, China, 2011), pp. 1126–1132.
- [5] BAJO, A., AND SIMAAN, N. Finding Lost Wrenches: Using Continuum Robots for Contact Detection and Estimation of Contact Location. In *2010 IEEE International Conference on Robotics and Automation* (Anchorage, AK, USA, 2010), pp. 3666–3673.
- [6] BAJO, A., AND SIMAAN, N. Kinematics-Based Detection and Localization of Contacts Along Multisegment Continuum Robots. *IEEE Transactions on Robotics* 28, 2 (Apr. 2012), 291–302.
- [7] BAKI, P., SZEKELY, G., AND KOSA, G. Miniature tri-axial force sensor for feedback in minimally invasive surgery. In *2012 4th IEEE RAS & EMBS International Conference on Biomedical Robotics and Biomechatronics (BioRob)* (Roma, Italy, June 2012), IEEE, pp. 805–810.
- [8] BASILEVSKY, A. *Applied Matrix Algebra in the Statistical Sciences*. Dover Publications, Inc., Mineola, NY, 1983.
- [9] BIRKFELLNER, W., WATZINGER, F., WANSCHITZ, F., EWERS, R., AND BERGMANN, H. Calibration of tracking systems in a surgical environment. *IEEE Transactions on Medical Imaging* 17, 5 (Oct. 1998), 737–42.
- [10] BOKELBORG, E. H., HUNT, K. H., AND RIDLEY, P. R. Spatial Motion-I: Points of inflection and the differential geometry of screws. *Mechanism and Machine Theory* 27, 1 (1992), 1–15.
- [11] BOTTEMA, O., AND ROTH, B. *Theoretical Kinematics*. Dover, New York, NY, 1979.

- [12] BOVÉ, M. J., JABBOUR, N., KRISHNA, P., FLAHERTY, K., SAUL, M., WUNAR, R., AND ROSEN, C. A. Operating room versus office-based injection laryngoplasty: a comparative analysis of reimbursement. *The Laryngoscope* 117, 2 (Feb. 2007), 226–30.
- [13] BURGNER, J., SWANEY, P. J., RUCKER, D. C., GILBERT, H. B., NILL, S. T., RUSSELL III, P. T. R., WEAVER, K. D., III, R. J. W., RUSSELL, P. T., AND WEBSTER, R. J. A Bimanual Teleoperated System for Endonasal Skull Base Surgery. In *2011 IEEE International Conference on Intelligent Robots and Systems* (San Francisco, CA, Sept. 2011), IEEE, pp. 2517–2523.
- [14] CAMARILLO, D. B., CARLSON, C. R., AND SALISBURY, J. K. Configuration Tracking for Continuum Manipulators With Coupled Tendon Drive. *IEEE Transactions on Robotics* 25, 4 (Aug. 2009), 798–808.
- [15] CAMARILLO, D. B., LOEWKE, K., CARLSON, C. R., AND SALISBURY, J. K. Vision based 3-D shape sensing of flexible manipulators. In *2008 IEEE International Conference on Robotics and Automation* (Pasadena, CA, 2008), pp. 2940–2947.
- [16] CAMARILLO, D. B., MILNE, C. F., CARLSON, C. R., ZINN, M. R., AND SALISBURY, J. K. Mechanics Modeling of Tendon-Driven Continuum Manipulators. *IEEE Transaction on Robotics* 24, 6 (2008), 1262–1273.
- [17] CAUBERG, E. C., DE LA ROSETTE, J. J., AND DE REIJKE, T. M. How to improve the effectiveness of transurethral resection in nonmuscle invasive bladder cancer? *Current Opinion in Urology* 19, 5 (2009), 504–510.
- [18] CHAN, T. F., AND DUBEY, R. V. A Weighted Least-Norm Solution Based Scheme for Avoiding Joint Limits for Redundant Joint Manipulators. *IEEE Transaction on Robotics and Automation* 11, 2 (1995), 286–292.
- [19] CHIRIKJIAN, G. S., AND BURDICK, J. W. An obstacle avoidance algorithm for hyper-redundant manipulators. In *Proceedings., IEEE International Conference on Robotics and Automation* (1990), IEEE Comput. Soc. Press, pp. 625–631.
- [20] CHIRIKJIAN, G. S., AND BURDICK, J. W. A Modal Approach to Hyper-Redundant Manipulator Kinematics. *IEEE Transaction on Robotics and Automation* 10, 3 (1994), 343–354.
- [21] CONZEN, P., AND PETER, K. Inhalation anaesthesia at the extremes of age: geriatric anaesthesia. *Anaesthesia* 50 Suppl (Oct. 1995), 29–33.
- [22] CROOM, J. M., RUCKER, D. C., ROMANO, J. M., AND WEBSTER, R. J. I. Visual Sensing of Continuum Robot Shape Using Self-Organizing Maps. In *2010 IEEE International Conference on Robotics and Automation* (Anchorage, AK, 2010), pp. 4591–4596.

- [23] DE LUCA, A., HADDADIN, S., AND HIRZINGER, G. Collision Detection and Safe Reaction with the DLR-III Lightweight Manipulator Arm. In *2006 IEEE/RSJ International Conference on Intelligent Robots and Systems* (Beijing, China, 2006), pp. 1623–1630.
- [24] DE LUCA, A., AND MANES, C. Modeling of Robots in Contact with a Dynamic Environment. *IEEE Transaction on Robotics and Automation* 10, 4 (1994), 542–548.
- [25] DEBUS, T., DUPONT, P., AND HOWE, R. Contact State Estimation using Multiple Model Estimation and Hidden Markov Models. *2The International Journal of Robotics Research* 23, 4-5 (2004), 399–413.
- [26] DEGANI, A., CHOSET, H., WOLF, A., AND ZENATI, M. A. Highly Articulated Robotic Probe for Minimally Invasive Surgery. In *2006 IEEE International Conference on Robotics and Automation* (Orlando, FL, USA, 2006), pp. 4167–4172.
- [27] DIMAIO, S. da Vinci and Beyond. In *2010 IEEE International Conference on Robotics and Automation Workshop on Medical Cyber-Physical Systems* (Anchorage, AK, 2010).
- [28] DING, J., GOLDMAN, R. E., XU, K., ALLEN, P. K., FOWLER, D. L., AND SIMAAN, N. Design and Coordination Kinematics of an Insertable Robotic Effectors Platform for Single-Port Access Surgery. *IEEE/ASME Transactions on Mechatronics* (2012), 1–13.
- [29] DING, J., XU, K., GOLDMAN, R. E., ALLEN, P. K., FOWLER, D. L., AND SIMAAN, N. Design, Simulation and Evaluation of Kinematic Alternatives for Insertable Robotic Effectors Platforms in Single Port Access Surgery. In *2010 IEEE International Conference on Robotics and Automation* (Anchorage, AK, 2010), pp. 1053–1058.
- [30] DUPONT, P., LOCK, J., ITKOWITZ, B., AND BUTLER, E. Design and Control of Concentric-Tube Robots. *IEEE Transaction on Robotics* 26, 2 (2010), 209–225.
- [31] EBERMAN, B. S., AND SALISBURY, J. K. Determinant of Manipulator Contact Information from Joint Torque Measurements. In *Experimental Robotics I*, vol. 139. Springer, 1990, pp. 463–473.
- [32] FEATHERSTONE, R. Modeling and Control of Contact Between Constrained Rigid Bodies. *IEEE Transaction on Robotics and Automation* 20, 1 (2004), 82–92.

- [33] FEATHERSTONE, R., THIEBAUT, S. S., AND KHATIB, O. A General Contact Model for Dynamically-Decoupled Force/Motion Control. In *1999 IEEE International Conference on Robotics and Automation* (1999), no. May, pp. 3281–3286.
- [34] FLS. FLS Laparoscopic Trainer Box.
- [35] GOLDMAN, R., BAJO, A., MACLACHLAN, L., PICKENS, R., HERRELL, S., AND SIMAAN, N. Design and Performance Evaluation of a Minimally Invasive Telerobotic Platform for Transurethral Surveillance and Intervention. *IEEE Transactions on Biomedical Engineering* (2012), 1–1.
- [36] GOLDMAN, R. E., BAJO, A., SUH, L. K., PICKENS, R. B., HERRELL, S. D., AND SIMAAN, N. Design and Evaluation of a Minimally Invasive Telerobotic Platform for Transurethral Intervention and Surveillance. *IEEE Transaction on Biomedical Engineering accepted* (2013).
- [37] GRAVAGNE, I. A., AND WALKER, I. D. Kinematic Transformations for Remotely-Actuated Planar Continuum Robots. In *2000 IEEE International Conference on Robotics & Automation* (San Francisco, 2000), no. April, pp. 19–26.
- [38] GUTHART, G., AND SALISBURY, K. The IntuitiveTM Telesurgery System: Overview and Application. In *2000 IEEE International Conference on Robotics and Automation* (2000), pp. 618–621.
- [39] HADDADIN, S., DE LUCA, A., AND HIRZINGER, G. Collision Detection and Reaction: A Contribution to Safe Physical Human-Robot Interaction. In *2008 IEEE/RSJ International Conference on Intelligent Robots and Systems* (Nice, France, 2008), pp. 3356–3363.
- [40] HAGBERG, C., GEORGI, R., AND KRIER, C. Complications of managing the airway. *Best Practice & Research Clinical Anaesthesiology* 19, 4 (Dec. 2005), 641–659.
- [41] HANNAN, M. W., AND WALKER, I. D. Kinematics and the Implementation of an Elephant's Trunk Manipulator and Other Continuum Style Robots. *Journal of Robotic Systems* 20, 2 (2003), 45–63.
- [42] HILLEL, A. T., KAPOOR, A., SIMAAN, N., TAYLOR, R. H., AND FLINT, P. Applications of robotics for laryngeal surgery. *Otolaryngologic clinics of North America* 41, 4 (Aug. 2008), 781–91, vii.
- [43] HO, S. C., HIBBERD, R. D., AND DAVIES, B. L. Robot Assisted Knee Surgery. *IEEE Engineering in Medicine and Biology Magazine* 14, 3 (1995), 292–299.

- [44] HOGAN, N. Impedance Control: An Approach to Manipulation: Part I Theory. *Journal of Dynamic Systems, Measurement, and Control* 107, 1 (1985), 1.
- [45] HOWELL, L. L. *Compliant Mechanisms*. Wiley-Interscience, 2001.
- [46] IKITS, M., BREDERSON, J. D., HANSEN, C. D., AND HOLLERBACH, J. M. An Improved Calibration Framework for Electromagnetic Tracking Devices. In *2001 IEEE Virtual Reality* (Yokohama, Japan, 2001), IEEE Comput. Soc, pp. 63–70.
- [47] IKUTA, K., YAMAMOTO, K., AND SASAKI, K. Development of remote micro-surgery robot and new surgical procedure for deep and narrow space. In *2003 IEEE International Conference on Robotics and Automation* (Taipei, Taiwan, 2003), vol. 1, IEEE, pp. 1103–1108.
- [48] INSTITUTE, N. C. Bladder Cancer.
- [49] JONES, B. A., AND WALKER, I. D. Kinematics for Multisection Continuum Robots. *IEEE Transactions on Robotics* 22, 1 (Dec. 2006), 43–57.
- [50] JONES, D. B., MAITHEL, S. K., AND SCHNEIDER, B. E. *Atlas of Minimally Invasive Surgery*. Cine-Med, Inc., 2006.
- [51] KAPOOR, A., SIMAAN, N., AND TAYLOR, R. Suturing in Confined Spaces: Constrained Motion Control of a Hybrid 8-DoF Robot". In *12th International Conference on Advanced Robotics* (International Conference on Advanced Robotics (ICAR'2005), 2005), IEEE, pp. 452–459.
- [52] KAPOOR, A., AND TAYLOR, R. H. A Constrained Optimization Approach to Virtual Fixtures for Multi-Handed Tasks. In *IEEE International Conference on Robotics and Automation* (Pasadena, CA, 2008), pp. 3401–3406.
- [53] KESNER, S. B., AND HOWE, R. D. Design and Control of Motion Compensation Cardiac Catheters. In *2010 IEEE International Conference on Robotics and Automation* (Anchorage, AK, 2010), pp. 1059–1065.
- [54] KESNER, S. B., AND HOWE, R. D. Force Control of Flexible Catheter Robots for Beating Heart Surgery. In *2011 IEEE International Conference on Robotics and Automation* (Shanghai, China, Jan. 2011), pp. 1589–1594.
- [55] KESNER, S. B., HOWE, R. D., AND MEMBER, S. Position Control of Motion Compensation Cardiac Catheters. *IEEE Transaction on Robotics* 27, 6 (2011), 1045–1055.
- [56] KHATIB, O. A Unified Approach for Motion and Force Control of Robot Manipulators: The Operational Space Formulation. *IEEE Journal of Robotics and Automation* 3, 1 (1987), 43–53.

- [57] KRAGIC, D., MARAYONG, P., LI-MING SU, OKAMURA, A. M., AND HAGER, G. D. Human-Machine Collaborative Systems for Microsurgical Applications. *The International Journal of Robotics Research* 24, 9 (Sept. 2005), 731–741.
- [58] LAWSON, G., MATAR, N., REMACLE, M., JAMART, J., AND BACHY, V. Transoral robotic surgery for the management of head and neck tumors: learning curve. *European archives of oto-rhino-laryngology : official journal of the European Federation of Oto-Rhino-Laryngological Societies (EUFOS) : affiliated with the German Society for Oto-Rhino-Laryngology - Head and Neck Surgery* 268, 12 (Dec. 2011), 1795–801.
- [59] LIPKIN, H., AND DUFFY, J. Hybrid Twist and Wrench Control for a Robotic Manipulator. *Transaction of the ASME* 110 (1988), 138–144.
- [60] LOCK, J., AND DUPONT, P. E. Friction Modeling in Concentric Tube Robots. In *2011 IEEE International Conference on Robotics and Automation* (Shanghai, China, Jan. 2011), pp. 1139–1146.
- [61] LUMELSKY, V. J., AND CHEUNG, E. Real-Time Collision Avoidance in Tele-operated Whole-Sensitive Robot Arm Manipulators. *IEEE Transactions on Systems, Man, and Cybernetics* 23, 1 (1993), 194–203.
- [62] MA, S., AND KONNO, M. An obstacle avoidance scheme for hyper-redundant manipulators-global motion planning in posture space. In *Proceedings of International Conference on Robotics and Automation* (1997), vol. 1, IEEE, pp. 161–166.
- [63] MAHVASH, M., AND DUPONT, P. E. Mechanics of dynamic needle insertion into a biological material. *IEEE transactions on bio-medical engineering* 57, 4 (Apr. 2010), 934–43.
- [64] MAHVASH, M., AND DUPONT, P. E. Stiffness Control of Surgical Continuum Manipulators. *IEEE Transaction on Robotics* 27, 2 (2011), 334–345.
- [65] MAHVASH, M., AND OKAMURA, A. M. Friction Compensation for a Force-Feedback Telerobotic System. In *2006 IEEE International Conference on Robotics and Automation* (Orlando, FL, 2006), no. May, pp. 3268–3273.
- [66] MASON, M. T. Compliance and Force Control for Computer Controlled Manipulators. *IEEE Transaction on Systems, Man, and Cybernetics smc-11*, 6 (1981), 418–432.
- [67] MASON, M. T., AND SALISBURY, J. K. *Robot Hands and the Mechanics of Manipulation*. MIT Press, Cambridge, MA, 1985.

- [68] MATSUMOTO, T., AND KOSUGE, K. Collision Detection of Manipulator Based on Adaptive Control Law. In *2001 IEEE/ASME International Conference on Advanced Intelligent Mechatronics* (Como, Italy, 2001), pp. 177–182.
- [69] McMULLIN, B. T., BLUMIN, J. H., AND MERATI, A. L. Thermal injury to the tongue from an operative laryngoscope. *Otolaryngology-head and neck surgery : official journal of American Academy of Otolaryngology-Head and Neck Surgery* 137, 5 (Nov. 2007), 798–802.
- [70] NAKAMURA, Y. *Advanced Robotics: Redundancy and Optimization*. Addison-Wesley Longman Publishing Co., Inc., Boston, MA, USA, 1990.
- [71] PARK, J., AND KHATIB, O. Robot Multiple Contact Control. *Robotica* 26, 05 (2008), 667–677.
- [72] PATRONIK, N. A., ZENATI, M. A., AND RIVIERE, C. N. Crawling on the Heart : A Mobile Robotic Device for Minimally Invasive Cardiac Interventions. In *Medical Image Computing And Computer-Assisted Intervention - MICCAI 2004* (2004), pp. 9–16.
- [73] PENNING, R. S., JUNG, J., BORGSTADT, J. A., FERRIER, N. J., AND MICHAEL, R. Towards Closed Loop Control of a Continuum Robotic Manipulator for Medical Applications. In *2011 IEEE International Conference on Robotics and Automation* (Shanghai, China, 2011), pp. 4822–4827.
- [74] PETROVSKAYA, A., PARK, J., AND KHATIB, O. Probabilistic Estimation of Whole Body Contacts for Multi-Contact Robot Control. In *2007 IEEE International Conference on Robotics and Automation* (Rome, 2007), no. c, pp. 568–573.
- [75] PHEE, S. J., LOW, S. C., SUN, Z. L., HO, K. Y., HUANG, W. M., AND THANT, Z. M. Robotic system for no-scar gastrointestinal surgery. *The international journal of medical robotics + computer assisted surgery : MRCAS* 4, 1 (Mar. 2008), 15–22.
- [76] PICCIGALLO, M., SCARFOGLIERO, U., QUAGLIA, C., PETRONI, G., VALDASTRI, P., MENCIASSI, A., AND DARIO, P. Design of a Novel Bimanual Robotic System for Single-Port Laparoscopy. *IEEE/ASME Transaction on Mechatronics* 15, 6 (2010), 871–878.
- [77] POTTMANN, H., AND WALLNER, J. *Computational Line Geometry*. Springer, New York, 1999.
- [78] RAIBERT, M. H., AND CRAIG, J. J. Hybrid Position/Force Control of Manipulators. *Journal of Dynamic Systems, Measurement, and Control* 103, 2 (1981), 126.

- [79] RAY, E. R., AND O'BRIEN, T. S. Should Urologists Be Spending more Time on the Golf Course? *BJU International* 100, 4 (2007), 728–729.
- [80] REITER, A., BAJO, A., ILIOPoulos, K., SIMAAN, N., AND ALLEN, P. K. Learning-Based Configuration Estimation of a Multi-Segment Continuum Robot. In *The Fourth IEEE RAS/EMBS International Conference on Biomedical Robotics and Biomechatronics* (Roma, Italy, 2012), p. accepted.
- [81] REITER, A., GOLDMAN, R. E., BAJO, A., ILIOPoulos, K., SIMAAN, N., AND ALLEN, P. K. A Learning Algorithm for Visual Pose Estimation of Continuum Robots. In *2011 IEEE/RSJ International Conference on Intelligent Robots and Systems* (San Francisco, CA, USA, 2011), pp. 2390–2396.
- [82] RIVERA-SERRANO, C. M., JOHNSON, P., ZUBIATE, B., KUENZLER, R., CHOSET, H., ZENATI, M., TULLY, S., AND DUVVURI, U. A transoral highly flexible robot: Novel technology and application. *The Laryngoscope* 122, 5 (May 2012), 1067–71.
- [83] ROBINSON, G., AND DAVIES, J. Continuum robots - a state of the art. In *1999 IEEE International Conference on Robotics and Automation* (Detroit, MI, USA, 1999), vol. 4, Ieee, pp. 2849–2854.
- [84] ROSENBERG, L. Virtual fixtures: Perceptual tools for telerobotic manipulation. In *Proceedings of IEEE Virtual Reality Annual International Symposium* (1993), Ieee, pp. 76–82.
- [85] RUCKER, D. C., JONES, B. A., AND WEBSTER III, R. J. A Geometrically Exact Model for Externally Loaded Concentric-Tube Continuum Robots. *IEEE Transaction on Robotics* 26, 5 (2010), 769–780.
- [86] RUCKER, D. C., AND WEBSTER, III, R. J. Deflection-Based Force Sensing for Continuum Robots : A Probabilistic Approach. In *2011 IEEE/RSJ International Conference on Intelligent Robots and Systems* (2011), pp. 3764–3769.
- [87] SAITO, S. Transurethral en bloc resection of bladder tumors. *The Journal of urology* 166, 6 (Dec. 2001), 2148–50.
- [88] SALISBURY, J. Active stiffness control of a manipulator in cartesian coordinates. In *1980 19th IEEE Conference on Decision and Control including the Symposium on Adaptive Processes* (1980), pp. 95–100.
- [89] SEIBOLD, U., KUBLER, B., AND HIRZINGER, G. Prototype of Instrument for Minimally Invasive Surgery with 6-Axis Force Sensing Capability. In *Proceedings of the 2005 IEEE International Conference on Robotics and Automation* (Barcelona, Spain, 2005), 496-501, Ed., IEEE, pp. 496–501.

- [90] SENTIS, L., PARK, J., AND KHATIB, O. Compliant Control of Multicontact and Center-of-Mass Behaviors in Humanoid Robots. *IEEE Transactions on Robotics* 26, 3 (June 2010), 483–501.
- [91] SEVERN, A. Anaesthesia and the preparation and management of elderly patients undergoing surgery. *European journal of cancer (Oxford, England : 1990)* 43, 15 (Oct. 2007), 2231–4.
- [92] SICILIANO, B., SCIavicco, L., VILLANI, L., AND ORIOLO, G. *Robotics: Modelling, Planning, and Control*. 2009.
- [93] SICILIANO, B., AND VILLANI, L. *Robot Force Control*. Kluwer Academic Publishers, Boston, MA, 1999.
- [94] SIMAAN, N. Snake-Like Units Using Flexible Backbones and Actuation Redundancy for Enhanced Miniaturization. In *2005 IEEE International Conference on Robotics and Automation* (Barcelona, Spain, 2005), IEEE, pp. 3023–3028.
- [95] SIMAAN, N., TAYLOR, R., AND FLINT, P. High Dexterity Snake-like Robotic Slaves for Minimally Invasive Telesurgery of the Upper Airway. In *International Conference on Medical Image Computing and Computer-Assisted Intervention (MICCAI '04)*, LNCS 3217 (2004), C. Barillot, D. R. Haynor, and P. Hillier, Eds., vol. LNCS 3217, pp. 17–24.
- [96] SIMAAN, N., TAYLOR, R. H., AND FLINT, P. A Dexterous System for Laryngeal Surgery. In *2004 IEEE International Conference on Robotics and Automation* (New Orleans, LA, 2004), IEEE, pp. 351–357.
- [97] SIMAAN, N., XU, K., WEI, W., KAPOOR, A., KAZANZIDES, P., TAYLOR, R. H., AND FLINT, P. Design and Integration of a Telerobotic System for Minimally Invasive Surgery of the Throat. *The International Journal of Robotics Research* 28, 9 (2009), 1134–1153.
- [98] SU, H., CARDONA, D. C., SHANG, W., CAMILO, A., COLE, G. A., RUCKER, D. C., WEBSTER, R. J., AND FISCHER, G. S. A MRI-Guided Concentric Tube Continuum Robot with Piezoelectric Actuation: A Feasibility Study. In *2012 IEEE International Conference on Robotics and Automation* (St. Paul, MN USA, 2012), no. May.
- [99] TAYLOR, R., JENSEN, P., WHITCOMB, L., BARNES, A., KUMAR, R., STOIANOVICI, D., GUPTA, P., WANG, Z., DEJUAN, E., AND KAVOUSSI, L. Steady-hand robotic system for microsurgical augmentation. *International Journal of Robotics Research* 18, 12 (1999), 1201–1210.
- [100] TORRES, L. G., AND ALTEROVITZ, R. Motion Planning for Concentric Tube Robots Using Mechanics-based Models. In *2011 IEEE/RSJ International Conference on Intelligent Robots and Systems* (San Francisco, CA, USA, 2011), pp. 5153–5159.

- [101] TULLY, S., BAJO, A., KANTOR, G., CHOSET, H., AND SIMAAN, N. Constrained Filtering with Contact Detection Data for the Localization and Registration of Continuum Robots in Flexible Environments. In *2012 IEEE International Conference on Robotics and Automation* (St. Paul, MI USA, 2012).
- [102] UKAI, R., KAWASHITA, E., AND IKEDA, H. A new technique for transurethral resection of superficial bladder tumor in 1 piece. *The Journal of Urology* 163, 3 (2000), 878–879.
- [103] VALDASTRI, P., HARADA, K., MENCIASSI, A., BECCAI, L., STEFANINI, C., FUJIE, M., AND DARIO, P. Integration of a miniaturised triaxial force sensor in a minimally invasive surgical tool. *IEEE transactions on bio-medical engineering* 53, 11 (Nov. 2006), 2397–400.
- [104] WAGNER, C. R., STYLOPOULOS, N., JACKSON, P. G., AND HOWE, R. D. The Benefits of Force Feedback in Surgery: Examination of Blunt Dissection. *Presence: Teleoperators and Virtual Environments* 16, 3 (2007), 252–262.
- [105] WEBSTER III, R. J., AND JONES, B. A. Design and Kinematic Modeling of Constant Curvature Continuum Robots: A Review. *The International Journal of Robotics Research* (June 2010).
- [106] WEBSTER III, R. J., ROMANO, J. M., AND COWAN, N. J. Mechanics of Precurved-Tube Continuum Robots. *IEEE Transaction on Robotics* 25, 1 (2009), 67–78.
- [107] WEI, W., AND SIMAAN, N. Modeling, Force Sensing, and Control of Flexible Cannulas for Microstent Delivery. *Journal of Dynamic Systems, Measurement, and Control* 134, 4 (2012), 041004.
- [108] WEI TECH, A., KHOSLA, P., AND RIVIERE, C. An Intelligent Hand-Held Microsurgical Instrument for Improved Accuracy. In *23rd Annual International Conference of the IEEE Engineering in Medicine and Biology Society* (Istanbul, Turkey, 2001), pp. 25–28.
- [109] WEINSTEIN, G. S., O’MALLEY, B. W., MAGNUSON, J. S., CARROLL, W. R., OLSEN, K. D., DAIO, L., MOORE, E. J., AND HOLINGER, F. C. Transoral robotic surgery: A multicenter study to assess feasibility, safety, and surgical margins. *The Laryngoscope* (July 2012), 1–7.
- [110] WHITNEY, D. E. Resolved Motion Rate Control of Manipulators and Human Prostheses. *IEEE Transaction on Man-Machine Systems MMS-10*, 2 (June 1969), 47–53.
- [111] WHITNEY, D. E. Force Feedback Control of Manipulator Fine Motions. *Journal of Dynamic Systems, Measurement, and Control* 99, 2 (1977), 91.

- [112] WOLF, A., AND DEGANI, A. Classifying Knee Pathologies Using Instantaneous Screws of the Six Degrees-of-Freedom Knee Motion. In *2006 IEEE International Conference on Robotics and Automation (ICRA '06)* (Orlando, FL, 2006), no. May, pp. 2946–2951.
- [113] XU, K., GOLDMAN, R. E., DING, J., ALLEN, P. K., FOWLER, D. L., AND SIMAAN, N. System Design of an Insertable Robotic Effector Platform for Single Port Access (SPA) Surgery. In *IEEE International Conference on Intelligent Robots and Systems* (St. Louis, USA, 2009), IEEE, pp. 5546–5552.
- [114] XU, K., AND SIMAAN, N. Actuation Compensation for Flexible Surgical Snake-like Robots with Redundant Remote Actuation. In *2006 IEEE International Conference on Robotics and Automation* (Orlando, FL, USA, 2006), no. May, pp. 4148–4154.
- [115] XU, K., AND SIMAAN, N. An Investigation of the Intrinsic Force Sensing Capabilities of Continuum Robots. *IEEE Transactions on Robotics* 24, 3 (June 2008), 576–587.
- [116] XU, K., AND SIMAAN, N. Analytic Formulation for Kinematics, Statics, and Shape Restoration of Multibackbone Continuum Robots Via Elliptic Integrals. *ASME Journal of Mechanisms and Robotics* 2, 1 (2010).
- [117] XU, K., AND SIMAAN, N. Intrinsic Wrench Estimation and Its Performance Index for Multisegment Continuum Robots. *IEEE Transactions on Robotics* 26, 3 (June 2010), 555–561.
- [118] YOSHIKAWA, T. Force Control of Robot Manipulators. In *2000 IEEE International Conference on Robotics and Automation* (San Francisco, CA, USA, 2000), no. April, pp. 220–226.
- [119] ZANGANEH, K. E., AND ANGELES, J. The Inverse Kinematics of Hyper-Redundant Manipulators Using Splines. In *1995 IEEE International Conference on Robotics and Automation* (Nagoya , Japan, 1995), pp. 2797–2802.
- [120] ZHANG, Y., AND TING, K.-L. Point-Line Distance Under Riemannian Metrics. *Journal of Mechanical Design* 130, 9 (2008), 092304.
- [121] ZHOU, J., SHEN, X., PETRIU, E. M., AND GEORGANAS, N. D. Linear Velocity and Acceleration Estimation of 3 DOF Haptic Interface. In *IEEE International Workshop on Haptic Audio Visual Environments and their Application (HAVE 2008)* (Ottawa, Canada, 2008), pp. 137–142.